Synthesis of magnetic nanoparticles and carbon based nanohybrid materials for biomedical and energy application

Xiao Jie Liu

▶ **To cite this version:**

Xiao Jie Liu. Synthesis of magnetic nanoparticles and carbon based nanohybrid materials for biomedical and energy application. Chemical Physics [physics.chem-ph]. Université de Strasbourg, 2014. English. NNT : 2014STRAF055 . tel-01127352

HAL Id: tel-01127352

https://theses.hal.science/tel-01127352

Submitted on 7 Mar 2015

HAL is a multi-disciplinary open access archive for the deposit and dissemination of scientific research documents, whether they are published or not. The documents may come from teaching and research institutions in France or abroad, or from public or private research centers.

L'archive ouverte pluridisciplinaire **HAL**, est destinée au dépôt et à la diffusion de documents scientifiques de niveau recherche, publiés ou non, émanant des établissements d'enseignement et de recherche français ou étrangers, des laboratoires publics ou privés.

UNIVERSITÉ DE STRASBOURG

ÉCOLE DOCTORALE DES SCIENCES CHIMIQUES

ICPEES, UMR 7515 CNRS

IPCMS, UMR 7504 CNRS

THÈSE

présentée par

Xiao Jie LIU

soutenue le: **18 Décembre 2014**

pour obtenir le grade de

Docteur de l'université de Strasbourg

Discipline / Spécialité : Chimie /Chimie Physique

Synthesis of Magnetic Nanoparticles and Carbon Based Nanohybrid Materials for Biomedical and Energy Application

Synthèse de matériaux hybrides à base de carbone et de nanoparticules magnétiques : application dans le biomédical et dans le domaine de l'énergie

Membres du jury

Directeur de Thèse:	**Dr Dominique BEGIN**	Chargé de recherche, UDS, Strasbourg
Co-Directeur de thèse:	**Prof. Sylvie BEGIN-COLIN**	Professeur, UDS, Strasbourg
Rapporteur externe:	**Dr Katerina SOULANTIKA**	Chargé de recherche, INSA Toulouse
Rapporteur externe:	**Prof. Alain CELZARD**	Prof. ENSTIB, Université de Lorraine
Examinateur:	**Prof. Corinne PETIT**	Professeur, UDS, Strasbourg
Examinateur:	**Dr Olivier SANDRE**	Directeur de recherche, Bordeaux

RESUME

Dans les dernières décennies, les nanomatériaux et leurs propriétés uniques ont été largement étudiés, du point de vue des nanosciences, mais également pour leur utilisation dans le domaine des nanotechnologies. La science des nanomatériaux ouvre un champ infini de recherche et d'applications pratiques: la miniaturisation des composants dans l'industrie électronique, le stockage de plus en plus d'énergie dans de plus en plus petits volumes, le développement de nanomatériaux permettant de diagnostiquer et de traiter des maladies... Parmi les nanoparticules largement développées, nous pouvons citer les nanoparticules magnétiques. En effet, les nanoparticules (NPs) magnétiques, font l'objet de nombreuses études et suscitent un très grand intérêt scientifique en raison de leurs propriétés magnétiques particulières liées à leur taille et à leur rapport surface/volume élevé. En effet, quand la taille des particules magnétique diminue, ces nanoparticules deviennent super-paramagnétiques, c'est-à-dire qu'elles ne présentent plus d'aimantation à température ambiante. Mais leurs propriétés magnétiques ne sont pas seulement dépendantes de la taille mais aussi de leur forme et de leur composition (coeur-coquille par exemple. … La maîtrise de la synthèse de nanoparticules magnétiques avec des compositions, des formes et des tailles contrôlées est donc un sujet très important actuellement et l'objectif est de bien comprendre les mécanismes de synthèse et les relations structure-propriétés magnétiques.

De plus l'association de nanoparticules avec des nanostructures (nanotubes, nanofibres, graphènes...) afin d'élaborer des composites combinant les propriétés des deux nanomatériaux est actuellement un sujet en plein développement tant dans la recherche "académique" qu'industrielle pour lesquelles les applications potentielles sont nombreuses. Parmi de tels nano-composites, on peut notamment citer les nanoparticules (NPs) d'oxydes métalliques associées avec des nanostructures de carbone (nanotubes, nanofibres, graphènes...) afin d'exploiter les propriétés essentielles des deux matériaux : propriétés mécaniques, conductivités électriques et thermiques, inertie pour le carbone et propriétés magnétiques et stabilité chimique des NPs. Du coté des nanostructures carbonées (et en particulier les nanotubes de carbone), elles sont de plus en plus utilisées dans divers secteurs proches du biomédical (tels la fluorescence dans le proche infrarouge, dans la spectroscopie Raman, dans la tomographie et les ultrasons) mais surtout dans le domaine de l'énergie (comme tout carbone conducteur...). L'association de nanoparticules d'oxydes métalliques avec des nanotubes ou des feuillets de graphène est très prometteuse dans de nombreux domaines comme la catalyse, le biomédical et l'énergie. En particulier dans le domaine de l'énergie, elle peut conduire à de nouveaux matériaux d'électrodes pour les supercondensateurs ou batteries Li-ion en combinant les propriétés de support et les propriétés électriques des nanomatériaux carbonés à celles de nanoparticules d'oxyde métallique. En effet les nanoparticules d'oxyde métallique sont développées dans ce domaine en raison de leur coût, abondance et de leur haute capacité spécifique théorique. L'association des propriétés en imagerie et hyperthermie des nanotubes de carbones à celles des nanoparticules d'oxyde de fer est également prometteuse pour développer des nano-objets théranostiques pour le traitement du cancer, c'est-à-dire combinant diagnostique et thérapie.

Dans ce contexte, les travaux de cette thèse ont été centrés sur la synthèse de nanoparticules magnétiques d'oxyde de fer et d'oxyde de cobalt et de nanoparticules cœur-coquille constituées d'un cœur d'oxyde de fer recouvert d'oxyde de cobalt et l'élaboration de nanomatériaux composites nanostructures carbonées/nanoparticules d'oxyde métallique pour des applications dans le domaine biomédical et celui de l'énergie. Les résultats de ce mémoire résultent d'un travail interdisciplinaire effectué essentiellement à l'ICPEES (Institut de Chimie et des Procédés pour l'Energie, l'Environnement et la Santé) et à l'IPCMS (Institut de Physique et Chimie des Matériaux de Strasbourg). Pour l'application des nanomatériaux composites dans le domaine biomédical avec comme finalité l'hyperthermie et l'imagerie, une collaboration a été initiée avec l'Institut de Biologie Moléculaire et Cellulaire (IBMC à Strasbourg) et le Laboratoire de la Matière et des Systèmes Complexes (MSC à Paris Diderot). L'étude des propriétés des nanocomposites dans le domaine de l'énergie (batterie lithium-ion) a été effectuée en collaboration avec le Centre Inter-universitaire de Recherche et d'Ingénierie des Matériaux (CIRIMAT) de Toulouse.

Ce travail est divisé en cinq chapitres. Après un chapitre introductif, le chapitre 2 est consacré à la synthèse de NPs d'oxyde de fer et de cobalt par la méthode de décomposition thermique et en particulier à l'influence de la nature des ligands sur la forme et la taille de ces NPs. Le chapitre 3 est centré sur la synthèse de nanoparticules de composition cœur-coquille Fe_3O_4@CoO présentant des propriétés originales en raison du couplage magnétique entre l'oxyde de cobalt qui est antiferromagnétique et l'oxyde de fer qui est ferrimagnétique. Le chapitre 4 concerne l'élaboration de nanostructures composites nanotubes de carbone/nanoparticules d'oxydes magnétiques pour le biomédical : l'objectif a été d'encapsuler des NPsd'oxyde de fer et de CoO à l'intérieur des nanotubes de carbone avec un rendement élevé pour les tester ensuite *in vitro* en tant qu'agents de diagnostic et de thérapie. Enfin, dans le dernier chapitre, des nanocomposites à base d'oxydes de niobium et de graphènes ou nanotubes de carbone ont été élaborés et testés comme matériaux d'électrode pour les batteries Lithium-ions.

Le chapitre 1 présente un état de l'art assez général sur les nanoparticules d'oxydes métalliques et sur les nanostructures carbonées et leurs applications. Le second chapitre s'intéresse en particulier à l'influence de la nature des ligands sur la composition, la taille et la forme de nanoparticules de $Fe_{3-x}O_4$ et CoO synthétisées par décomposition thermique. Cette méthode de synthèse consiste à décomposer thermiquement un précurseur métallique (ici le stéarate de fer et le stéarate de cobalt) en présence de ligands agissant comme surfactant dans un solvant ayant une haute température d'ébullition. La synthèse de nanoparticules d'oxyde de fer par décomposition thermique du stéarate de fer est bien maitrisée mais la synthèse de nanoparticules d'oxyde de cobalt à partir du stéarate de cobalt apparait plus difficile. En effet bien que le fer et le cobalt soient voisins dans le tableau périodique des éléments, la synthèse de NPs de CoO par la décomposition du stéarate de cobalt conduit à de très faibles rendements en NP et en plus la morphologie est différente. Pour augmenter ce rendement, un ligand amine a été testé et a conduit à des nanoparticules présentant une nouvelle morphologie. Dans ce contexte, nous nous sommes intéressés à l'influence de la nature des ligands amine ou carboxylate sur la taille, la forme et la composition des NPs. Quelle que soit la nature des

ligands, des nanoparticules sphériques d'oxyde de fer ont été synthétisées (Figure 1), seule la taille moyenne et la distribution en taille étant modifiées suivant la nature du ligand

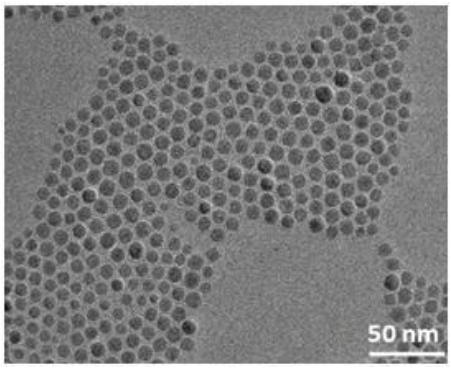

Figure 1 : NPs d'oxyde de fer synthétisées en utilisant l'acide oléique comme ligand

Dans le cas de l'oxyde de cobalt, comme le montre la figure 2, la morphologie et la taille des NPs de CoO va beaucoup dépendre de la nature du ligand. La décomposition thermique du stéarate de cobalt en présence d'acide oléique se produit avec un faible rendement en NPs et conduit à des NPs de forme tétraédrique. Les ligands amines permettent d'augmenter le rendement en NPs et conduisent à des « nanofleurs » (clusters de nanocristaux/nanostructures). Un mélange d'acide oléique et d'hexadécylamine conduit à des nanostructures « multipodes ». De plus, les NPs de CoO synthétisées avec des ligands aminés sont constitués de CoO de structure cubique alors que celles synthétisées avec ou en présence de l'acide oléique sont composées des phases de CoO cubique et wurtzite. Nous avons essayé de comprendre pourquoi le stéarate de fer et le stéarate de cobalt ont un comportement si différent lors de la synthèse par décomposition thermique. Des mesures thermogravimétriques et des études par photoémission X en température ont montré que la décomposition du stéarate de cobalt a lieu à une température beaucoup plus élevée que celle de stéarate de fer, Des résultats préliminaires de simulations effectuées par l'équipe de Carlo Massobrio et Mauro Boero (IPCMS) suggèrent que les chaînes stéarates peuvent se désorber facilement des atomes de fer et les libérer pour former des germes. En revanche, les atomes de cobalt "réagissent" avec les chaînes stéarates, les décomposent, peut-être d'une façon catalytique, et interagissent avec les atomes d''oxygène et d'hydrogène. Ces atomes ne sont donc pas "libres" pour former des germes. D'autres simulations seront nécessaires pour confirmer ces premières hypothèses..

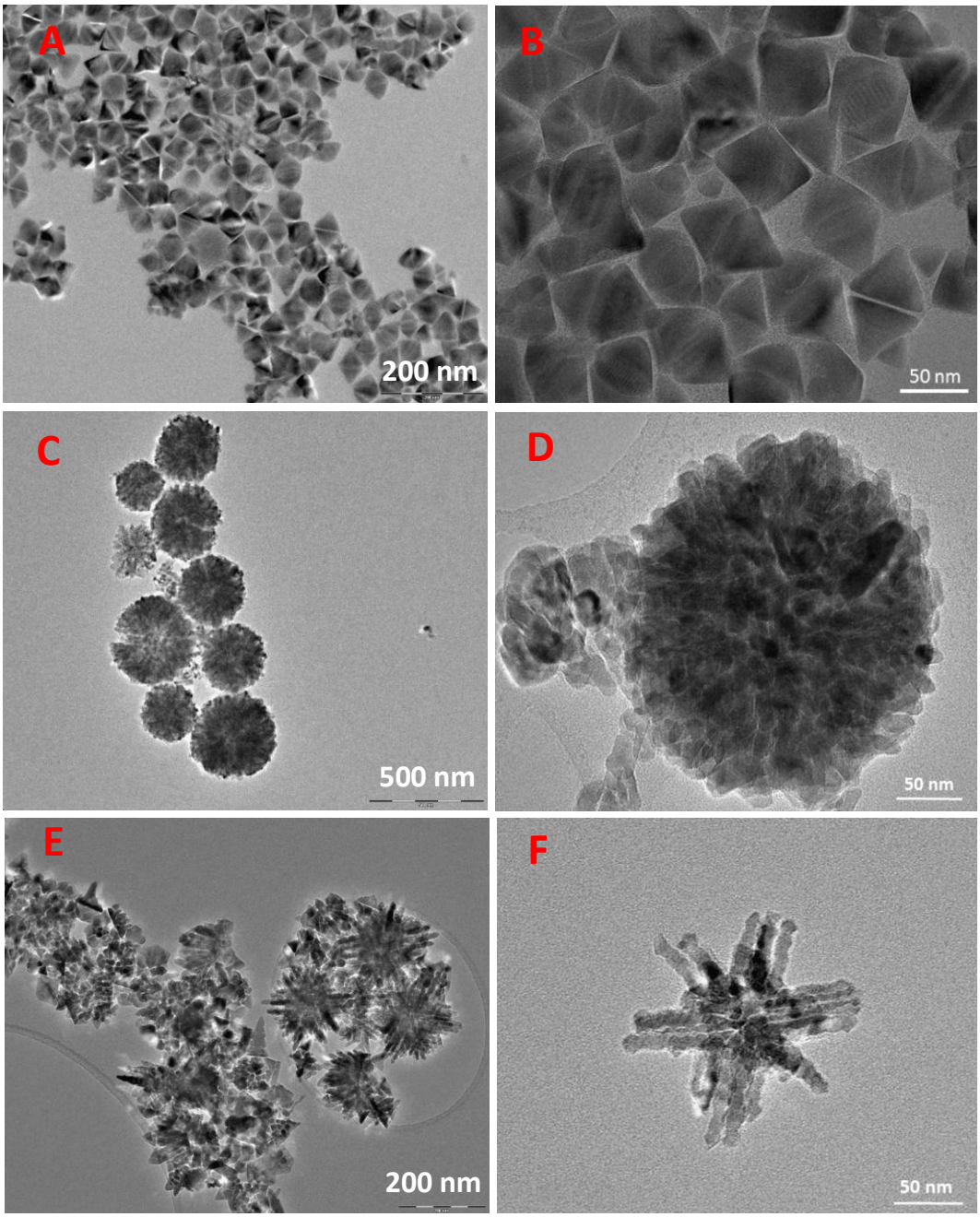

Figure 2 : Images TEM de NPs d'oxyde de cobalt en utilisant comme ligands : l'acide oléique (A-B), l'hexadecylamine (C-D) et un mélange d'acide oléique et d' hexadecylamine (rapport 1:1) (E-F)

Dans le troisième chapitre, des nanoparticules cœur-coquilles permettant de combiner l'oxyde de fer qui est ferrimagnétique et l'oxyde de cobalt qui est antiferromagnétique ont été élaborées et caractérisées. Il est bien connu que de telles structures coeur-coquille (core-shell) peuvent présenter de nouvelles propriétés magnétiques intéressantes dues à un couplage magnétique entre les deux phases appelé échange bias. L'intérêt de ce couplage est qu'il permet d'augmenter l'anisotropie des nanoparticules et d'augmenter leur température de blocage. Dans ce chapitre, des nanoparticules coeur-coquilles de Fe_3O_4@CoO ont été synthétisées avec pour objectif de faire varier l'épaisseur de la coquille à base d'oxyde de

cobalt sur la surface d'une nanoparticule d'oxyde de fer. Les NPs coeur-coquille de Fe_3O_4@CoO ont été obtenues par croissance de CoO sur des germes d'oxyde de fer préformés "speed-mediated growth". Nous avons suivi l'évolution de la structuration de la couche de CoO en fonction de la quantité de précurseur de cobalt introduite dans le mélange réactionnel. La figure 3 présente l'évolution de la structure de la coquille de CoO en fonction du rapport molaire Co/Fe.

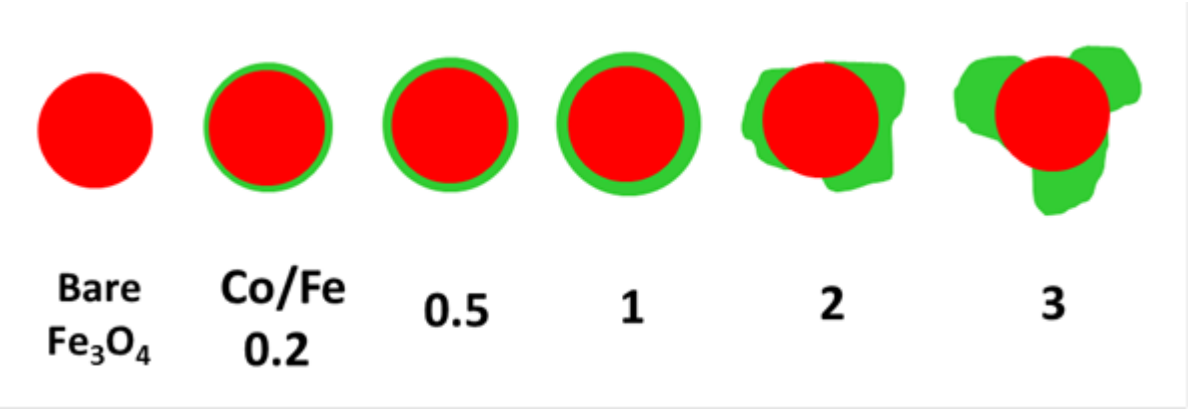

Figure 3: Représentation schématique des NPs cœur-coquille Fe_3O_4@CoO (CoO -coquille, en vert et cœur de Fe_3O_4 en rouge) en fonction du rapport molaire Co /Fe.

La structuration de la couche de CoO à la surface des NPs évolue fortement suivant la quantité de complexe de stéarate ajoutée et elle peut s'expliquer par le fait que cette quantité de précurseurs introduite va fortement influer sur les mécanismes de nucléation hétérogène et sur la croissance de la coquille à la surface des NPs. De faibles quantités de stéarate de cobalt favorisent la formation d'une coquille de CoO d'épaisseur homogène sur la surface des NP d'oxyde de fer et d'une phase interfaciale de ferrite de cobalt entre le noyau d'oxyde de fer et la coquillede CoO. De grandes quantités de stéarate de cobalt favorisent la nucléation et la croissance simultanée de nanocristaux de CoO sur des faces particulières des NPs d'oxyde de fer (présentant l'énergie de surface la plus élevée), ce qui se traduit par la formation d'une coquille de structure non homogène.

La structure de la coquille influe très fortement les propriétés magnétiques de ces NPs c comme le montre le tableau 1. Cette étude systématique souligne l'importance de l'épaisseur, de la continuité, de la cristallinité et des interfaces. Les nanoparticules combinant la plus haute qualité d'interface et la couche épaisse la plus homogène présentent des propriétés d'échange très intéressantes (He = 5100 Oe et Hc=12 500 Oe). Les propriétés magnétiques des NPs constituées d'un coeur d'oxyde de fer avec des nanocristaux de CoO sur des faces spécifiques de l'oxyde de fer (NP-2 et NP-3) ont montré que la qualité de l'interface ferrimagnétique/antiferromagnétique et sa continuité sont des paramètres importants puisque les valeurs de Hc et He sont plus faibles pour ces NPs.

Tableau 1 Propriétés magnétiques des NPs en fonction du rapport molaire des précurseurs NP-0.2-long, NP-0.2, NP-0.5, NP-1, NP-2 et NP-3. Np-0.2-lon est un échantillon qui a été maintenu à reflux plus longtemps. He = champ d'échange induit par l'échange bias, Hc = champ coercitif, T_B = temperature de blocage, Ms = aimantation à saturation et Mr = aimantation rémanente.

Sample	NP-0.2-long	NP-0.2	NP-0.5	NP-1	NP-2	NP-3
H_E(Oe)-FC	0	276	1426	5102	4300	1870
H_c(Oe)-FC	19605	18017	20618	16038	8400	6140
H_c(Oe)-ZFC	19274	17371	19456	12520	5996	5625
Mr/Ms	0.86	0.84	0.75	0.64	0.57	0.56
T_B-ZFC max (K)	240	225	264	256	125 and 254	174 and 225
T_B-imaginary part(K)	223	212	233	182	155 and 229	152 and 243
Ms (emu/g)	26.7	29.5	41.9	30.6	30.5	18.4

D'autre part, nous avons observé que lorsque l'épaisseur de la coquille de CoO (NP0.2) diminue, le couplage d'échange diminue alors que le champ coercitif augmente considérablement. Ce résultat très surprenant a été expliqué par la formation d'une couche mince de ferrite de cobalt à l'interface entre l'oxyde de fer et le CoO. Cette couche interfaciale de ferrite de cobalt induit un couplage magnétique supplémentaire : matériau magnétique doux/matériau magnétique dur à la différence de l'anisotropie magnétique des deux composés. La très grande valeur de Hc obtenue avec NP-0,5 s'explique par la contribution de ces deux types d'échange doux/dur et bias.

Enfin, à la fin de ce chapitre, nous avons assemblé de telles structures coeur-coquilles en film très mince par la technique Langmuir-Blodgett : d'intéressantes propriétés magnétiques "collectives" ont ensuite été mises en évidence et notamment une diminution des propriétés d'échange bias.

La quatrième partie est consacrée à la synthèse de nano-composites NPs@CNTs et se décompose en deux sous chapitres : le premier est consacré au remplissage des NTCs par les deux oxydes métalliques $Fe_{3-x}O_4$ et CoO et à leur caractérisation alors que dans la deuxième partie, une double imprégnation est effectuée afin d'optimiser les taux de remplissage : les matériaux ont ensuite été fonctionnalisés (IBMC – Strasbourg) avec des fonctions ammonium afin de pouvoir les mettre en suspension en milieu aqueux, puis injectés dans des cellules (collaboration avec le LMSC – Paris Diderot) afin d'étudier leur comportement en imagerie et en hyperthermie.

Le but d'associer les nanotubes de carbone et les NPs d'oxydes métalliques est d'essayer d'exploiter au mieux les propriétés spécifiques des deux entités (conductivités électrique et thermique, propriétés mécaniques, stabilité pour les NTCs et propriétés magnétiques principalement pour les NPs). La synthèse de tels matériaux a été réalisée dans les mêmes conditions que celles décrites dans le deuxième chapitre (synthèse des NPs) : les NTCs sont introduits dans le milieu réactionnel et la synthèse des NPs est réalisée en leur

présence. Ces derniers ont été au préalable traités thermiquement sous atmosphère inerte à 900 °C pour évacuer le maximum de fonctions oxygénées (carbonyles, hydroxyles…) de leur surface pour favoriser la diffusion du précurseur à l'intérieur des NTCs comme nous le verrons ultérieurement. La figure 4 représente typiquement des NTCs remplis avec des NPs de Fe_3O_4 (Fe_3O_4@NTCs) dont la structure spinelle a été confirmée par diffraction des rayons X. Le paramètre de maille calculé est de 0.381 nm, valeur intermédiaire entre celui de la magnétite (Fe_3O_4) et celui de sa forme oxydée, la maghémite (Fe_2O_3), ce qui confirme bien que les NTCs protègent les matériaux encapsulés de l'oxydation. En effet, l'ion Fe^{2+} dans Fe_3O_4 est très sensible à l'oxydation, et ce d'autant plus que la taille des nanoparticules est petite.

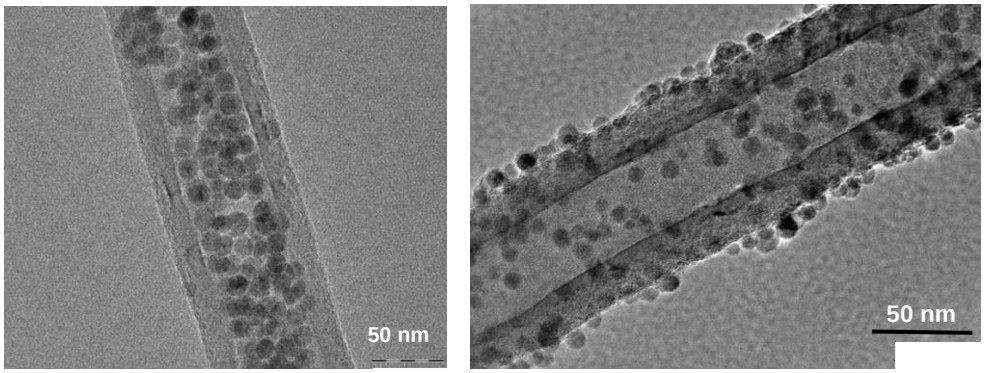

Figure 4 : Images TEM de nanoparticules de Fe_3O_4 encapsulées dans des nanotubes de carbones (à gauche) ou déposées sur la surface des NTCs.

La figure 4 nous montre également que lorsque les NTCs ne sont pas traités thermiquement, voire oxydés en surface par un traitement avec de l'acide nitrique, les NPs ont tendance à se fixer sur la surface des NTCs. De plus, une étude statistique a montré que le diamètre des NPs à l'intérieur des NTCs est supérieur à celui des NPs à l'extérieur (12,5 nm et 9.8 nm respectivement), attestant du rôle de nano-réacteur des NTCs et de leur effet de confinement.

La même démarche a été effectuée à partir de stéarates de cobalt : alors qu'en absence de NTCs on obtient difficilement des nanoparticules de CoO dont il est très difficile d'éliminer les produits organiques résiduels, le stéarate de cobalt se décompose beaucoup plus facilement à l'intérieur des NTCs pour former des clusters de nanoparticules (figure 5) dont la taille est limitée par le diamètre du NTC, mettant encore en avant le rôle de nanoréacteur joué par les NTCs. La diffraction des rayons X a mis en évidence la présence de deux phases bien distinctes : du CoO (comme en l'absence de CNTs) mais aussi du cobalt métallique montrant le rôle préventif des NTCs contre l'oxydation. Des études ont également été effectuées pour étudier le rôle des ligands sur la synthèse de ces NPs : comme le montre la figure 5, nous obtenons toujours des agrégats/clusters de nanoparticules dont la taille est limitée par le diamètre du tube, ce qui n'est pas le cas des NPs de fer dont la taille dépend de la nature du ligand. Contrairement aux résultats du chapitre 2, la morphologie des particules à base de cobalt obtenues à l'intérieur des CNTs n'est pas influencée par la nature des ligands et cela peut-être lié au confinement à l'intérieur des CNTs.

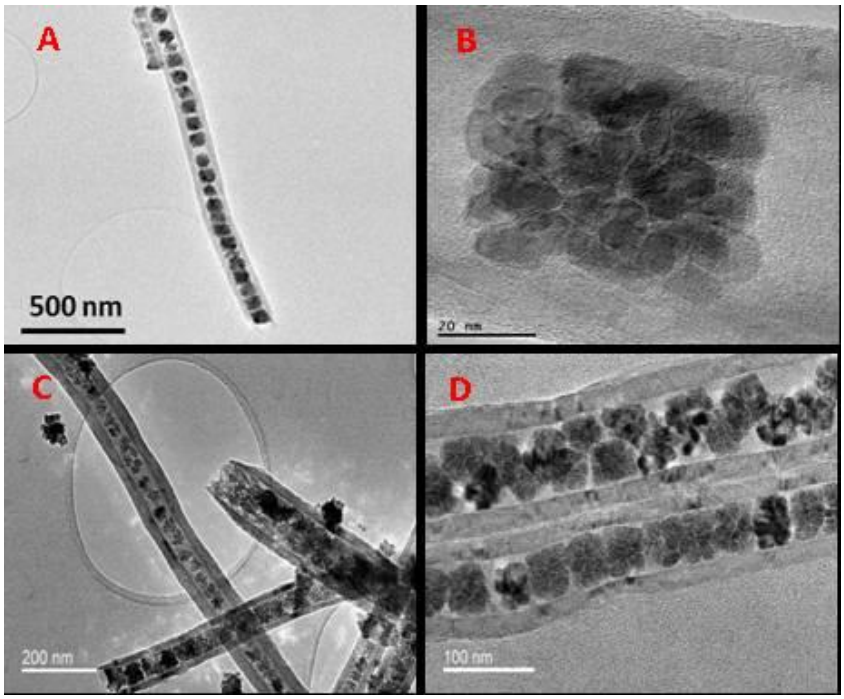

Figure 5 : Images TEM de nanoparticules de CoO et de Co encapsulées dans les NTCs obtenues avec trois ligands différents (acide oléique, hexadécylamine et oléyamine)

Ces nano-composites Fe_3O_4@NTCs ont ensuite été testés en tant qu'agents d'imagerie et agents d'hyperthermie. En effet, les NPs magnétiques sont bien connues dans le monde médical en tant qu'agent de contraste pour l'IRM et les nanotubes de carbone soumis à un rayonnement dans le proche infrarouge sont capables de dégager de l'énergie sous forme de chaleur. Cependant les NTCs remplis par les NPs d'oxyde de fer ne sont pas toujours suffisamment remplis et ensuite les NPs ayant un diamètre inférieur au diamètre des NTCs ont tendance à sortir des NTCs. Les NPs d'oxyde de cobalt occupant la totalité du diamètre des NTCs, nous avons pensé pouvoir bloquer les NPs d'oxyde de fer en effectuant une synthèse de NPs de CoO en présence de ces NTC@Fe_3O_4. Nous avons, dans un premier temps, rempli les NTCs avec des NPs de Fe_3O_4, puis effectué un second remplissage avec des NPs de CoO de grande taille afin de bloquer celles de Fe_3O_4 dans la cavité des NTCs. Pour comparaison, nous avons également effectué une double synthèse de NPs d'oxyde de fer en présence des NTCs. Contrairement à ce que nous attendions, nous n'avons pas formé des clusters de CoO mais en fait les caractérisations fines faites par MET ont montré que le CoO soit forme une couche homogène autour des NPs d'oxyde de fer conduisant à des structures cœur-coquille, soit est présent sous la forme de nano-cristaux à la surface des NPs d'oxyde de fer. La structure du CoO à la surface des NPs d'oxyde de fer est semblable à celle observée dans le chapitre 3 sur les NPs cœur-coquille et les deux structures « extrêmes » sont observées à l'intérieur des NTCs. Ces nano-composites présentent de plus un champ coercitif élevé et une température de blocage élevée qui s'expliquent par la présence, comme avec les NPs cœur-coquilles présentant une fine couche de CoO dans le chapitre 3, d'une couche interfaciale de ferrite de cobalt.

Avant d'étudier le comportement de ces nano-composites dans les cellules, il a été nécessaire de fonctionnaliser chimiquement la surface des NTCs en y greffant des groupes ammoniums afin de pouvoir leur assurer une bonne suspension en milieu aqueux. En effet, l'encapsulation des NPs dans les NTCs a nécessité de les « défonctionnaliser » en surface, ce qui a nécessité la mise en place d'une réaction chimique de surface ultérieure pour les fonctionnaliser avec une molécule hydrophile. Les travaux réalisés en collaboration avec le MSC de Paris Diderot ont montré qu'une fois incorporés dans les cellules (figure 6), ces nano-composites sont manipulables et orientables par aimantation et l'hyperthermie s'est révélée être efficace en présence de cellules tumorales. Il a été également montré que les NPs d'oxyde de fer sont de bons agents de contraste pour l'IRM et que de la photo-ablation thermique peut-être induite par les NTCs. Ces résultats montrent que ces nanocomposites sont prometteurs comme agents théranostiques mais des caractérisations complémentaires *in vivo* sont nécessaires pour valider toutes ces observations. Ces travaux ont fait l'objet d'une publication dans la revue ACS Nano.

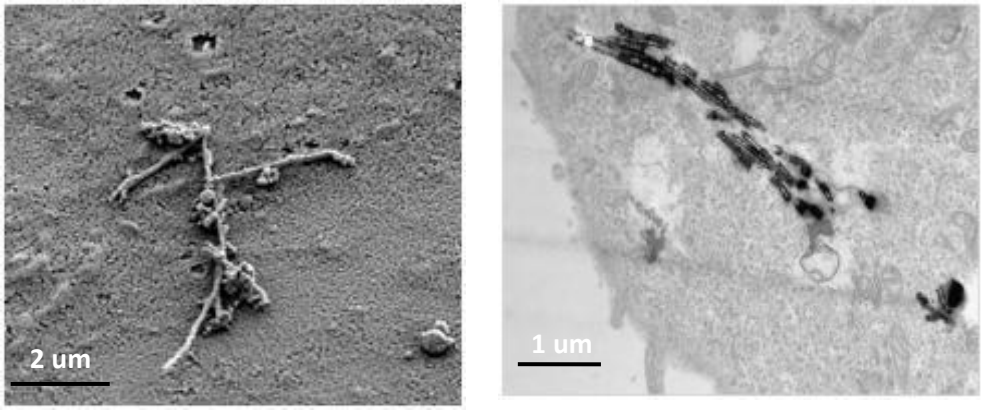

Figure 6 : Nano-composites Fe_3O_4@CoO@NTCs à l'intérieur de cellules tumorales

Enfin, dans le dernier chapitre nous abordons une toute autre application, cette fois dans le domaine de l'énergie. De nombreux travaux ont été consacrés au cours de ces dernières années à l'utilisation d'oxydes métalliques comme matériaux d'électrode dans les batteries lithium-ions pour suppléer (voire être complémentaires) les matériaux carbonés au niveau de l'anode. En effet, de par leurs structures, de nombreux oxydes métalliques présentent des capacités de stockage de lithium impressionnantes, mais deux problèmes majeurs restent en suspens à l'heure actuelle : un problème purement physique dû au phénomène de contrainte induite par les cycles d'insertion/désinsertion des ions lithium conduisant à une fragilisation du matériau et un problème de conduction électrique. En effet ces oxydes métalliques doivent être systématiquement accompagnés d'une charge conductrice (souvent des noirs de carbone) pour assurer le transport des électrons et des ions avec les problèmes de contact qui en découlent. C'est la raison pour laquelle nous nous sommes intéressés à la synthèse de nano-composites constitués d'un oxyde métallique prometteur et encore peu étudié (l'oxyde de niobium, Nb_2O_5) associé à des nanotubes de carbone ou à du graphène. Deux voies de synthèse de ces nanocomposites ont été testées : la méthode de décomposition thermique (utilisée dans les chapitres précédents) et la voie hydrothermale (en autoclave) plus classiquement utilisée dans ce domaine. La décomposition thermique a

conduit à la synthèse de NPs de Nb_2O_5 de structure tétragonale avec des NPs en forme de plaquettes, alors que la voie hydrothermale a conduit à des NPs en forme de nano-bâtonnets de structure rhombo édrique. Dans les deux cas, le recouvrement des matériaux carbonés par les NPs a été total et homogène avec des prises de masse supérieures à 50% comme le montre la figure 7 dans le cas du composite Nb_2O_5/graphène.

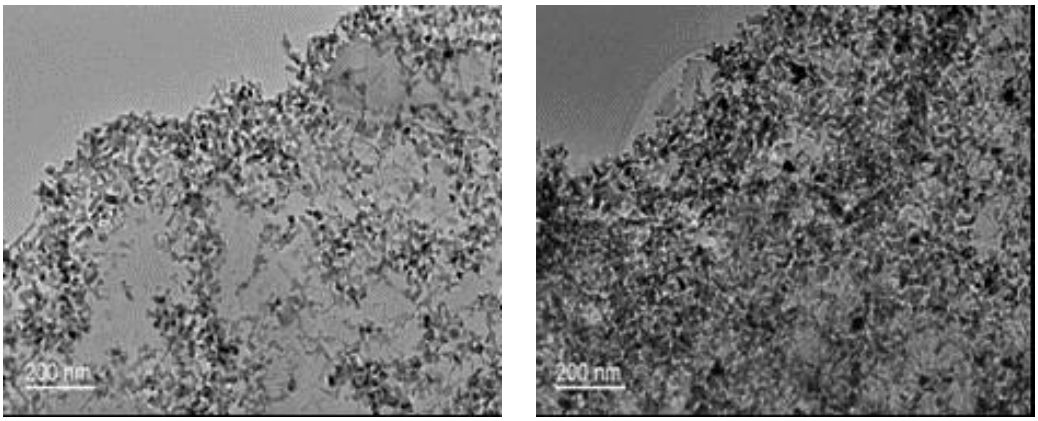

Figure 7 : images TEM de nano-composites Nb_2O_5/graphène montrant un fort recouvrement du graphène par les NPs de Nb_2O_5

Les premières mesures électrochimiques ont montré une nette amélioration en termes de capacité quand on passe du système NPs/ noir de carbone aux systèmes NPs/CNTs ou graphène, attestant de bons contacts entre les NPs et les matériaux carbonés. Des valeurs supérieures à 500 mAh/g ont été obtenues dans certains cas mais seulement au cours du premier cycle de charge/décharge, une grande partie de cette capacité étant irréversible suite à la formation d'une interface solide d'électrolyte limitant par la suite la diffusion des ions Li.

Table of content

Chapter Ⅰ. Introduction

I.1 Iron oxide nanoparticles

I.1.1 Magnetite Fe_3O_4 and maghemite γFe_2O_3 structures

The majority of iron oxide nanoparticles studied is often composed of magnetite (Fe_3O_4) and its oxidized form maghemite (γ-Fe_2O_3). Both oxides exhibit an inverse spinel structure with a general formula of AB_2X_4 in which A and B are cations and X are anions.[1,2]. These crystals adopt a face-centered cubic crystalline structure. Anions delimit the network of the face-centered cubic crystal system and the cations are distributed in tetrahedral and octahedral sites. The unit cell is composed of eight cubic units with a lattice *d*-spacing of 8.396 Å (JCPDS 00-019-0629). Specifically, the crystalline structure of magnetite is based on 32 anions of oxygen and contains both divalent and trivalent iron as cations. For one unit cell of magnetite containing 32 oxygens, 64 tetrahedral and 32 octahedral sites are generated. For each unit cell, 8 divalent atoms and 8 trivalent atoms of iron fill the octahedral sites of magnetite. In the tetrahedral sites, 8 trivalent iron ions are present. It can be labeled as $(Fe^{3+})^{tetr}_8[Fe^{3+}Fe^{2+}]^{oct}_8O_{32}$.The composition of a unit cell of the magnetite can be written as follows:

$[Fe3+]_{Td}[Fe3+Fe2+]_{Oh}O_4$

Figure I.1 illustrates the inverse spinel structure of magnetite. In total, each unit cell of magnetite contains 56 atoms in which there are 32 ions of oxygens, 16 iron(III) and 8 iron(II). Therefore, the quarter of unit cell is filled with the divalent and the trivalent iron ions.

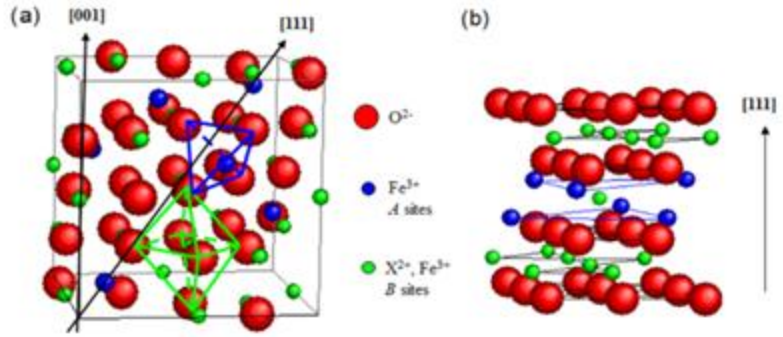

Figure I.1. (a) Schematic representation of the inverse spinel structure of Fe_3O_4 with tetrahedral (A) and octahedral (B) sites. (b) Stacking of the cationic and anionic plans along the [1 1 1] crystallographic direction [3].

In addition, the oxidation of magnetite leads to another iron oxide phase named maghemite γ-Fe_2O_3which has the same spinel structure as magnetite but contains only Fe^{3+}.The oxidation of iron(II) in iron(III) induces the apparition of vacancies (□) in the octahedral sites. The formula of maghemite can be written as follows:$\mathbf{[}Fe^{3+}]_{Td}[Fe^{3+}_{5/3}\square_{1/3}]_{Oh}O_4$. This spinel structure is cubic with a lattice *d*-spacing of 8.33 Å (JCPDS 13-0458).

The vacancies in Oh sites are more or less ordered depending on the synthesis conditions. Therefore maghemite often displays superstructure forms, which arise as a result of cationic and vacancy ordering. The vacancies can be randomly distributed (space group *Fdım* as in magnetite), or partially (*P*4332) or totally ordered (*P*43212).

In order to distinguish the magnetite and maghemite, the combination of different techniques have to be utilized because both of them have the similar spinel structure. XRD is common method to understand the composition of NPs. Since the cell parameter of magnetite 8.396 Å (JCPDS 00-019-0629) and maghemite 8.33 Å (JCPDS 13-0458) are very close, XRD was not precise enough to identify these two iron oxide phases but allow to evaluate if they are more or less oxidized.

Another characterization method allowing to discriminate between the magnetite and maghemite phases is infrared spectroscopy as both phases display characteristic Fe-O IR bands. In Figure I.2, are given the IR spectra of magnetite (NPs of 40 nm synthesized by coprecipitation) and maghemite (maghemite was obtained by subsequent annealing of magnetite NPs of 40 nm synthesized by coprecipitation).[4,5] The magnetite normally displays only one single broad band located at 580-590 cm^{-1} and here there is a shoulder at about 700 cm^{-1} attributed to surface oxidation. The maghemite phase displays several bands between 800-400 cm^{-1} which number and resolutions depend on the structural order of vacancies in maghemite.[6] The IR spectrum of the maghemite phase in Figure I.2 is characteristic of a partially ordered maghemite.

The most adapted method to determine the composition of iron oxide phase is Mössbauer spectroscopy which is generally done in collaboration with J.M. Grenèche, Université du Mans.

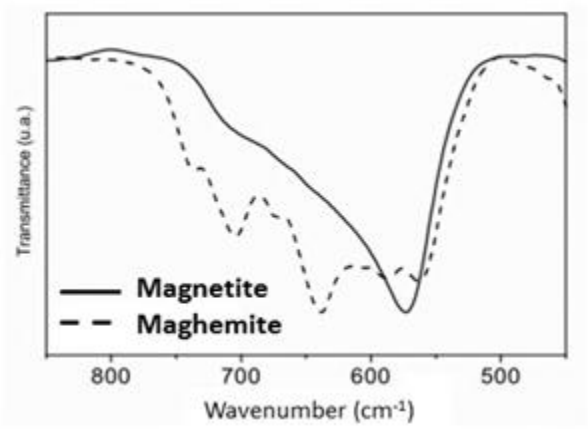

FigureI.2. IR spectroscopy of a slightly oxidized magnetite Fe_3O_4 (black line) and of a partially ordered maghemite γ-Fe_2O_3 (dashed line) in Fe-O wave number range.[7]

At the nanoscale, it is now well established that the Fe^{2+} ions located at the surface of magnetite particles are very sensitive to oxidation and when the size decreases, their sensitivity to oxidation increases. NPs synthesized by thermal decomposition with sizes in the range 5-20 nm have been characterized structurally and magnetically by different techniques. The small NPs (<8 nm) are quite fully oxidized and display a composition close to that of maghemite. The NPs with sizes larger than 12 nm are constituted of a magnetite core with an oxidized shell and the amount of magnetite in the NPs increases when the size increases. For intermediate sizes (8-12 nm), the composition is found to be intermediate between those of magnetite and maghemite without a clear core-shell structure and with the occurrence of a perturbed oxidized state with defects.

However the oxidation state of NPs depends also on the synthesis method. Indeed similar results were also noticed with NPs synthesized by coprecipitation but the size limit is around 10 nm. For sizes smaller than 20 nm, the composition of NPs was reported to be close to that of maghemite and for sizes higher than 20 nm, NPs were found to display a core-shell structure with a core of stoichiometric magnetite surrounded by an oxidized layer. It was suggested that the oleic acid coating and the organic solvent for NPs synthesized by thermal decomposition should prevent them from oxidation by comparison with those synthesized by coprecipitation which are "naked" and in water.

I.1.2 Synthesis methods of iron oxide NPs

In this section, the conventional synthetic methods of nanoparticles (NPs) are briefly presented and then the synthesis method, which has been used in these works, the thermal decomposition, is detailed. The influence of the synthesis parameters on the size, shape an decomposition will be explained.

I.1.2.1 Main synthesis methods

Until now, a variety of chemical and physical methods have been utilized for synthesizing various kinds of nanoparticles (NPs).[8,9,10] Amongst them, there are several common methods, such as co-precipitation, polyol approach, thermal decomposition, hydrothermal synthesis and so on. In Table I.1, the characteristics of the main synthesis methods are compared.

Méthode de synthèse	**Conditions de synthèse**	**T (°C)**	**Temps de réaction**	**Solvant**	**Taille (nm)**	**Distribution en taille**	**Contrôle de la morphologie**	**Rendement**
Coprécipitation	Très simple	20-90	Minutes	Eau	< 20	Moyenne	Moyen	Très élevé
Microémulsion	Compliqué	20-50	Dizaines de minutes	Eau/ organique	< 50	Relativement étroite	Bon	Faible
Milieu polyol	Très simple	>180	Dizaines de minutes	Organique	< 10	Relativement étroite	Très bon	Moyen
Hydrothermale	Simple mais haute pression	>200	Heures	Eau Eau/ Ethanol	< 1000	Relativement étroite	Très bon	Moyen
Décomposition thermique	Compliqué	200-400	Heures	Organique	< 20	Etroite	Très bon	Elevé

Table I.1. Advantages and drawbacks of the main synthesis methods of iron oxide NPs [11,12]

Among the synthesis methods of iron oxide NPs, the synthesis by thermal decomposition[13,14,15] of metal complexes in a high boiling solvent in presence of surfactants is interesting because it allows controlling the size and morphology of the NPs and leads to their *in situ* functionalization limiting their aggregation in suspension. Through this approach, monodisperse, uniform and well defined nanocrystals with a narrow size distribution can be obtained. By tuning the synthetic conditions, the shape and size of NPs can be controlled well. The "heating up" thermal decomposition approach described by Heyon et al.[16] has been chosen in our work because the synthesis system is simple with one iron complex, one type of ligands (mainly oleic acid) and a high boiling point organic solvent.

I.1.2.1 Thermal decomposition method

The thermal decomposition method consists in the thermal decomposition of coordination metal complexes in a high-boiling solvent in presence of co-surface ligands. Monodisperse magnetic crystals such as Co[17], CoPt[18], Fe[19], Fe_3O_4[20] have been prepared

according to this procedure by heating-up[16] or hot injection[22]. In particular, iron oxide magnetic nanoparticles with narrow size distribution have been obtained by thermal decomposition of different metal-organic complex precursors, such as for example $Fe(CO)_5$[23,24] , iron oleate[25,26,27] and iron acetylacetonate[28]. In general, the ligands are mainly a mixture of oleic acid and oleyamine. This chemical synthetic approach permits further finer adjustments of the initial reaction conditions in order to obtain a large modulation in size[29], shape [30] and composition[31]. Moreover, varying the surfactant and the heating conditions allow to obtain different morphologies[32,33].

The good control in nanosize obtained by this method is due to the fact that it allows to separate the nucleation and growth steps. The La Mer theory [34] allows explaining mainly the evolution of the size as a function of synthesis parameters. During the thermal decomposition process, the iron precursor is decomposed which leads to the formation of monomers. Monomers, the minimum building units, of iron oxide nanocrystals, are supposed to be intermediate species such as polyironoxo clusters, which concentration increases as the reaction proceeds.[30] In the La Mer model (Figure I.3), the energy barrier of the nucleation process is much higher than that of the growth process. When the supersaturation of the monomer ($C>C_{min}$) is high enough to overcome this energy barrier, burst nucleation will take place, resulting in the formation and accumulation of stable nuclei (Figure I.3). The minimum radius of a stable nucleus that can grow spontaneously in the supersaturated solutions is inversely proportional to the supersaturation.[30,35] At high supersaturation (high C_{max}), a large amount of nuclei are generated but with small radius while for small supersaturation (small C_{max}), a lower amount of nuclei is formed but with larger radius.

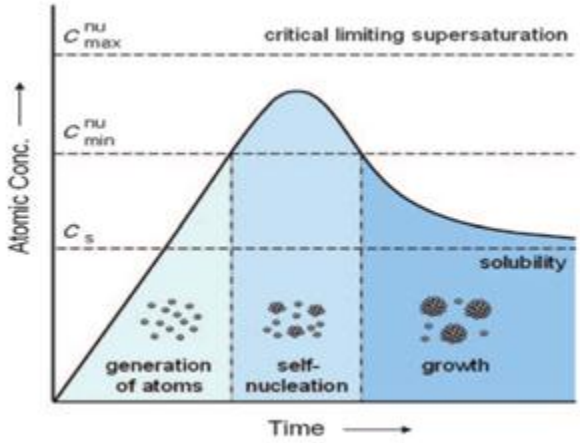

Figure I.3. Variation of the monomer concentration during the germination and growth steps (Cs is the solid solubility) according to LaMer model.

a) Control of the nanosize.

The size is mainly controlled by the nature of the solvant and the ratio : ligand/metal precursor [36,37]. The NP size increases with the boiling point of solvent which is consistent with the Lamer model (Figure I.4).The iron precursor decomposes progressively on a large range of temperature, the higher is the temperature, the larger is the amount of monomers and the nanosize increases. It is the case for alcene solvants in Figure I.4: the higher is the boiling point, the longer is the grain growth step and thus the larger are the NPs. With octyl ether, the

nucleation occurs at low temperature with a low amount of nuclei and the growth step is favored. Hexadecanol is supposed to stabilize the precursor leading to its decomposition (and then germination) at higher temperature (coordinating solvent) with a high C_{max}.
An increase in the ligand concentration may result, depending on the nature of solvants, in the increase of the average diameters observed with octyl ether or a decrease as observed with the non polar solvent octadecene (Figure I.4). In octyl ether, it is mainly explained by the stabilization of the iron precursor by oleic acid, which slows down the nucleation step so that small number of nuclei are formed in solution. Therefore the growth step is favored. With octadecene, its higher boiling point than octyl ether leads to NPs with larger mean sizes. However due to the non polar nature of this solvent, when the ligand concentration increases, the amount of oleic acid at the surface and around nuclei becomes higher which contributes to slow down or inhibit the growth process.

Besides, other strategies are also studied to control the size of magnetite NPs. Shouheng S. and Zeng H. [38] reported a seed-mediated growth route to obtain NPs with various size of (4nm, 8nm, 12 nm and 16 nm) based on the continuous growth of 4 nm magnetite seed.

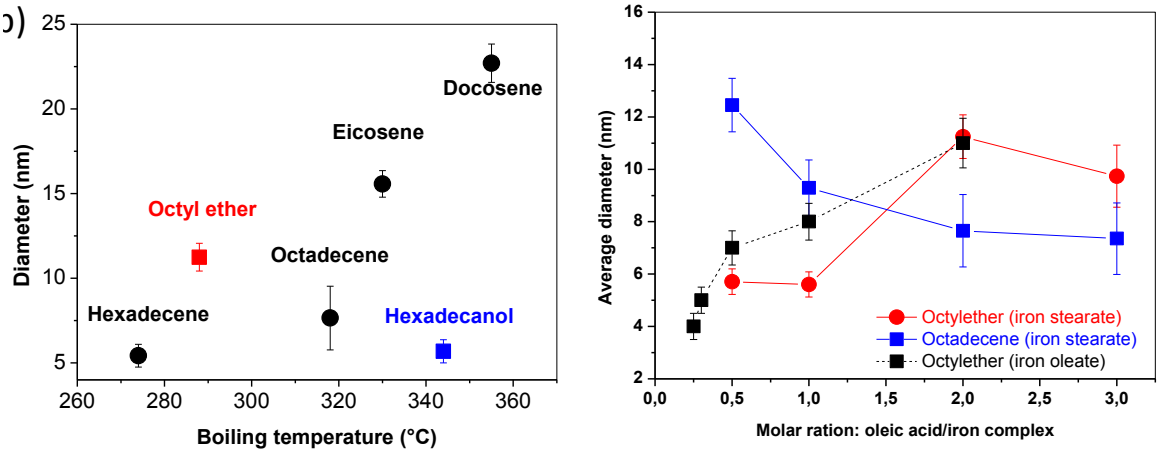

Figure 1.4 Average diameter of NPs of the boiling point of solvents (left**)** and the molar ratio : oleic acid/iron stearate.

b) Control of the shape

Many parameters have been studied in the literature to control the shape. By adapting the experimental conditions, NPs of cubic forms, truncated octahedron, tetrapod were obtained.(In Figure I-5) However the control of the morphology does not seem trivial and synthesis conditions reported in the literature are often difficult to reproduce. During the synthesis, the shape of the seed is controlled by the thermodynamics and kinetics of the system consisting of the inorganic core, ligands and synthesis solution containing the precursor and ligands. The kinetic control of the final shape during the growth step is then achieved by controlling the rate of rise in temperature, the reaction time and the system temperature. These parameters were studied and their variation yielded cubic NPs. Bao et al and Xi et al have observed the appearance of successive shapes when increasing the duration of aging.

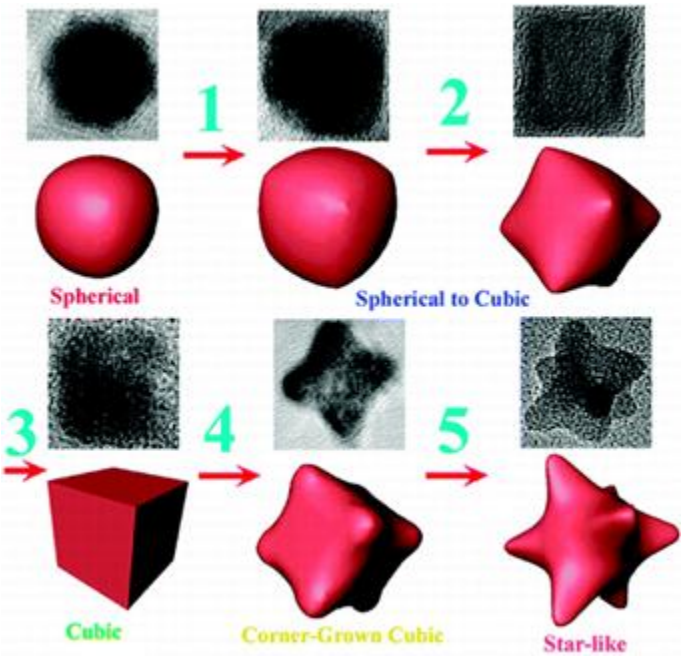

Figure 1.5. Evolution of the NPs shape as a function of the reaction time.

To synthesize nanoparticles of different shapes, it is necessary to control the growth rate on different faces of nuclei. But this control is not easy and specific ligands are often used. These ligands stick to specific crystal facets (faces of high surface energy), decrease their energy and slow down the growth of these faces. The facets of low energy grow faster than the high-energy facets which disappear when the crystal grows.[39,40] For example, sodium oleate associated to oleic acid is the most used ligand to favor the growth of nanocubes.

I.1.3 Magnetic properties of iron oxide NPs

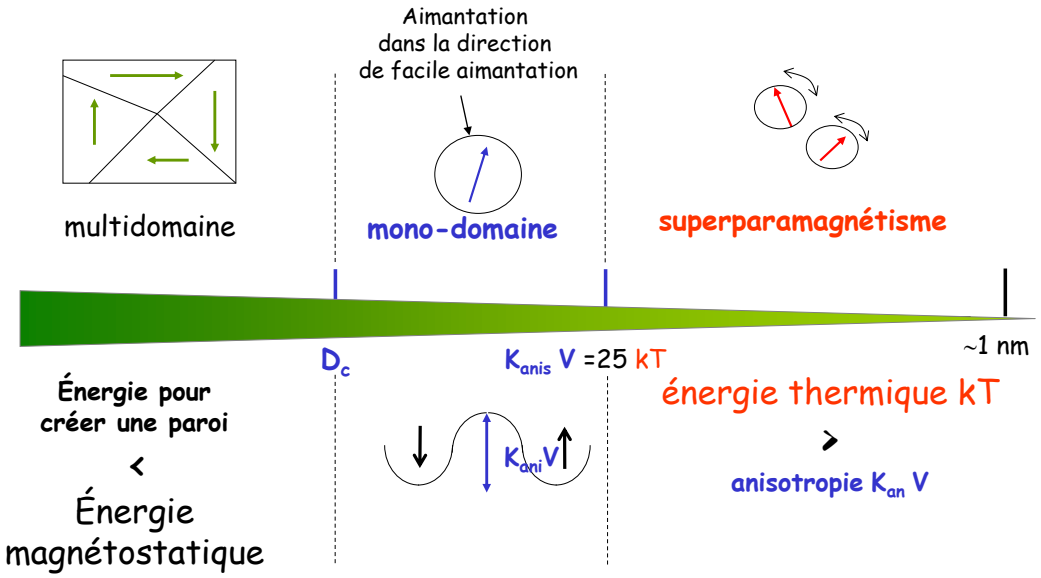

Figure I.6. Evolution of magnetic properties of magnetic materials as function of their size.

The magnetism of ferrite materials mainly results from the antiparallel coupling of the unpaired 3d electrons of ferrous and ferric ions that are located in tetrahedral and octahedral

sites of the face centered cubic lattice. As the magnetic moments of the spins do not compensate in the subnets, there is a non-zero resulting magnetization at low temperature. :

Sites octaédrique: Fe^{3+} 5 µB ↑↑↑↑↑↑↑↑ ; Fe^{2+} 4 µB ↑↑↑↑↑↑↑↑

Sites tétraédriques: Fe^{3+} -5 µB ↓↓↓↓↓↓↓↓

This electronic arrangement defines the ferrimagnetic behavior of magnetic compounds that is a particular case of ferromagnetism. Beyond a critical temperature (called Néel temperature), the magnetic order disappears at the same time as a spin alignment. Consequently, the magnetic moment becomes zero.

The bulk magnetite is a natural material in which the magnetic domains are divided in Weiss domains separated thanks to walls called Bloch walls. Inside of each domain, the magnetic moments possess uniform directions whereas the surrounding magnetic domains exhibit a different direction of magnetic moments (Figure I.6). The disposition in magnetic domains optimizes the system energy

If an external magnetic field (H) is applied, the Bloch walls move and induce an increase of the magnetic domains oriented in the same direction as an external magnetic field. Depending on the strength of the external magnetic field, the predominant magnetic domains expanded much more compared to the other domains. A high magnetic field is required to completely remove the Blochwalls. This phenomenon is at the origin of the remanent magnetization (Mr)and of the hysteresis observed (Figure I.7 left) during the measurement of magnetic moments as a function of applied magnetic field.

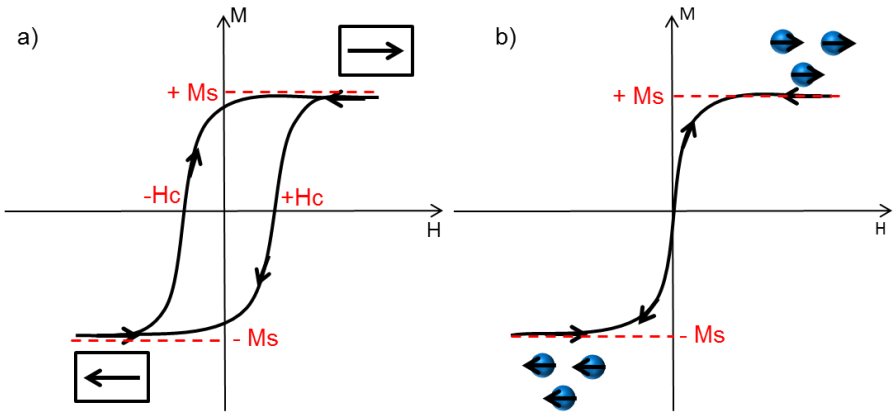

Figure I.7. Hysteresis curve of a ferrimagnetic compound with the representation of the saturation magnetization (Ms), the coercive field (Hc) and the remanent magnetization (Mr) (left) and of superparamgnetic NPs (right).

Initially, the material is not magnetized and the magnetic moment increases while an external magnetic field (H) is applied (Figure 1.7 left). The magnetic moment increases until reaching the saturation magnetization (Ms), corresponding to the state at which all the magnetic moments are aligned with the external magnetic field. If the intensity of magnetic field is then reduced, the magnetic moment will decrease. At zero magnetic field, the magnetic moment is equal to a value corresponding to the remanent magnetization (Mr). This resulting magnetization is a fundamental characteristic of the ferromagnetic substances and it is due to the presence of domain structure. To demagnetize the materials (**e**), it is necessary to apply an

opposite magnetic field called coercive field (Hc). By a continuous increase of the magnetic field in opposite direction, the magnetic moment decreases to a minimum value (-Ms). At this point, an increase of H induces an enhancement of magnetization to the saturation magnetization; however, a larger value of H will be needed to reach a zero magnetization. The final curve describes the hysteresis cycle that is an important characteristic of the ferromagnetic compounds. It is important to determine the remanent magnetization and the coercive field. Both parameters depend on the nature and the size of the materials. On the contrary, the saturation magnetization does not depend on the material size and it is only influenced by chemical composition.

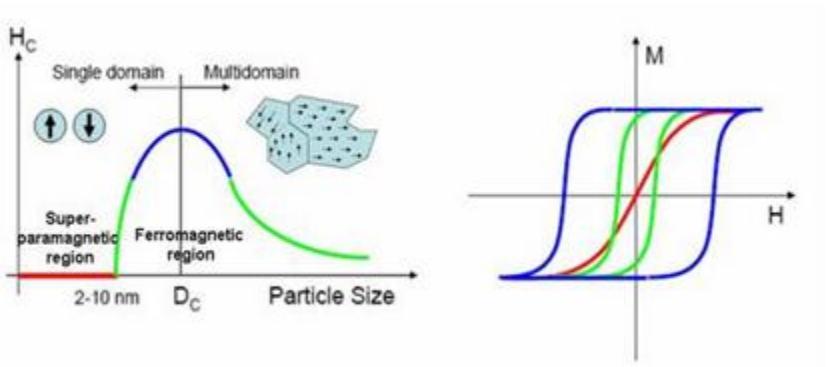

Figure I.8. Evolution of coercive field as a function of the size (left), magnetization curves as a function of the nature of materials: superparamagnetic material (red line), soft ferrimagnetic materials (green line) and hard ferrimagnetic materials (blue line).

If the material size is small enough, the coercive field will become equal to zero and the remanent magnetization will disappear (Figure I.6). Consequently, these materials react as a paramagnetic compound. However, the size of these magnetic substances must be small enough to form a single crystal domain in which these materials acquire uniform high magnetization with all the spins aligned in the same direction Figure I.6). This phenomenon is called superparamagnetism and differs from paramagnetism. Indeed, the magnetic moments of these compounds are much larger than those of electrons responsible of paramagnetic behavior. To have superparamagnetic materials, the size must be less than a Weiss domain of the corresponding material bulk. The magnetization curve of superparamagnetic materials is not defined by a hysteresis curve as observed for the ferromagnetic compounds (Figure 1.7 right). The curve is reversible with no remanence and no coercive field.

For superparamagnetic particles, the directions of magnetization vector are generally aligned on preferred positions called easy direction magnetization or anisotropy axes in order to minimize the anisotropy energy of the system. The anisotropy energy can be defined as an energy required to move the magnetization between two positions of easy magnetization axis. The anisotropy energy (Ea) of a single domain is proportional, in a first approximation, to its volume(V). In the simplest case of uniaxial anisotropy, the energy barrier between two easy magnetization directions is proportional to K_aV and is defined as:

$E_a=K_aV\sin^2\theta$ ……
Where K_a is the anisotropy constant and θ is the angle between both anisotropy axis positions.

K_a constant can be influenced by four contributions for isolated nanoparticles:(1) the chemical composition and the crystallographic structure of the material, (2) the nanoparticle shape, (3) the coating nature and (4) the inter-distance between the nanoparticles. In the case of agglomerated nanoparticles, only the distance between the nanoparticles contributes to Ka. The anisotropy energy of magnetic crystal dramatically increases with the crystal volume and thus with the particle radius. Consequently, for large crystal, the energy barrier is high and the transitions from an easy axis to another one are not favored. The magnetization vector is thus locked on an anisotropy axis. On the contrary, for small particles, the transitions of the magnetization from one easy axe to another one are thus easier.

The changeover of magnetic moment vector from an easy axis to another is observed when the thermal energy is sufficient to break the anisotropy energy barrier. The average time to switch from one direction to another is called "Néel relaxation time (t_N)" and is given by:

$$\tau_N = \tau_0 \exp\left(\frac{KV}{k_B T}\right)$$

Where τ_N is the Néel relaxation time, k_b is the Boltzmann constant, T is the temperature and $\tau_0(E_a)$ corresponds to the pre-exponential factor of the Néel relaxation time expression.

The alignment of magnetization vector is influenced by two contributions: the anisotropy energy (KaV) and the thermic agitation energy (k_bT) (Figure I.6). The ratio between both energies induces two situations as described below:

- If $K_aV >> k_bT$, the magnetic moment is locked in one of the easy directions. Consequently, the changeover of the magnetic vector to another easy axis involves the complete rotation of the particle.
- If $K_aV<<k_bT$, the thermal agitation is a dominant factor, the free transition of the magnetization vector on the easy axes occurs without the particle rotation.

I.2 CoO and FeO nanoparticles

I.2.1 CoO and FeO structures

CoO and FeO display the same NaCl type structure and space group Fm-3m with a cell parameter of a = 4.326 Å (JCPDS 01-89-687) and a = 4.2615 Å (JCPDS 00-43-1004) for FeO and CoO respectively.

Wustite FeO is a highly non stoechiometric iron deficient phase with a defective NaCl structure, consisting of two interpenetrating face-centered cubic structures of Fe^{2+} and O^{2-} (Figure I.9). The formula is usually expressed as $Fe_{1-x}O$ or $Fe_{1-x}\square_xO$ and if we consider all iron cations, the formula is $Fe^{2+}_{1-3x}Fe^{3+}_{2x}\square_xO$ avec $0,83<x<0,96$.The high number of vacancies in the lattice enables a high mobility of the reactants (Fe^{2+} toward the surface and vacancies, and Fe^{3+} toward the oxidation interface) in wüstite

Wüstite is a metastable phase which is reported to undergo a disproportionation reaction to iron and magnetite or oxidation to magnetic phases such as magnetite or maghemite. However under controlled conditions, wustite has been stabilized at the nanoscale.[41,42,43] When exposed to air, Fe^{2+} cations, which are not thermodynamically stable in air oxidized and their surface is oxidized. Moreover the smaller is the particle size, the higher is their oxidation rate as the large specific area presents a high reactivity toward oxygen.Therefore, in air a significant quantity of $Fe^{2+}$is oxidized at room temperature. Fe^{2+} oxidation takes place at the gas/solid

interface and under normal oxygen pressure, the oxidation process begins by dissociative oxygen adsorption on the nanoparticle surface. This phenomenon induces an electronic exchange between Fe^{2+} cations located at the surface and oxygen atoms. This generates Fe^{3+} cations and cation vacancies at the surface of the nanoparticles, thus inducing composition gradients between the nanoparticle surface and the nanoparticle core. These gradients do not generate any crystallographic transformation but induce the diffusion of the different cations. Vacancies which are created at the surface during the incorporation of oxygen into the lattice diffuse into the nanoparticle. The vacancy diffusion occurs in conjunction with the diffusion of iron cations.

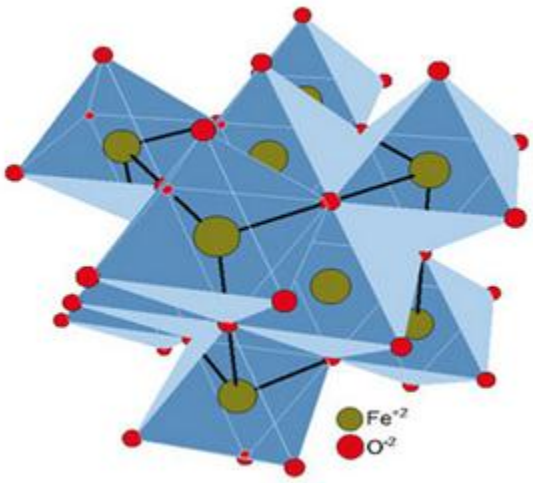

Figure I-9. Schematic representation of the wüstite struture**.**

CoO is less sensitive to oxidation than FeO. CoO NPs have been synthesized and are more stable in air than FeO NPs. At the nanoscale, two structures of CoO have been observed the cubic one and also a wurtzite hexagonal phase.

I.2.2Synthesis of CoO NPs

The synthesis of CoO NPs is not easy as depending on the synthesis conditions, several size and shapes have been obtained. Tetrahedral CoO nanocrystals with 4-5 nm size were synthesized by Yin and Wang,[44,45] via the decomposition of $Co_2(CO)_8$ in toluene in the presence of the surfactant Na(AOT) at 130 ℃. Pure quite spherical CoO nanoparticles with size ranging in 4.5-18 nm were produced by the decomposition of Co(II) cupferronate in decalin under solvothermal route.[46] Rod-shaped and cubic CoO nanocrystals were obtained by the decomposition of cobalt-(III) acetylacetonate in oleylamine by modifying the ratio of precursor/ligands ($Co(acac)_3$/oleylamine).[47] Uniformed tetrapodal CoO NPs were synthesized by the dissolution of Co_3O_4 in oleic acid and then alcoholysis of the formed Co(III)-oleate complex.[48] The size was tuned by modifying the ratio of dodecanol/oleic acid. Zhongping C. et al[49] decomposed cobalt oleate in octadecene in presence of oleic acid : they observed the formation of small needles when the mixture reaches the reflux temperature and then the formation of nanoflowers with reflux time. They suggest that the CoO nanoparticles could be the result of growth of the seeds along [11] direction in a dendritic fashion, resulting in the highly anisotropic flower-like shape. Under the same experimental conditions but with a vigorous stirring, An et al. synthesized pencil-shaped CoO nanorods.[50]

Zhang Y et al.[51] have obtained cubic CoO nanocrystals with various morphologies and sizes via the decomposition of cobalt(II) oleate complex at 280-320 ℃ in octadecene by using dodecanol/oleic acid ligands. The morphology of CoO nanostructures was reported to be tuned from the simple isolated tetrahedral shape to the complex 3D flowerlike shape by increasing the concentration of oleic acid, while with increasing concentration of dodecanol, the morphology of the CoO structures can be tuned from the 3D nanoflower to isolated spheres.

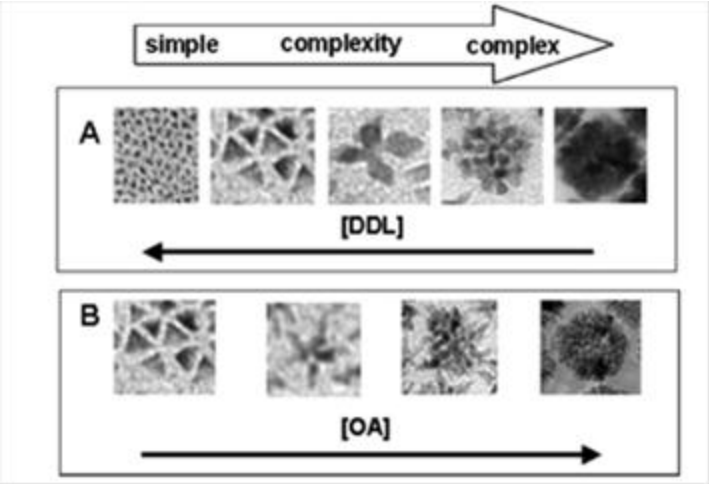

Figure I-10. Schematic illustration of the morphology evolution of CoO nanostructures: (A) morphology changing from complex 3D flowerlike to simple isolated dot shape with increasing amounts of DDL; (B) morphology changing from simple tetrahedron to complex 3D flower-like with increasing amounts of OA.[51]

In addition, hexagonal and cubic nanocrystals, nanotetrapodal shape and pencil-shape of CoO were also reported by different groups.[47,48,50] In particular, pencil-shape of CoO [50] can be transformed to nanorod or triangle shape by modifying the synthetic condition, which is explained by different growth rates of the crystal planes affected by the factors, including the heating rate and ligands.

I.3 Core-shell Fe_3O_4@CoO Nanoparticles

Since few years, growing interests were devoted to induce additional anisotropy to the NPs in order to enhance their magnetic properties by strategies such as tuning the NPs morphology to favour shape anisotropy or synthesizing core-shell NPs to induce exchange magnetic properties.[52,53,54] Indeed, core-shell structures with antiferromagnetic and ferrimagnetic (AFM/FIM) materials display exchange bias properties, which lead to large coercive fields and allow to shift the superparamagnetic limit towards room temperature useful to envision recording media applications.

Magnetic properties of nanoparticles (NPs) are highly dependent on their shape, size, high surface volume ratio, composition, and interfacial characteristics. The NP size which influences directly the magnetic moment and the magnetocrystalline anisotropy energy is critical for applications such as magnetic recording media and biomedicine which require room temperature blocked nanomaterials.[55] Such NPs are characterized by a blocking temperature (T_B) which corresponds to the ferro(i)magnetism to superparamagnetism cross-over and which depends on the NP size.[56-58] Below a critical size, monodomain NPs become

superparamagnetic at room temperature, that is, the orientation of their magnetic moment becomes unblocked against the thermal fluctuations.[59,60] Although superparamagnetic NPs are suitable for biomedical applications,[61] they cannot fulfill all the requirements necessary for spintronic and magnetic recording applications.[55,62]

Since the discovering of exchange bias coupling in Co@CoO NPs by Meiklejohn and Bean in 1956,[63] NPs combining a ferro(i)magnetic (F(I)M) core and an antiferromagnetic (AFM) shell were revealed as a very promising way to push back the superparamagnetic limit.[64] Exchange bias coupling originates from the coupling of the magnetic moments of reversible F(I)M phase at the interface with the ones of the irreversible AFM phase below the Néel temperature (T_N) (Figure I.11).[64-67] Interfacial spins of the AFM phase, which are featured by a very high anisotropy, remain frozen while reversing the magnetic field in the opposite direction. It results in the modification of the magnetocrystalline energy to which is ascribed a supplementary term which refers to the F(I)M/AFM interface.

Figure I.11 demonstrated how the exchange coupling takes place in the interface of FM/AFM when cooled down to a temperature that is lower than the Néel temperature (T_N) under a magnetic field.

(i) When applied under external field (H), spins of the ferromagnetic material get aligned with the direction of field H and spins of antiferromagnetic material are in disorder in the temperature range $T_N < T < T_C$.

(ii) As cooling down the system lower than T_N, the interfacial spins of AFM align parallel with those of FM, which is due to the interaction in AFM/FM interface. Besides, the remaining AFM spins align by antiferromagnetic order, leading to a net zero magnetization.

(iii) In this step, when the field is reversed to negative direction, the FM could start to rotate following the field direction. However, the AFM spins remain unaffected because of the large AFM anisotropy. Thus, in the interface, the AFM spins can prevent the FM spins from changing the initiative orientation. In other words, there is a microscopic torque established on the interface between the AFM spins and FM spins, which make a larger resistance to rotate.

(iv) The stronger applied field is required to overcome the microscopic torque so as to align the FM spins parallel with field.

(v) Because of the interaction between AFM spins and FM spin that tend to reverse FM spins back, a smaller applied field can drive the FM spin to original position. Finally, a negative horizontal shift can be observed in the hysteresis loop.

So far, core-shell magnetic NPs represent a very promising way to increase the effective magnetic anisotropy energy of the raw NPs and to favour blocked NPs at room temperature with the smallest size as possible.

The exchange bias properties are generally established by performing magnetic measurements after having cooleed down the sample under an applied field. It results generally in a horizontal shift of the hystersis curve allowing determining the exchange field and the coercive field.

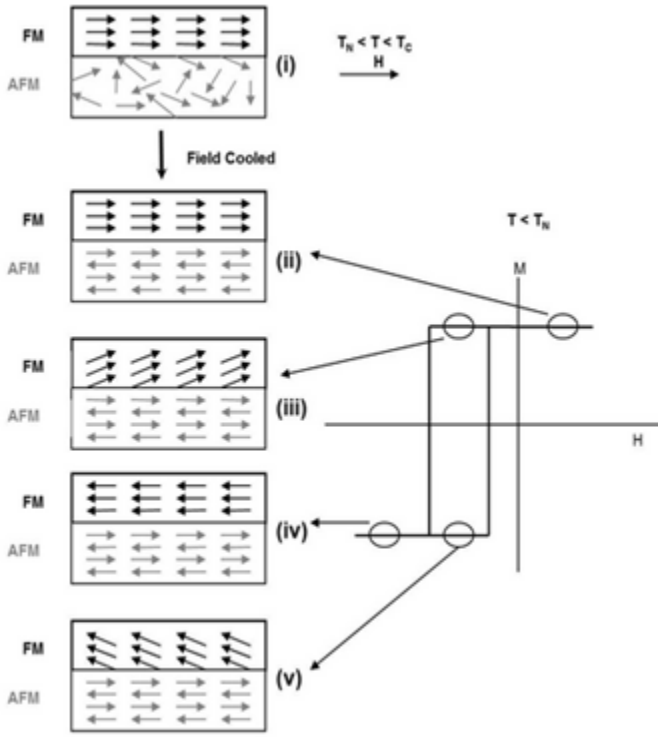

Figure I.11: Classic model of exchange bias.[68]

While first investigations went on partially oxidized metallic NPs, core-shell NPs have been further synthesized to generate and to study exchange bias coupling leading to enhanced coercive field and blocking temperature.[66,69] In recent years, the production of a variety of core-shell nanoparticles resulted on the better understanding on the structure properties relationship.[65] For instance, the shell thickness and hollow structures in Co@CoO NPs have been shown to modulate the exchange coupling.[70] The AFM phase also has to display a larger anisotropy than the FIM phase and the interface exchange energy to maintain the coupling of spins at the FIM/AFM interface upon reversing the magnetic field as pointed out for $CoFe_2O_4$@$ZnFe_2O_4$ [71]and CoO@$CoFe_2O_4$ [72] NPs. Masala *et al* also reported on the importance of the FIM/AFM interface quality in $CoFe_2O_4$@MnO NPs.[73] Inverted structures such as FeO@Fe_{3-} O_4,[74] CoO@$CoFe_2O_4$,[72] $Mn_xFe_{3-x}O_4/Fe_xMn_{3-x}O_4$ have been also synthesized and favor exchange coupling at the core-shell interface. Recently, magnetically coupled exchange core-shell NPs which consist in two different ferrites containing Co, Fe or Mn have been demonstrated to be efficient for magnetic thermal induction.[75]

I.4 Carbon nanotubes composite materials

I.4.1 Carbon nanotubes

Carbon nanotubes (CNTs) have attracted a broad range of interest due to their potential unique chemical and physical properties since Iijima observed them for the first time in 1991 after the synthesis of fullerenes by the arc discharge technique[76]. CNTs can be considered as rolled up graphitic sheets, which form a cylindrical shape along a tube axis with a cavity and with a large length-to-diameter ratio. The walls of CNTs tubes are made up of a hexagonal lattice of carbon atoms, which is analogous to the atomic planes of graphite.The CNTs can be

classified into single-walled nanotubes (SWNTs), double-walled nanotubes (DWNTs) and multi-walled nanotubes (MWNTs) (FigureI-12). Concerning the SWNTs, how the sheet of graphene is rolled is supposed to lead to different orientations of CNTs. In Figure Ⅰ-12A, we can see that the structure of a nanotube can be completely specifiedby its chiral vector (n, m), which is the ratio of the based tube axis to the hexagonal lattice. The architecture of nanotubes, such as zigzag (m=0) and armchair (n=m),is determined by the geometric arrangement of the carbon atoms at the cylinders. When m is not equal to n(m≠n), nanotubes are chiral. Typically, the diameters of SWNTs and MWNTs are 0.8 to 2 nm and 5 to 100 nm, respectively. The length of CNTs can be in a broad range of less than 100 nm to several centimeters.[77]

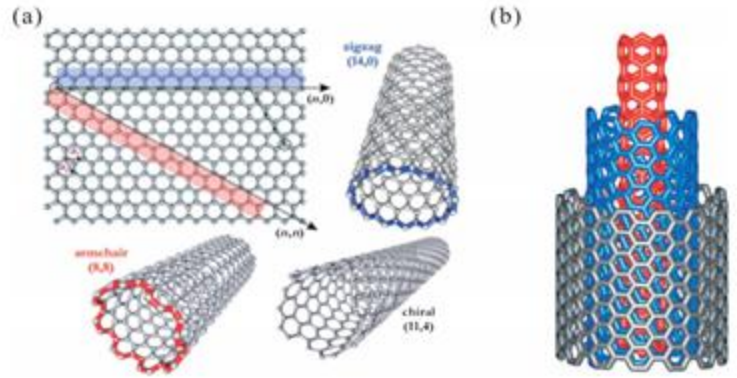

Figure I-12. (a) Roll-up of a graphene sheet leading to three different types of SWCNTs; (b) Schematic structure of a multi-walled carbon nanotube**.**[78]

CNTs can be produced by many ways such as laser ablation[79], arc discharge[80], two "high temperature" techniques which generally produce high-purity CNTs but in rather small quantities. At this time, the most commonly used is the chemical vapor deposition (CVD)[81] which have been developed by several industrial groups. The principle is rather simple and consists to "crack" an hydrocarbon in the presence of a catalyst (iron, nickel...) at moderate temperature (typically 600 - 800 ℃). At this time and according the experimental conditions, this technique allows producing all kinds of NTCs (single, double, multi-walled); however, they need several post treatments to remove the catalyst and its support.

Because of their 1D structure and their theoretical exceptional properties, the use of NTCs have been envisaged in many fields such as supercapacitors[82,83], field emission electron sources[84], Sensors and Probes[85], hyperthermia therapy[86], so on and so forth. In order to enhance/adjust their properties CNTs surface can be chemically modified (oxidation, reduction, chemical grafting…) in order to deposit particules inside or outside of their channel or to adapt them according to the used solvent.

I.4.2 Carbon nanotubes: filling method

The strategy of filling CNTs plays an important role on determining the quality of encapsulation of NPs inside CNTs regarding the uploading of NPs and the morphology of NPs. Here, we are introducing three common methods to insert NPs into the cavity of CNTs.

I.4.2.1 Incipient wetting impregnation techniques

This method is the main route to fill NPs inside CNTs (but also to impregnate all kind of porous carbon with a given salt. The detailed procedure is firstly to mix the salt solution with the CNTs, the salt penetrate the channel driven by capillary forces. CNTS are then filtered, then dried and heat treated as a fonction of the nature of the wanted nano-particule. The CNTs wetting is certainly the step the most important part for the filling. According to the reported result of Dujardin et al[87], the surface tension of the solution plays a crucial role on wetting the cavity of CNTs. When the liquid acting on the outer surface of the CNTs, F_{out} is supposed to be only liquid force that push on the tube, which can be described as:

$F_{out} = \gamma_\ell \pi d_{out} \cos\theta_{out}$[88],

where $\gamma_\ell$is the liquid surface tension, d_{out} is the CNTs outer diameter, and θ_{out} is the contact angle between the liquid and the nanotube surface. Meanwhile, internal wetting force (Fin) takes place on the internal surface, which can be described as:

$F_{in} = \gamma_\ell \pi d_{in} \cos\theta_{in}$,

where d_{in} is the CNTs internal diameter, and θ_{out} is the contact angle of the internal liquid with interior wall of CNTs. The combined force acting on the nanotube is determined by internal and external nanotube wetting. More precisely, there is upper limitation for the surface tension of suspension (180 mN/m) beyond which the wetting is not favorable. It is also reported that as for the smaller CNTs (diameter around 2 nm), they have some intrinsic wetting features. In Young-Laplace equation[89], it is expressed that with respect to the capillary action, at the interface in equilibrium, there is a balance between the hydrostatic pressure, the applied pressure and the effects of surface tension.In most cases, wetting can be achieved as surface tensions of common solvents are all lower than 80 mN/m(Table Ⅰ-2). In addition, the viscosity of the solution is another parameter which can affect the liquid entering inside the CNTs.

solvent	γ (mN · m^{-1})[a]	solubility in water (wt %)	boiling point (K)
water	71.99	/	373
octane	21.14	7.1×10^{-5}	398
ethylbenzene	28.75	1.6×10^{-2}	409
benzene	28.22	1.78×10^{-1}	353
trichloromethane	26.67	8.0×10^{-1}	334
ethylene glycol	47.99	soluble	469
N,*N*-dimethylformamide	37.10	soluble	426
ethanol	21.82	soluble	351
tetrahydrofuran	26.4	soluble	339

[a]Surface tension at 298 K.

Table I-2. Physical Properties of the common Organic Solvents

Green et al.[90] conducted an experiment, in which suspension of CNTs produced by arc vaporization and hydrated nickel nitrate in nitric acid solution was refluxed for 4.5h in an oil bath. The black precipitations was obtained and dried overnight. At the end, the sample was annealed at 450 ^{o}C for 5h. HRTEM (Figure Ⅰ-13a) showed that 60-70% CNTs contained the Nickel oxide NiO inside the cavity and that some particles were also observed on the outer wall. NiO NPs were very well defined : their shape and size of NPs were dependent on the

diameter and the length of the CNTs. Moreover, NiO-filled precursor can be reduced to metallic Ni-filled CNTs by hydrogen at 400 ^{o}C (Figure Ⅰ-13b). So, at early investigation stage, it implies that the route can be useful, easily-manipulated way to gain the goal of NPs filling CNTs.

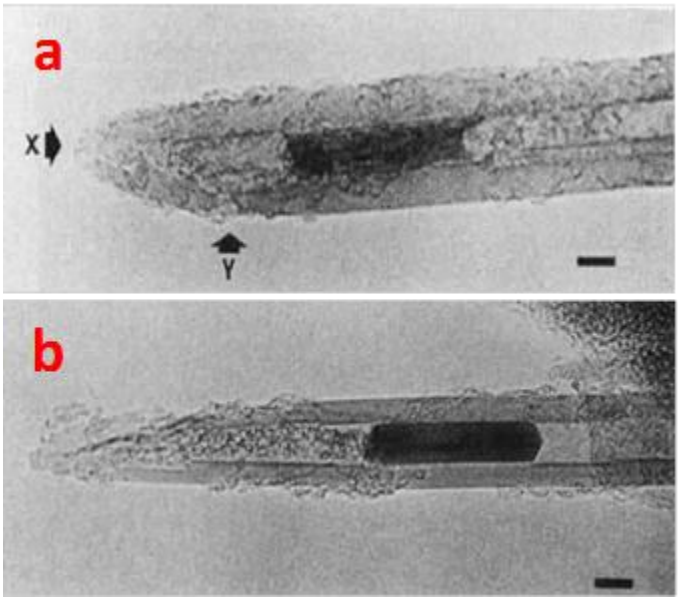

Figure Ⅰ-13. HRTEM of NiO filled CNTs also at points X and Y(a) and Nickel metal by hydrogen reduction of NiO-filled precursor (b).[90]

In order to enhance the catalytic properties of NPs, various materials, such as Ru, Ag and FeN, were confined inside the channel of CNTs for different catalytic reaction, for example the conversion of CO and H_2 to ethanol.[91,92,93] Conclusively, the presence of NPs inside can effectively enhance the catalytic reaction, which is ascribed to the peculiar interaction of the interior nanotube surface with the metal particles, resulting in the increment of the dissociation of CO. Wei et al.[94] applied the same approach to insert FeNi alloy inside CNTs.

The walls of CNTs filled with NPs are anchored with NPs, which can enable the material more useful and functional. The challenges to avoid or to allow the deposition of other kind of NPs on the outer walls of the CNTs. On the other hand, if we want to avoid the salts penetrating inside the chanel, a functionalization of the outer walls will be needed. Capobianchi et al.[95] (Figure I-14) reported a new bifunctional material shortly referred to as FePt@MWCNTs/Ru (NPs) : nanoparticles (NPs) of a magnetically soft FePt alloy encapsulate the MWCNTs cavity, whereas catalytic Ru NPs decorate the external wall. The cavity of CNTs and enormous wall surface were provided for magnetic FePt and catalytic Ru, respectively. By this way, the combination of several different properties of NPs with CNTs can be gained. First of all, FePt was inserted inside CNTs. Before decoration of Ru NPs on the exterior wall instead of inside, on one hand, the CNTs must be functionalized to coat organic groups on the wall so as to enhance the coating and on the other hand, FePt-filled MWCNTs were filled with mesitylen to protect the cavities so as to avoid the Ru NPs entering the channel. Finally, FePt-filled CNTs was mixed with ruthenium chloride hydrate solution.

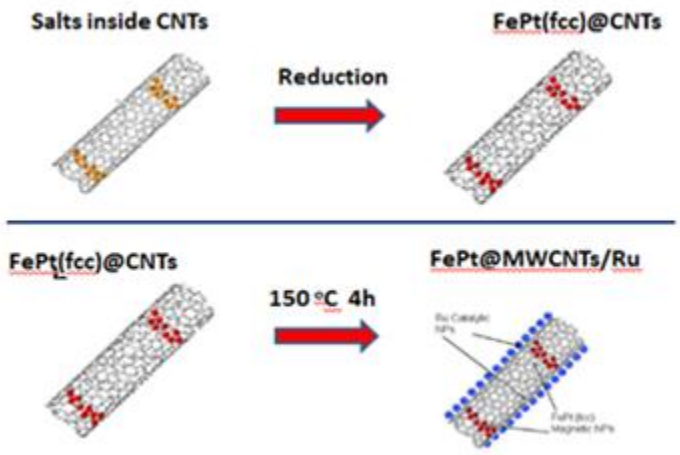

Figure Ⅰ-14. Schema of filling of FePt inside CNTs (a) and decoration of Ru NPs on the wall (b). [95]

At this time, a large number of different metals (or alloys) NPs have been encapsulated into the CNTs cavity, including Fe [96], FeCo Nanowires[97], FeCo alloy [98], FeCo single crystal nanowire [97], $LaNi_2$ alloy[99], Cu NPs[100], Ru NPs[101], Pt NPs[102], Ag[103,104] or Au[105], CdS clusters[106], Rh based alloy[107], Copper Azide [108], SnO_2[109].

More recently, the association of carbon nanotubes (CNTs) with metal oxide NPs has known a drastic interest taking into account the specific properties of each of them: electrical and thermal conductivities, mechanical properties, stability in the case of the CNTs and magnetism the case of metal oxides NPs.[110-115]

The team of Pham Huu reported the synthesis of $CoFe_2O_4$ nanowires in carbon nanotubes by wetting method.[116] In order to have a deeper insight on this materials, electron tomography (or 3D-TEM) was performed to fully investigate their microstructure, such as spatial distribution and nanoparticle orientation.[117,118] It is confirmed that $CoFe_2O_4$ magnetic particle consists of the nanowire and that their size of NPs is dependent on the location of the particle within the nanotube.

Pan X.'s group also synthesized iron oxide NPs inside CNTs, which can be used as a catalyst for Fisher Tropsch and ammonia synthesis (Figure Ⅰ-15 [119,120]). The redox properties of iron oxide was investigated, the result has shown that the encapsulated iron oxide favors the autoreduction in comparison with nanoparticles outside the NTCs.

Recently, our group[121,122] has shown that Co oxide or iron oxide was successfully encapsulated inside CNTs (Figure Ⅰ-16) with a solvothermal approach and we obtained filling rate rather high up to 40 wt%.

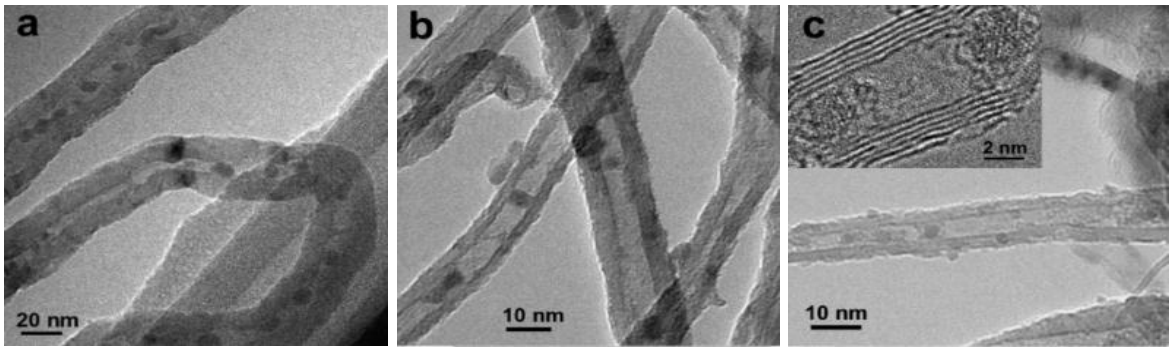

Figure Ⅰ-15. TEM images of Fe_2O_3 inside CNTs with different inner diameters: (a) 8-12 nm, (b) 4-8 nm and (c) 2-5 nm.[119]

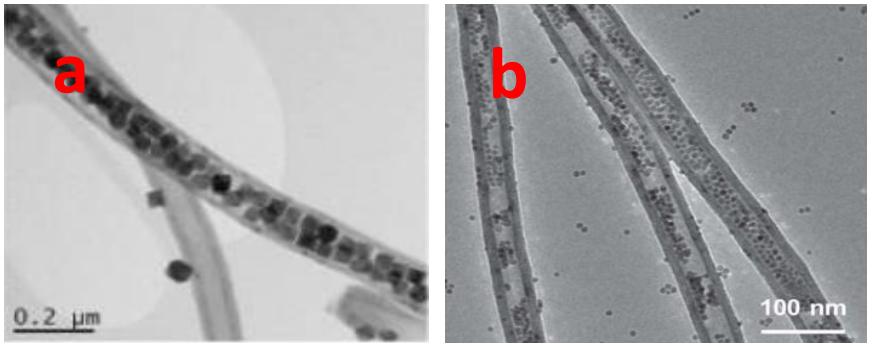

Figure Ⅰ-16. TEM of CoO (a) and Fe_3O_4 (b) inside CNTs.[122]

They have shown that such an encapsulation of NPs prevent them from oxidation and enhanced their chemical inertness. Indeed in cobalt based NPs encapsulated in CNTs, chemical characterizations have shown a relatively high Co/O atomic ratio.

I.4.2.2 Filling CNTs obtained from templates

In this method, the nano channels of an anodic aluminum oxide (AAO) film are used as a template[121]. First of all, AAO templates were produced by the two-step anodic oxidation of pure aluminum sheets under direct current in an acid electrolyte (see fig I-17). Then, Chemical vapor deposition was performed to fabricate the CNTs on the interior of the wall of the AAO templates. Incipient wetting impregnation technique was utilized to synthesize the iron oxide inside the CNTs-AAO. the AAO templates can be dissolved by immersing them in a 5 M NaOH aqueous solution. Such a the hybrid material showed good electrochemical performances, including a high reversible capacity and cycling stability attributed to the small size of NPs and to their confinement inside CNTs.

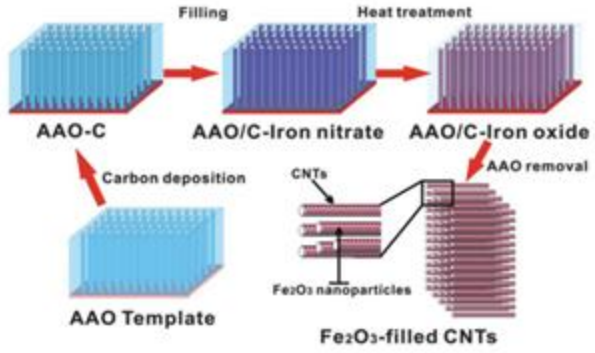

Figure Ⅰ-17. A schematic presentation showing the preparation process of the Fe_2O_3 nanoparticle-filled CNTs.[121]

Korneva G. et al [122] used the same method to synthesize iron oxide NPs high filled CNTs. In his case, the "solution" is a suspension of magnetic iron oxide ferrofluid (instead of iron salt). Finally, carrying fluid inside channel is evaporated and nanotubes are left with magnetic particles inside. In other works, such a method has been used to fill the channel with iron magnetic alloy – NiFe[123,124]

Jang et al [125,126] synthesized polypyrrole nanotubes using reverse microemulsion polymerization as intermediate nanotubes (Figure Ⅰ-18). Then Fe ions penetrate polypyrrole nanotubes by mixing sodium bis(2-ethylhexyl) sulfosuccinate (AOT) and $FeCl_3$. $FeCl_3$ plays an important role on enhancing the ionic strength and decreasing the second critical micelle concentration of AOT. So, the iron-doped polypyrrole nanotubes were fabricated by self-assembly via chemical oxidation polymerization. Simultaneously, the iron oxide γ-Fe_2O_3 was generated inside the obtained polypyrrole nanotubes. Subsequently, the PPy nanotubes were carbonized to transform to CNTs structure.

Chemical vapor deposition (CVD) is indeed a conventional route to produce well aligned multi-walled CNTs within the pores of alumina templates. Pal S. [127] used opened and uniform CNTs produced by CVD (ethylene as precursor). As described previously CNTs were filled directly by Fe_3O_4 nanoparticles ferrofluid. By this method, a broad range of NPs-filled CNTs have been synthesized, such as Co-filled CNTs [128], Fe-filled [129], Fe_3O_4 NPs [130]

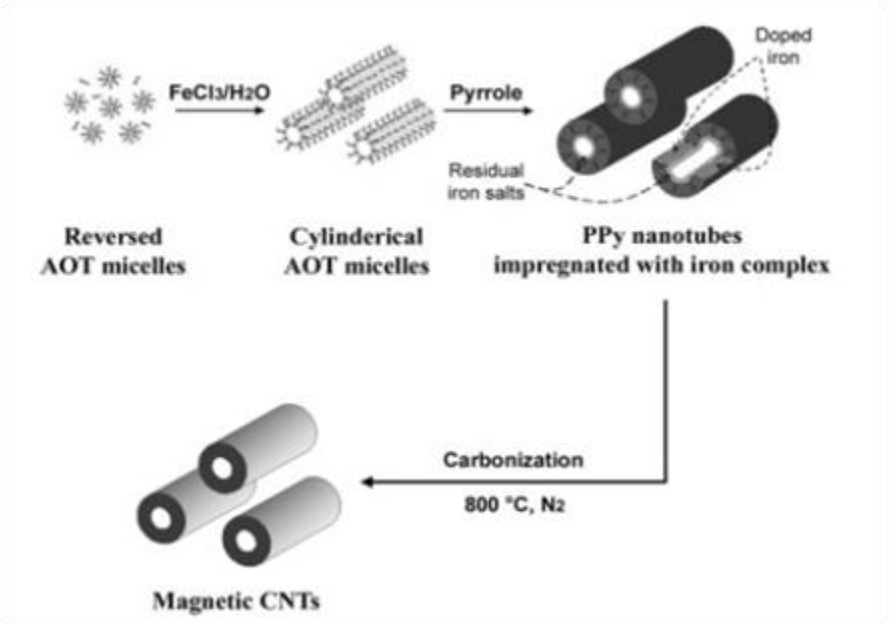

Figure I.18. Schematic diagram for the fabrication of magnetic CNTs using PPy nanotubes as Carbon precursor.[125]

I.4.2.3 Sublimation route

Sublimation route [131, 132] is another method to encapsulate NPs inside CNTs, but this method is not utilized in a large broad of NPs compared with the above two mentioned approaches. In specific uses, it can be a promising route to fill the CNTs. Costa P. et al. [133]

used Re_2O_7as precursor then reduced to form metallic Re. Additionally, the composite model of the CNTs associated with Re cluster is demonstrated. The assumed mechanism was also proposed that the Re_2O_7 bulk sublimate as ReO_3-O-ReO_3 architecture and then enter the nanotubes and condense again to generate clusters. Dynamic rearrangement was studied to demonstrate how the cluster Re_2O_7 was formed in CNTs.

Other nanoparticles, such as cobalt phthalocyanine [134], Fe [135], Cu nanoneedles [136] were also encapsulated inside CNTs by the sublimation approach. A nearby method, the MOCVD (metal-organic chemical vapor deposition) technique [137] was employed to insert iron oxide NPs inside CNTs by the decomposition of ferrocene ($Fe(C_5H_5)_2$ as iron precursor. in this case, the size and the filling rate of nanoparticles can be highly controlled via tuning the MOCVD temperature and reaction time.

I.5 General conclusion

In this chapter, we introduced the state of art in my field of research, which is highly related with the field of my study. At first, we present the basic knowledge on magnetite and cobalt oxide, which are used as main materials for my study as well as the synthesis methods of CoO and iron oxide NPs. The magnetic properties of iron oxide NPs are described. In addition to other magnetic anisotropies, exchange coupling is also considered to be a promising one for tuning the magnetic properties, which primarily takes place on AFM/FM interface. Thus the synthesis of core-shell NPs has been described as well as the exchange bias properties. Finally, since the composite of carbon material, such as CNTs and graphenes, and NPs draw a lot of attention to explore their intrinsic and extrinsic properties, a systematic and concrete introduction is done to present current research on this area.

References:

1. Bragg W. H. *Nature* **1915**, *95*, 561.
2. Nishikawa S.; Proc. Tokyo Math. *Phys. Soc.* **1915**, *8*,199.
3. Moussy, J. B. From epitaxial growth of ferrite thin films to spin-polarized tunnelling. *J. Phys. D. Appl. Phys.* **2013**, *46*, 143001.
4. Daou T. J.; Begin Colin S.; Greneche J. M.; Thomas F.; Derory A.; Bernhardt P.; Legaré P.; Pourroy G. Phosphate Adsorption Properties of Magnetite-Based Nanoparticles. *Chem. Mater.* **2007**, *19*, 4494-4505.
5. Daou, T. J.; Grenèche, J. M.; Pourroy, G.;Buathong, S.; Derory, A.; Ulhaq-Bouillet, C.; Donnio, B.; Guillon, D.; Bégin-Colin, S. Coupling Agent Effect on Magnetic Properties of Functionalized Magnetite-Based Nanoparticles. *Chem. Mater.* **2008**, *20*, 5869-5875.
6. Morales, M. P.; Montero, M. I.; Serna, C. J. Structural effects on the magnetic properties of FeO nanoparticles. *J. Magn. Magn. Mater.***1999**, *203*, 146-148.
7. Daou, T. J.; Grenèche, J. M.; Pourroy, G.;Buathong, S.; Derory, A.; Ulhaq-Bouillet, C.; Donnio, B.; Guillon, D.; Bégin-Colin, S. Coupling Agent Effect on Magnetic Properties of Functionalized Magnetite-Based Nanoparticles. *Chem. Mater.* **2008**, *20*, 5869-5875.
8. Wu, W.; He, Q.; Jiang, C. Magnetic iron oxide nanoparticles: synthesis and surface functionalization strategies. *Nanoscale Res. Lett.* **2008**, *3*, 397-415.

9. Laurent, S.; Forge D.; Port M.; Roch A.; Robic C.; Vander Elst L.; Muller N. R. Magnetic iron oxide nanoparticles: synthesis, stabilization, vectorization, physicochemical characterizations, and biological applications. *Chem. Rev.* **2008**, *108*, 2064-110.
10. Frey, N.; Peng, S.; Cheng, K.; Sun, S. Magnetic nanoparticles: synthesis, functionalization, and applications in bioimaging and magnetic energy storage. *Chem. Soc. Rev.* **2009**, *38*, 2532-2542.
11. Gupta, A. K.; Gupta, M. Synthesis and surface engineering of iron oxide nanoparticles for biomedical applications. *Biomaterials* **2005**, *26*, 3995-4021.
12. Colombo, M.; Carregal-Romero S.; Casula F. M.; Gutiérrez L.; Morales P. M.; Böhm B. I.; Heverhagen J. T.; Prosperi D.; Parak J. W. Biological applications of magnetic nanoparticles. *Chem. Soc. Rev.* **2012**, *41*, 4306-4334.
13. Hyeon, T.; Lee, S. S.; Park, J.; Chang Y.; Na, H. B. Synthesis of Highly Crystalline and Monodisperse Maghemite Nanocrystallites without a Size-Selection Process. *J. Am. Chem.Soc.* **2001**,*123*, 12798-12801.
14. Park, J.; An, K. J.; Hwang, Y. S.; Park, J. G.; Noh, H. J.; Kim, J. Y.; Park, J. H.; Hwang, N. M.; Hyeon, T. Ultra-large-scale Syntheses of Monodisperse Nanocrystals. *Nature Mater.* **2004**, *3*, 891-895.
15. Sun, S.; Zeng, H.; Robinson, D. B.;Raoux, S.; Rice, P. M.; Wang, S. X.; Li, G. Monodisperse MFe_2O_4 (M = Fe, Co, Mn) Nanoparticles. *J. Am. Chem. Soc.* **2004**,*126*, 273-279.
16. Kwon S. G.; Piao Y.; Park J.; Angappane S.; Jo Y.; Hwang N. M.; Park J. G.; Hyeon T. Kinetics of Monodisperse Iron Oxide Nanocrystal Formationby "Heating-Up" Process. J. am. chem. soc. **2007**, 129, 12571-12584.
17. Puntes V.F.; Krishnan K.M.; Alivisatos P. Synthesis, self-assembly, and magnetic behavior of a two-dimensional superlattice of single-crystal ε-Co nanoparticles. *Appl. Phys. Lett.* **2001**, *78*, 2187.
18. Sun X.; Jia Z. Y.; Huang Y. H.; Harrell J. W.; Nikles D. E.; Sun K.; Wang L. M. Synthesis and magnetic properties of CoPt nanoparticles. *J. Appl. Phys.* **2004**, *95*, 6747-6749.
19. Peng S.; Wang C.; Xie J.; Sun S. Synthesis and stabilization of monodisperse Fe nanoparticles. *J. Am. Chem. Soc.* **2006**, *128*, 10676.
20. Sun, S.; Zeng, H.; Robinson, D.B.; Raoux, S.; Rice, P.M.; Wang, S. X. and Li, G. Monodisperse MFe2O4 (M = Fe, Co, Mn) nanoparticles. *J. Am. Chem. Soc*. **2004**, *126*, 273.
21. Kwon S. G. ; Piao Y.; Park J. ; Angappane S. ; Jo Y. ; Hwang N.M.; Park J.G.; Hyeon T. Kinetics of monodisperse iron oxide nanocrystal formation by "heating-up" process. *J. Am. Chem. Soc*. **2007**,*129*, 12571.
22. Talapin D. V.; Rogach A. L.; Kornowski A.; Haase M.; Weller H. Highly luminescent monodisperse CdSe and CdSe/ZnS nanocrystals synthesized in a hexadecylamine-trioctylphosphine oxide-trioctylphospine mixture. *Nano Letters*, **2001**, *1*, 207-211.
23. Hyeon T.; Lee S. S.; Park J.; Chang Y.; Na H. B. Synthesis of Highly Crystalline and Monodisperse Maghemite Nanocrystallites without a Size-Selection Process. *J. Am. Chem. Soc*. **2001**, *123*, 12798-12801.
24. Woo K.; Hong J.; Choi S.; Lee H.W.; Ahn J.P.; Kim C. S.; Lee S.W. Easy Synthesis and Magnetic Properties of Iron Oxide Nanoparticles. *Chem. Mater.*.**2004**, *16*, 2814-2818.

25. Park J.; Lee E.; Hwang N. M.; Kang M.; Kim S. C.; Hwang Y.; Park J.G.; Noh H. J.; Kim J.Y.; Park J. H.; Hyeon T. One-Nanometer-Scale Size-Controlled Synthesis of Monodisperse Magnetic Iron Oxide Nanoparticles. *Ang. Chem. Inter. Ed.* **2005**, *44*, 2872-2877.
26. Park J.; An K.; Hwang Y.; Park J.-G.; Noh H. J.; Kim J. Y.; Park J.H.; Hwang N. M.; Hyeon T. Ultra-large-scale syntheses of monodisperse nanocrystals. *Nature Mater.* **2004**, *3*, 891-895.
27. Bronstein, L. M.; Huang, X.; Retrum, J.; Schmucker, A.; Pink M.; Stein B.D.; Dragnea B. Influence of Iron Oleate Complex Structure on Iron Oxide Nanoparticle Formation. *Chem. Mater.* **2007**,*19*, 3624-3632.
28. Sun, S.; Zeng, H. Size-Controlled Synthesis of Magnetite Nanoparticles. *J. Am. Chem. Soc*. **2002**, *124*, 8204.
29. Pichon, B. P.; Gerber, O.; Lefevre, C.; Florea, I.; Fleutot, S.; Baaziz, W.; Pauly, M.; Ohlmann, M.; Ulhaq, C.; Ersen, O.; Pierron-Bohnes, V.; Panissod, P.; Drillon, M.; Begin-Colin, S. Microstructural and Magnetic Investigations of Wustite-Spinel Core-Shell Cubic-Shaped Nanoparticles. *Chem. Mater.* **2011**, *23*, 2886.
30. Baaziz, W. Thesis entitled 'Synthèse et caractérisation des nanoparticules spinelles et cœur-coquille à base d'oxyde de fer et de cobalt' Strasbourg. **2011**.
31. Bao, N.; Shen, L.; Padhan, P.; Gupta, A. Self-assembly and magnetic properties of shape-controlled monodisperse $CoFe_2O_4$ nanocrystals. *Appl. Phys. Lett.* **2008**, *92*, 173101.
32. Cheon, J.; Kang, N. J.; Lee, S. M.; Yoon, J. H.; Jun Oh, S. Shape Evolution of Single-Crystalline Iron Oxide Nanocrystal. *J. Am. Chem. Soc.*, **2004**, *126*, 1950-1951.
33. Kovalenko, M. V.; Bodnarchuk, M. I.; Lechner, R. T.; Hesser, G.; Schaffler, F.; Heiss, W. Fatty Acid Salts as Stabilizers in Size- and Shape-Controlled Nanocrystal Synthesis: The Case of Inverse Spinel Iron Oxide. *J. Am. Chem. Soc.* **2007**,*129*, 6352-6353.
34. LaMer, V. K.; Dinegar, R. H. Theory, Production and Mechanism of Formation of Monodispersed Hydrosols. *J. Am. Chem. Soc.* **1950**, *72* ,4847-4854.
35. Park, J.; Joo, J.; Kwon, S.G.; Jang, Y.; Hyeon, T. Synthesis of Monodisperse Spherical Nanocrystals. *Angew. Chem. Int. Ed.* **2007**, *46*, 4630-4660.
36. Demortière, A.; Panissod, P. ; Pichon, B. P. ; Pourroy, G. ; Guillon, D. ; Donnio, B. ; Bégin-Colin, S. Size-dependent properties of magnetic iron oxide nanocrystals. *Nanoscale* **2011**, *3*, 225-232.
37. Baaziz, W., Pichon B. P. ; Fleutot, S. Magnetic Iron Oxide Nanoparticles: Reproducible Tuning of the Size and Nanosized-Dependent Composition, Defects, and Spin Canting. *J. Phys. Chem. C*, **2014**, *118*, 3795-3810.
38. Sun, S., Zeng, H. Size-Controlled Synthesis of Magnetite Nanoparticles. *J. Am. Chem. Soc*. **2002**, *124*, 8204-8205.
39. WALTER A. Thesis entitled 'Elaboration de nano-objets magnétiques dendronisés à visée théranostique.' Strasbourg, **2014**.
40. Xu, Z.; Shen, C.; Tian, Y.; Shi, X.; Gao, H. J. Organic phase synthesis of monodisperse iron oxide nanocrystals using iron chloride as precursor.*Nanoscale*, **2010**, *2*, 1027.
41. Baaziz, W.; Begin, S.; Pichon, B.P.; Florea, I.; Ersen, O.; Zafeiratos, S.; Barbosa, R.; Begin, D.; Pham-Huu, C. High-Density Monodispersed Cobalt Nanoparticles Filled into Multiwalled Carbon Nanotubes. *Chem. Mater.* **2012**, *24*, 1549-1551.
42. Greenwood, N. N. Chemistry of the Elements. Elsevier, **1997**.

43. Wells, A. F. Structural Inorganic Chemistry. Oxford University Press **1984**.
44. Yin, J. S.; Wang, Z. L. In Situ Structural Evolution of Self-Assembled Oxide Nanocrystals. *J. Phys. Chem. B*, **1997**, *5647*, 8979-8983.
45. Yin, J. S.; Wang, Z. L. Ordered Self-Assembling of Tetrahedral Oxide Nanocrystals. *Phys. Rev. Lett.* **2000**, *79*, 2570.
46. Ghosh, M. ; Sampathkumaran, E. V. ; Rao, C. N. R. Synthesis and Magnetic Properties of CoO Nanoparticles. *Chem. Mater.* **2005**, *17*, 2348-2352.
47. Seo, W. S. ; Shim J. H.; Oh, S. J. ; Lee E. K. ; Hur N. H. ; Park J. T. Phase-and size-controlled synthesis of hexagonal and cubic CoO nanocrystals. *J. Am. Chem. Soc.* **2005**, *127*, 6188-61899.
48. Zhang, Y. ; Zhong, X. ; Zhu, J. ; Song, X. Alcoholysis route to monodisperse CoO nanotetrapods with tunable size. *Nanotechnology* **2007**, *18*, 195605.
49. Chen, Z. ; Xu, A. ; Zhang, Y. ; Gu, N. Preparation of NiO and CoO nanoparticles using M2+-oleate (M=Ni, Co) as precursor. *Curr. Appl. Phys.* **2010**, *10*, 967-970.
50. Nanorods, P. C.; Lee, N. ; Park, J. ; Kim S. C. , Hwang, Y. ; Park J. G ; Kim J. Y. ; et al. Synthesis , Characterization , and Self-Assembly of Pencil-Shaped CoO Nanorods. J. Am. Chem. Soc.**2006**,*128*,9753-9760 .
51. Zhang, Y. ; Zhu, J. ; Song, X. ; Zhong, X. Controlling the Synthesis of CoO Nanocrystals with Various Morphologies. *J. Phys. Chem. C* **2008**,*112*, 5322-5327 .
52. Sun, X. ; Huls NF. ; Sigdel A. ; Sun S. Tuning exchange bias in core/shell FeO/Fe3O4 nanoparticles. *Nano Lett.* **2012**,*12*, 246-251.
53. Khurshid, H.; Chandra, S. ; Li W.; et al. Synthesis and magnetic properties of core/shell FeO/Fe3O4 nano-octopods. *J. Appl. Phys.* **2013**;*113*, 17B508.
54. German, S. A. ; Jordi S. ; Santiago, S. ; Baró, M. D. ; Nogués, J. Synthesis and Size-Dependent Exchange Bias in Inverted Core−Shell MnO|Mn_3O_4 Nanoparticles. *J. Am. Chem. Soc.***2007**,*129*, 9102-9108.
55. Jeong, U. ; Teng, X. W. ; Wang, Y. ; Yang H. ; Xia,Y. N. Superparamagnetic Colloids: Controlled Synthesis and Niche Applications. *Advanced Materials* **2007**, 19, 33-60.
56. Hao, R. ; Xing, R. ; Xu, Z. ; Hou, Y. ; Gao, S. ; Sun, S. Synthesis, Functionalization, and Biomedical Applications of Multifunctional Magnetic Nanoparticles. *Advanced Materials* **2010**, *22*, 2729-2742.
57. Jeong, U. ; Teng, X. ; Wang, Y. ; Yang, H. ; Xia, Y. Superparamagnetic colloids: controlled synthesis and niche applications. *Advanced Materials*, **2007**, *19*, 33-60.
58. Bedanta S.; Wolfgang, K. *Journal of Physics D: Applied Physics*, **2009**, 42, 013001.
59. Demortiere, A. ; Panissod, P. ; Pichon, B. P. ; Pourroy, G.; Guillon, D.; Donnio, B.; Begin-Colin, S. Size-dependent properties of magnetic iron oxide nanocrystals. *Nanoscale*, **2011**, 3, *225*.
60. Pichon, B. P. ; Louet, P. ; Felix, O. ; Drillon, M. ; Begin-Colin, S. ; Decher, G. Magnetotunable Hybrid Films of Stratified Iron Oxide Nanoparticles Assembled by the Layer by Layer Technique. *Chem. Mater.* **2011**, *23*, 3668-3675.
61. Basly, B. D. ; Felder-Flesch, P. ; Perriat, C. ; Billotey, J.; Taleb, G. Pourroy ; Begin-Colin S. Dendronized iron oxide nanoparticles for biomedical applications. Chemical Communications **2010**, 46, 985-987.

62. Tartaj, P. ; Morales, M. P. ; Gonzalez-Carreño, T. ; Veintemillas-Verdaguer, S.; Serna, C. J. The Iron Oxides Strike Back: From Biomedical Applications to Energy Storage Devices and Photoelectrochemical Water Splitting. *Advanced Materials* **2011**, *23*, 5243-5249.
63. Meiklejohn, W. H. ; Bean, C. P. New Magnetic Anisotropy**.** *Phys. Rev. B* **1956**, *102*, 1413.
64. Skumryev, V. ; Stoyanov, S.; Zhang, Y.; Hadjipanayis, G.; Givord D.; Nogués J. Beating the superparamagnetic limit with exchange bias. *Nature*, **2003**, *423*, 850-853.
65. Nogues, J.; Schuller, I. K. Exchange bias. *Journal of Magnetism and Magnetic Materials*, **1999**, *192*, 203-232.
66. Iglesias, O.; Labarta A. ; Batlle X. Exchange Bias Phenomenology and Models of Core/Shell Nanoparticles. *Journal of Nanoscience and Nanotechnology*, **2008**, *8*, 2761-2780.
67. Papaefthymiou G. C. Nanoparticle magnetism. *Nano Today* **2009**, *4*, 438.
68. Fan, Y. ; Smith K. J. ; Lüpke, G. ; Hanbicki A. T. ; Goswami R. ; Li, C. H. ; Zhao, H. B. B. ; Jonker, T. Exchange bias of the interface spin system at the Fe/MgO interface. *Nat. Nanotechnol.* **2013**, *8*, 438-444.
69. Nogues, J. ; Sort, J. ; Langlais, V. ; Skumryev, V. ; Surinach, S. ; Munoz, J. S. ; Baro, M. D. Exchange bias in nanostructures. *Physics Reports*, **2005**, 422, 65-117.
70. Simeonidis, K. ; Martinez-Boubeta, C. ; Iglesias, O. ; Cabot, A. ; Angelakeris, M. ; Mourdikoudis, S. ; Tsiaoussis, I. ; Delimitis, A. ; Dendrinou-Samara C. ; Kalogirou, O. Morphology influence on nanoscale magnetism of Co nanoparticles: Experimental and theoretical aspects of exchange bias. *Physical Review B* **2011**, *84*, 144430.
71. Masala, O. ; Hoffman, D. ; Sundaram, N. ; Page, K. ; Proffen, T. ; Lawes G. ; Seshadri, R. Preparation of magnetic spinel ferrite core/shell nanoparticles: Soft ferrites on hard ferrites and vice versa. *Solid State Sciences*, **2006**, 8, 1015-1022.
72. Lima, J. E. ; Winkler, E. L. ; Tobia, D. ; Troiani, H. E. ; Zysler, R. D. ; Agostinelli, E. ; Fiorani, D. Bimagnetic CoO Core/CoFe2O4 Shell Nanoparticles: Synthesis and Magnetic Properties. Chemistry of Materials, 2012, 24, 512-516.
73. Masala O. ; Seshadri, R. Spinel Ferrite/MnO Core/Shell Nanoparticles: Chemical Synthesis of All-Oxide Exchange Biased Architectures. *Journal of the American Chemical Society*, **2005**, 127, 9354-9355.
74. Pichon, B. P. ; Gerber, O. ; Lefevre, C. ; Florea, I. ; Fleutot, S. ; Baaziz, W. ; Pauly, M. ; Ohlmann, M. ; Ulhaq, C. ; Ersen, O. ; Pierron-Bohnes, V. ; Panissod, P. ; Drillon M. ; Begin-Colin, S. Microstructural and Magnetic Investigations of Wustite-Spinel Core-Shell Cubic-Shaped Nanoparticles. *Chem. Mater.* **2011**, *23*, 2886-2900.
75. Lee, J.H. ; Jang, J.T. ; Choi, J. S. ; Moon, S. H. ; Noh, S. h. ; Kim, J. W. ; Kim, J. G. ; Kim, I. S. ; Park K. I. ; Cheon, J. *Nat. Nano*, *6*, 418.
76. Iijima S. Helical microtubules of graphitic carbon. *Nature*, **1991**, *354*, 56-58.
77. De Volder, M. F. L.; Tawfick, S. H. ; Baughman, R. H. ; Hart, A. J. Carbon nanotubes: present and future commercial applications. *Science* **2013**, 339, 535-539.
78. Balasubramanian, K. ; Burghard, M. Chemically functionalized carbon nanotubes. *Small* **2005**, 1, 180-192.
79. Zhang, Y. ; Iijima, S. Formation of single-wall carbon nanotubes by laser ablation of fullerenes at low temperature. *Appl. Phys. Lett.* **1999,** *75*, 3087.

80. Anazawa, K. ; Shimotani, K. ; Manabe, C. ; Watanabe, H. ; Shimizu, M. High-purity carbon nanotubes synthesis method by an arc discharging in magnetic field. *Appl. Phys. Lett.* **2002**, 81, 739.
81. Kong, J. ; Cassell, A. M. Chemical vapor deposition of methane for single-walled carbon nanotubes. *Chemical Physics Letters*, **1998**, *292*, 567-574.
82. Kay, B. Electrochemical Properties of High-Power Supercapacitors Using Single-Walled Carbon Nanotube Electrodes. *Advanced Functional Materials*, **2001**, 387–392.
83. Niu, C. ; Sichel, E. K. ; Hoch, R. ; Moy, D. ; Tennent, H. High power electrochemical capacitors based on carbon nanotube electrodes. *Appl. Phys. Lett.* **1997,** 70, 1480.
84. Murray, C. A. ; Lubachevsky, B. ; Walt A. de Heer, A. ; Chatelain, D. ; Ugarte, A. Carbon Nanotube Field-Emission Electron Source. *Science*, **1995**, 270 , 1179-1180.
85. Nanotweezers, N. ; Kim, P. ; Lieberl, C. M. Nanotube Nanotweezers. *Science*,*286*,2148-2150.
86. Singh, R. ; Torti, S. V. Carbon nanotubes in hyperthermia therapy. *Adv. Drug Deliv. Rev.* **2013,** *65*, 2045–2060.
87. Dujardin, B. E. ; Ebbesen, T. W. ; Krishnan, A. ; Treacy, M. M. J. Wetting of Single Shell Carbon Nanotubes. *Adv. Mater.* **1998**, 10, 1472–1475.
88. Barber, A. ; Cohen, S. ; Wagner, H. External and internal wetting of carbon nanotubes with organic liquids. *Phys. Rev. B* **2005**, 71, 115443.
89. Ebbesen, W. Wetting, filling and decorating. *J. Phys. Chem. Solids.* **1996**, *57*, 951-955.
90. Tsang, S. C. ; Chen, Y. K. ; P. Harris, J. F. ; Green, M. L. H. A simple chemical method of opening and filling carbon nanotubes. *Nature*, **1994**, *372*, 159-162.
91. Pan, X. Enhanced ethanol production inside carbon-nanotube reactors containing catalytic particles. *Nat. Mater.* **2007**, *6*, 507-511.
92. Wang, C. ; Guo, S. ; Pan, X. ; Chen, W. ; Bao, X. Tailored cutting of carbon nanotubes and controlled dispersion of metal nanoparticles inside their channels. *J. Mater. Chem.* **2008**, *18*, 5782.
93. Yang, Z. ; Guo, S. ; Pan, X., Wang, J., Bao, X. FeN nanoparticles confined in carbon nanotubes for CO hydrogenation. *Energy Environ. Sci.* **2011**, 4, 4500.
94. Wu, H.-Q. ; Wei, X.-W. ; Shao, M.-W. ; Gu, J.-S. ; Qu, M.-Z. Preparation of Fe-Ni alloy nanoparticles inside carbon nanotubes via wet chemistry. *J. Mater. Chem.* **2002**, *12*, 1919-1921.
95. Astinchap, B. ; Moradian, R. ; Ardu, A. ; Cannas, C. ; Varvaro, G. ; Capobianchi A. Bifunctional FePt @ MWCNTs/Ru Nanoarchitectures : Synthesis and Characterization. *Chem. Mater.* **2012**, *24*, 3393-3400.
96. Camilli, L. et al. High coercivity of iron-filled carbon nanotubes synthesized on austenitic stainless steel. Carbon N. Y. 50, 718–721 (2012).
97. El ás, L. Production and characterization of single-crystal FeCo nanowires inside carbon nanotubes. *Nano Lett.* **2005**, *5*, 467-72.
98. Zhang, J. Individual FeCo Alloy Nanoparticles on Carbon Nanotubes : Structural and Catalytic Properties. *Nano Lett.* **2008**, *8*, 2738-2743.
99. Gao, X. P. Carbon nanotubes filled with metallic nanowires. *Carbon* **2004**, *42*, 47-52.
100. Wang, D. Confinement Effect of Carbon Nanotubes : Copper Nanoparticles Filled Carbon Nanotubes for Hydrogenation of Methyl Acetate. *ACS Catal.* **2012**, *2*, 1958-1966.

101. Wang, C. ; Guo, S. ; Pan, X. ; Chen, W. ; Bao, X. Tailored cutting of carbon nanotubes and controlled dispersion of metal nanoparticles inside their channels. *J. Mater. Chem.* **2008**, *18*, 5782.
102. Chen, Z. ; Guan, Z. ; Li, M. ; Yang, Q. ; Li, C. Enhancement of the performance of a platinum nanocatalyst confined within carbon nanotubes for asymmetric hydrogenation. *Angew. Chem. Int. Ed.* **2011**, *50*, 4913-4917.
103. Corio, P. Characterization of single wall carbon nanotubes filled with silver and with chromium compounds. *Chem. Phys. Lett.* **2004**, *383*, 475–480.
104. Ugarte, D. ; Chatelain, A. ; de Heer W. A. Nanocapillarity and Chemistry in Carbon Nanotubes. *Science* **1996**, 274, 1897-1899.
105. Chu, A. Filling of Carbon Nanotubes with Silver, Gold, and Gold Chloride. *Chem. Mater.* **1996**, *8*, 2751-2754.
106. Capobianchi, A. Controlled filling and external cleaning of multi-wall carbon nanotubes using a wet chemical method. *Carbon N. Y.* **2007,** 45, 2205–2208.
107. Pan, X. Enhanced ethanol production inside carbon-nanotube reactors containing catalytic particles. *Nat. Mater.* **2007**, *6*, 507–511.
108. Pelletier, V. Copper Azide Confined Inside Templated Carbon Nanotubes. *Adv. Funct. Mater.* **2010**, *20*, 3168-3174.
109. Zhang, H. ; Song, H. ; Chen, X. ; Zhou, J. ; Zhang, H. Preparation and electrochemical performance of SnO2@carbon nanotube core–shell structure composites as anode material for lithium-ion batteries. *Electrochim. Acta* **2012**, *59*, 160-167.
110. Schauermann, S. ; Nilius, N. ; Shaikhutdinov, S. ; Freund, H.-J. Nanoparticles for heterogeneous catalysis: new mechanistic insights. *Acc. Chem. Res.* **2013**, *46*, 1673–1681.
111. Yin, Y. ; Talapin, D. The chemistry of functional nanomaterials. *Chem. Soc. Rev.* **2013**, *42*, 2484-2487.
112. Pichon, B. P. ; Barbillon, G. ; Marie, P. ; Pauly, M. ; Begin-Colin, S. Iron oxide magnetic nanoparticles used as probing agents to study the nanostructure of mixed self-assembled monolayers. Nanoscale **2011**, *3*, 4696–4705.
113. Papaefthimiou, V. Effect of the Specific Surface Sites on the Reducibility of α-Fe2O3/Graphene Composites by Hydrogen. *J. Phys. Chem. C* **2013**,*117*, 20313–20319.
114. Baaziz, W. Few layer graphene decorated with homogeneous magnetic Fe3O4 nanoparticles with tunable covering densities. *J. Mater. Chem. A* **2014**, 2, 2690.
115. Kim, I. T. ; Magasinski, A. ; Jacob, K. ; Yushin, G. ; Tannenbaum, R. Synthesis and electrochemical performance of reduced graphene oxide/maghemite composite anode for lithium ion batteries. *Carbon* **2013**, *52*, 56–64.
116. Pham-Huu, C. ; Keller, N. ; Estournès, C. ; Ehret, G. ; Ledoux, M. J. Synthesis of CoFe2O4 nanowire in carbon nanotubes. A new use of the confinement effect. *Chem. Commun. (Camb)*. **2002**, 1882–1883.
117. Ersen, O. Microstructural Investigation of Magnetic CoFe2O4 Nanowires inside Carbon Nanotubes by Electron Tomography. *Nano Lett.* **2008**, *8*,1033-1040.
118. Pham-Huu, C. Microstructural investigation and magnetic properties of CoFe2O4 nanowires synthesized inside carbon nanotubes. Phys. Chem. Chem. Phys. 5, 3716 (2003).
119. Chen, W. ; Pan, X. ; Bao, X. Tuning of redox properties of iron and iron oxides via encapsulation within carbon nanotubes. *J. Am. Chem. Soc.* **2007**, *129*, 7421–7426.

120. Chen, W. ; Pan, X. ; Willinger, M.-G. ; Su, D. S. ; Bao, X. Facile autoreduction of iron oxide/carbon nanotube encapsulates. *J. Am. Chem. Soc.* **2006**, *128*, 3136–3137.
121. Baaziz, W. Carbon nanotube channels selectively filled with monodispersed Fe3-xO4 nanoparticles. *J. Mater. Chem. A* **2013**,*1*, 13853-13861.
122. Baaziz, W. High-Density Monodispersed Cobalt Nanoparticles Filled into Multiwalled Carbon Nanotubes. *Chem. Mater.* **2012**, *24*, 1549-1551.
121. Yu, W.-J. ; Hou, P.-X. ; Li, F. ; Liu, C. Improved electrochemical performance of Fe2O3 nanoparticles confined in carbon nanotubes. *J. Mater. Chem.* **2012**, *22*, 13756.
122. Korneva, G. Carbon nanotubes loaded with magnetic particles. *Nano Lett.* **2005**, 5, 879–884.
123. Orikasa, H. ; Inokuma N. ; Ittisanronnachai, S. ; Wang, X. H. ; Kitakamia O. ; Kyotania, T. Template synthesis of water-dispersible and magnetically responsive carbon nano test tubes. *Chem. Commun. (Camb).* **2008**, 2215-2217.
124. Wang, X. H. Controlled filling of Permalloy into one-end-opened carbon nanotubes. *J. Mater. Chem.* **2007**, *17*, 986.
125. Jang, J. ; Yoon, H. Fabrication of Magnetic Carbon Nanotubes Using a Metal-Impregnated Polymer Precursor. *Adv. Mater.* **2003**, *15*, 2088–2091.
126. Jang, J.,Yoon, H. Facile fabrication of polypyrrole nanotubes using reverse microemulsion polymerization. *Chem. Commun. (Camb).* **2003**, 720–721.
127. Pal, S. ; Chandra, S. ; Phan, M. H. ; Mukherjee, P. ; Srikanth, H. Carbon nanostraws: nanotubes filled with superparamagnetic nanoparticles. *Nanotechnology* **2009**, *20*, 485604.
128. Bao, J. ; Tie, C. ; Xu, Z. ; Suo, Z. ; Zhou, Q. ; Hong, J. A Facile Method for Creating an Array of metal filled carbon nanotubes. *Adv.mater.* **2002**,*14*, 1483-1486.
129. Weissker, U. ; Hampel, S. ; Leonhardt, A. ; Büchner, B. Carbon Nanotubes Filled with Ferromagnetic Materials. *Materials (Basel).* **2010**, *3*, 4387–4427.
130. Kopyl, S. ; Bystrov, V. ; Bdikin, I. ; Maiorov, M. ; Sousa, A. C. M. Filling carbon nanotubes with magnetic particles. *J. Mater. Chem. C* **2013**, *1*, 2860.
131. Demoncy, N.; Stephan, O. ; Brun, N.; Colliex, C.; Loiseau, A.; Pascard1, H. Filling carbon nanotubes with metals by the arc-discharge method: the key role of sulfur. *Eur. Phys. J. B* **1998**, *4*, 147-157.
132. Guldi, D. M. ; Martin, N. Carbon Nanotubes and Related Structures: Synthesis, Characterization, Functionalization, and Applications. February 2010, Wiley.
133. Costa, P. M. F. J. ; Sloan, J. ; Rutherford, T. ; Green, M. L. H. Encapsulation of RexOy Clusters within Single-Walled Carbon Nanotubes and Their in tubulo Reduction and Sintering to ReMetal. *Chem. Mater.* **2005**, *17*, 6579-6582.
134. Schulte, K. Assembly of Cobalt Phthalocyanine Stacks inside Carbon Nanotubes. *Adv. Mater.* **2007**, *19*, 3312-3316.
135. Leonhardt, A. ; Hampel, S. ; Müller, C. ; Mönch, I. ; Koseva, R. ; Ritschel, M. ; Elefant, D. ; Biedermann, K. ; Büchner, B. Synthesis, Properties, and Applications of Ferromagnetic-Filled Carbon Nanotubes. *Chem. Vap. Depos.* **2006**, *12*, 380-387.
136. Tao, X. Y. Thermal CVD synthesis of carbon nanotubes filled with single-crystalline Cu nanoneedles at tips. *Diam. Relat. Mater.* **2006**, 15, 1271–1275.

137. Pradhan, B. K., Toba, T., Kyotani, T., Tomita, A. Inclusion of Crystalline Iron Oxide Nanoparticles in Uniform Carbon Nanotubes Prepared by a Template Carbonization Method. *Chem. Mater.* **1998**, 10, 2510-2515.

Chapter Ⅱ :Influence of the nature of ligands on the synthesis of $Fe_{3-x}O_4$ and CoO Nanoparticles

II.1 Introduction

IPCMS has developped the synthesis of iron oxide nanoparticles (NPs) by thermal decomposition of iron stearate in presence of oleic acid in a high boiling solvant. By controling the amount of ligand, the reaction temperature, the heating rate, the nature of solvents, nanoparticles with mean size in the range 4-28 nm[1] were obtained.

The synthesis of CoO nanoparticles (NPs) by thermal decomposition of Co stearate has been shown to be more difficult by comparison with that of Fe_3O_4 NPs in the same experimental conditions.[2] The yield in CoO NPs is very low and the products are not pure including a large amount of viscous chemicals, which is mainly due to the fact that cobalt stearate decomposes at higher temperature than iron stearate as shown by TGA curves (Figure II-1). Indeed TGA curves show that the precursor decomposition occurs on the wide range of temperatures between 200 and 400 ℃. The TGA curve of Fe stearate is similar to that of the iron oleate complex, which has been widely studied.[1,3,4,5,6,7] The first weight loss at 250 ℃ correponds to the nucleation step and it corresponds to the dissociation of iron oleate leading to the formation of monomers.[1,3] Monomers, the minimum building units of iron oxide nanocrystals, are supposed to be intermediate species such as polyironoxo clusters, which concentration increases as the reaction proceeds.[7] At this first decomposition step, the monomer concentration increases and the germination occurs as predicted by the La Mer model.[8] In the La Mer model (Figure II-2), the energy barrier of the nucleation process is much higher than that of the growth process. When the supersaturation of the monomer ($C>C_{min}$) is high enough to overcome this energy barrier, burst nucleation will take place, resulting in the formation and accumulation of stable nuclei (Figure II-2). The minimum radius of a stable nucleus that can grow spontaneously in the supersaturated solutions is inversely proportional to the supersaturation. At high supersaturation (high C_{max}), a large amount of nuclei are generated but with small radius while for small supersaturation (small C_{max}), a lower amount of nuclei is formed but with larger radius. Then the growth of NPs is favored by the continuous decomposition of the iron complex with the increase in the temperature (in the range 200-400 ℃ from TGA). This temperature-dependent growth rate is supported by the increase of the NPs size with the reaction temperature (e.g. the boiling point of solvents) in particular with alkene solvents.[1]

The comparison of TGA curves of iron and cobalt stearates clearly demonstrates that cobalt stearate decompose at higher temperature than iron stearate and thus the nucleation step of NPs occurs at higher temperature around 300 ℃. In order to improve the yield of CoO NPs, the synthesis of cobalt oxide NPs has been performed by using amine ligands. Indeed, amine ligands are known to destabilize the iron stearate precursor due to acido-basic reaction between amine ligands and carboxylate ligands of iron complex,[9] leading to its decomposition at lower temperature. With the iron stearate complex, we observed the formation of smaller

NPs with amine ligands by comparison by carboxylate ligands: the presence of amine favors the decomposition of iron stearate and thus the increase in the concentration of monomers C_{max} leading to the formation of a larger amount of nuclei with a smaller size according to the La Mer theory. Therefore the synthesis of CoO NPs has been performed with oleylamine instead of oleic acid. However, it is observed that even if the CoO NPs yield was higher, the morphology and size of CoO NPs were completely different.

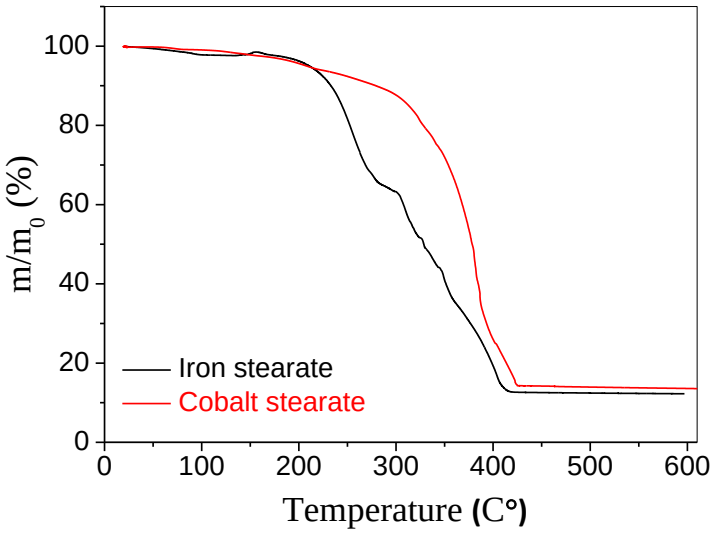

Figure II-1. TGA curves of Fe stearate (black line) and Co stearate (red line).

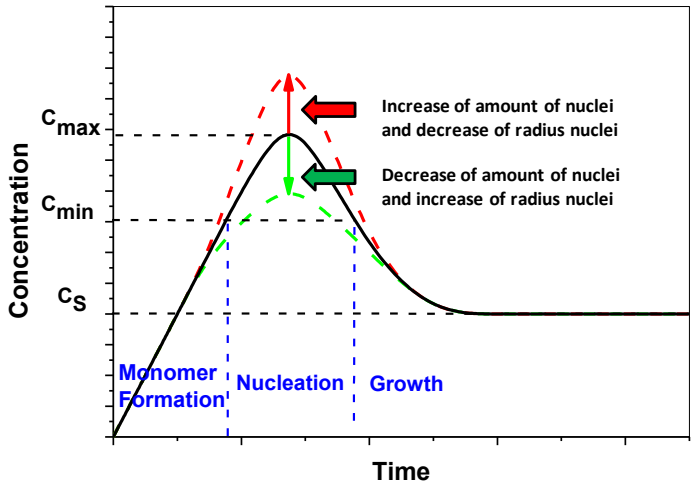

Figure II-2. Variation of the monomer concentration during the germination and growth steps (Cs is the solid solubility) according to LaMer et al.[8]

So far, the influence of nature of the ligands on the shape of CoO has been investigated by some scientists. Tetrahedral CoO nanocrystals with 4-5 nm size were synthesized by Yin and Wang,[10,11] via the decomposition of $Co_2(CO)_8$ in toluene in the presence of the surfactant Na(AOT) at 130 ℃. Pure quite spherical CoO nanoparticles with size ranging in 4.5-18 nm were produced by the decomposition of Co(II) cupferronate in decalin under solvothermal route.[12] Rod-shaped and cubic CoO nanocrystals were obtained by the decomposition of

cobalt-(III) acetylacetonate in oleylamine by modifying the ratio of precursor/ligands ($Co(acac)_3$/oleylamine).[13] Uniformed tetrapodal CoO NPs were synthesized by the dissolution of Co_3O_4 in oleic acid and then alcoholysis of the formed Co(III)-oleate complex.[14] The size was tuned by modifying the ratio of dodecanol/oleic acid. Zhongping C. et al[15] decomposed cobalt oleate in octadecene in presence of oleic acid : they observed the formation of small needles when the mixture reaches the reflux temperature and then the formation of nanoflowers with reflux time. They suggest that the CoO nanoparticles could be the result of growth of the seeds along [11] direction in a dendritic fashion, resulting in the highly anisotropic flower-like shape. Under the same experimental conditions but with a vigorous stirring, An et al. synthesized pencil-shaped CoO nanorods.[16]

Zhang Y et al.[17] have obtained cubic CoO nanocrystals with various morphologies and sizes via the decomposition of cobalt (II) oleate complex at 280-320 ℃ in octadecene by using dodecanol/oleic acid ligands. The morphology of CoO nanostructures was reported to be tuned from the simple isolated tetrahedral shape to the complex 3D flowerlike shape by increasing the concentration of oleic acid, while with increasing concentration of dodecanol, the morphology of the CoO structures can be tuned from the 3D nanoflower to isolated spheres.

Therefore one may conclude that the effect of ligands on the morphology of CoO NPs is not trivial and depends strongly on the experimental conditions (solvants, nature of ligand, concentration, heating rate, reaction time, stirring..). To study the impact of the nature of ligands on the morphology of CoO NPs, we have investigated the synthesis of CoO and Fe_3O_4 NPs by thermal decomposition by varying the nature and amount of ligands which were either amine or carboxylate ligands. As the decomposition temperature of cobalt stearate is high, the decomposition has been conducted in octadecene but also with octyl ether with iron oxide NPs. Then we have tried to understand why Co stearate and Fe stearate, which have a similar complex structure, decompose differently and lead to such different morphology. Preliminary results of simulation on the decomposition of Fe stearate and Co stearate allow insight on the mechanism of decomposition.

II.2 Experimental details

II.2.1 Synthesis of Fe_3O_4 and CoO NPs

II.2.1.1 Synthesis of $Fe_{3-x}O_4$ NPs

The typical procedure is as follows: First of all, 1.38 g (2.22 mmol) $Fe(stearate)_2$ (9.47% Fe, Strem Chemicals), 1.24 g (4.41 mmol) oleic acid (99%, Alfa-Aesar) as ligand, 20 ml octadecene (90%, Alfa Aesar) as solvent were mixed. Then, the mixture was sonicated, stirred and kept at 120 ^oC for 1h to evaporate residual trace of water or ethanol. Subsequently, the

temperature rose up to 318 °C (boiling point of octadecene) with 5°C/min heating ramp and kept at this temperature for 2h under air (Set-up in Figure II-3). Finally, the resultant products were cooled and the NPs were precipitated by the addition of an excess of acetone the first time and then washed three times with a mixture of chloroform/ethanol (1/3) by centrifugation (14 000 rpm, 10 min), followed by the suspension of the sample in THF. Hexadecylamine (98%, Sigma-Aldrich), oleylamine (70% Technical grade, Sigma-Aldrich) and mixture of oleic acid and hexadecylamine (mass ratio of 1:1) were used to synthesize the Fe_3O_4 NPs instead of typical ligand oleic acid by keeping the amount of ligands the same.

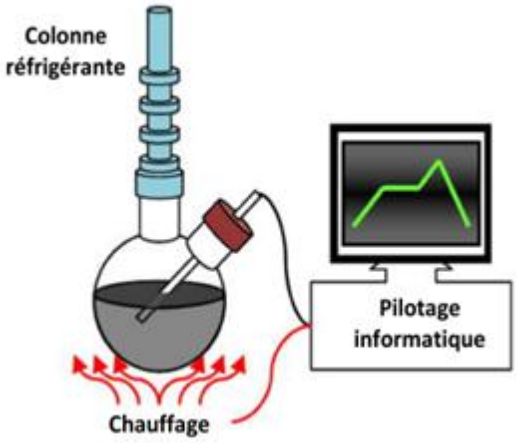

Figure II-3. Set-up for the thermal decomposition process.

II.2.1.2 Synthesis of CoO NPs

First of all, 1.38 g (2.22 mmol) $Co(stearate)_2$ (9-10% Co, Strem Chemicals), 1.24 g (4.41 mmol) oleic acid and 20 ml Octadecene were mixed. Then, the mixture was sonicated, stirred and kept at 120 °C for 1h to evaporate residual trace of water or ethanol. Subsequently, the temperature rise up to 318 °C (boiling point of octadecene) with 5 °C/min ramp and kept at this temperature for 2h under Ar gas. Finally, the resultant products were cooled and the NPs were precipitated by the addition of an excess of acetone the first time and then washed three times with a mixture of hexane/ethanol (1/3) by centrifugation (14 000 rpm, 10 min). Hexadecylamine, oleylamine and mixture of oleic acid and hexadecylamine (mass ratio of 1:1) were used to synthesize the CoO NPs instead of typical ligand oleic acid by keeping the amount of ligands the same.

II.2.2 Characterization techniques of NPs

Transmission Electron Microscopy has been carried out using a JEOL 2100F (voltage 200 kV) microscopy with a point resolution of 0.2 nm. The sample was dispersed in ethanol by ultrasonication during 5 min and a drop of the solution was then deposited on a copper grid (covered with a carbon membrane). The structure of NPs was investigated in the high-resolution mode (HR-TEM) and by electron diffraction. The size distribution of NPs was

calculated from the size measurements of more than 300 NPs by using image J software. STEM images were taken in high-angle annular dark field HAADF mode with a 0.12 nm probe. EELS spectra were recorded in the diffraction mode and EFTEM images were taken on the Fe and Co edges with a 20 eV window, which gives a 1.5 nm resolution imaging. EDX were performed with a JEOL Si (Li) detector.

X-ray Diffraction (XRD) was carried out using a Bruker D8 Advance in the 27-75 ° (2Θ) range with a scan step of 0.03 °. The detector was a three degrees wide analysis detector ("Lynx Eye)"). Profile matching refinements were performed through the Fullprof program20 using the modified Thompson-Cox-Hasting (TCH) pseudo-Voigt profile function.21 Such a procedure enabled us to calculate cell parameters and crystal sizes.

X-ray Photoelectron Spectroscopy (XPS) measurements were carried out in an ultrahigh vacuum (UHV) setup equipped with a VSW ClassWA hemispherical electron analyzer (150 mm radius) with a multi-channeltron detector. A monochromated Al Kα X-ray source (1486.6 eV; anode operating at 240 W) was used as incident radiation. The base pressure in the measurement chamber was ~ $1x10^{-9}$ mbar. XP spectra were recorded in the fixed transmission mode using pass energy of 20 eV resulting in an overall energy resolution better than 0.4 eV. The binding energies were calibrated based on the graphite C 1s peak at 284.5 eV. The CASA XPS program with a Gaussian-Lorentzian mix function and Shirley background subtraction was employed to deconvolute the XP spectra. The % oxygen content was calculated by O 1s and C 1s core level peaks, properly normalized to the photoemission cross section and assuming a homogeneous distribution arrangement model.

Scanning Electron Microscopy (SEM) JEOL 6700F is equipped with a field emission gun (FEG) and operating at 3 kV.

Fourier Transform Infrared Spectroscopy (FTIR) was performed using a Digilab Excalibur 3000 spectrophotometer (CsI beam splitter) in the wavenumber range 4000-400 cm^{-1} on samples diluted in KBr pellets.

Thermal Gravimetric Analyses (TGA) was carried out with a TA Instrument (Q-5000 model). They were performed under an air flow up to 600 ℃ with a heating rate of 5 ℃/min.

II.3 Morphological and structural characterizations of NPs

II.3.1 Influence of the nature of ligands on the morphology of NPs

Precursor	Ligand	TEM size	Crystalline size	Lattice parameter	Morphology
Fe stearate	Oleic acid	9.6 ±0.9	5.9 nm	×	Spherical
	Hexadecylamine	4.9 ±0.9	5.1 nm	×	Spherical
	Oleylamine	5.1 ±1.6	4.5 nm	×	Spherical
	Mixture of Oleic acid Hexadecylamine(1:1)	10.1 ±3.3	6.8 nm	×	Spherical
Co stearate	Oleic acid	50 nm	22	4.262 Å	Triangular/ Tetrahedral
	Hexadecylamine	269±55nm	18	4.263 Å	nanoflowers
	Oleylamine	227±50nm	25	4.258 Å	nanoflowers
	Mixture of oleic acid Hexadecylamine(1:1)	×	18	4.256 Å	Multipod

Table II-1. Synthesis parameters of $Fe_{3-x}O_4$ and CoO NPs. Fe_3O_4 NPs synthesize in octyl ether.

II.3.1.1 $Fe_{3-x}O_4$ NPs

The parameters of the synthesis of $Fe_{3-x}O_4$ NPs are presented in Table II-1. Figure II-4 shows the TEM images of Fe_3O_4 NPs as a function of the nature of ligands: either carboxylic acid or amine ligands and in octyl ether as solvant. In the typical synthesis with oleic acid, the shape of NPs is spherical and uniform in size. The size distribution of NPs is very narrow (9.6 ± 0.9 nm) and was calculated from size measurements on more than 300 NPs. When amine ligands are used, as expected, the average NPs size is smaller [1]: 4.9 ± 0.9 and 5.1 ± 1.6 for hexadecylamine and oleylamine respectively. No clear difference is observed between both amine ligands. As explained in the introduction part, amine ligands are known to destabilize the iron stearate precursor leading to its decomposition at lower temperature. The resulting increase in the concentration of monomers induces the formation of a larger amount of nuclei with a smaller size according to the La Mer theory. When a mixture of hexadecylamine and oleic acid is used, the size distribution becomes broader: 10.1 ± 3.3 nm. Such a broad distribution may originate from a distribution of iron complexes with different stability. In contrary to amine ligands, oleic acid is known to stabilize cobat stearate in octyl ether. One may conclude that in octyl ether, NPs display a spherical shape and the amine ligands induce a decrease of the NPs size.

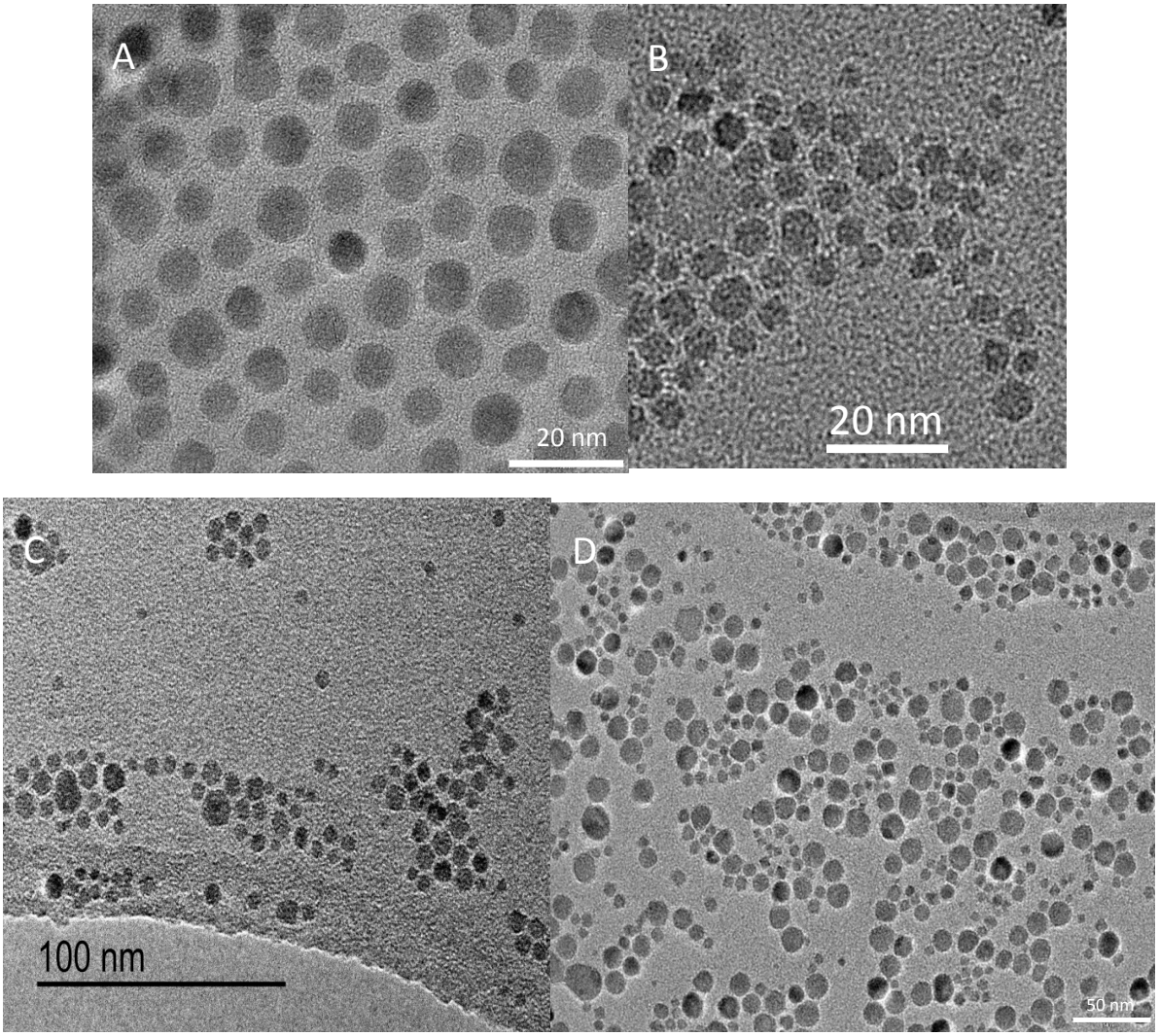

Figure II-4. TEM images of $Fe_{3-x}O_4$ NPs and their size distribution by using oleic acid (A), hexadecylamine (B), oleylamine (C) and a mixture of oleic acid and hexadecylamine (1:1) (D) in octyl ether as solvant.

As shown in Figure II-5a, the synthesis of iron oxide NPs in octadecene with oleic acid leads to spherical NPs but the size distribution is less homogeneous with some bigger NPs as already observed in earlier studies.[1] When amine ligands are used, the NPs remain spherical but their size distribution becomes very broad. These results show that oleic acid favors the monodispersity of NPs. The amine ligands should induce a distribution of iron complexes with different stabilities which nucleate at different temperature (the fact that the synthesis is performed without stirring should favour that).

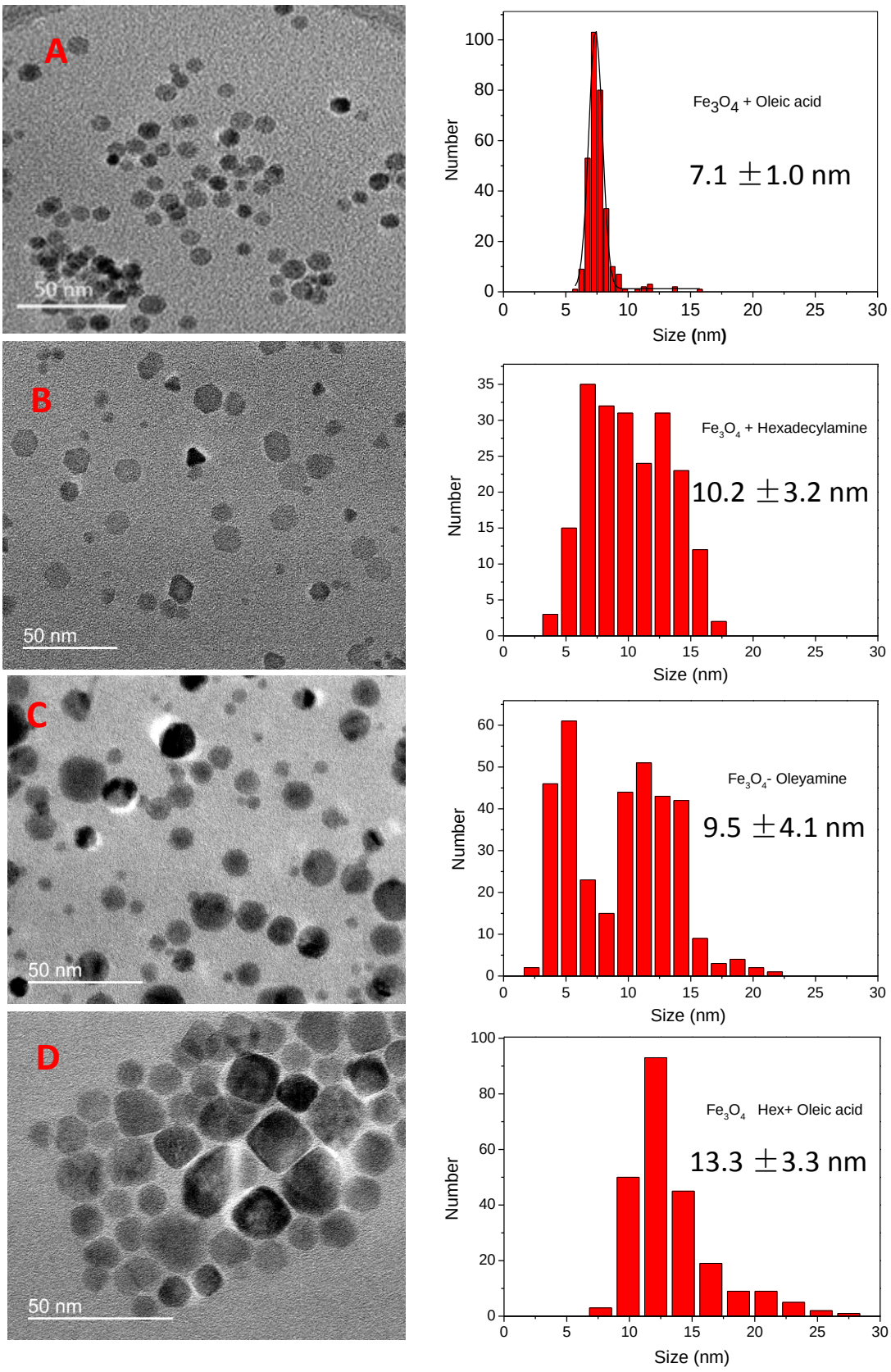

Figure II-5. TEM images of $Fe_{3-x}O_4$ NPs and their size distribution by using oleic acid (A), hexadecylamine (B), oleylamine (C) and a mixture of oleic acid and hexadecylamine (1:1) (D) in octadecene as solvant**.**

II.3.1.2 CoO NPs

The same synthetic conditions were used to synthesize CoO NPs in octadecene and the parameters are also presented in Table II-1.

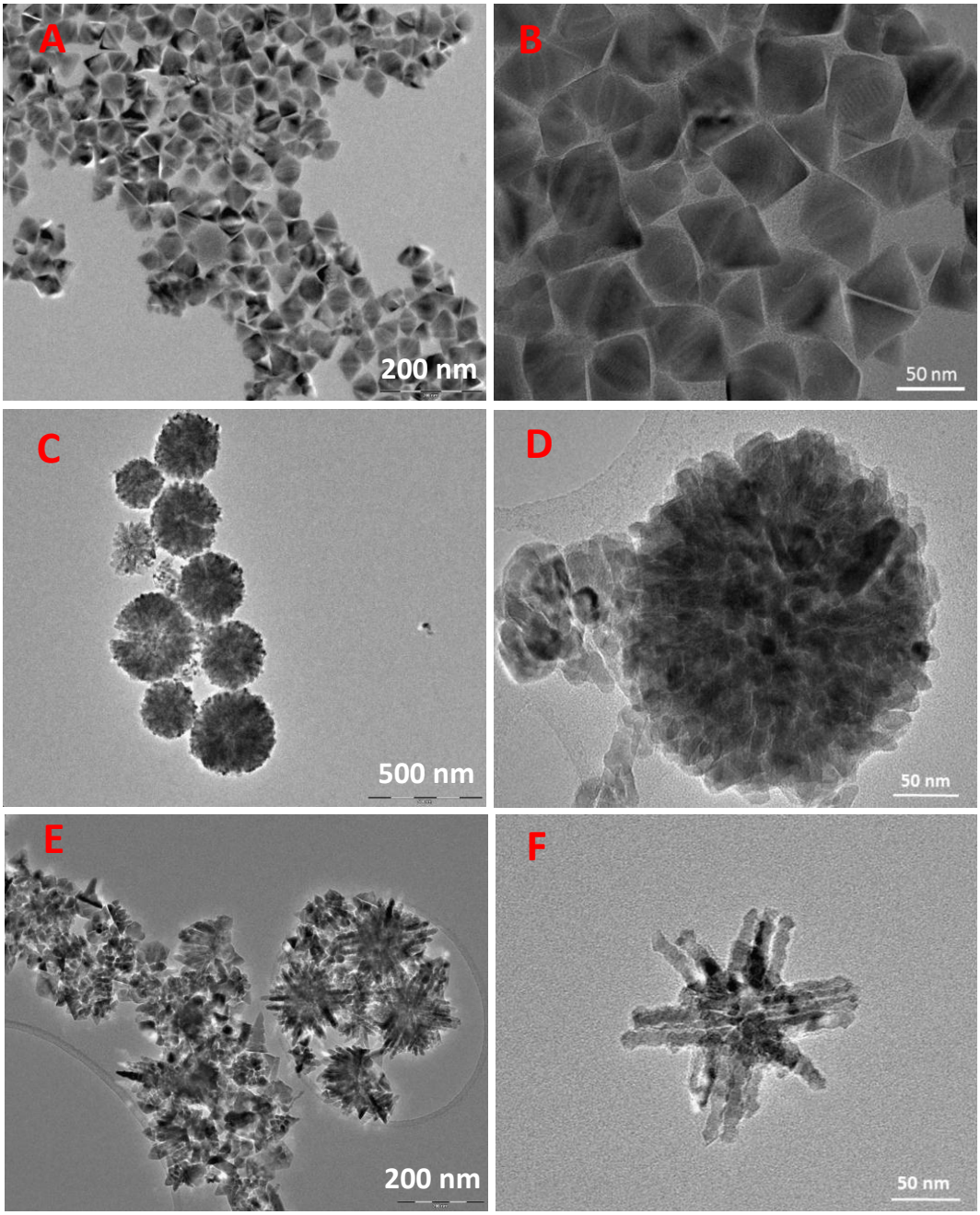

Figure II-6. TEM and HRTEM images of CoO nanoparticles by using oleic acid (A-B), hexadecylamine (C-D) and a mixture of oleic acid and hexadecylamine (mass ratio of 1:1) (E-F).

Figure II-6A showed that in presence of oleic acid, the shape of CoO NPs is mainly triangular in 2D but certainly tetrahedral in 3D as already reported in other papers. Such a shape with oleic acid is in a good agreement with reported results.[13,16] But the reaction time in our case is a little bit longer and we can observe that some triangular NPs tend to aggregate

and form octahedral quite cubic shaped NPs. In Figure II-6B, HRTEM image showed that the size of the triangle edge is around 50 nm. One may remind that, the yield in NPs is very low with oleic acid.

When hexadecylamine is used instead of oleic acid, the NPs are no longer triangular. Their morphology is spherical and porous and their size is very large in the range 200-380 nm, as shown in Figure II-6C, with a mean size of 269 ± 55 nm. Such observation is confirmed by SEM images in Figure II-7A, which show porous spherical particles. Moreover, some spherical particles are found broken and they seem to be hollow. From HRTEM image in Figure II-6D, we can observe that the particles consist of aggregates of smaller nanocrystals and are often named nanoflowers. The individual nanocrystals are not spherical but a little bit elongated with a mean size in the range 18-25 nm as seen in Figure II-8.

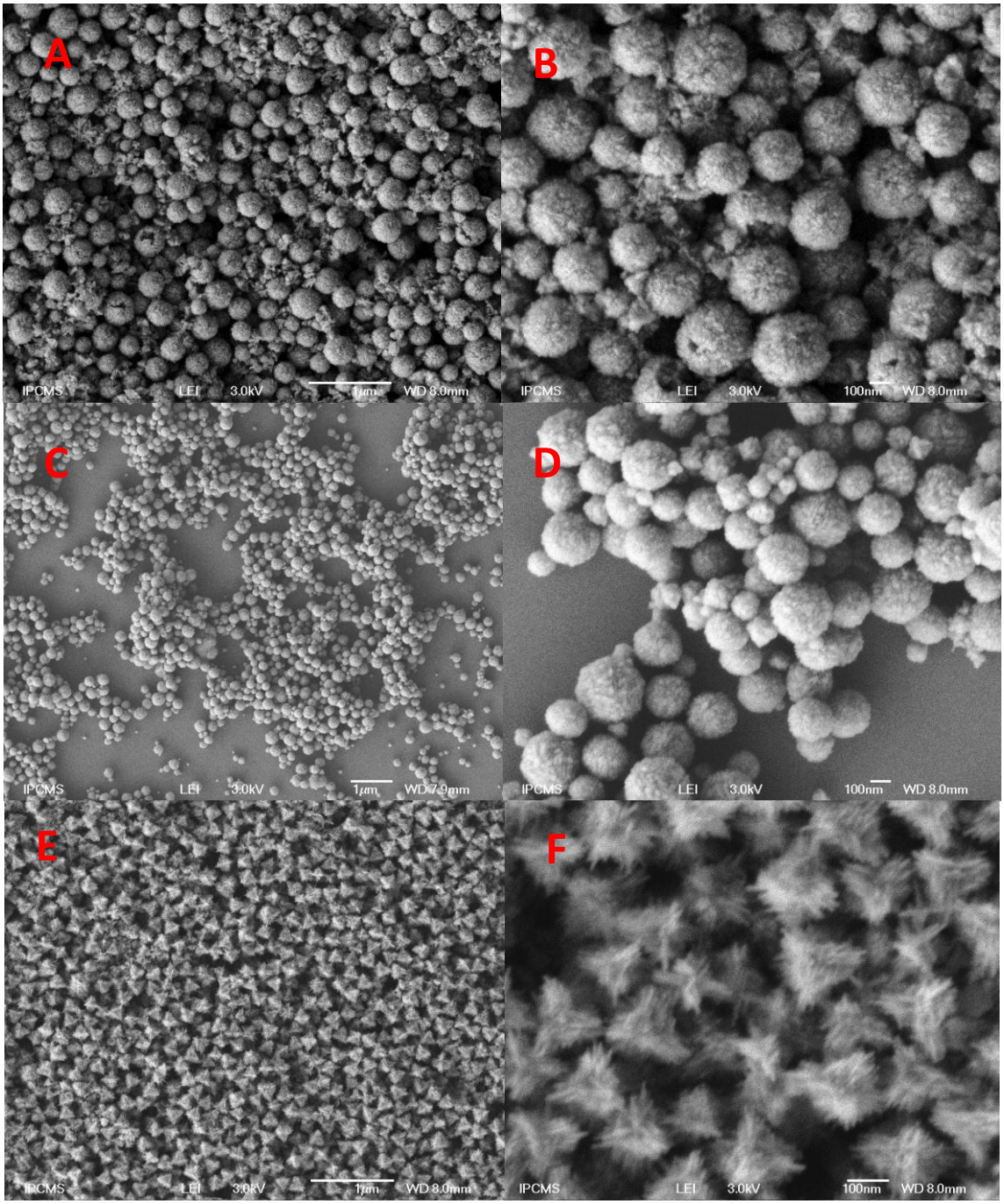

Figure II-7. SEM images of nanoparticles by using hexadecylamine(A-B), oleylamine (C-D) and a mixture of oleic acid and hexadecylamine (1:1) (E-F) in octadecene.

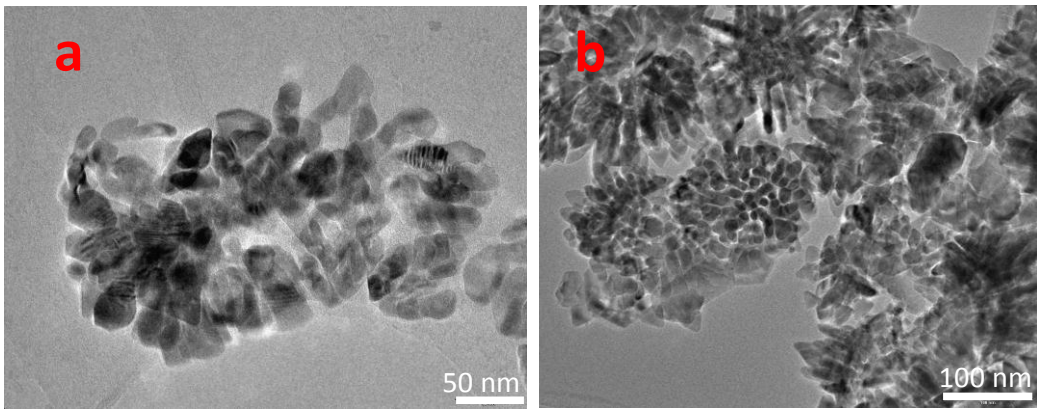

Figure II-8. TEM images of a) not well formed nanoflowers with hexadecylamine allowing to show the nanocrystals b) of particles obtained from a mixture of hexadecylamine and oleic acid.

Oleylamine was also used to replace hexadecylamine as ligand. The so obtained particles display a similar spherical porous morphology (Figure II-7 C-D) with a slightly smaller mean size around 227±50 nm. Furthermore, one may notice that there are fewer broken spherical particles suggesting perhaps that, in that case, the nanoflowers are not hollow. One may conclude that both amine ligands lead to the formation of nanoflower shaped NPs.

Finally, the mixture of oleic acid and hexadecylamine with weight ratio of 1:1 was observed to change again the shape of CoO particles. As it can be seen in Figure II-7-E-F, polypod-like structures with a global tetrahedral shape are formed. TEM images in Figure II.6 E-F allow to better see the morphology of particles which may be named polypodal or multipodal particles, and are composed of well-organized nanorods. The mean diameter of rods is around 18 nm.

To try to better understand the effect of ligands on the observed morphologies: the reaction time has been varied as well as the amount of ligands. To remind: after 2 hours of reflux with oleylamine, the nanoflowers/nanostructures appear compact without broken particles by comparison with hexadecylamine. After 30 minutes at the reflux temperature with oleylamine, one observes the formation of hollow nanostructures constituted of aggregates of nanocrystals and a lot of nanostructures are broken (Figure II.9). The biggest nanostructures display a mean size of 156 nm ± 56 nm from TEM images. After one hour at the reflux temperature, the nanostructures are more homogeneous in size with a mean size of around 350 ±75 nm and very few broken nanostructures are observed (Figure II.9). The nanostructures after reflux for 30 minutes with oleylamine seem very similar to those obtained after 2 hours of reflux with hexadecylamine. This suggests that the nanostructures formation kinetic is faster with oleylamine than with hexadecylamine and thus the nanostructures should have time to sinter with the reaction time. This may be explained by the double bond (C=C) in the middle of the oleylamine molecule, which would also affect the coordination with Co complex.[18] Therefore the decomposition and the germination would occur quicker than with

hexadecylamine.

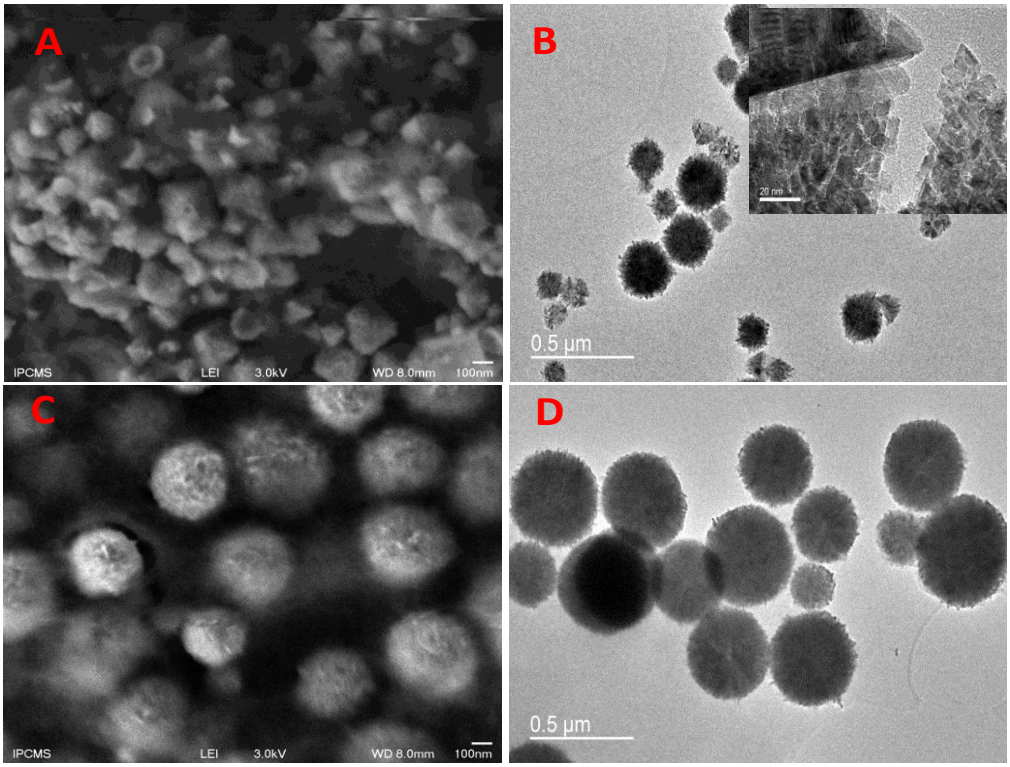

Figure II-9. SEM and TEM images of CoO nanoparticles synthesized by using oleylamine and a reflux time of 30 min (A-B) and 1h (C-D). Inset : HRTEM of small cluster in image B.

By taking into account these results, it can be suggested that CoO nanocrystals were formed initially and assembled into spherical nanostructures because of minimizing the surface energy and with reaction proceeding, the formed spherical clusters become more compact and denser, which is driven by the surface effect. Aggregation of particles is reported to be a common feature of nanoparticle synthesis and can occur because of the amount and type of capping agents used or magnetic effects.[19]

Indeed thermolysis and solvothermal synthesis are known to favor the formation of colloidal nanoparticle clusters and the key parameter may be the concentration in capping ligands which has to be not enough to protect the primary NPs against aggregation but sufficient to stabilize the resulting 3D nanostructures.[20] By reducing the degree of ligand protection to the domain of so-called ‘‘limited ligand protection’’ (LLP), complex three-dimensional (3D) nanostructures can be produced through the oriented attachment of primary NPs.[21] Peng et al. produced 3D nanoflower-like structures for metal oxides such as In_2O_3, CoO, MnO and ZnO by reducing the amount of stabilizing organic ligands to the point that the primary NPs were insufficiently protected.[22,23] Thus one key to the formation of nanostructures would be to maintain an appropriate concentration of capping ligands, which is not enough to protect the primary nanoparticles against aggregation but sufficient to stabilize the resulting 3D nanostructures.

In addition, it has been recently shown that such clustering may be favored by magnetic

interactions.[19] Indeed the nuclei growth, reach a critical size where their magnetization is no more negligible and then they aggregate by magnetic interactions. In our case, this mechanism is not to exclude because the reaction proceeds under argon and during the synthesis, cobalt NPs may form with a diameter close to the superparamagnetic-ferromagnetic diameter limit (7 or 15 nm depending on their cristalline structure) and thus they may agregate under magnetic interactions.

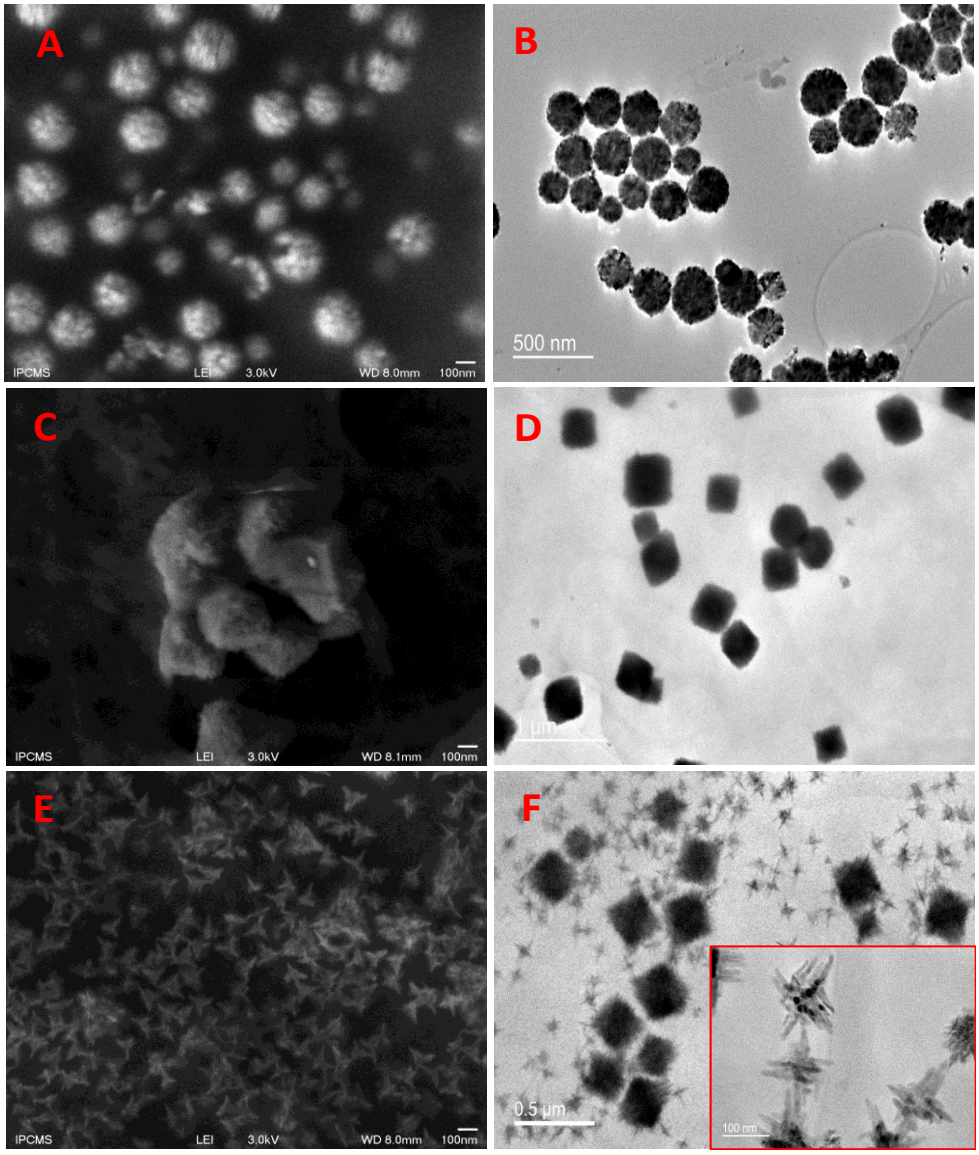

Figure II-10. SEM and TEM images of CoO nanoparticles synthesized by using different amount of ligand instead of typical mass (1.24 g): oleylamine 2.48 g (A-B), oleylamine 0.48 g (C-D); oleic acid 0.26 g (E-F). Inset : HRTEM of multipod**.**

Therefore, the investigation of the effect of amount of ligand on the clusters was performed (Figure II-10). By increasing the amount of oleylamine twice to 2.48 g, always spherical clusters/nanostructures are formed with an average diameter of 221±35 nm as shown in Figure II-10A-B. The size and morphology do not change whereas we would expect the formation of individuel nanograins if the clustering was induced by a ligand concentration

effect.

Besides, the amount of oleylamine was decreased to 0.48 g (Figure II-10 C-D), the obtained particles display a cubic shape with a mean size of 360±66 nm. A few spherical CoO clusters were present. The formation of such big particles may be explained by the fact that the amount of oleylamine being small, the decomposition of the precursor is lower and thus few monomers are formed leading to the formation of nuclei with a low yield during the nucleation step. Then, the growth process is favored with the reaction time leading to big particles.

Finally, the amount of oleic acid was decreased to 0.26 g, multipodals particles were obtained with a global tetrahedral shape and with different sizes (Figure II-10-E-F). From TEM images, on may observe that these multipodal particles tend to aggregate to form cubic/octahedral shaped particles (Figure II-10-F). The formation of cubic CoO clusters (by aggregation) may be due to the lower amount of oleic acid and/or magnetic interactions. It is worth noting that in presence of low amount of OA, pure CoO was synthesized.

III.3.1.3 Discussion

We may conclude here that whatever the nature of ligands, amine or carboxylate ligands, spherical iron oxide NPs are formed by thermal decomposition: their main effect is on the nanosize. Indeed amine ligands favor the decomposition of the precursor and thus the nucleation step with a high yield in nuclei. The growth step is then limitated due to the lower amount of precursor available in the solution after the nucleation.

With cobalt stearate, the behavior is completely different and the nature of ligands has a strong influence on the morphology of particles. With oleic acid, tetrahedral shaped NPs are formed as reported in litterature with a low yield. A decrease of the amount of oleic acid leads to multipodal particles similarly to what was obtained by using a mixture of hexadecylamine and oleic acid. It is well known that shaped nanoparticles such as nanodisks, nanorods, and nanoscale polyhedral structures can be synthesized by taking advantage of the selective adhesion of certain ligands to particular crystalline facets to kinetically control the relative growth rates along different crystalline directions.[24] These first results suggest that oleic acid would be responsible for the multipodal shape of NPs.

With amine ligands, clusters of nanocrystals/nanostructures are formed. Their kinetic of formation and growth seems faster with oleylamine than with hexadecylamine. The results obtained with the variation of the amount of ligands do not allow to conclude on a possible effect of the ligand amount on the clustering of nanograins but a clustering induced by magnetic interaction is not to exclude.

II.3.2 Structural characterization of NPs

III.3.2.1 X-Ray diffraction

XRD patterns of $Fe_{3-x}O_4$ and CoO NPs obtained by using the different ligand oleic acid, hexadecylamine, oleylamine and mixture of oleic acid and hexadecylamine are given in Figure II-11. For CoO particles synthesized with amine ligands, the XRD patterns correspond to the cubic CoO phase (JCPDS JCPDS file 70-2856). The experimental lattice parameters are 0.4263 nm and 0.4258 nm for hexadecylamine and oleylamine respectively in good agreement with the expected one 0.426 nm for cubic CoO. With oleic acid and the mixture of hexadecylamine and oleic acid, new peaks appear which correspond in fact to a hexagonal wurtzite phase,[13,25] which has been evidenced first in 2005 by thermal decomposition of a single molecular precursor $Co(acac)_3$ in oleylamine [13] and by thermal decomposition of $Co(acac)_2$ in benzyl ether.[13] Cubic CoO is a cubic rocksalt with the Co^{2+} cations occupying the octahedral sites and hexagonal wurtzite with Co^{2+} cations occupying the tetrahedral sites. No spinel Co_3O_4 is identifed in XRD patterns.

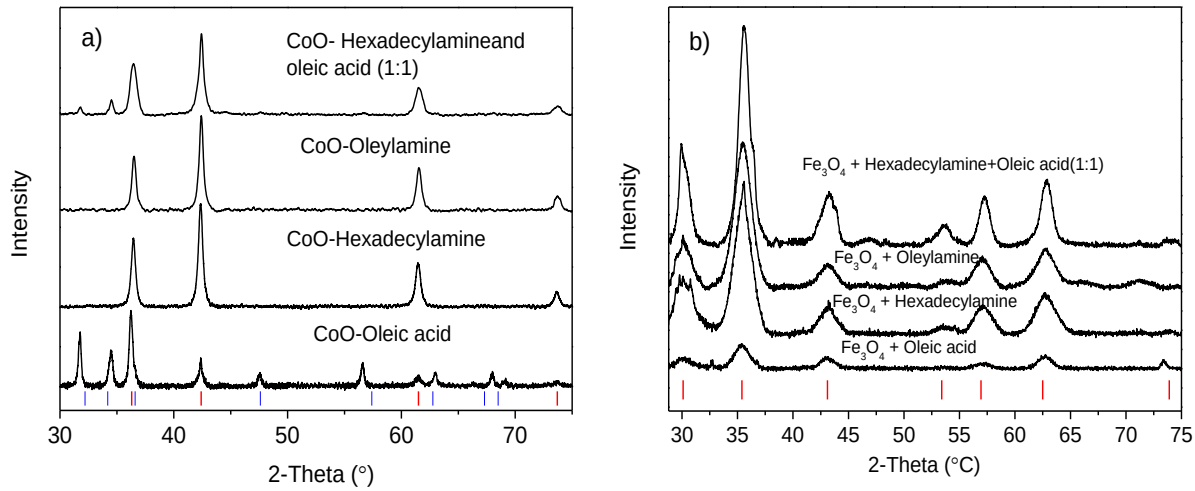

Figure II-11. XRD patterns of CoO (a) and $Fe_{3-x}O_4$ (octyl ether) (b) particles obtained by using oleic acid, hexadecylamine, oleylamine and mixture of oleic acid and hexadecylamine. a: Reference XRD peaks of cubic CoO in red and hexagonal CoO in blue vertical bars. and b: Reference XRD peaks of Fe_3O_4 in vertical bars**.**

For iron oxide NPs, whatever the kinds of ligands, the XRD peaks of a cubic iron oxide spinel phase are identified. The calculated parameters are intermediate with those of stoechiometric magnetite and maghemite and show that the NPs are oxidized at their surface as already reported.[1]

III.3.2.2 IR spectroscopy

The IR spectrum of iron oxide NPs coated with oleic acid between 4000 cm^{-1} and 400 cm^{-1} is given in figure in Figure II-12. Three distinct zones are present, the bands between 3000 cm^{-1} and 2800 cm^{-1} are attributed to alkyl chains of ligands at the surface of NPs, those

between 1800 cm^{-1} and 900 cm^{-1} to the asymetric and symmetric COO^- bands of oleate and those between 800-400 cm^{-1} to Fe-O bands of iron oxide. With amine ligands, the COO^- bands are no more present and N-based bands appear (Figure II-13). The C–N vibration of amine ligands are around 1460 cm^{-1}. The N–H asymmetric stretch bands in the range 3100-3300 cm^{-1} are more or less weak and broadened depending on the presence or not of free ligands: the broadening is mainly due to the amine ligands bound to the nanocrystal surfaces. Their intensity is lower with oleylamine due to an extensive washing to try to remove undecomposed iron stearate. The IR bands around 2300 cm^{-1} are due to adsorbed carbonates.

Figure II-14b compares the Fe-O IR bands of all samples. The stoechimetric magnetite displays normally a single broad band located at 580-590 cm^{-1} (a shoulder at about 700 cm^{-1} may be observed attributed to surface oxidation at the nanoscale), while the maghemite phase displays several bands between 800-400 cm^{-1} which number and resolutions depend on the structural order of vacancies in maghemite.[1] The IR spectra of all iron oxide NPs exhibit a broad Fe-O band intermediate between those of magnetite and maghemite, which confirms an intermediate composition of these NPs between magnetite and maghemite.[1] The supplementary IR peak at 722 cm^{-1} observed for iron oxide NPs synthesized with oleylamine is due to the presence of iron stearate which has not been removed completely by washing.

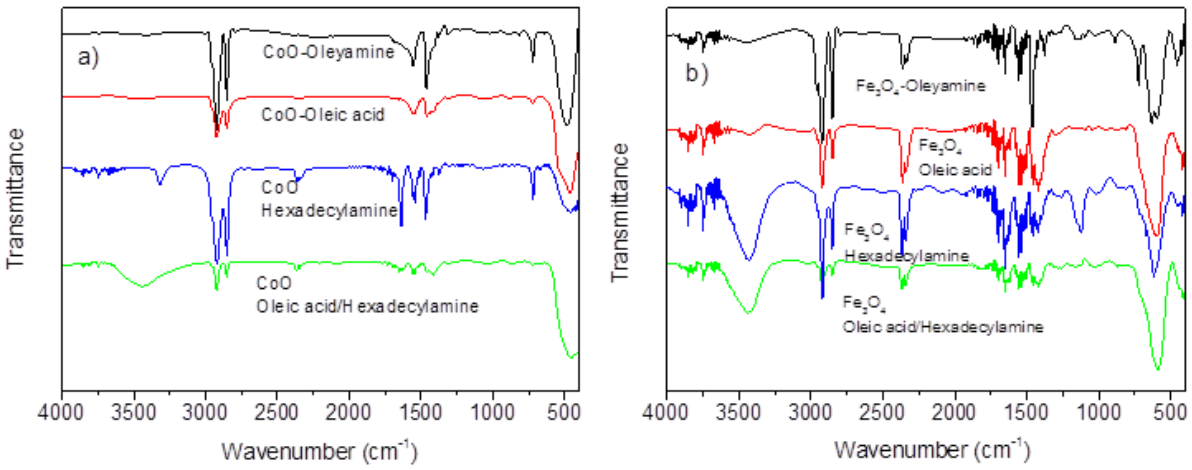

Figure II-12. Infrared spectra of CoO (a) and $Fe_{3-x}O_4$ (b) as function of the ligand oleic acid, hexadecylamine, oleylamine and mixture of oleic acid and hexadecylamine**.**

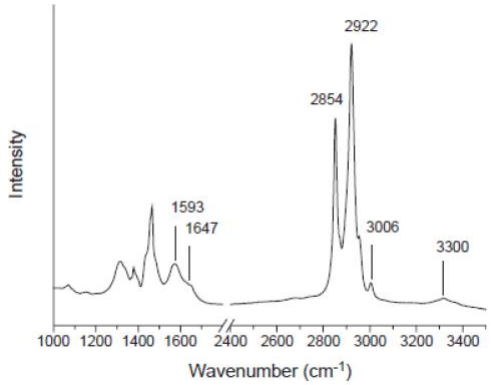

Figure II-13. IR spectra of oleylamine.[9]

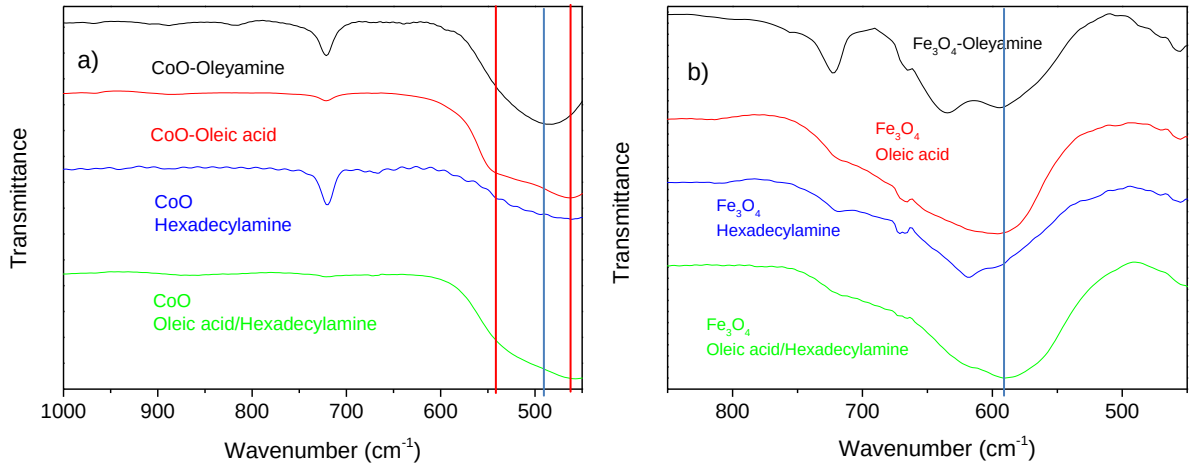

Figure II-14. Enlarged IR spectra of (a) CoO NPs in the range of 1000-450 cm^{-1} (Red vertical bars= cubic and wurtzite CoO, blue bar = cubic CoO) and of (b) $Fe_{3-x}O_4$ NPs in the range 850-450 cm^{-1} (blue vertical bar: Fe-O band of magnetite).

Similarly the IR bands of ligands are identified in IR spectra of CoO NPs (Figure II-14a). They show that there is lower amount of free ligands as the IR bands are better defined. The indexation of Co-O bands is very difficult as large discrepancies are noted in the bibliography certainly due to the fact that CoO and Co_3O_4 are normally non-stoichiometric with excess of oxygen. The IR spectrum of Co_3O_4 would display two distinctive bands originating from the stretching vibrations of the metal-oxygen bond at 570±30 cm^{-1} (Co^{3+} in Oh) and 661±20 cm^{-1} (Co^{2+} in Td) and cubic CoO would display one IR band at 507±50 cm^{-1}.[26] The IR spectrum of cubic CoO is difficult to ascertain. For wurtzite CoO, no published IR bands are found.
The magnification of the Co-O bands in Figure II-14a shows that no IR band is observed at 660 cm^{-1} indicating that the samples do not contain the Co_3O_4 phase. The CoO NPs synthesized with amine ligands are cubic and display one broad band at around 490 cm^{-1} which is very close to the expected band for cubic CoO at 507 cm^{-1}. Such a small difference may be attributed to a non stoechiometric phase. CoO NPs synthesized with oleic acid or a mixture of oleic acid and hexadecylamine are composed of cubic and wurtzite CoO and display two main bands at 465 and 545 cm^{-1}.

II.3.3 Conclusion

Iron and cobalt stearate complexes have been decomposed in presence of either amine or carboxylate ligands. The nature of ligands has been shown to have no influence on the morphology of iron oxide NPs which remains spherical but on their sizes. By contrast, the nature of ligands has a strong influence on the morphology of CoO NPs and even on their

cristalline phase. Oleic acid leads to tetrahedral shapes particles which consist in a mixture of cubic and wurtzite CoO phases. Amine ligands lead to nanoflowers (cluster of nanocrystals) which composition corresponds to cubic CoO. The formation of the wurtzite phase is quite original. The IR bands of the different CoO phases appear difficult to clearly indexed certainly due to the fact that they are non stoechiometric. The formation of nanoflowers is suggested to be induced by the synthesis process and magnetic interactions.

II.4 Comparison of iron and cobalt stearates

To try to understand why both cobalt and iron stearates behave differently when they are used to synthesize NPs by the thermal decomposition method, XPS analyses on both stearates have been performed as a function of the temperature as well as preliminary simulation of their decomposition in collaboration with the team of Carlo Massobrio and Mauro Boero at IPCMS.

II.4.1 XPS analyses of Fe and Co stearate as a function of temperature

A pellet of Fe stearate was annealed at 0.2 mbar O_2 from 180 up to 270 °C in the preparation chamber. The cobalt stearate presenting a higher decomposition temperature (TGA curves), the pellet of Co stearate was annealed at 0.2 mbar O_2 from 280 up to 370 °C in the preparation chamber. After each annealing step, C1s, O1s and Fe2p XPS spectra were acquired. A flood gun was used in this case in order to compensate for the electrostatic charging of the surface, and all XPS peaks were corrected based on literature values [27].

After annealing at 180 °C, a shrinkage of the Fe stearate pellet was observed, while after annealing at 270 °C the sample was dissociated and converted to carbon (its color changed from dark red to black). After annealing at 280 °C, the Co-stearate was melted and with the increase of the annealing temperature, a more intense shrinkage of the pellet was observed.

The relative surface atomic ratio (AR) of the C, Fe and O components have been deduced from C1s, O1s and Fe2p XPS spectra as a function of the annealing temperature (Tables II-2&3). The carbon AR decreases, while the oxygen and iron/ cobalt ARs increase upon first annealing at 180 °C and 280 °C for Fe and Co stearates respectively. When the annealing temperature increases, the oxygen uptake increases more smoothly as well as the Fe or Co AR.

Annealing temperature (±20°C)	Oxygen	Carbon	Iron
RT	11	87	2
180	17	78	5
210	18	76	6
240	19	75	6
270	20	73	7

Table II-2: C, O and Fe surface atomic ratios measured by XPS for Fe stearate**.**

Annealing temperature (±20°C)	Oxygen	Carbon	Cobalt
RT	11	86	3
280	17	72	11
310	15	76	9
340	17	70	13
370	18	70	12

Table Ⅱ-3: C, O and Fe surface atomic ratios measured by XPS for the Co stearate

The main C1s peak was set at 285 eV (aliphatic carbon chain) and the small peak at ca. 288.6 eV corresponds to the carboxyl atoms of the stearate chains. The C1s peak of the as-received Fe stearate is identical to the one of the Co stearate. The relative ratio of the two C1s peak components in the as-received sample is 0.053, in good agreement with the molecule's stoichiometry (Formula: iron stearate $C_{36}H_{70}FeO_4$, the ratio is in this case also 0.059). The relative ratio of the two C1s peak components in the as-received cobalt stearate sample is 0.061, in good agreement with the molecule's stoichiometry (Formula:$C_{36}H_{70}CoO_4$, two carbons connected with carboxyl groups, therefore the ratio is 2:34=0.059). During the annealing treatment of iron stearate, a low binding energy (BE) peaks at around 282 eV appears in the C1s spectrum (Figure II-15, C1s spectra) indicating a partial decomposition of the stearate chains. At 270 ℃, the stearate chains are totally decomposed, as the C1s XPS spectrum is completely different from that of the iron stearate. It confirms that iron stearate begins to decompose from 200 ℃.

The O1s peaks of cobalt stearate and iron stearate are not located at the same position: around 533.5 eV for Fe stearate and 532 eV for cobalt stearate showing that the oxygen environement is different between both stearates. A peak located at 532.3 eV could be associated to $-COO^-$ bonds when a peak at 532.9 eV is characteristic of C-O bonds. The O1s peak in Figure II-15&16 also changes with the annealing treatment with the appearance of a low binding energy peak at around 532 eV for iron stearate and 531 eV for cobalt stearate which intensity increases with the increase in temperature. One may notice that cobalt stearate needs to be annealed at higher temperature than iron stearate (340 ℃ by comparison with 240 ℃) to observe the intensity of this new peak to reach the same intensity than that with iron stearate. It confirms that the decomposition of cobalt stearate occurs at higher temperature. The O1s peak attributed to the lattice oxygen (O^{2-}) in the metal oxide is generally located around 530±0.5 eV and one may advance that after annealing at 340 ℃, Co-O bonds are observed. The new observed O1s peak with iron stearate at 240 ℃ could be attributed to hydroxide suggesting a partial decomplexation of iron stearate at this temperature associated to the modification of the C1s peak.

In the as-prepared sample, the Fe2p XPS spectrum is characteristic of the presence of Fe^{2+}. Indeed, when Fe^{2+} ions are present at the surface, the satellite of the 2p3/2 peak around 719 eV characteristic of Fe^{3+} ions becomes less resolved due to the main 2p3/2 and 2p1/2 peaks broadening and to rising intensity at about 716 eV of the satellite for the Fe^{2+} ions. The presence of Fe^{2+} at the probed surface is shown by the quiet absence of the satellite around 719 eV between the main Fe 2p peaks but the comparison with the FeO spectrum shows that Fe^{3+} ions are also present as the Fe2p bands are slightly shifted. The Fe2p XPS spectrum evolves upon annealing, with the satellite peak that is characteristic of Fe^{3+} appearing more resolved in the spectrum. Therefore, the iron oxydation degree is shown to be modified during annealing.

In the as-prepared sample, the Co 2p peak is characteristic of cobalt in the Co^{2+} state. The shape of this peak changes already upon first annealing at 280 °C; its width increases and the intensity of the satellite peak decreases. Such changes in the shape of the Co 2p spectra are compatible with the conversion of part of Co^{2+} to Co^{3+}.[28] On the whole, annealing in oxygen induces partial oxidation of Co^{2+} (attached on the stearate chains) to Co^{3+} (probably oxide, taking also into account the changes observed in the O1s peak) that segregates on the sample's surface as is evident from the increase of the ARs of both oxygen and cobalt. Since the shape of the C 1s peak does not change upon treatments and the relative ratio of its two components remains the same, one can assume that the stearate chains do not dissociate.

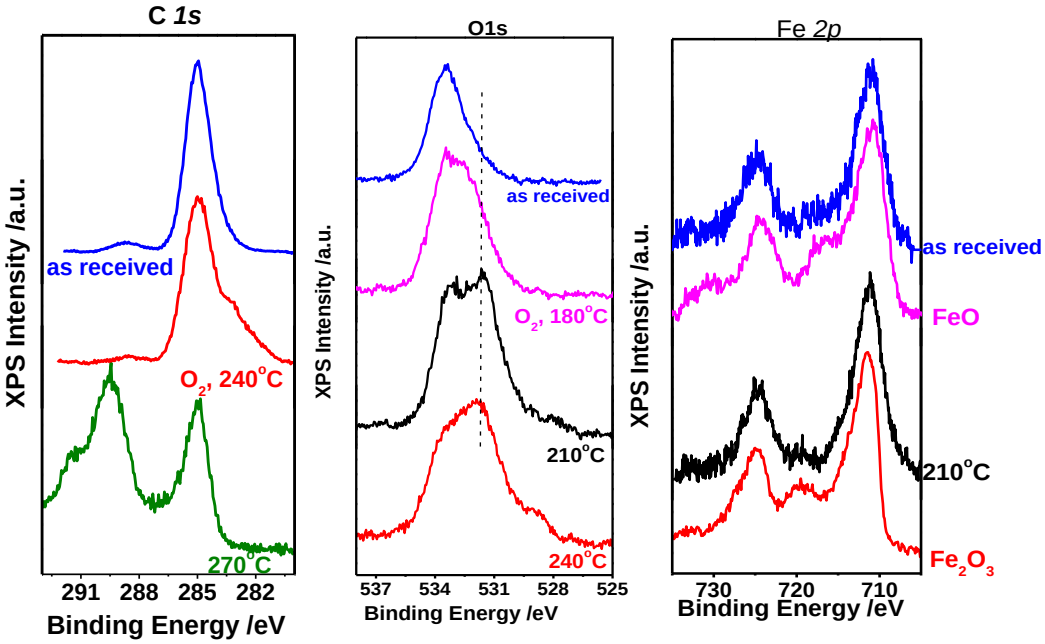

Figure II-15. C1s, O1s and Fe2p XPS spectra of the as-received Fe-stearate and after annealing.

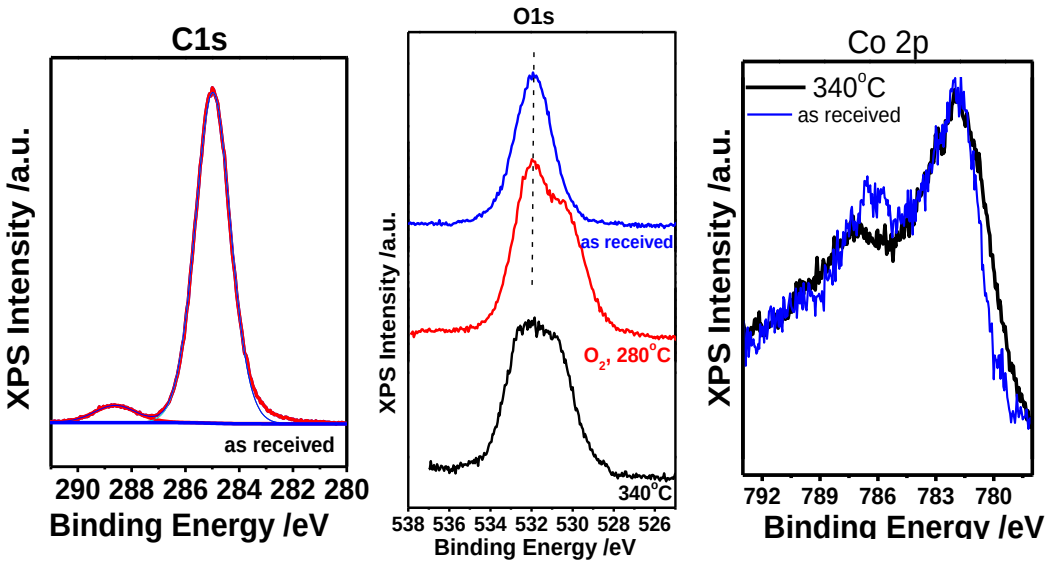

Figure II-16. C 1s, O 1s and Co 2p XPS spectra of the as-received Co-stearate and after annealing

To conclude, the evolution of C1s, O1s and M 2p XPS spectra with the annealing temperature is not easy to interprete. Nevertheless, they confirm that both stearates decompose at different temperature. Furthermore the oxygen environnement is found to be different in iron and cobalt stearate.

II.4.2 Preliminary simulations on the stability of iron and cobalt stearates

The stability of Co and Fe stearates either in the presence or in the absence of water has been investigated via first principles molecular dynamics simulations [29] within the density functional theory framework.[30] Since the central metal atom is four-fold coordinated with oxygen atoms of the -COO moieties terminating the hydrocarbon chains, and being this coordination planar, two additional coordination sites are in principle available to complete the hydration shell of Co [31] and Fe,[32] one above this coordination plane, and one below.

Starting from relaxed geometries at 0 K, shown in Figure II-17, one or two water molecules are inserted in the empty coordination sites along the axis orthogonal to the –COO M OOC– plane passing across M (M=Fe, Co). As a consequence, the metal center can become either five- or six-fold coordinated.

Starting from the case of Fe stearates, in dry conditions non-planar –COO Fe OOC– coordinations may arise as a result of thermal fluctuations at finite (room) temperature. The situation at 300 K is sketched in Figure II.18. In the case of partial (five-fold) or full (six-fold) hydration, a damped dynamics, performed to quench the structure and allow the system to find a stable local minimum, has shown that the water molecules can stabilize around the Fe center as shown in Figure II.19. This situation, however, can change significantly at 300 K.

Namely, (see Figure II.19-22) when one H_2O molecule is present, it can form strong hydrogen bonds with the nearby carboxylate group of the stearate chain surrounding the iron cation. This strong interaction can even give rise to an exchange of protons between the water molecules and the carboxylate group as in a Zundel-like[33] complex. When two water molecules are present, at 300K a destabilization of the hydration shell of Fe arises. The net effect is the evaporation of one of the two water molecules, which leaves the coordination shell of Fe. At the same time large conformational changes of the hydrocarbon chains occur, summarized by the snapshot in the fourth panel of Figure II.22.

To inspect the desorption process of the stearate chain, since non-negligible activation barriers might exists and since these are beyond the reach of standard molecular dynamics simulations, we resorted on the free energy sampling technique known as Blue Moon ensemble.[34] The reaction coordinate inspected within this approach was the distance between the metal atom and the carboxylate group of one of the two stearate chain. Results in dry and wet conditions are summarized in Figure II.23 and II.24. From these simulations on iron stearate, stearate chains desorb from iron cations, releasing iron atoms and thus the nucleation of iron oxide NPs may occur. However, the desorption seems to be easier in dry conditions, where a free energy barrier of about 15.02 kcal/mol has to be overcome, than in wet conditions, where this same activation barrier and increase to larger values, thus making energetically more demanding the desorption of stearate chains.

The same simulations performed on cobalt stearate (Figure II.25-27) show that this complex evolves rather differently, cobalt atoms react with oxygen and hydrogen of stearate chains and induce a decomposition of stearate chains. Byproducts are thus generated such as CO_2 and **O=C=C=CH$_2$** and cobalt atoms interact with oxygen and hydrogen. Cobalt atoms so generated are not free to react together making the nucleation difficult. Such a behavior may explain why amine ligands allow increasing the yield in NPs: amine ligands react with the carboxylate groups of stearate chains and thus limitate the reaction of cobalt atoms of these chains making them more free to form NPs.

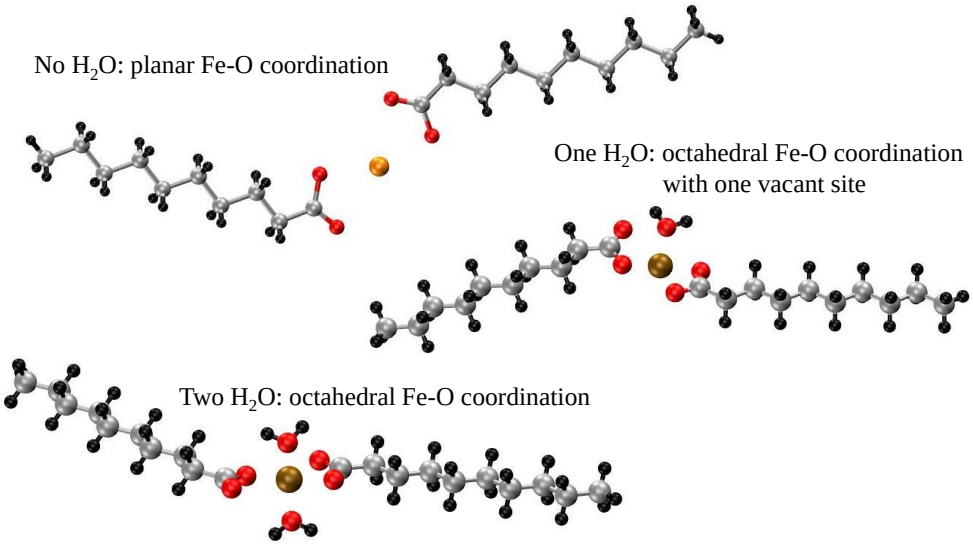

Figure II-17. Equilibrium geometries of Fe stearates at 0 K in the absence and in presence of water.

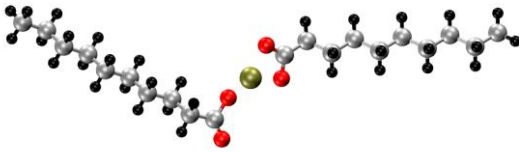

Figure II-18. Equilibrium geometries of Fe stearates at 300 K (dry) in the absence of water.

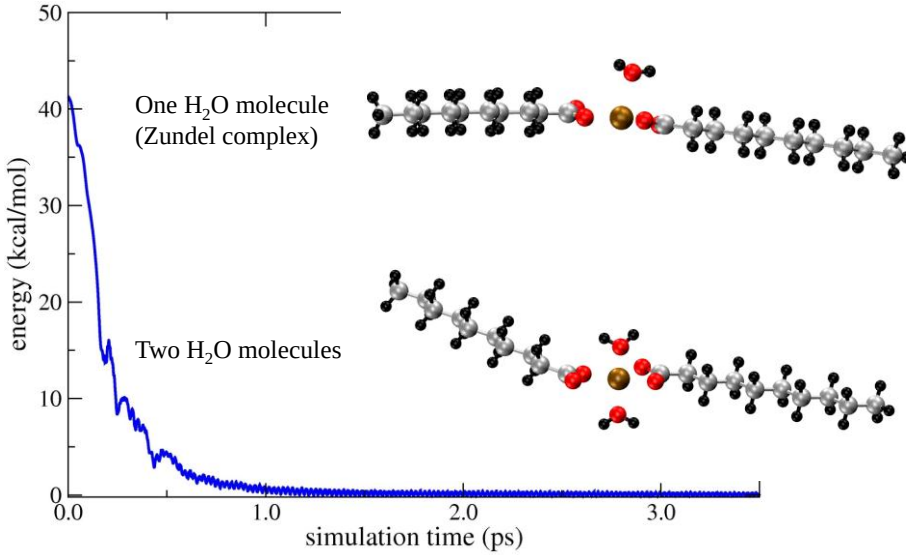

Figure II-19. Fe-based stearates: quenched (stable) configurations in wet conditions

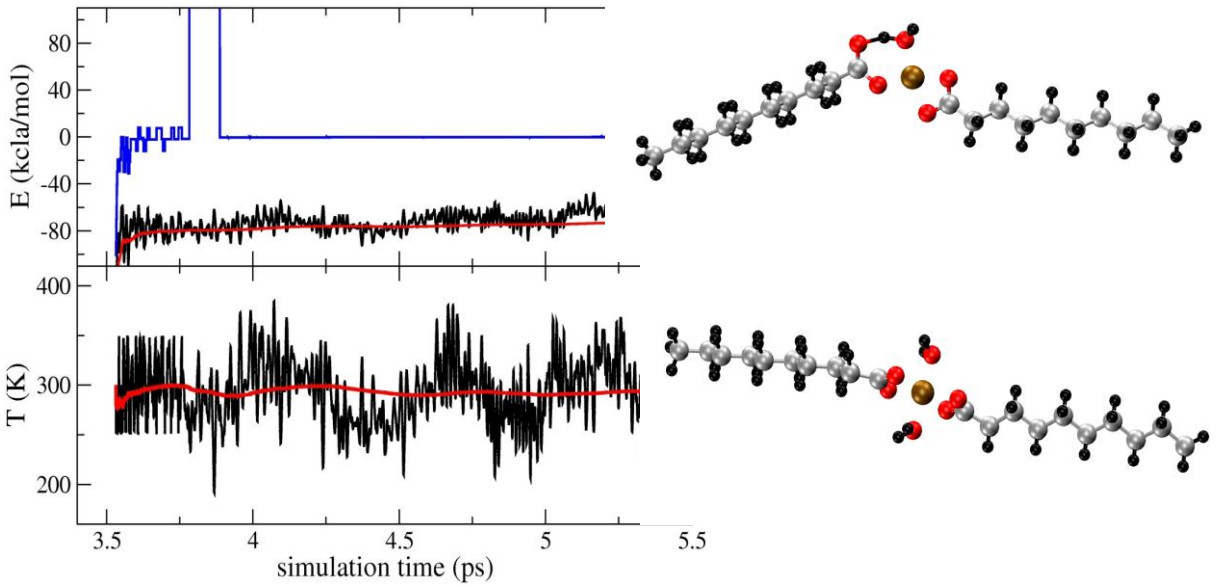

Figure II-20. Thermal evolution of Fe stearate at 300 K in wet conditions.

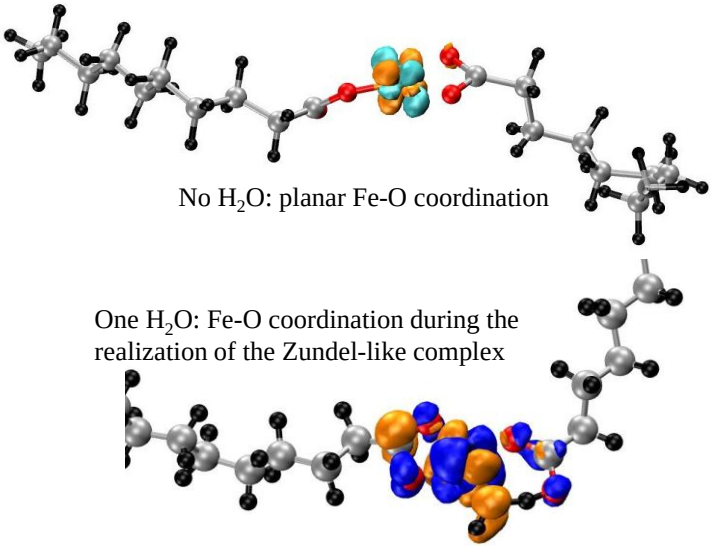

Figure II-21. Fe-based stearates: Spin density distribution at 10^{-3} e/Å^3

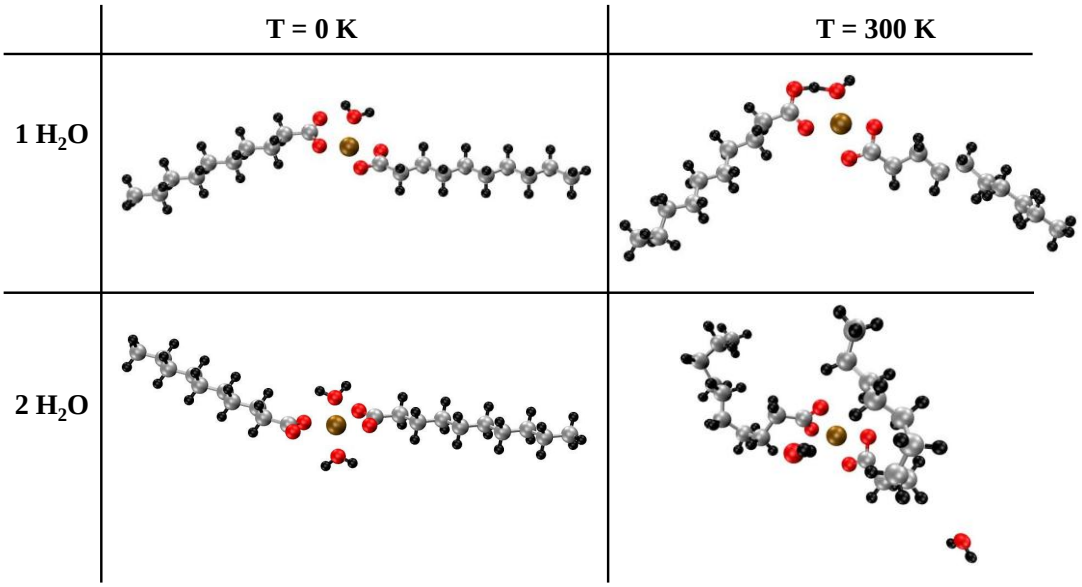

Figure II-22: Summary of the equilibrium geometries at 0 and 300K in presence of one to two water molecules.

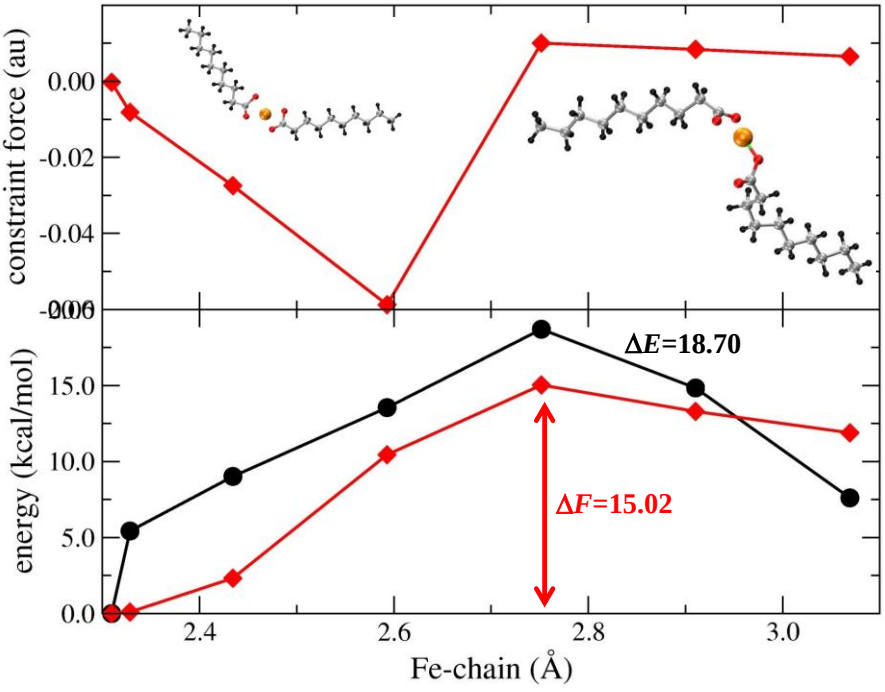

Figure II-23. Equilibrium geometries of Fe-based stearates at 300 K in wet conditions. Constraint force (upper panel) and free and total energies (lower panel) for the desorption of the chain in Fe-based stearates at 300 K in dry conditions. The free energy profile is shown by the red line and the total energy one by the black line. The free energy barrier to the desorption, indicated in the lower panel, amounts to 15.02 kcal/mol.

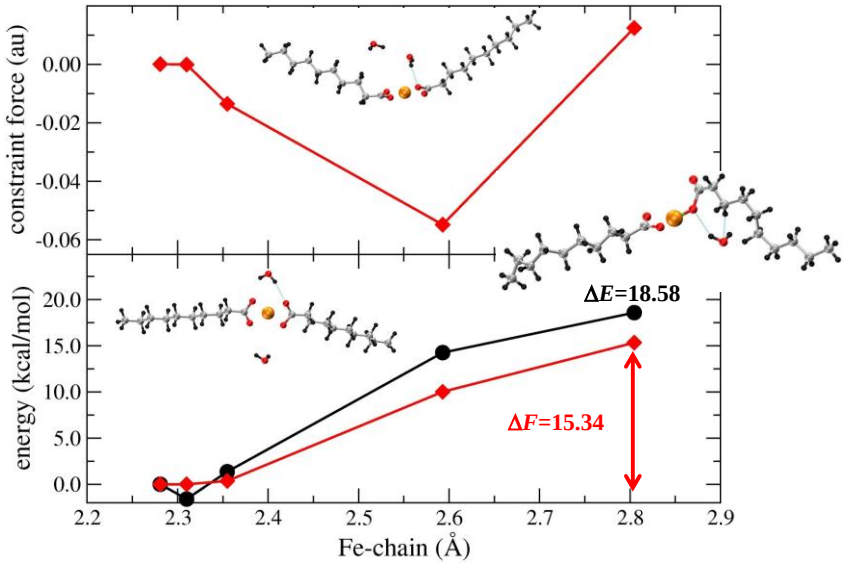

Figure II.24. Fe-based stearates at 300 K in wet conditions. Constraint force (upper panel) and free and total energies (lower panel) for the desorption of the Fe-based stearates at 300 K in wet conditions. The free energy profile is shown by the red line and the total energy one by the black line. The free energy barrier to the desorption, indicated in the lower panel, is already larger than 15.34 kcal/mol (calculations still in progress) before the completion of the desorption process.

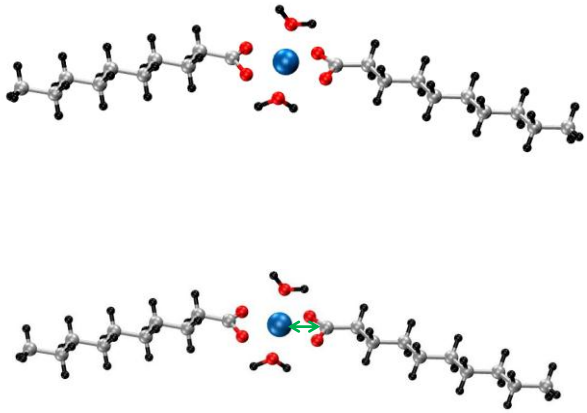

Figure II.25. Co-based stearates at 300 K in wet conditions. The green arrow indicates the reaction coordinate used in Blue Moon ensemble simulations to desorb the stearate chain.

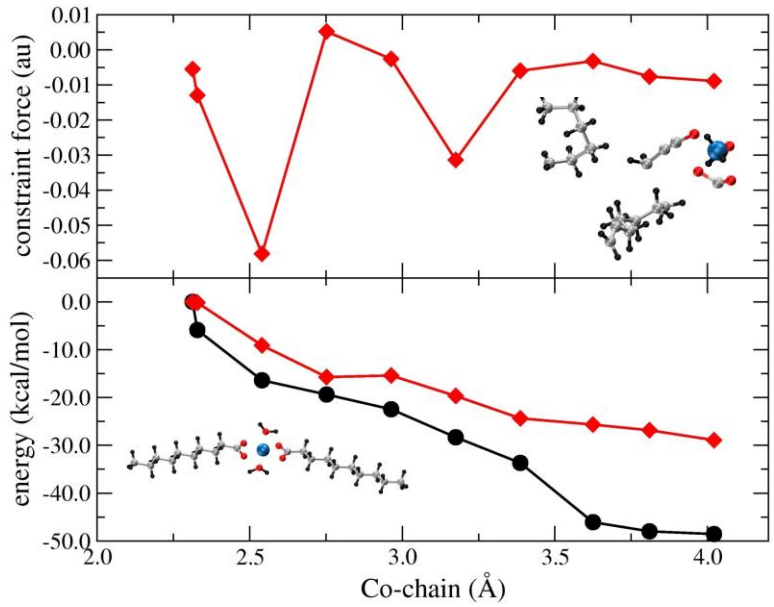

Figure II.26. Co-based stearates at 300 K in wet conditions.

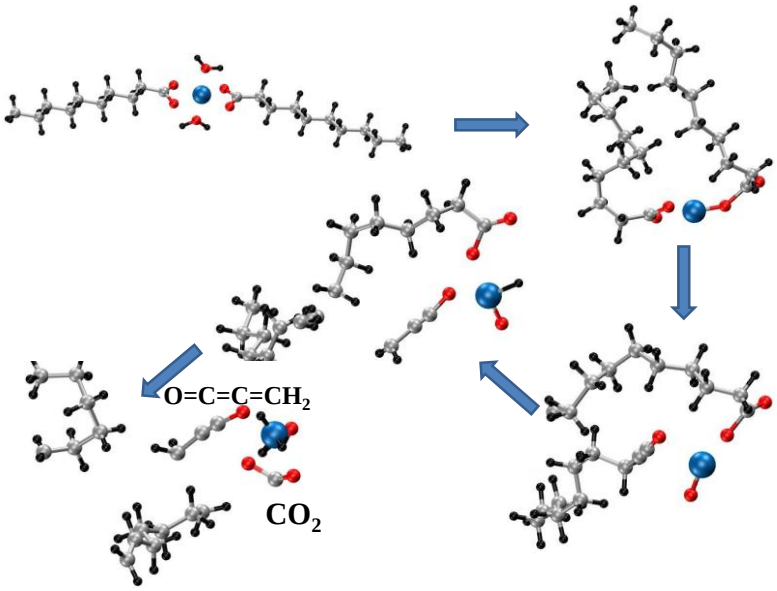

Figure II.27. Co-based stearates at 300 K in wet conditions

II.5 Conclusion

Iron stearate and cobalt stearate have been shown to decompose thermally differently despite their close structure. The thermal decomposition of iron stearate in presence of ligands in a high boiling solvant leads to spherical iron oxide NPs whetever the nature of ligands (amine based or carboxylate based ligands), only the size is modified. By contrast, the thermal decomposition of cobalt stearate in presence of oleic acid occurs with a low yield in NPs and leads to tetrahedral shaped NPs. Amine ligands allow improving the yield in NPs and lead to

nanoflowers (cluster of nanocrystals) shaped particles. Furthermore CoO particles synthesized with amine ligands are constituted of cubic CoO when those synthesized with or in presence of oleic acid are composed of cubic and wurtzite CoO phases.

The decomposition of cobalt stearate occurs at higher temperature than that of iron stearate as shown by TGA and XPS experiments. Preliminary simulations suggest that stearate chains may desorb from iron atoms and liberate them to form nuclei. By contrast, cobalt atoms "react" with stearate chains, decompose them, perhaps in a catalytic way, and interact with oxygen and hydrogen atoms. These atoms are thus not "free" to form nuclei. Further simulations will be necessary to conclude.

References:

1. Baaziz, W. *et al.* Magnetic Iron Oxide Nanoparticles: Reproducible Tuning of the Size and Nanosized-Dependent Composition, Defects, and Spin Canting. *J. Phys. Chem. C* **118,** 3795–3810 (2014).
2. Baaziz, W. *et al.* High-Density Monodispersed Cobalt Nanoparticles Filled into Multiwalled Carbon Nanotubes. *Chem. Mater.* **24,** 1549–1551 (2012).
3. Hyeon, T., Lee, S. S., Park, J., Chung, Y., Na, H. Bin. Synthesis of Highly Crystalline and Monodisperse Maghemite Nanocrystallites without a Size-Selection Process. *J. Am. Chem. Soc.* **123,** 12798–12801 (2001).
4. Demortière, A *et al.* Size-dependent properties of magnetic iron oxide nanocrystals. *Nanoscale* **3,** 225–32 (2011).
5. Pichon, B. P. Microstructural and Magnetic Investigations of Microstructural and Magnetic Investigations of Wustite-Spinel Core-Shell Cubic-Shaped Nanoparticles. *Chem. Mater.* **23,** 2886–2900 (2011).
6. Bronstein, L. M. *et al.* Influence of Iron Oleate Complex Structure on Iron Oxide Nanoparticle Formation. Chem. Mater.**19**, 3624–3632 (2007).
7. Kwon, S. G. *et al.* Kinetics of monodisperse iron oxide nanocrystal formation by "heating-up" process. *J. Am. Chem. Soc.* **129,** 12571–84 (2007).
8. Dinegar, H. Thoery, production and mechanism of monodispersed hydrosol. *J. Am. Chem. Soc.* **72,** 4847–4854 (1950).
9. Mourdikoudis, S. and Liz-marza, L. M. Oleylamine in Nanoparticle Synthesis. *Chem. Mater.**25*, 1465–1476 (2013).
10. Yin, J. S. and Wang, Z. L. In Situ Structural Evolution of Self-Assembled Oxide Nanocrystals. *J. Phys. Chem. B* **5647,** 8979–8983 (1997).
11. Yin, J. S. and Wang, Z. L. Ordered Self-Assembling of Tetrahedral Oxide Nanocrystals. Phys. Rev. Lett.***79***, 2570 – 2573 (2000).
12. Ghosh, M., Sampathkumaran, E. V & Rao, C. N. R. Synthesis and Magnetic Properties of CoO Nanoparticles.*Chem. Mater.**17*, 2348–2352 (2005).
13. Seo, W. S. *et al.* Phase- and size-controlled synthesis of hexagonal and cubic CoO nanocrystals. *J. Am. Chem. Soc.* **127,** 6188–9 (2005).
14. Zhang, Y., Zhong, X., Zhu, J. & Song, X. Alcoholysis route to monodisperse CoO nanotetrapods with tunable size. *Nanotechnology* **18,** 195605 (2007).

15. Chen, Z., Xu, A., Zhang, Y. & Gu, N. Preparation of NiO and CoO nanoparticles using M2+-oleate (M=Ni, Co) as precursor. *Curr. Appl. Phys.* **10,** 967–970 (2010).
16. Nanorods, P. C. *et al.* Synthesis, Characterization, and Self-Assembly of Pencil-Shaped CoO Nanorods. *J. Am. Chem. Soc.* **128,** 9753–9760 (2006).
17. Zhang, Y., Zhu, J., Song, X. & Zhong, X. Controlling the Synthesis of CoO Nanocrystals with Various Morphologies. *J. Phys. Chem. C **112**,* 5322–5327 (2008).
18. Ma, Y. *et al.* Seed-mediated synthesis of truncated gold decahedrons with a AuCl/oleylamine complex as precursor. *Adv. Mater.* **22,** 1930–1934 (2010).
19. Lagrow, A. P., Ingham, B., Toney, M. F. & Tilley, R. D. Effect of Surfactant Concentration and Aggregation on the Growth Kinetics of Nickel Nanoparticles. *J. Phys. Chem. C **113**,* 16709-16718 (2013).
20. Lu, Z. & Yin, Y. Colloidal nanoparticle clusters: functional materials by design. *Chem. Soc. Rev.* **41,** 6874–87 (2012).
21. Penn, R. L. Imperfect Oriented Attachment: Dislocation Generation in Defect-Free Nanocrystals. *Science* . **281,** 969–971 (1998).
22. Narayanaswamy, A., Xu, H., Pradhan, N. & Peng, X. Crystalline Nanoflowers with Different Chemical Compositions and Physical Properties Grown by Limited Ligand Protection. *Angew. Chemie* **118,** 5487–5490 (2006).
23. Narayanaswamy, A., Xu, H., Pradhan, N. & Kim, M. Formation of Nearly Monodisperse In2O3 Nanodots and Oriented-Attached Nanoflowers : Hydrolysis and Alcoholysis vs Pyrolysis. *J. Am. Chem. Soc.***118,** 10310–10319 (2006).
24. Yin, Y. & Alivisatos, a P. Colloidal nanocrystal synthesis and the organic-inorganic interface. *Nature* **437,** 664–70 (2005).
25. Risbud, A. S., Snedeker, L. P., Elcombe, M. M., Cheetham, A. K. & Seshadri, R. Wurtzite CoO. *Chem. Mater.* **17**,834–838 (2005).
26. Tang, C.-W., Wang, C.-B. & Chien, S.-H. Characterization of cobalt oxides studied by FT-IR, Raman, TPR and TG-MS. *Thermochim. Acta* **473,** 68–73 (2008).
27. Kundu, S., Maidul Islam, a. K. M. & Mukherjee, M. Iron sulphide formation in the ferric stearate Langmuir–Blodgett films. *Appl. Surf. Sci.* **257,** 2000–2003 (2011).
28. Zafeiratos, S. *et al.* Methanol oxidation over model cobalt catalysts: Influence of the cobalt oxidation state on the reactivity. *J. Catal.* **269,** 309–317 (2010).
29. Car, R., Parrinello, M., Unified Approach for Molecular-Dynamics and Density-Functional Theory. *Phys. Rev. Lett.* **55**, 2471-2474 (1985).
30. Kohn, W., Sham, L. J. Self-Consistent Equations Including Exchange and Correlation Effects, *Phys. Rev.* **140**, A1133-A1138 (1965).
31. Powell, H. K. J., Nancollas, G. H. Coordination of oxygen by cobalt(II) complexes in aqueous solution. A calorimetric study. *J. Am. Chem. Soc.* **94**, 2664-2668 (1972).
32. Wagner, B., Reinen, D., Brunold, T. C., Guedel, H. U. Iron(VI) in tetrahedral oxo coordination: A single crystal EPR study. *Inorg. Chem.* **34**, 1934-1942 (1995).
33. D. Marx, M. E. Tuckerman, J. Hutter, M. Parrinello, The nature of the hydrated excess proton in water, *Nature* **397**, 601– 604 (1999)
34. Sprik, M., Ciccotti, G. Free Energy from Constrained Molecular Dynamics. *J. Chem. Phys.* **109**, 7737-7744 (1998).

Chapter III : Synthesis and assembly of core-shell $Fe_{3-\delta}O_4$@CoO Nanoparticles

Part A : Modulation of magnetic properties induced by the shell in core-shell $Fe_{3-\delta}O_4$@CoO nanoparticles

Abstract

Although single magnetic domain nanoparticles are very promising for many applications, their size reduction may result in low magnetic anisotropy and unblocked domain at room temperature, e.g. superparamagnetism. An alternative approach is core-shell nanoparticles featured by exchange bias coupling between F(i)M and AFM phases. Exchange bias is influenced by many parameters among which the shell structure has been seldomly reported. We report here on a systematic study which consists in the modulation of the shell structure and its influence on the exchange bias coupling. A serie of $Fe_{3-\delta}O_4$@CoO core-shell nanoparticles has been sunthesized by a seeded growth method based on the thermal decomposition technique. The shell structure is demonstrated to be strongly influenced by the kinetic of the CoO growth. It enables to tune the shell thickness, cristallinity and interface with the iron oxide core. The magnetic properties are shown to be strongly modulated by the shell structure. Strong exchange bias coupling is favored by the thickest CoO shell and the largest $Fe_{3-\delta}O_4$/CoO interface. Very high values of coercive field (19 000 Oe) and M_R/M_S ratio (0.86) were obtained. The most stricking results consist in the enhancement of the coercive field with low exchange field when the CoO thickness decreases : it is ascribed to the diffusion of Co species in the surface layer of iron oxide which generates cobalt ferrite and induces hard/soft coupling.

A-I. Introduction

Superparamagnetic iron nanoparticles (NPs) have driven a tremendous interest during recent years because of their potential applications in a large range of advanced research fields, such as data storage, diagnostic by MRI, catalyst recycling, ferrofluid, therapy by hyperthermia.[1,2,3,4] However, the magnetic properties of NPs are usually lower than those of their bulk form due to surface and size effects. Indeed, the saturation magnetization of magnetite Fe_3O_4 NPs is lower than that of spinel iron oxide bulk phases: magnetite or its fully oxydized form: maghemite (γ-Fe_2O_3). It is mainly attributed to the presence of oxidation defects, surface (due to the breaking of the crystalline symmetry at the surface of nanocrystals) and volume (due to oxidation or the synthesis process) spin canting as a function of NPs diameter.[5]

Thanks to advances in the chemical synthesis methods, it is now possible to synthesize core-shell NPs and to combine materials displaying different magnetic properties and thus to enhance and provide new enhanced magnetic properties. Indeed, the development of new synthesis methods led to the fine control of the structure of core-shell nanoparticles (core size, shell thickness and composition). Therefore, it opened new perspectives toward the definition of new interfaces for various combination of components and structures of NPs in order to accurately tailor the magnetic properties with regard to specific applications. Among promising magnetic core-shell NPs [6,7,8] are those displaying a ferrimagnetic (FIM) core and shelled by an antiferromagnetic (AFM) material. Such combinaison at the nanoscale of two different magnetic materials induces the coupling of the magnetic moments of reversible F(I)M phase at the interface with the ones of the irreversible AFM phase below the Néel temperature (T_N).[9-12] Interfacial spins of the AFM phase, which are featured by a very high anisotropy, remain frozen while reversing the magnetic field in the opposite direction. It results in the modification of the magnetocrystalline energy to which is ascribed a supplementary term which refers to the F(I)M/AFM interface and in an increase of the blocking temperature of the FIM core. So far, core-shell magnetic NPs represent a very promising way to increase the effective magnetic anisotropy energy of the raw NPs and to push back the superparamagnetic limit.[9] However if the exchange properties have been widely investigated, few studies are devoted on a systematic investigation of the effect of the AFM shell structure on magnetic properties.

Discovered initially by Meiklejohn,[3] exchange bias coupling in Co@CoO has been studied as function of the core-shell structure for many years. Several studies have reported on the variation of the FM/AFM interface by varying the thickness of the shell upon surface oxidation which represents a pretty easy way to modulate the core-shell structure but it is thus difficult to control isolated effects of the core and of the shell as both evolved simultaneously with oxidation.[4,13] Nevertheless, the anisotropy energy of the AFM having to be larger than the interfacial exchange coupling energy, a minimum critical shell thickness has been demonstrated experimentally and calculated by modelling approaches.[5] There is also a maximum limit of the shell thickness above which it has no more influence on the exchange bias (EB) coupling. A rather high exchange field has been also reported for similar core size and shell thickness which enables the largest interface.[14] Although the oxidation surface of Co nanoparticles enables to study exchange bias coupling with same overall volume, it involves

the concomitant variation of the core size and the shell thickness and so the interface.[9,15] In addition, oxidation induces some diffusion mechanism which favors disordering at the interface and strains which alter the exchange bias.

New NPs synthesis methods have paved the way towards the design of core-shell NPs with different compositions. Metal oxides have been widely investigated for many reasons among which the epitaxial growth relationship which warrant a high crystallinity of the interface between F(i)M and AFM phases. The role of the F(i)M/AFM interface in core-shell NPs has been widely studied as function of the core size,[10,11] strains and distorsion,[9,12] or spin disorder.[16,17] Inverted AFM/FiM core/shell FeO/Fe_3O_4 NPs have been also synthesized by exposure of FeO to air in a dry air atmosphere.[9-11,18] With increasing oxidation temperature, the coercivity and exchange field decreased, which is attributed to the reduction of AFM/FiM interface area and AFM (FeO) core anisotropy energy. Also, Salazar-Alvarez *et al.* reported similar results in the case of core-shell nanoparticles of MnO/Mn_3O_4 by increasing the core diameter of MnO.[19] The shell structure (thickness,[20] multiple crystal,[12] surface spin disorder and roughness) also plays a key role in mediating exchange bias but it has been seldomly reported.[21-23] Recently, the formation of interfacial layer produced by intermixing of FM and AFM phases has been also reported [24-26] and in some cases it has been demonstrated to have some strong effect on the overall magnetic properties of NPs.

Herein, we report on a fine modulation of the shell structure of $Fe_{3-\delta}O_4$@CoO nanoparticles and on its influence on the resulting exchange bias coupling properties. Core-shell NPs have been synthesized by a seeded growth method based on thermal decomposition in a similar way as we reported recently.[15] The CoO shell has been grown at the surface of $Fe_{3-\delta}O_4$ NPs by the thermal decomposition of different amount of cobalt stearate. Besides the modulation of the thickness of the CoO shell, the kinetics of the growth reaction has been observed to have a strong influence on the FiM/AFM interface and to result in either a continuous monocristalline or discontinuous polycristalline shell (Scheme III 1). The exchange bias coupling and the overall magnetic properties of these NPs were studied systematically as function of the structure of the shell and of the FiM/AFM interface and were found to strongly depend on the shell structuration leading either to NPs with enhanced exchange coupling properties or to NPs with enhanced coercive fields resulting from soft/hard magnetic interactions.

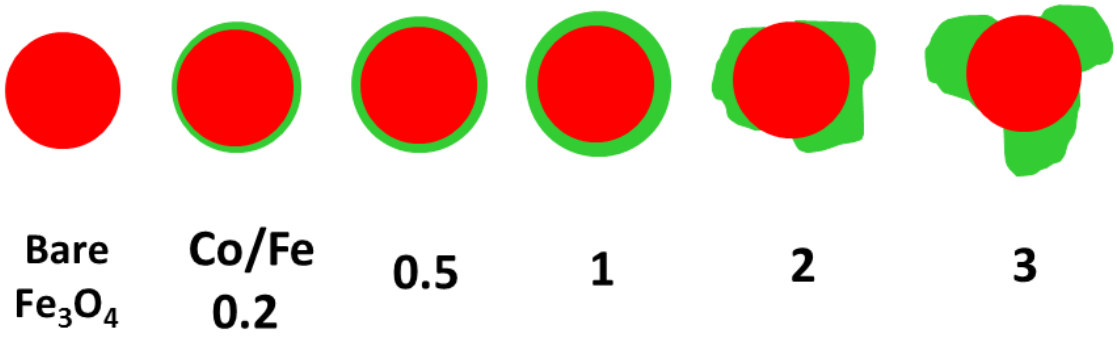

Scheme III-1. Schematic illustration of core-shell structures of $Fe_{3-\delta}O_4$@CoO nanoparticles as a function of the $Co(stea)_2/Fe(stea)_2$ molar ratio R. $Fe_{3-\delta}O_4$ in red and CoO in green.

A-II Experimental details

A-II.1 Synthesis of core-shell nanoparticles.

The typical procedure is as follows: First of all, 1.38 g of Fe(stearate)$_2$, 1.24 g of oleic acid and 20 ml of octylether were mixed, and then heated to 100 ^{o}C for 1 h to evaporate residual traces of water or ethanol. Subsequently, the temperature was increased up to 288 ^{o}C (boiling point of octylether) for 2 h under air with a heating rate of 5 ^{o}C/min. The resultant black solution was then cooled down to 80 ^{o}C, followed by extraction of 10 mL of solution from the flask for characterization of iron oxide nanoparticles. In a second step, 0.67 g of Co(stearate)$_2$, which roughly correspond to a Co(stearate)$_2$/Fe(stearate)$_2$ molar ratio of 1, were dissolved in 20 mL of octadecene and subsequently added to the remaining solution kept at 80 ℃. The reaction medium was heated again to reflux (which considering the octylether/octadecene mixture, is about 318 ^{o}C) for 3 h under argon with a heating rate of 1 ^{o}C/min. Finally, the black products were washed four times by centrifugation by adding ethanol and chloroform. The final suspension of nanoparticle was stored in THF. The obtained core-shell Fe_3O_4@CoO was denoted as NP-1. By keeping the amount of Fe(stearate)$_2$ constant, the other 4 samples of core-shell Fe_3O_4@CoO were obtained from different batches by varying the mass of Co(stearate)$_2$ to 0.134 g, 0.335 g, 1.34 g and 2.01 g which correspond to Co(stearate)$_2$/Fe(stearate)$_2$ molar ratios of 0.2, 0.5, 2 and 3, respectively. The obtained core-shell Fe_3O_4@CoO nanoparticles were denoted NP-0.2, NP-0.5, NP-2 and NP-3, respectively. Besides, an extra sample, denoted as NP-0.2-long, was synthesized by following precisely the experimental conditions determined for NP-0.2 in the exception of the reaction time which was increased to 8 h.

A-II.2 Structural characterization techniques.

Transmission electron microscopy (TEM) has been carried out by using a JEOL 2100F (voltage 200kV) micrsocope with a point resolution of 0.2 nm. Each sample was dispersed in ethanol by ultrasons during 5 minutes and a drop of the solution was then deposited on a copper grid (covered with a carbon membrane) by spin coating. The structure of nanoparticles was investigated in the high-resolution mode (HR-TEM) and by electron diffraction. The size distribution of nanoparticles was calculated from the size measurements of more than 300 nanoparticles by using image J software. STEM images were taken in high-angle annular dark field HAADF mode with a 0.12 nm probe. EELS spectra were recorded in the diffraction mode and EFTEM images were taken on the Fe and Co edges with a 20 eV window, which gives a 1.5 nm resolution imaging. EDX were performed with a JEOL Si(Li) detector.

X-ray diffraction (XRD) was carried out using a Bruker D8 Advance in the 28-75 ° (2Θ) range with a scan step of 0.03 °. The detector is a three degrees wide analysis detector ("Lynx Eye"). Profile matching refinements were performed through the Fullprof program [27] using the modified Thompson-Cox-Hasting (TCH) pseudo-Voigt profile function.[28] Such a procedure enabled us to calculate cell parameters and crystal sizes. High purity silicon powder (a = 0.543082 nm) was systematically used as an internal standard.

Thermal gravimetric analyses (TGA) were carried out on a TA Instrument (Q-5000 model). They were performed under an air flow up to 1000 °C with a heating rate of 5 °C/min.

FTIR spectroscopy was performed using a Digilab Excalibur 3000 spectrophotometer (CsI beamsplitter) in the wavenumber range 4000-400 cm^{-1} on samples diluted in KBr pellets.

A-II.3 Magnetic characterization.

Magnetization measurements were carried out by using a Superconducting Quantum Interference Device (SQUID) magnetometer (Quantum Design MPMS-XL5). Zero-field cooled (ZFC) and field cooled (FC) magnetization curves as function of the temperature (M(T) curves) were recorded as follows: the sample was introduced in the SQUID at room temperature and cooled down to 5 K with no applied field after applying a careful degaussing procedure. A magnetic field of 7.5 mT was applied, and the ZFC magnetization curve was recorded upon heating from 5 to 400 K. The sample was then cooled down to 5 K under the same applied field, and the FC magnetization curve was recorded upon heating from 5 to 400 K. AC measurements were performed to measure the susceptibility under an alternating magnetic field of 3.5 Oe at a frequency of 1 Hz from 5 to 400 K after having cooled down the sample in zero Field.

Magnetization curves as a function of an applied magnetic field (M(H) curve) have been measured at 5 and 400 K. The sample was introduced in the SQUID at high temperature and cooled down to 5 K with no applied field (ZFC curve) after applying a subsequent degaussing procedure. The magnetization was then measured at constant temperature by sweeping the magnetic field from +7 T to -7 T, and then from -7 T to +7 T. To evidence exchange bias effect, FC M(H) curves have been further recorded after heating up at 400 K and cooling down to 5 K under a magnetic field of 7 T. The FC hysteresis loop was then measured by applying the same field sweep as for the ZFC curve.

A-III RESULTS

A-III.1 Synthesis and characterization of core-shell NPs

$Fe_{3-\delta}O_4$@CoO NPs have been synthesized by the successive thermal decomposition of $Fe(stea)_2$ and $Co(Stea)_2$ complexes that we have described earlier.[29] Briefly, $Fe_{3-\delta}O_4$ NPs were at first synthesized and then shelled by CoO following a seeded mediated growth process. The shell thickness was modified by varying the amount of cobalt stearate which was defined by the molar ratio R = $Co(stea)_2/Fe(Stea)_2$ (Scheme III-1). Transmission electron micrographs of the as obtained $Fe_{3-\delta}O_4$@CoO NPs are shown in Figure III-2 and can be compared to pristine $Fe_{3-\delta}O_4$ NPs (Figure III-1).

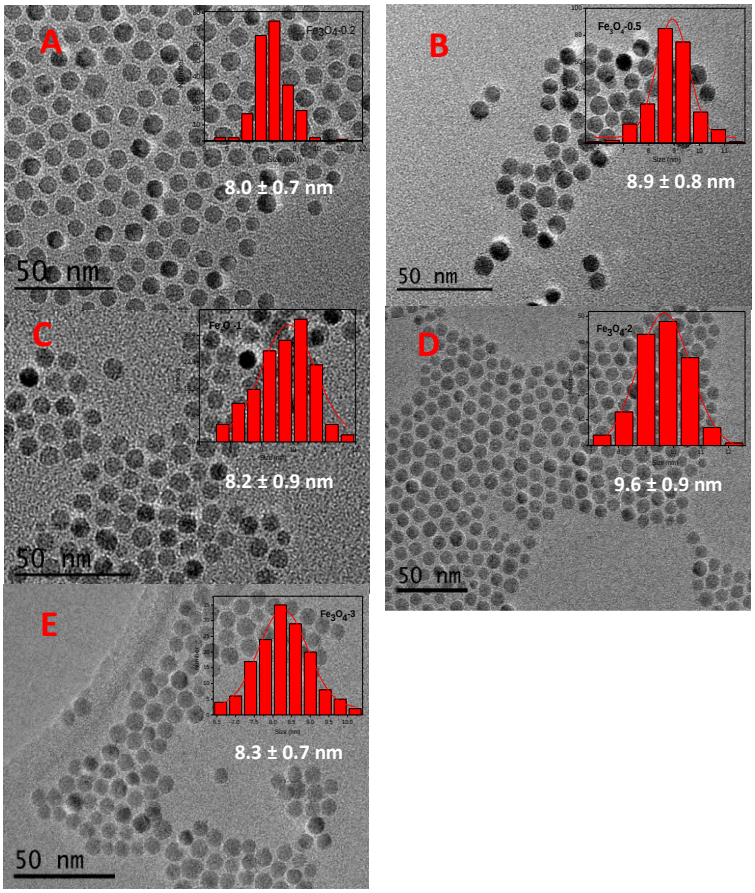

Figure III-1. TEM images of uncoated $Fe_{3-\delta}O_4$ of NP-0.2 (A), NP-0.5 (B), NP-1(C), NP-2(D) and NP-3(E) before CoO coating. Histograms (inset) correspond to size distributions.

Low amounts of cobalt stearate (R = 0.2, 0.5 and 1) led to $Fe_{3-\delta}O_4$@CoO NPs which are spherical in shape and uniform in size. Size distributions of NPs are rather narrow, with dispersion below 10 % of the standard deviation/size ratio (Table III-1). Since the pristine $Fe_{3-\delta}O_4$ NPs were synthesized from five different batches (Figure III-1), causing a slight variation of the core size, the shell thickness was determined by measuring the increase of nanoparticle size after CoO growth for each of sample (Table III-1). Clearly, as the Co amount increases, the shell thickness increases from 0.3 ± 0.05 to 1.0 ± 0.05 nm. EDX measurements performed on single NPs also confirmed Co/Fe atomic ratios which were very close to the ones of $Co(stea)_2/Fe(Stea)_2$ ratios used for the synthesis of each NPs (Table III-2). The high crystallinity of NPs was demonstrated by HRTEM (Figure III-2). Due to the close electron densities of Co and Fe elements, no obvious phase contrast could be observed between core and shell. Nevertheless, continuous atomic lattice fringes suggest an epitaxial growth of the CoO shell at the surface the iron oxide core. Distances measured between atomic layers all agree with an iron oxide spinel structure (Fe_3O_4, JCPDS 19-0629 and γ-Fe_2O_3, JCPDS file 39-1346) for each samples.

Table III-1. Sizes of pristine $Fe_{3-\delta}O_4$ NPs and core-shell $Fe_{3-\delta}O_4$@CoO NPs and size variations corresponding to the shell thickness.

	NP-0.2 (nm)	NP-0.5 (nm)	NP-1 (nm)	NP-2 (nm)	NP-3 (nm)
$Fe_{3-\delta}O_4$	8.0 ±0.7	8.9 ±0.8	8.2 ±0.9	9.6 ±0.9	8.3 ±0.7
$Fe_{3-\delta}O_4$@CoO	8.6 ±0.8	10.6 ±1.1	10.1 ±0.8	12.6 ±1.4	13.4 ±1.5
Shell thickness	0.3 ±0.05	0.85 ±0.15	1.0 ±0.05	1.5 ±0.3	2.5 ±0.7

Table III-2. Fe and Co content of core-shell NPs by Energy-dispersive X-ray analysis combined to TEM.

	NP-0.2	**NP-0.5**	**NP-1**	**NP-2**	**NP-3**
Fe Mass (%)	83.8	69.4	55	31.4	26
Co Mass (%)	16.2	30.6	45	68.6	74
Co:Fe ratio	0.19	0.43	0.82	2.1	2.8

Higher amounts in cobalt stearate led to larger average shell thicknesses of 1.5 nm and 2.5 nm for NP-2 and NP-3, respectively (Table III-1). However, the spherical shape is no more preserved and NPs become less uniform with the increase of the amount of cobalt stearate (Figure III-2G and I). HRTEM micrographs revealed further a core-shell structure arising from a considerable lattice mismatch between both phases (Figure III-2H and J). While the core is featured by a unique lattice spacing of 0.25 nm which corresponds to the (020) reflection of the iron oxide spinel structure, the shell displays interface boundaries which result from the presence of large CoO domains with different crystal orientations. Lattice planes were indexed to the (200) and (111) reflections of the cubic CoO structure (JCPDS file 70-2856) with an interplanar angle of 54.8 ^{o} which fits well the theoretical value. Moreover, it is worthy to note that some facets of the iron oxide core remain uncovered by CoO.

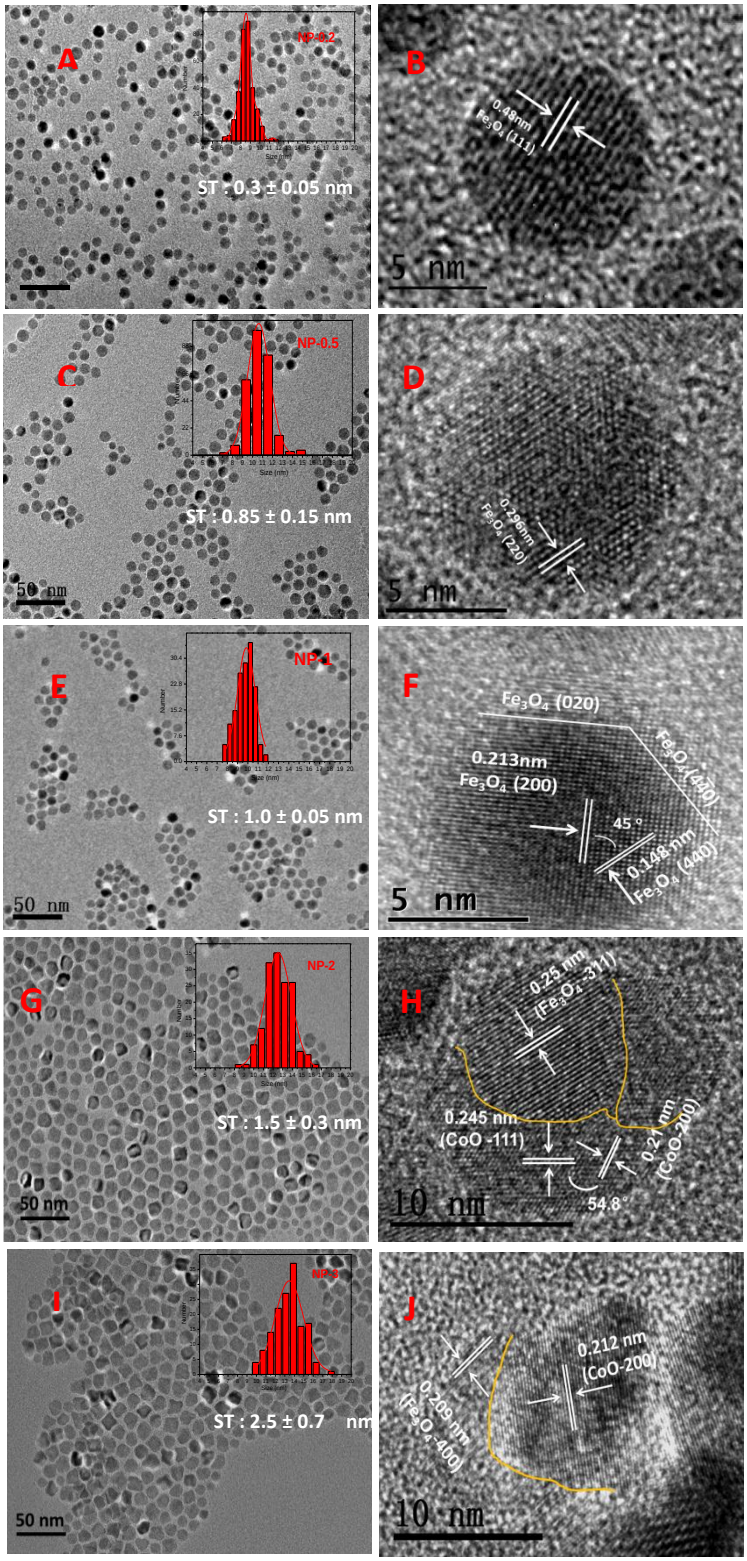

Figure III-2. TEM (A,C,E,G,I) and HRTEM (B, D,F,H, J) micrographs of NP-0.2 (A-B), NP-0.5 (C-D), NP-1 (E-F), NP-2 (G-H) and NP-3 (I-J). Insets show the histograms depicting the size distribution of each NP. Yellowish lines show interface boundaries in CoO shell.

The crystallographic structure of core-shell NPs has also been investigated by selected-area electron diffraction (SAED) which patterns display spotty polycrystalline diffraction rings which are indexed to $Fe_{3-\delta}O_4$ or CoO phases (Figure III-3). Although rings

related to $Fe_{3-\delta}O_4$ were observed for all samples, the intensity of the ones corresponding to CoO were very faint for NP-0.5 and NP-0.2 which is correlated to thinner shells.

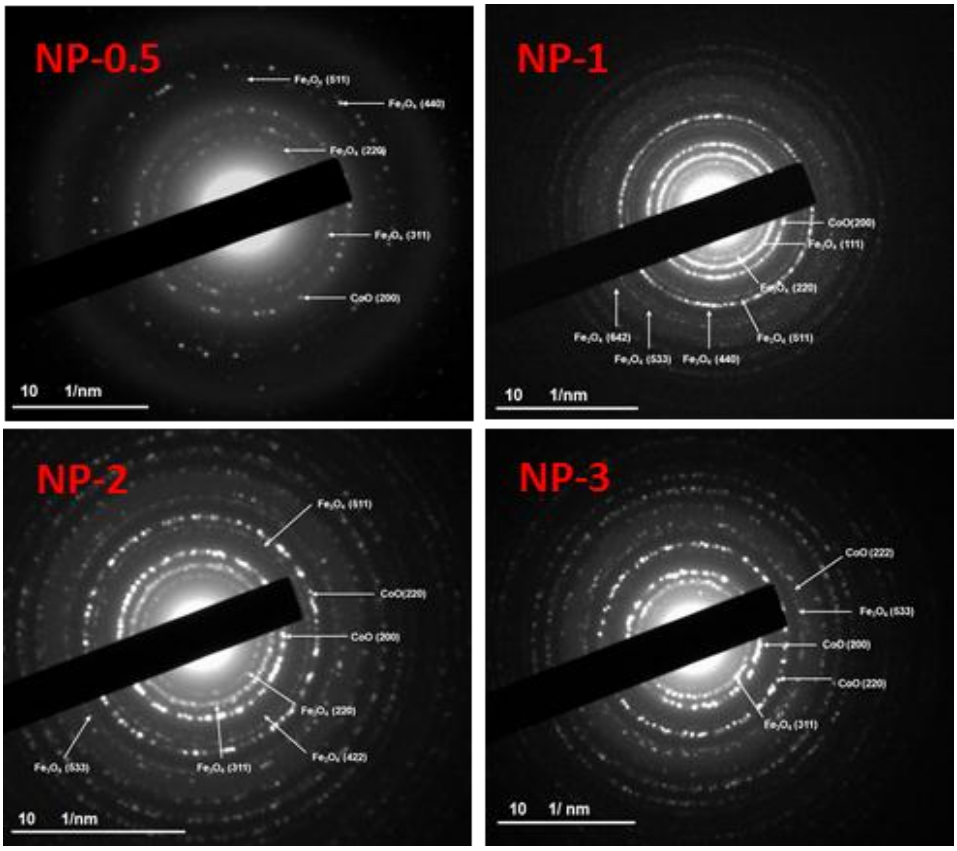

Figure III-3. SAED patterns of NP-0.5, NP-1, NP-2 and NP-3.

X-ray diffraction (XRD) patterns of each core-shell nanoparticles show peaks which can be indexed to the iron oxide spinel structure (Figure III-4). Moreover, in the exception of NP-0.2, all patterns display an extra peak at $2\theta = 36.5^o$ as well as enlarged peaks at 42.6^o and 62.5^o which can be indexed to the cubic CoO. As expected, these contributions increase with the amount of cobalt stearate and agree with the increase of shell thickness. The absence of CoO contributions in the case of NP-0.2 is easily explained by the very thin shell.

In order to have a better understanding on the structure of core-shell nanoparticles, Rietveld refinements of XRD patterns have been performed (Table III-3).[18,29] As we have already reported on the synthesis of pristine iron oxide nanoparticles of similar sizes,[30,31] the cell parameter and the crystal domain size were set to 8.372 Å and to the nanoparticle size measured by TEM, respectively. Indeed it is difficult to stabilize the stoechiometric magnetite Fe_3O_4 phase at the nanoscale as Fe^{2+} at the surface of NPs are very sensitive to oxidation. Therefore iron oxide NPs with such size display a lattice parameter intermediate between that of magnetite (8.396 Å, JCPDS file 19-0629) and that of maghemite (8.346 Å, JCPDS file 39-1346). Such NPs have been synthesized several times and displayed reproducibly this lattice parameter. However, good refinements were only obtained by adding an extra component corresponding to a cell parameter which is very close to the one of stoechiometric Fe_3O_4. It is indicative of the presence of substantial stoechiometric Fe_3O_4 cores due to the sysnthesis process itself involving two successive steps avoiding thus the exposition of iron oxide NPs to

air.[30,31] On the other hand, cell parameters of CoO shells were calculated to be slightly lower than the theoretical value (4.252 Å, JCPDS file 04-8987), which may be explained by the lattice mismatch (1.3 %) between spinel and wüstite phases. Moreover, a second component corresponding to a larger crystal domain size of CoO was necessary to refine more accurately XRD patterns of NP-2 and NP-3. Although this contribution is very weak, (it corresponds to less than 1 wt % of CoO nanocrystals with a mean size of 8 nm), higher amount of cobalt stearate is expected to favor homogeneous germination of CoO nanoparticles directly in solution.

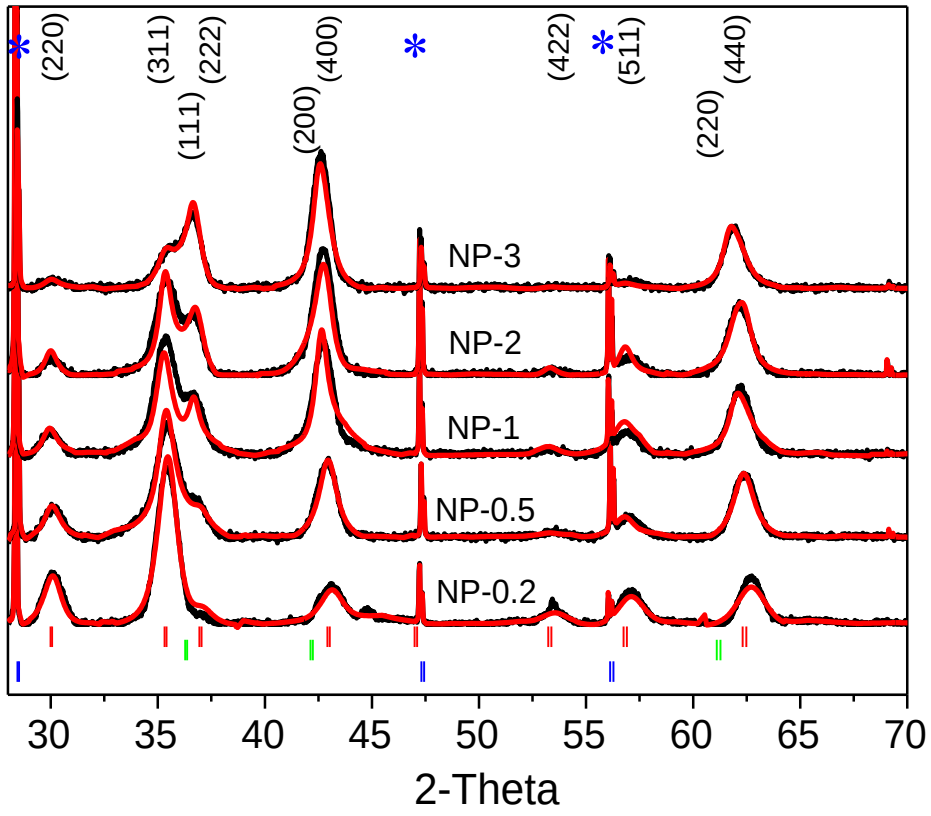

Figure III-4. XRD patterns (black) and their refinement (red) for NP-0.2, NP-0.5, NP-1, NP-2 and NP-3. The vertical bars represent theoretical peaks for Fe_3O_4 (red) and CoO (green). Silicon (blue) was used as a reference for refinement of patterns. Silicon (blue bars) was used as a reference for refinement of patterns and is indicated by stars.

Table III-3. Cell parameters of core-shell NPs calculated from XRD pattern refinement.

	spinel (1) Å	spinel (2) Å	CoO Å
NP-0.5	8.372	8.391	4.225
NP-1	8.372	8.395	4.224
NP-2	8.372	8.397	4.230
NP-3	8.372	8.393	4.244

Fourier-transform infrared (FT-IR) spectroscopy was performed to further investigate the composition of core-shell NPs (Figure III-5). The spectra display absorption bands attributed to C-H (2919 and 2850 cm^{-1}) and COO^- (1551 and 1400 cm^{-1}) vibration modes of alkylene

chains and carboxylic acid group of oleic. The very weak absorption band at 1703 cm^{-1} which is commonly attributed to C=O vibration of free carboxylic acid groups, confirms that the majority of oleic acid is adsorbed at the nanoparticle surface. The spectra of NP-3 also shows an extra peak at 722 cm^{-1} which was ascribed to the residual precursor complex, indicating that the decomposition, is not complete for the highest amount of cobalt stearate.

All spectra display absorption bands in the metal oxide region which correspond either to the Fe-O (single band at 580-590 cm^{-1} for magnetite and in the range 800-400 cm^{-1} for its oxidized form maghemite) or/and Co-O vibration modes (in the range 600-400 cm^{-1} depending on the cristalline structure of CoO). The area displaying the metal-oxygen bonds has been enlarged in Figure III-6. One broad single band at 597 cm^{-1} is observed for the iron oxide phase, especially for NP-O.2 and NP-0.5 and it confirms the presence of magnetite slightly oxidized [5]. The intensity of this band decreases as the amount of cobalt oxide increases. The indexation of Co-O bands is very difficult as large discrepancies are noted in the bibliography certainly due to the fact that CoO and Co_3O_4 are normally non-stoichiometric with excess of oxygen. The IR spectrum of Co_3O_4 would display two distinctive bands originating from stretching vibrations of the metal-oxygen bond at 570 ± 30 cm^{-1} (Co^{3+} in Oh) and 661 ± 20 cm^{-1} (Co^{2+} in Td) and cubic CoO would display one IR band at 507 ± 50 cm^{-1}.[32] The IR spectrum of cubic CoO is thus difficult to ascertain. For wurtzite CoO, no published IR bands are found. The IR spectrum of CoO NPs composed of both cubic and wurtzite CoO phases have been shown to display two main bands at 465 and 545 cm^{-1} when the cubic CoO phase diplays one broad band around 490 cm^{-1} (chapter 2).

No Co-O band is clearly observed with NP-0.2 but as the amount of cobalt stearate increases, a broad Co-O band appears at around 420 cm^{-1} and is shifted towards higher wavenumbers (440 cm^{-1}) when the cobalt stearate amount increases. Its increasing intensity with respect to the Fe-O band is correlated to thicker CoO shells. The IR bands of Co_3O_4 phase are not clearly seen on these spectra. Therefore the Co-O bands observed here are ascribed to a cubic Co-O phase in agreement with XRD patterns. The fact that the Co-O band position evolves as a function of the cobalt stearate amount and is located at lower wavenumbers than that obtained with cublic CoO NPs suggest that these CoO phases are non stoechiometric.

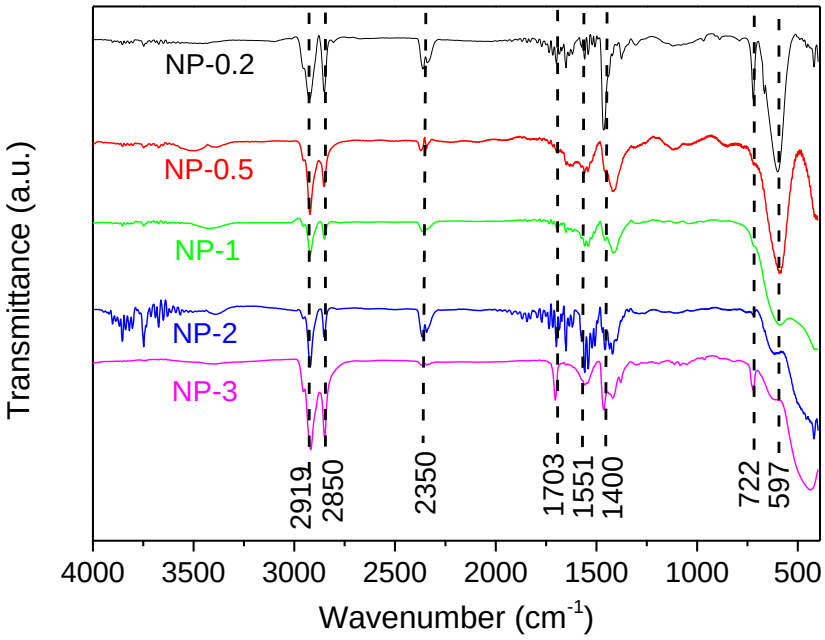

Figure III-5. FT-IR spectra of NP-0.2 (black), NP-0.5 (red), NP-1 (green), NP-2 (blue) and NP-3 (pink). Dashed lines indicate the absorption bands, blue bar Fe-O band and red bars Co-O bands.

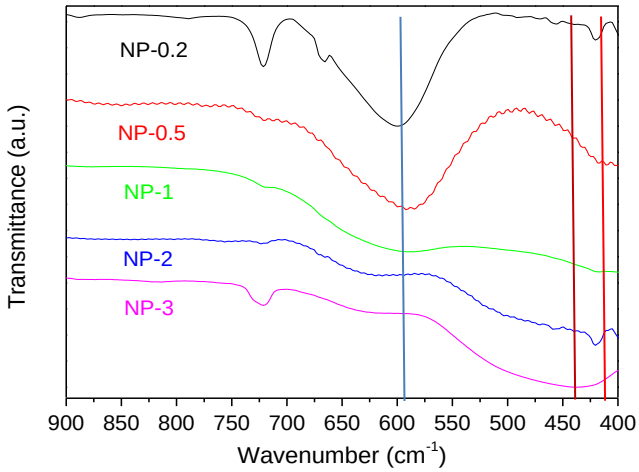

Figure III-6. Enlargement of FT-IR spectra of NP-0.2 (black), NP-0.5 (red), NP-1 (green), NP-2 (blue) and NP-3 (pink) in the range 900-400 cm^{-1} of Figure III-5. Dashed lines indicate the absorption bands, blue bar Fe-O band and red bars Co-O bands.

The core-shell structure was further investigated by electron energy-loss spectroscopy (EELS) (Figure III-7). EELS mapped images of NP-0.5 (Figure III-7A-C) and NP-1 (Figure III-8) revealed the homogeneous distribution of Fe and Co atoms in nanoparticles. The overlay spectrum shows that Co atoms are mostly observed which is consistent with an iron oxide core coated by a CoO shell. Although, the distribution of Co atoms could not be observed for NP-0.2, the EELS spectrum showed a weak but noticeable peak (Figure III-9). These results agree with either the very thin CoO shell or the insertion of Co atoms in the spinel lattice. On the other hand, EELS mapped images of NP-2, show the inhomogeneous distribution of Co atoms with regard to the Fe atoms in the core (Figure III-7D and E). The

overlay spectrum shows unambiguously that CoO does not cover homogenously Fe_3O_4 cores for large amount of cobalt stearate (Figure III-7F).

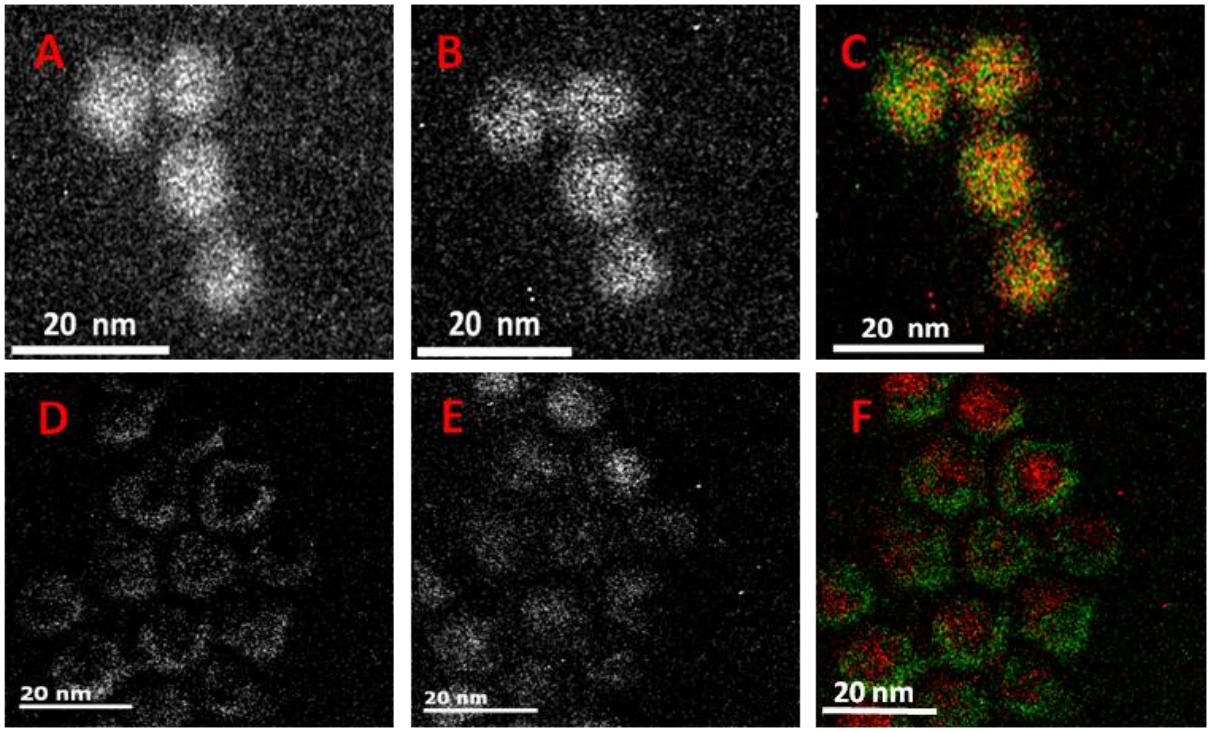

Figure III-7. EELS mapped images of NP-0.5 (A, B, C) and NP-2 (D, E, F). Co mapped images (A, D), Fe mapped images (B, E), overlay mapped images of Fe (red) and Co (green) (C, F). EELS mapped images of NP-2 (D,E,F).

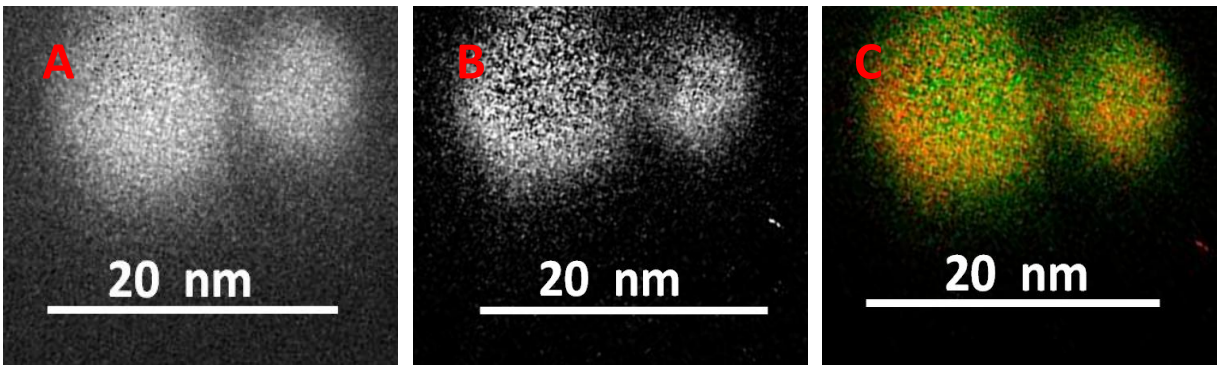

Figure III-8. A-C, EELS mapped images of NP-1: Co mapped image (A), Fe mapped image(B) and overlay mapped image Fe (red)-Co (green) (C).

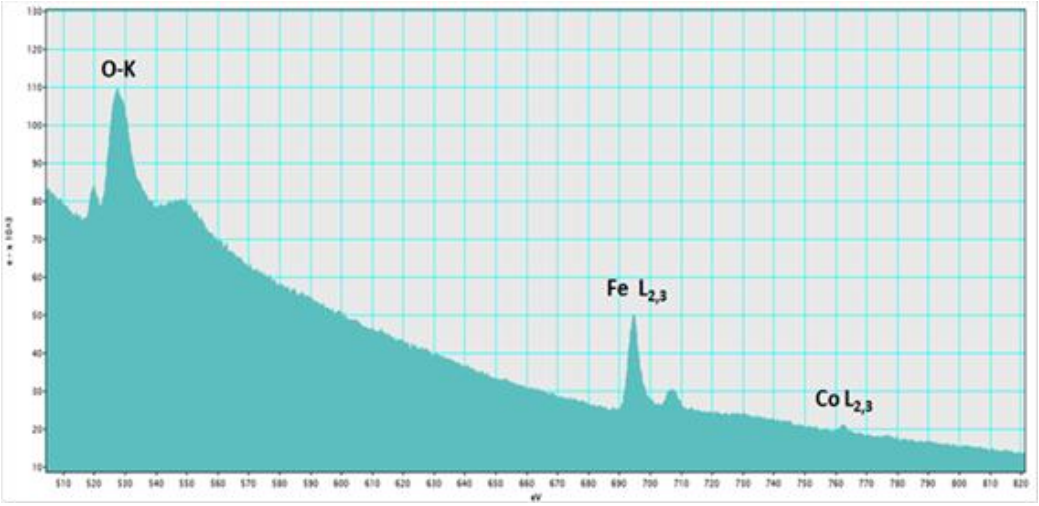

Figure III-9. EELS spectrum of NP-0.2 showing the presence of Co atoms.

A better insight on the distribution of Fe and Co atoms was obtained by performing EELS line scans across the section of individual NPs. Co atoms are distributed all along the section with higher amounts on the extremities which correspond to core-shell structure for NP-0.5 (Figure III-10A) and NP-1 (Figure III-11A). In contrast, the section measured for NP-2 shows that CoO does not coat uniformly the surface of $Fe_{3-\delta}O_4$ (Figure III-10B). These results are confirmed for NP-3 (Figure III-11B) and confirm again that the increase of the average CoO shell thickness leads to a transition from homogeneous to heterogeneous coating.

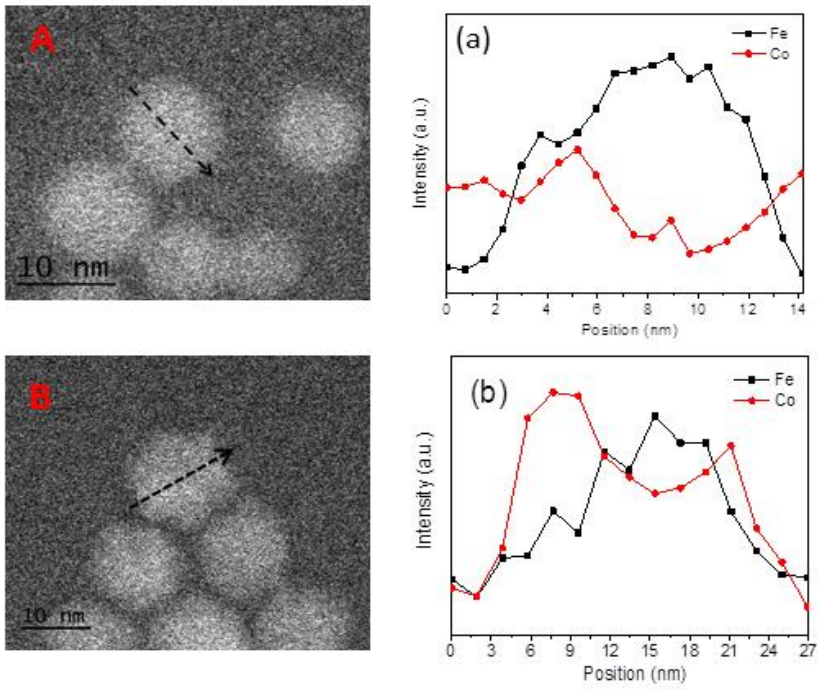

Figure III-10. STEM images of NP-0.5 (A) and NP-2 (B) and their corresponding Fe and Co line scans (a, b) performed across nanoparticle sections indicated by arrows.

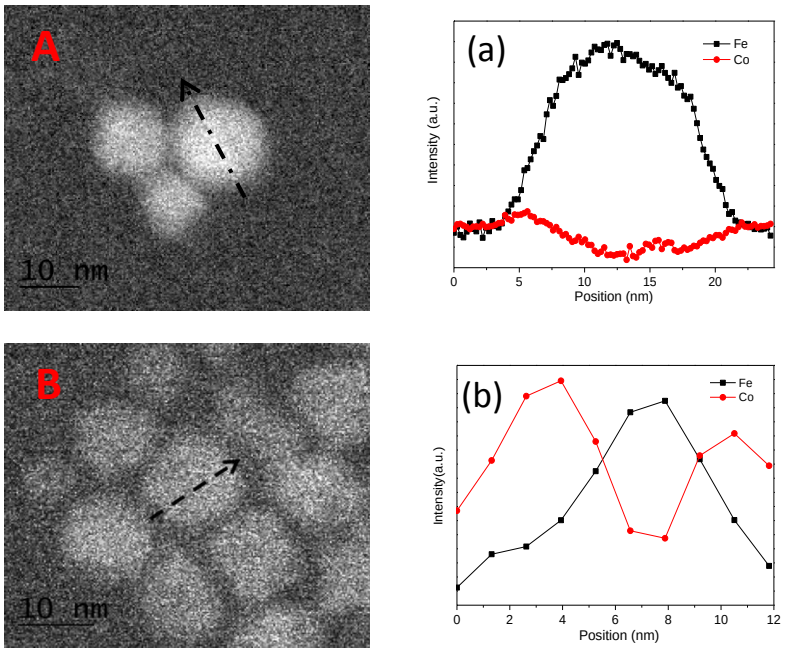

Figure III-11. Fe and Co line-scanned EELS profiles of a nanoparticle: (A-a) NP-1 and (B-b) NP-3.

A-III.2 Magnetic properties of core-shell NPs

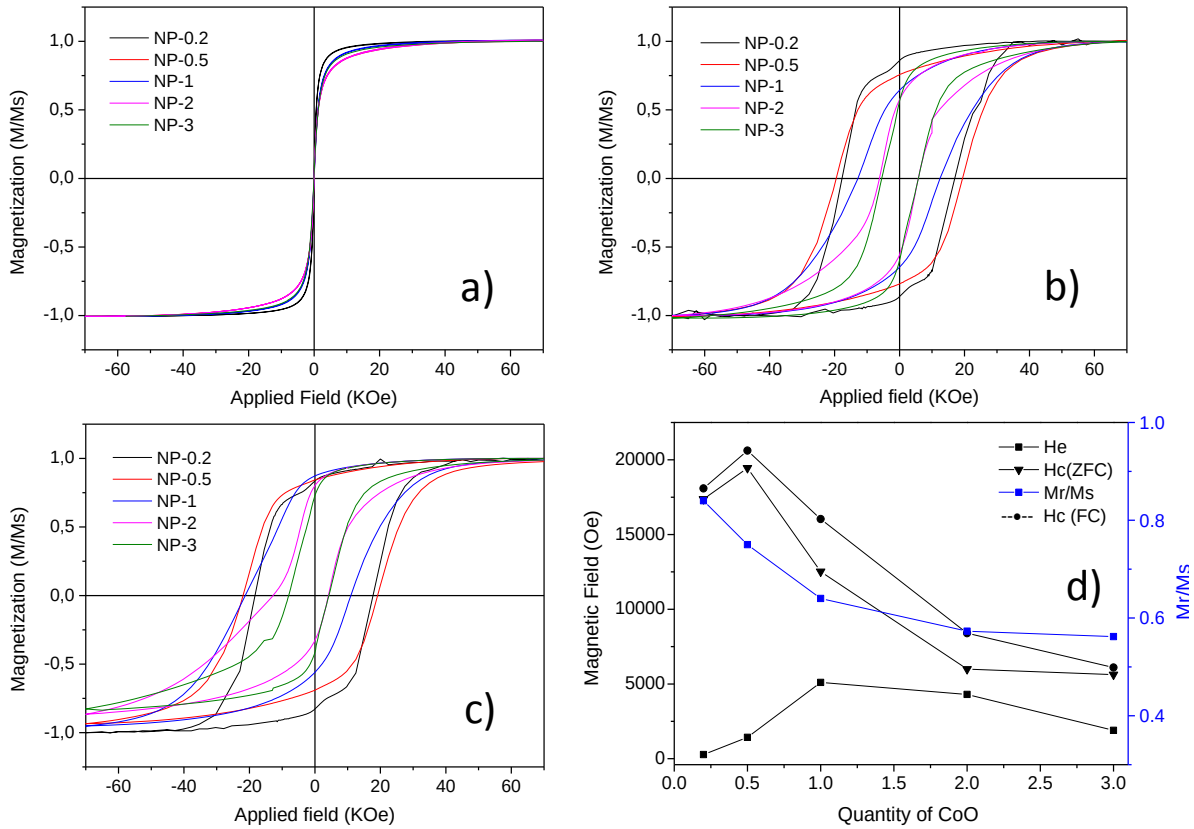

Figure III-12. a) Magnetization (M) curves as function of applied field (H) at 400K. b) M-H curves at 5K (ZFC). c) M-H curves at 5K after field cooling (FC). d) Exchange field (H_E ■),

Coercive field (H_c ▼) after ZFC and (H_c●) after FC and reduced remanence Mr/Ms (blue line ■) versus Co amount (0.2, 0.5, 1, 2 and 3) calculated from M-H curves.

The magnetic properties of these core-shell NPs have been studied by means of superconducting quantum interference device (SQUID) magnetometer. Magnetization (M) curves recorded as function of a magnetic field (H) at 400 K (Figure III-12a) show that all NPs are superparamagnetic whatever their structure. In contrast, hysteresis loops measured at 5 K after cooling under a zero field (ZFC) demonstrate their ferrimagnetic behavior (Figure III-12b). However one may notice that very large cycles were measured for NP-0.2 and NP-0.5 which evidence a very huge coercive field (H_C) of 20 000 Oe for NP-0.5 (18 000 Oe for NP-0.2) and M_R/M_S ratio of 0.86 for NP-0.2 (0.75 for NP-0.5). The hysteresis cycles become "smaller" with the increase of shell thickness which means that coercive fields and M_R/M_S ratio decrease (Table III-4).

In order to study the exchange coupling at the FiM/AFM interface, M(H) curves have been recorded at 5 K after cooling down under a magnetic field of 7 T (FC) (Figure III-12c). Their comparison with ZFC M(H) curves shows a negative horizontal shift for each sample which is characteristic of exchange bias coupling (Figure III-13). Such a phenomenon consists in the pinning of FiM spins with AFM spins at the FiM/AFM interface which is motivated by the magnetic field applied upon cooling. It arises from the anisotropy energy of CoO which is higher than the coupling energy between FiM and AFM phases. Therefore, spins of the FiM phase which do reverse experience the strong unidirectional anisotropic barrier created by the exchange coupling at the FIM/AFM interface. Additionally, a positive vertical shift is observed for all samples in the exception of NP-0.2. It increases with the shell thickness and becomes the largest for NP-2 and NP-3 which means it is amplified by the discontinuous structure of the shell which results in a large surface roughness.[33] Indeed, such a shell structure favors high surface anisotropy and spin disorder which enhance the exchange bias coupling and vertical shift.[18,23,34]

Table III-4. Magnetic characteristics of NP-0.2-long, NP-0.2, NP-0.5, NP-1, NP-2 and NP-3.

Sample	NP-0.2-long	NP-0.2	NP-0.5	NP-1	NP-2	NP-3
H_E(Oe)-FC	0	276	1426	5102	4300	1870
H_c(Oe)-FC	19605	18017	20618	16038	8400	6140
H_c(Oe)-ZFC	19274	17371	19456	12520	5996	5625
Mr/Ms	0.86	0.84	0.75	0.64	0.57	0.56
T_B-ZFC max (K)	240	225	264	256	125 and 254	174 and 225
T_B-imaginary part(K)	223	212	233	182	155 and 229	152 and 243
Ms (emu/g)	26.7	29.5	41.9	30.6	30.5	18.4

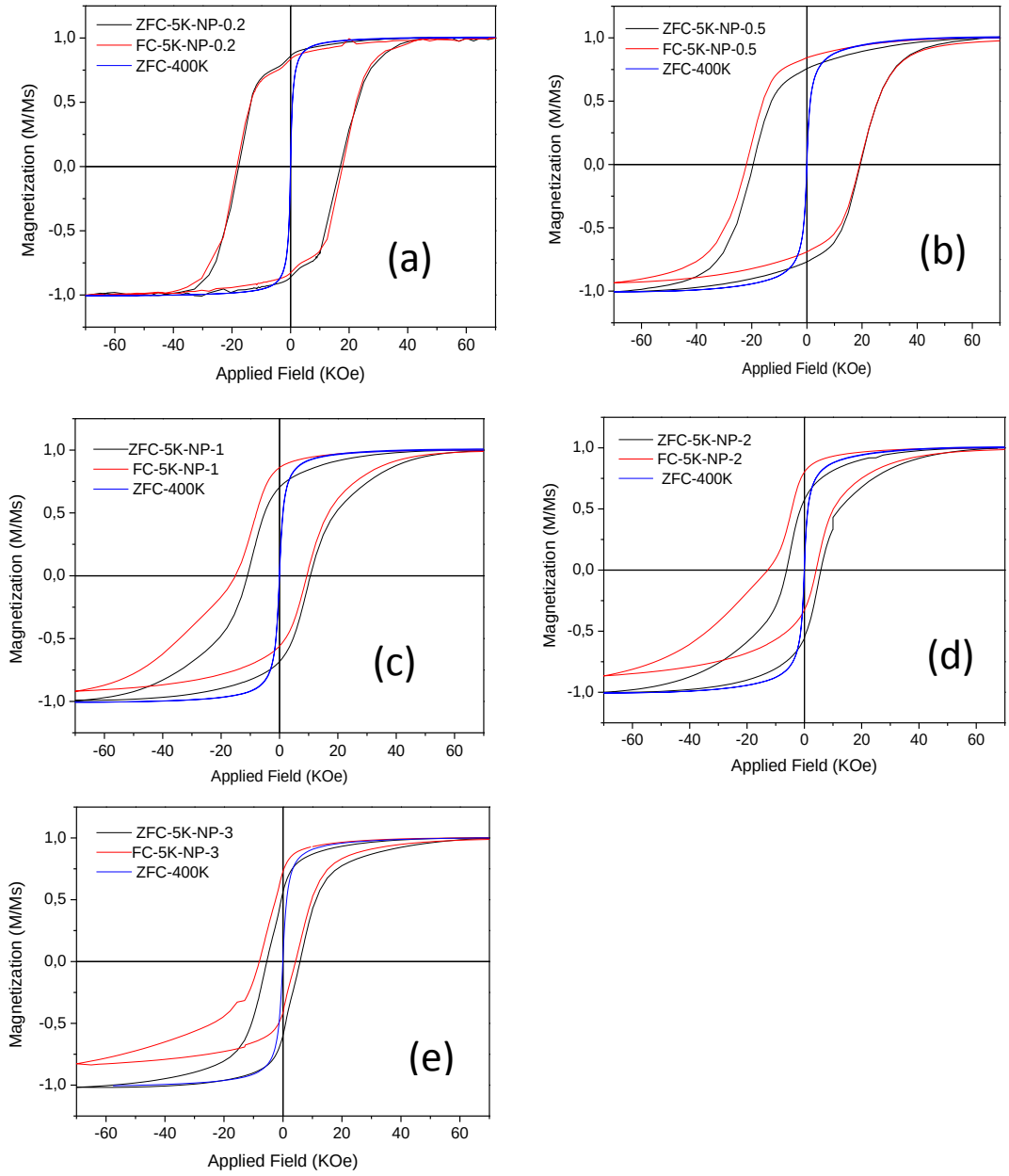

Figure III-13. Magnetization (M) curves recorded as function of a magnetic field (H) for NP-0.2(a), NP-0.5(b), NP-1(c), NP-2(d) and , NP-3(e) at 400K and 5K before zero-field cooling (ZFC) and after field cooling (FC) from 400 K to 5 K under magnetic field of 7 T.

To gain deeper insight of the impact of the CoO shell thickness on the magnetic properties, the magnetic characteristics have been measured precisely for all samples (Figure III-12d, Table III-4). The saturation magnetization values have been obtained after removing the weight contribution of the organic coating (deduced from TGA curves). The Ms values decrease as expected with the increase of the CoO shell thickness as AFM CoO does not contribute to Ms. The slight difference observed between NP-0.2 and NP-0.5 may be related to the larger $Fe_{3-\delta}O_4$ core diameter of NP-0.5 (8.9 nm) by comparison with that of NP-0.2 (8 nm).

The exchange coupling at the FiM/AFM interface can be quantified by measuring the exchange field (H_E). Coercive field Hc is defined as Hc=|Hc right – Hc left|/2 from ZFC and FC hysteresis loop and H_E=|Hc right + Hc left|/2 from FC hysteresis loop. Obviously, NP-1 displays the largest exchange fied (5100 Oe) which is much higher than that reported for similar core-shell NPs.[35] In contrast, NP-2 and NP-3 are featured by lower values which indicate the predominance of the FiM/AFM interface against the average thickness of the AFM shell. The exchange field being commonly reported to enhance the coercive field, the latter which is quite high for NP-1 (12700 Oe), decreases accordingly.

In the case of samples NP-0.5 and NP-0.2, the exchange field is lower than that of NP-1 (even that of NP-2 and NP-3) and decreases strongly with the decrease of the shell thickness. This decrease of the exchange field may be correlated to the thinner AFM shell as reported for Co@CoO NPs.[20] However, this evolution is not consistent with the very high values of H_C and M_R/M_S ratio which increase dramatically from NP-0.2 to NP-0.5. Therefore the evolution of He and Hc values in NP-1, NP-2 and NP-3 appears coherent and correlated to the exchange bias effect (high He induces high Hc due to the increase in anisotropy induced by the exchange bias coupling). In the case of NP-0.2 and NP-0.5, very high coercive fields are obtained (larger than those of NP-1 up to -3) but they display the lowest exchange fields. Thus the observed Hc values in these samples can not be related only to an exchange bias effect. Knowing that cobalt ferrite is a stronger anisotropic magnetic phase than the spinel iron oxide and thus exhibits high coercive field, the formation of a cobalt ferrite shell at the surface of these NPs is not to exclude and has already been reported.[26] The magnetic properties observed here results from the combination of properties due to interfacial exchange with a CoO and the presence of a cobalt ferrite shell.

Magnetization curves recorded as function of the temperature gave a complementary insight on the magnetic properties (Figure III-14a). All NPs display ZFC/FC curves which are characteristic of superparamagnetic NPs and the maximum of the ZFC curve (T_{MAX}) is often assimilated to the blocking temperature (Table III-4). NP-0.5 present the highest temperature T_{MAX} at 264 K, much higher than that of pristine $Fe_{3-\delta}O_4$ nanoparticles (150 K).[31] Such a high value is the result of the increase in anisotropy induced by the cobalt ferrite shell and the exchange bias coupling. The lowest value of T_{MAX} (225 K) for NP-0.2 shows that the exchange bias coupling decreases with the AFM shell thickness. On the other hand, M(T) ZFC curves for NP-2 and NP-3 are much broader and two contributions are observed around 254 K and 125 K for NP-2 and 225 and 174 K for NP-3. The one at the highest temperature should correspond to the exchange bias coupling between FiM and AFM phases. The second one centered would be much correlated to the value of the pristine iron oxide NPs. As long as no pure iron oxide NPs have been observed, we think that this contribution may be due to NPs with a very low coating of CoO or with no epitaxial interface with CoO: CoO and iron oxide NPs are sticked but without common crystallographic planes lowering the exchange bias.

Magnetic measurements recorded under an alternative magnetic field afford a much accurate value of the blocking temperature (T_B). Indeed T_B corresponds to the highest value of the imaginary part of the susceptibility χ'' (Figure III-12b) and reflects the transition between blocked and unblocked magnetic domains, i.e. the temperature at which the anisotropy energy is equal the thermal energy. In NPs featured by a FiM/AFM coupling, the maximum value of T_B is the Néel temperature (T_N) above which the antiferromagnetic order disappears and

renders ineffective the exchange bias coupling. Although T_B values are much higher than that of the pristine iron oxide, they remain below T_N of CoO in its bulk state (290 K). The layer thickness being thinner than 2 nm, surface effects like spin disorder may reduce T_N as reported by Morales *et al.*[36] The so determined T_B evolved similarly to T_{MAX} with the CoO coating .

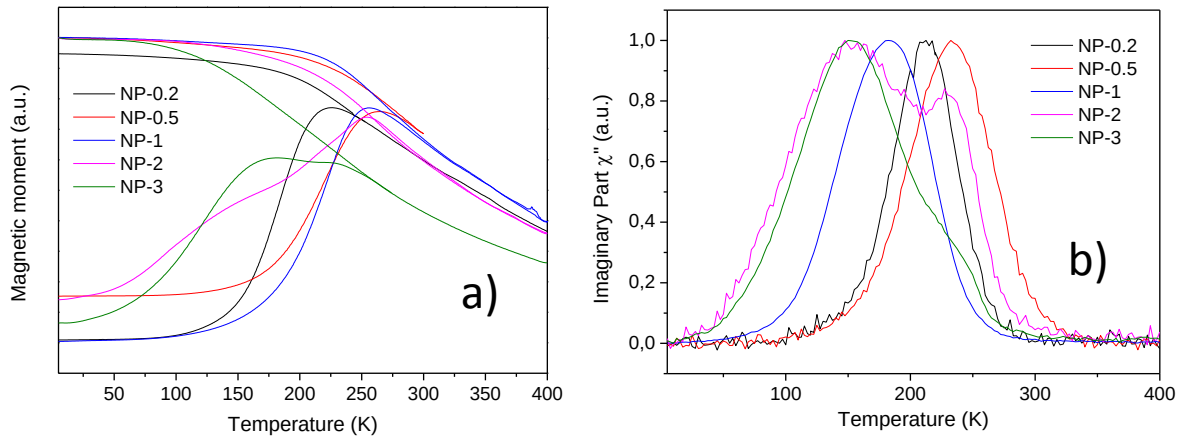

Figure III-14. a) Temperature dependence of magnetization measured after ZFC and FC for NP-0.2, 0.5, 1, 2 and 3. b) Imaginary part χ" of the AC susceptibility of all core-shell NPs as function of the temperature measured under magnetic field of 3.5 Oe at a frequency of 1 Hz.

A-III.3 Discussion

Discussion on the growth of CoO as function of the concentration of cobalt stearate and the kinetics of the reaction

The key point in this study is that the structure of the CoO shell can be efficiently modulated by the experimental conditions. All NPs consist in an iron oxide $Fe_{3-\delta}O_4$ core shelled by CoO. The shell thickness increases with the concentration of cobalt stearate from few angstroms for NP-0.2 to 2.5 ± 0.7 nm for NP-3. Nevertheless the amount of cobalt stearate used for the growth of CoO has a strong influence on the shell structure. While it consists in a monocrystalline shell which covers continuously the surface of the iron oxide seeds for NP-0.2, NP-0.5 and NP-1, it becomes polycrystalline and discontinuous for NP-2 and NP-3 with some facets of the iron oxide core remaining uncovered. The formation of such different structures can be understood as function of the nucleation and growth kinetics which depends on the concentration of cobalt stearate.

Cobalt stearate displays a higher decomposition temperature than iron stearate and has been shown to be difficult to decompose to form CoO NPs.[37,38] Therefore the heterogeneous nucleation of CoO at the surface of iron oxide seeds is favored. Indeed iron oxide nanocrystal seeds lower the free energy barrier for nucleation and enable the quasi selective growth of CoO at the surface of iron oxide whatever the amount of cobalt stearate, as shown by TEM micrographs and XRD pattern refinements. In addition HRTEM micrographs have shown that iron oxide seeds display different crystalline facets corresponding to different reflections. In the iron oxide spinel structure, it is likely the (111) facets which exhibit the highest growth rate and so, the highest chemical reactivity prior to the nucleation of CoO.[39] Nevertheless, the crystal growth may be strongly modulated by the nucleation kinetics.[40]

By considering the La Mer model,[41] the kinetics of nucleation and growth step is given by the concentration in monomers resulting from the thermal decomposition of cobalt stearate. Indeed when cobalt stearate decomposed with temperature, monomers are generated which are the minimum building units of cobalt-based nanocrystals and are supposed to be intermediate species such as polyironoxo clusters, which concentration increases as the reaction proceeds. [5,42] In the La Mer model (Figure II-2 in Chapter 2), the energy barrier of the nucleation process is much higher than that of the growth process. When the supersaturation of the monomer ($C>C_{min}$) is high enough to overcome this energy barrier, burst nucleation will take place, resulting in the formation and accumulation of stable nuclei. For homogeneous nucleation, the minimum radius of a stable nucleus that can grow spontaneously in the supersaturated solutions is inversely proportional to the supersaturation. At high supersaturation (high C_{max}), a large amount of nuclei are generated but with small radius while for small supersaturation (small C_{max}), a lower amount of nuclei is formed but with larger radius.

In our experimental conditions, heterogeneous nucleation is favored: when the concentration in cobalt stearate increases, the amount of monomers increases and induces the nucleation of CoO at the iron oxide surface when its concentration reaches a minimum concentration When the amount in cobalt stearate is low ($R < 2$), it generates low concentration in Co monomers in solution and allows the formation of a cobalt based shell all over the iron oxide surface whatever the surface energy of crystalline facets.[43] However for low amount of cobalt stearate, a low amount of cobalt should nucleate at the surface of iron oxide NPs which is certainly unstable and favor its diffusion in iron oxide: an interfacial cobalt doped γ -Fe_2O_3 layer would form that arose from Co^{2+} migration into vacant octahedral sites at the γ -Fe_2O_3 surface as reported in references 26,44. Mössbauer spectroscopy is currently realized on these samples to ascertain the formation of a cobalt ferrite phase. After this nucleation step, the growth step occurs : when the temperature increases, monomers continues to be formed [5] and induce the growth of a CoO shell at the surface of NPs. In the case of NP-0.2, as the amount in cobalt stearate is low, most of formed monomers have contributed to the nucleation step and the growth step is quite inhibited contrary to NP-0.5 and NP-1.

When high amounts in cobalt stearate ($R > 2$) are involved, large amount of monomers are generated and there should be a competition between heterogeneous and homogeneous nucleations and the nucleation and growth steps should occur simultaneously. All the facts result in the formation of a discontinuous shell. Indeed, the nucleation-growth process should be much sensitive to the chemical reactivity of iron oxide facets. As reported previously,[29] pristine iron oxide NPs are featured by the exhibition of different crystalline facets which correspond to different reflections. Each facet is featured by a different surface energy and the nucleation should first occur on the facets with the higher energy. As soon as Co based phase has already nucleated on the facets with the highest surface energy and as the growth step occurs simultaneously, most of monomers are involved, the monomer concentration has strongly decreased and the nucleation on other facets is no more possible.[45] Therefore growth of CoO prevails on nucleation and results in discontinuous and polycrystalline shell. Similar observations have been reported on multiple crystal growth of MnO from large Fe_3O_4 nanoparticles exposing large facets.[46]

Discussion on the magnetic properties as function of the core-shell structure

The magnetic properties of these core-shell NPs are directly dependent on the core-shell structure. Exchange bias coupling enhances the magnetic anisotropy of NPs. The observation of a high exchange field is therefore correlated to the increase of coercive field and blocking temperature. The highest coupling exchange characteristics account from NP-1 which displays the highest Fe_3O_4/CoO interface and the most homogeneous and thick AFM shell.

In contrast, the formation of a discountinuous and polycrystalline AFM shell results in the strong decrease of exchange field despite an increase of the average shell thickness. In fact the magnetic properties show two contributions: that of a typical two-layer (exchange bias) system and quite that of pristine iron oxide NPs. These results show that the quality of the interface on the exchange bias predominates significantly on the shell thickness. The pinning of FiM spins of the first layer at the interface is much efficient than in the thicker layers.[10] It is in agreement with the high exchange bias properties obtained with NP-1.

However with NP-0.2 and NP-0.5 which display thinner CoO shells, a decrease of the exchange field with the thickness of the AFM shell is observed with an increase of the coercive field. This huge increase of the coercive field while the exchange bias field decreases with the shell thickness is explained by the formation of an interfacial doped iron-oxide layer which may correspond to some extend to cobalt ferrite.[43] Skoropata *et al* have also reported very recently on similar γ-Fe_2O_3@CoO nanoparticles and incriminate the diffusion of cobalt cations from the shell into octahedral site vacancies resulting from the oxidation of the surface layer.[26] In this case, the exchange bias coupling would not proceed directly between FiM and AFM phases, but through an interfacial layer.

In order to verify our assumption on the existence of such a Co-dopped ferrite, one additional experiment was conducted by prolonging the reaction time of NP-0.2 from 2 h to 8 h. TEM images show the slight increase in size of uniform spherical $Fe_{3-\delta}O_4$ form 8.2 to 8.9 ± 0.8 nm (Figure III-15). The as obtained nanoparticles named NP-0.2-long, were featured by a narrow size distribution and XRD confirmed that they are made mainly of iron oxide (Figure III-16). No CoO phase was observed and the presence of cobalt ferrite could not be assessed with certainty because of its very close cell parameter to magnetite. Mossbauer spectrometry is currently in progress to confirm the formation of a cobalt ferrite phase. Nevertheless, ZFC and FC M(H) curves recorded at 5 K revealed the increase of the coercive fields to 19 600 Oe with respect to NP-0.2 while the exchange field totally vanished (Table III-4 and Figure III-17). These results show that longer reaction times favor the migration of Co in the iron oxide surface layers of the core and the formation of a thicker cobalt ferrite shell while no CoO is formed since no exchange field is observed. Furthermore, NP-0.2-long displays only one intermediate Tmax value (240 K) which is higher than the one of pristine iron oxide NPs. That means that the Co-doped iron oxide surface layers should induce a magnetic coupling leading to a larger anisotropy. Indeed cobalt ferrite is featured by a larger anisotropy constant (1.8-3.10^6 erg/cm^3) than magnetite (1.1×10^5 erg/cm^3) and there is certainly a magnetic coupling between soft (iron oxide) and hard (Co-doped) phases. However one may notice that the increase of coercive field is much significant in our case than in previous studies reported on core-shell NPs based on ferrites.[47,48] Only Song *et al* reported similar values on $MnFe_2O_4$/$CoFe_2O_4$ NPs.[49] Also a large coupling effect has been observed in the absence of

exchange field by Lima *et al* on inverse CoO@$CoFe_2O_4$ NPs.[50] Therefore the enhancement of the magnetic properties in NP-0.2 and NP-0.5 may not arise only from the exchange bias coupling but also from a soft/hard coupling. Such a soft/hard coupling predominates in NP-0.2 when NP-0.5 displays a combination of EB coupling to soft/hard coupling.

However if we compare NP-0.5 to NP-1: their CoO shell thickness is very close, 0.85 and 1 nm respectively, but NP-1 displays a larger He, lower Hc, slightly lower T_{MAX} and T_B than NP-0.5. Thus one may advance that when the shell thickness increases, the shof/hard coupling disappears or becomes negligible by comparison with exchange bias coupling. This may be related to the structure of the shell. Indeed different nucleation and growth processes have been observed to be different as function of the amount of cobalt stearate: low amount of cobalt stearate favor the formation of a cobalt ferrite shell when large amounts favor the growth of CoO nanocrystals at the surface of iron oxide NPs lowering thus the quality of the FM/AFM interfaces.

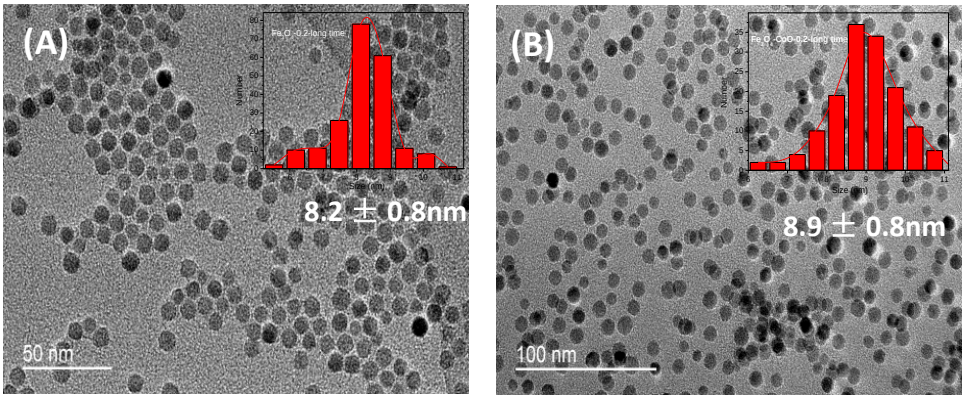

Figure III-15. TEM of iron oxide NPs (A) before performing the decomposition of cobalt stearate for 8 h in order to form NP-0.2-long time (B).

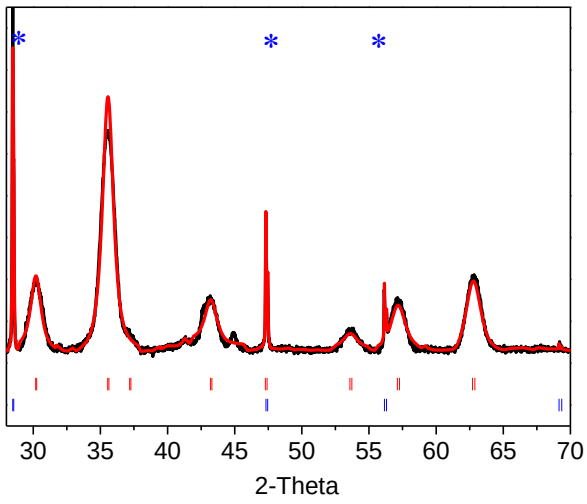

Figure III-16. XRD pattern (in black) of NP-0.2-long time and the corresponding refined data (in red). The vertical bars represent reference Fe_3O_4 in red and Silicon in blue (indicated by stars at the top) at the bottom.

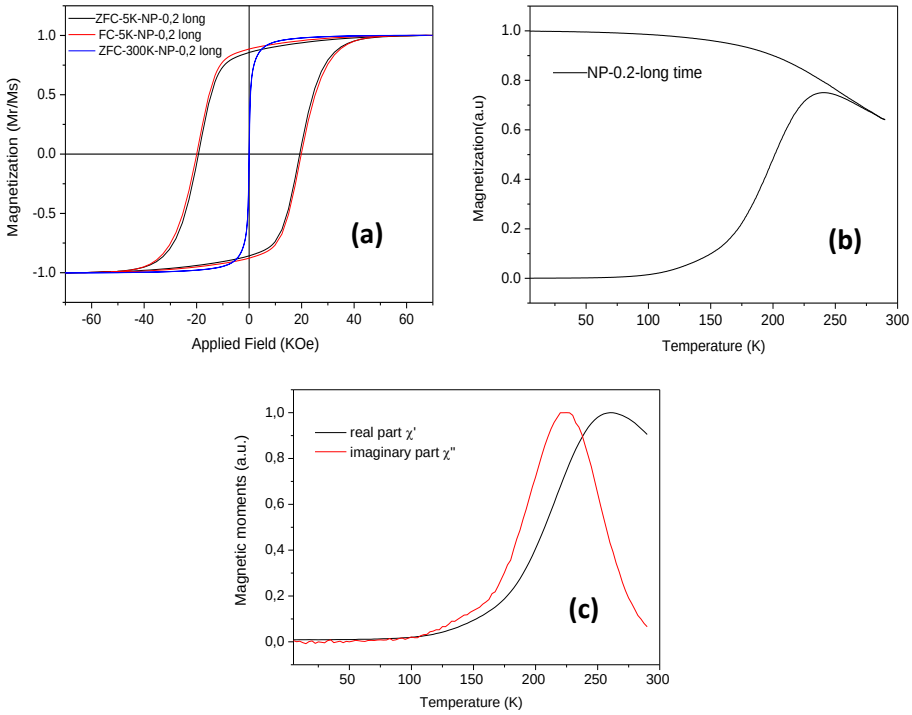

Figure III-17. a) Magnetization (M) curves as function of applied field (H) of NP-0.2-long time before zero-field cooling (ZFC) and after field cooling (FC) cooling from 400 K to 5 K under magnetic field. b) Temperature dependence of magnetization measured after ZFC and FC for all core-shell NPs. c) real part and imaginary part of susceptibility.

A-IV Conclusion

We have reported on the synthesis of $Fe_{3-\delta}O_4$@CoO core-shell NPs with tunable shell structure. The synthesis of NPs has been performed by a seed mediated of a CoO shell at the surface of iron oxide nanocrystal seeds on the basis of the thermal decomposition of a metal precursor. The nucleation and growth steps of the shell have been shown to strongly depend on the amount of cobalt stearate. Low amounts of cobalt stearate favor the formation of an homogeneous cobalt based shell at the surface of iron oxide NPs and of a cobalt ferrite interfacial phase between the iron oxide core and the CoO shell. Large amounts of cobalt stearate favor the nucleation and growth of CoO nanocrystals on particular facets of iron oxide seeds (displaying the highest surface energy) which result in a non homogeneous covering of the iron oxide core.

The shell structure has strongly influenced the resulting magnetic properties of core-shell NPs. This systematic study emphasizes the importance of thickness, continuity, crystallinity and interfaces. Nanoparticles combining the highest interface quality and the thickest homogeneous CoO shell display very unique exchange bias coupling (H_E = 5100 Oe) and coercive field (12 700 Oe). Magnetic properties of NPs constituted of a core of iron oxide with CoO nanocrystals grown on specific iron oxide facets (NP-2 and NP-3) have shown that the FiM/AFM interface quality and continuity prevails as the He and Hc values are observed to decrease.

On the other hand, the reduction of the shell thickness has been correlated to the decrease of the exchange bias coupling while the coercive field dramatically increases. This very surprising result was rationalized by the formation of a thin layer of Co-doped iron oxide layer with a composition close de cobalt ferrite. The cobalt-based shell induces an additionnal soft/hard coupling thanks to the different magnetic anisotropy of both compounds. The very large Hc value obtained with NP-0.5 is explained by a combination of both exchange bias and soft/hard couplings. Such complex interfacial coupling in magnetic NPs paves the way to a fine tuning of the magnetic properties of NPs and to the development of advanced applications such as high-density storage media, sensing, spin dependent transport or spin filters.

PART B : Monolayers of core-shell NPs by the Langmuir Blodgett technique

B-I Introduction

Nowadays, nanoparticles are considered as the building blocks of the future nanotechnological devices and the investigation of their properties when structured into thin films and devices has become a strategical challenge. Indeed arrays of non interacting ferrimagnetic nanoparticles appear as the future generation of high density magnetic storage media and films of magnetite nanoparticles have been reported to display very interesting magneto-resistance values for spintronic applications in comparison to conventional films elaborated by physical methods. In addition, the final magnetic properties of such nanostructures will be addressed by the dipolar interactions between nanoparticles which will induce collective properties modulated by the structuration parameters.

At IPCMS, monodisperse iron oxide nanocrystals with average sizes in the range 8-20 nm have been synthesized by the thermal decomposition of an iron stearate complex and have been assembled using the Langmuir-Blodgett technique and the parameters leading to uniform 2D and 3D arrays over large areas with a high density and degree of order have been determined. [51]

Then the dipolar interactions in such arrays have been investigated by comparing DC and AC SQUID measurements on powdered, diluted, 2D- and 3D-organized NPs.[52] The dipolar interactions in 2D arrays have been observed to be stronger by comparison with diluted and powder samples due to the 2D structuration. Indeed the magnetic moment of nanoparticles are found preferentially orientated in the film plane. The strength of these dipolar interactions has been shown to depend on the nanosize in agreement with simulations. In particular a superferromagnetic behaviour is observed in 2D arrays of 16 nm nanoparticles.

Thus the assembling of iron oxide NPs in 2D films by the Langmuir-Blodgett (Shown in Scheme III-2) has led to original collective properties with the appearance of a shape anisotropy. As core-shell NPs displaying exchange bias properties have been synthesized in the part A, it appears interessant to investigate the effect of their assembling on their collective magnetic. Thus 2D films of core-shell NPs have been elaborated by the Langmuir-Blodgett technique. Then their magnetic properties have been measured and compared to those of powdered core-shell NPs.

B-II Assembling of core-shell NPs in films by the Langmuir-Blodgett technique

Previous studies on the formation of LB films have demonstrated that the NPs suspension should be constituted of spherical NPs with a monodisperse size (very narrow size ditribution) and without free ligands to avoid the formation of a molecular Langmuir films between domains of NPs. [51] Bare silicon substrates are soaked at room temperature in a Piranha solution (3:1 H_2SO_4:H_2O_2) for 10 min, thoroughly rinsed with H_2O and dried before deposition. A small volume (150-200 µL) of a 5 mg/mL nanoparticle suspension in chloroform was spread on the water subphase of the Langmuir trough (KSV 5000, 576×150

mm^2) at room temperature. After 10 min stabilization, the area available to the NPs is reduced by compressing the barriers (compression rate: 5 mm/min), and the surface pressure-area isotherm is recorded during the film compression using a Wilhelmy plate. The pressure is stabilized for 10 min at 30 mN m^{-1}. At this pressure, the film reaches its maximum in density and then transfered onto optical glass (5 cm x 5 cm) or silicon substrate depending on the characterization. The transfer occurs by the concomitant pulling out of the substrate from the water subphase at a rate of 1 mm/min and by moving the barriers with the aim to maintain the surface pressure at 30 mN/M at the air-water interface.

Atomic Force Microscopy (AFM) was performed using a Veeco Multimode Nanoscope V (Brucker) to characterize the topography of the films. The images were obtained in contact mode in dry condition with silicon nitride cantilever with a spring constant of 0.6 N/m (model MSCT-AUHW, Veeco, CA). Deflection and height mode images were scanned simultaneously at a fixed scan rate (1 Hz) with a resolution of 512 × 512 pixels. The average roughness of the deposited films, corresponding to the root mean square values given by the Nanoscope software, was determined from 5 different areas of 1 × 1 μm^2.

B-III Characterization of LB films of core-shell NPs

B-III.1 SEM observations

SEM images in Figure III-18 show the formation of dense films with the 4 core-shell samples. The SEM images at low magnification for each sample demonstrate the formation of a dense film on large areas. Nevertheless brighter area are observed in Figure III-18 which may be due to the presence of traces of either free oleic acid molecules or residual precursor or to the formation of NPs multilayer. Some residual organic phases should be present for NP-0.5 and NP-1 films as a monolayer film is observed at high magnification. For NPs-2&3, the formation of multilayer is clearly observed even at low magnification.

The formation of monolayer with NP-0.5 and NP-1 is favored by the quite homogeneous size of these NPs even if their purification was not optimal. The formation of multilayers with NP-2&3 may be related to their heterogeneous shape with the heterogeneous growth of CoO nanocrystals at the surface of iron oxide NPs.

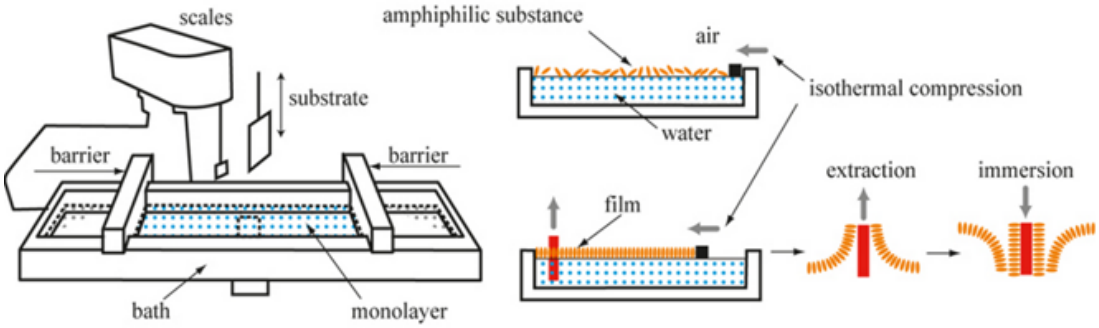

Scheme III-2. Schematic illustration of Langmuir-Blodgett (LB) set up.

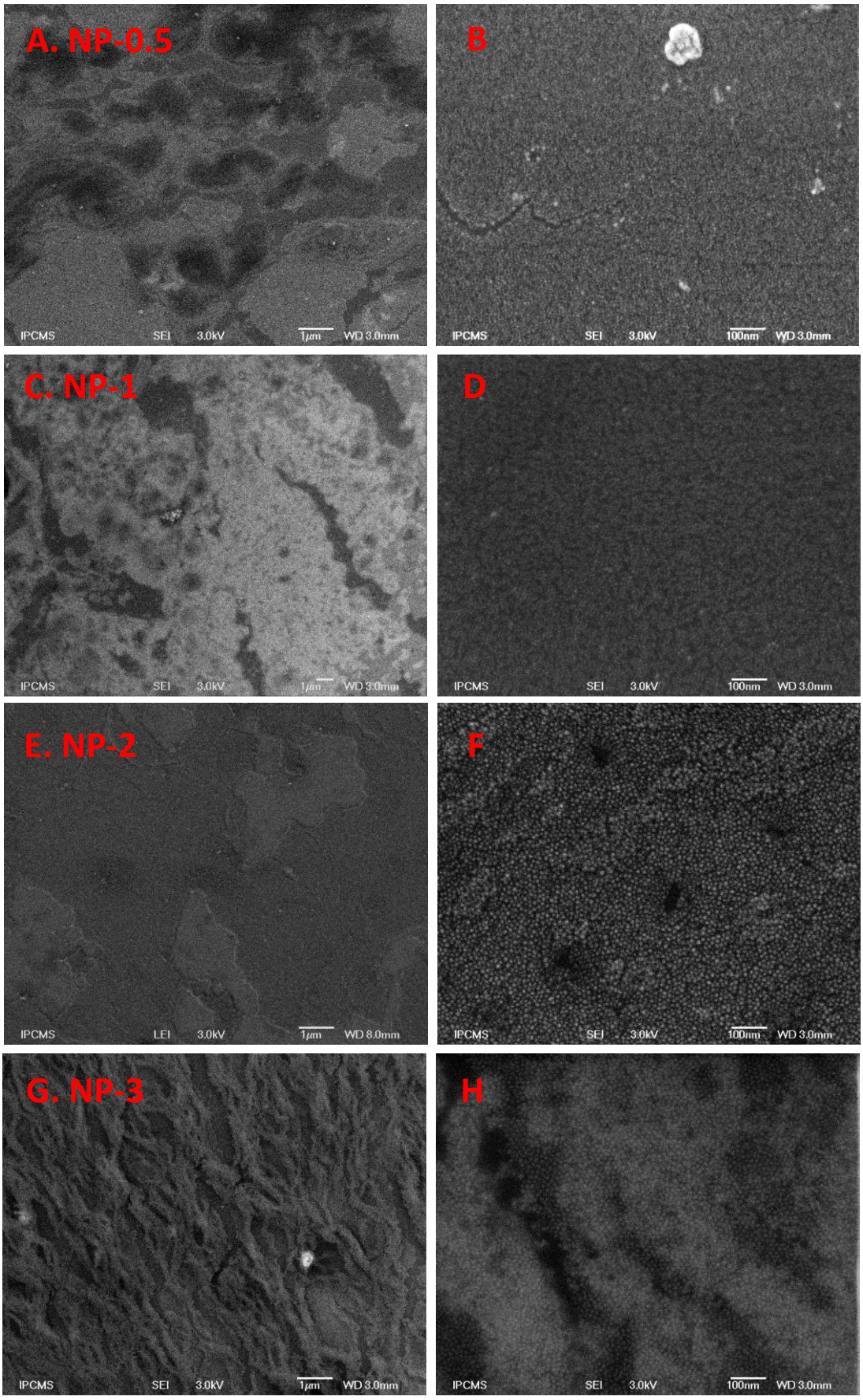

Figure III-18. LB films of (A-B) NP-0.5, (C-D) NP-1, (E-F) NP-2 and (G-H) NP-3.

B-III.2 AFM Characterization

AFM was performed to characterize the topography of the different core-shell films, (Figure III-19). It confirms the formation of dense films over 1 µm (Figure III-19A-C). AFM images show a dark region corresponding to the substrate which was considered as "0" height after scratching of the films. The measured thicknesses of NP-0.5, NP-1 and NP-2 films from this scratch zone were 9.5, 9.6 and 13 nm respectively (Figure III-19a-c). That confirms the formation of a monolayer for these films on the measured areas. Whereas, in the case of NP-3 film, a larger thickness was measured of about 93 nm showing the formation of a multilayer film.

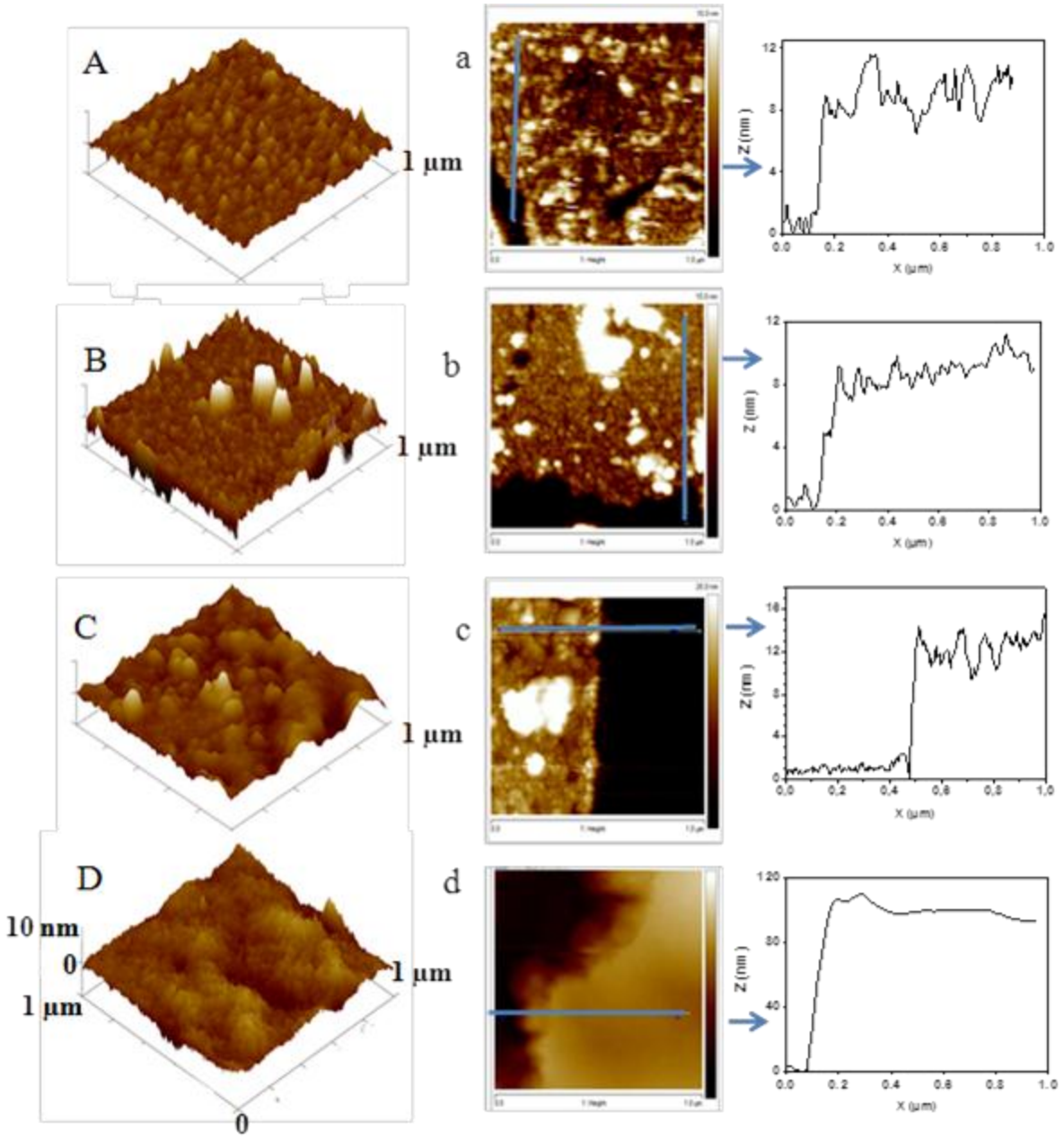

Figure III-19. AFM images on different films of core-shell NPs with the roughness of the surface on a 1 µm scale. A) 3D image of core-shell NP-0.5 monolayer. B) 3D image of core-shell NP-1 monolayer. C) 3D image of core shell NP-2 film. D) 3D image of core-shell NP-3 film. a) 2D image with the AFM profile after scratching. a) NP-0.5 monolayer with a

thickness of ~9.5 nm. b) NP-1 monolayer with the thickness of ~9.6 nm. c) NP-2 films with a thickness of ~13 nm. d) NP-3 films with a thickness of ~93 nm.

B-IV Magnetic Characterization of Monolayers

Once the NPs are well organized in films, the dipolar interaction between NPs may generate new collective properties different from those of individual NPs. In order to study the effect of dipolar interaction on the overall magnetic properties of films of core-shell NPs, magnetic measurements have been performed in a superconducting quantum interference device (SQUID) Magnetometer. Magnetization (M) curves as a function of the applied field (H) of core-shell NPs at 300K (Figure III-20C) are characteristic of superparamagnetic NPs. Hysteresis loops measured at 5K (Figure III-20D) demonstrate their ferrimagnetic behavior below their blocking temperature. The results from SQUID measurements are summarized in Table III-5. Large coercive field (Hc) can be observed for each core-shell films.

In order to study the FM/AFM exchange bias interaction in films, magnetization (M) curves as function of applied field (H) were recorded after cooling down under a magnetic field (Figure III-20D). To have a better comparison, coercive field and exchange field values of NPs as a function of Co amount and their corresponding films were plotted in Figure III-21. Thus it may be noticed that the core-shell NPs assembled in films display lower coercive and exchange fields than the powdered NPs.

Such a decrease of coercivity due to inter-particle interactions has been predicted by a Monte Carlo modeling study.[53] Therefore, the lower Hc values for the films may be the result of a lowered anisotropy barrier due to dipolar interactions.[54] These lower Hc values are also correlated to the lower exchange values and thus it means that the exchange bias properties are lower when the NPs are assembled in films or when the dipolar interaction strength are strong.

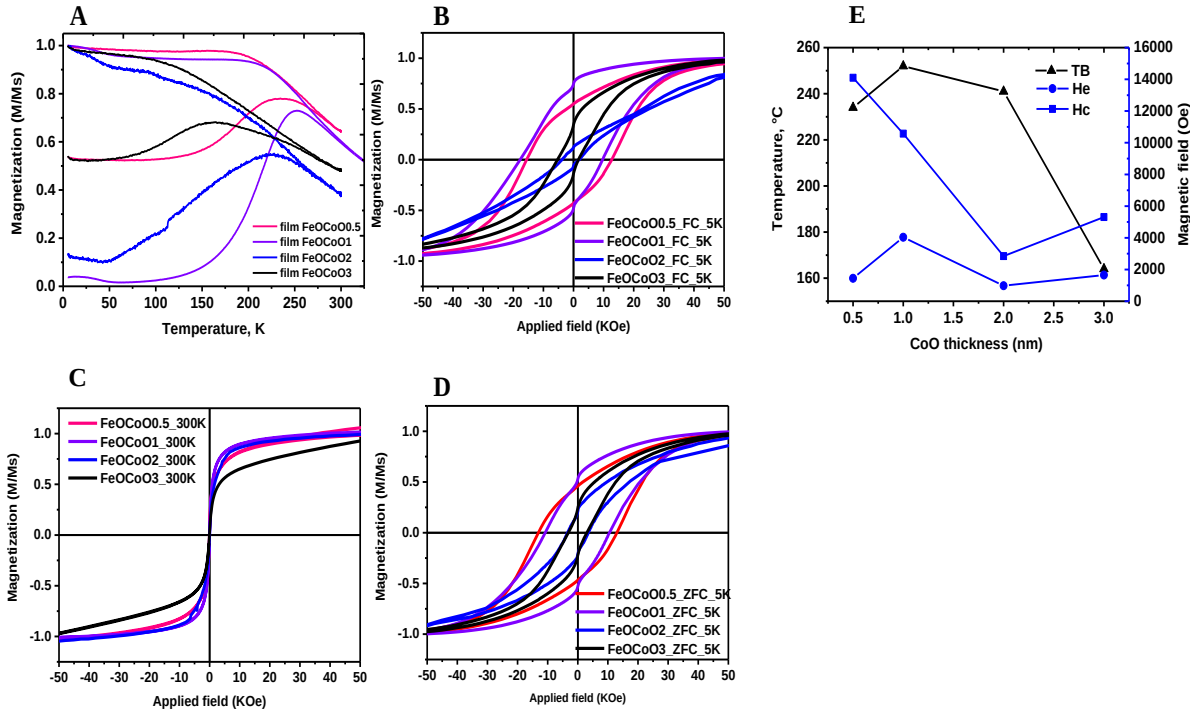

Figure III-20. A: Magnetization curve as a function of temperature under zero field cooling (ZFC) and field cooling (FC); B: M-H curves at 5K after field cooling (FC); C: Magnetization (M) curves as function of applied field (H) at 300K; D: M-H curves at 5K before zero-field cooling (ZFC); E: Exchange field (H_E ●), Coercive field (H_c ■) and blocking temperature (T_B ▲) as a function of Co amount (0.5, 1, 2 and 3) and calculated from M-H curves.

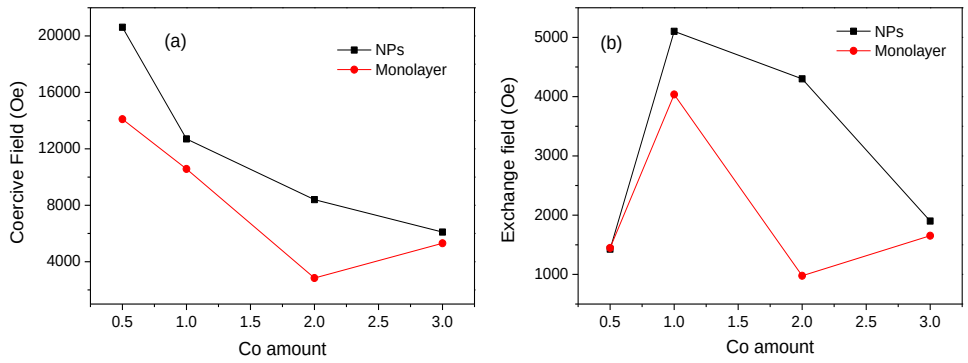

Figure III-21. Coercive field and exchange field of NPs and of their corresponding films as a function of Co stearate amount.

Table III-5. Magnetic data of LB films of NP-0.5, NP-1, NP-2 and NP-3 and TB max of NPs.

Sample	0.5	1	2	3
T_B max LB films	234	253	227	164
TBmax NP	264	256	125-254	174-225
H_E	1447	4037	977	1653
H_C	14100	10575	2846	5308

Magnetization measurements as a function of temperature is also used to evaluate the intensity of dipolar interaction. To the best of our knowledge, high dipolar interaction strength induces a shift of the blocking temperature towards higher values. In Figure III-20 E, Tmax of ZFC was plotted as a function of the CoO thickness. At the same time, the T_B values are summarized in Table III-5 and compared to that of powdered NPs. As with powdered NPs, the highest T_B of 253K is reached with the film of NP-1 in which the NPs were well organized in monolayer. The Tmax of films is lower than that of powdered NPs which suggests lower dipolar interaction in films. Therefore these T max measurements confirmed as the Hc and He measurements that the assembling of core-shell NPs in films induces a decrease in exchange bias properties.

B-V Conclusion

The core-shell NPs of Part A have been assembled in films by the Langmuir-Blodgett techniques. The quality of the films was related to the quality of NPs: NPs with a

homogeneous size assembled in monolayer films when NPs with a heterogeneous shape formed multilayer films. Magnetic measurements performed on films have shown that the dipolar interactions resulting from the assembling in films induce a decrease of the exchange bias properties of NPs.

REFERENCES

1. Nogues, J.; Sort, J.; Langlais, V.; Skumryev, V.; Surinach, S.; Munoz, J. S.; Baro, M. D. Exchange bias in nanostructures. *Physics Reports* **2005,** *422* (3), 65-117.
2. Skumryev, V.; Stoyanov, S.; Zhang, Y.; Hadjipanayis, G.; Givord, D.; Nogués, J. Beating the superparamagnetic limit with exchange bias. *Nature* **2003,** *423*, 850-853.
3. Meiklejohn, W. H.; Bean, C. P. New Magnetic Anisotropy. *Phys. Rev. B* **1956,** *102*, 1413-1414.
4. Tracy, J. B.; Weiss, D. N.; Dinega, D. P.; Bawendi, M. G. Exchange biasing and magnetic properties of partially and fully oxidized colloidal cobalt nanoparticles. *Physical Review B* **2005,** *72* (6), 064404.
5. Walid B., Benoit P. Pichon, Solenne Fleutot, et al. Magnetic Iron Oxide Nanoparticles: Reproducible Tuning of the Size and Nanosized-Dependent Composition, Defects, and Spin Canting. *J. Phys. Chem. C* **2014**, *118*, 3795−3810.
6. Rajib Ghosh Chaudhuri, Santanu Paria, Core/Shell Nanoparticles: Classes, Properties, Synthesis Mechanisms, Characterization, and Applications. *Chem. Rev.* **2012**, *112*, 2373–2433.
7. Iglesias O., Batlle X., Labarta A. Exchange bias and asymmetric hysteresis loops from a microscopic model of core/shell nanoparticles. *Journal of Magnetism and Magnetic Materials* **2007**, *316*, 140-142.
8. Patrice Mélinona, Sylvie Begin-Colin b, Jean Luc Duvail, et al. Engineered inorganic core/shell nanoparticles. *Physics Reports* **2014**, *543*, 163-197.
9. Feygenson, M.; Yiu, Y.; Kou, A.; Kim, K.-S.; Aronson, M. C. Controlling the exchange bias field in Co core/CoO shell nanoparticles. *Physical Review B 81* (19), 195445.
10. Nogu ès, J.; Skumryev, V.; Sort, J.; Stoyanov, S.; Givord, D. Shell-Driven Magnetic Stability in Core-Shell Nanoparticles. *Physical Review Letters* **2006,** *97* (15), 157203.
11. Martinez-Boubeta, C.; Simeonidis, K.; Angelakeris, M.; Pazos-Perez, N.; Giersig, M.; Delimitis, A.; Nalbandian, L.; Alexandrakis, V.; Niarchos, D. Critical radius for exchange bias in naturally oxidized Fe nanoparticles. *Physical Review B* **2006,** *74* (5), 054430.
12. Inderhees, S. E.; Borchers, J. A.; Green, K. S.; Kim, M. S.; Sun, K.; Strycker, G. L.; Aronson, M. C. Manipulating the Magnetic Structure of Co Core/CoO Shell Nanoparticles: Implications for Controlling the Exchange Bias. *Physical Review Letters* **2008,** *101* (11), 117202.
13. Iglesias; scar; Labarta, A.; lcar; Batlle, X. Exchange Bias Phenomenology and Models of Core/Shell Nanoparticles. *Journal of Nanoscience and Nanotechnology* **2008,** *8* (6), 2761.
14. Feygenson, M.; Yiu, Y.; Kou, A.; Kim, K.-S.; Aronson, M. C. Controlling the exchange bias field in Co core/CoO shell nanoparticles. *Physical Review B* **2010,** *81* (19), 195445.
15. Kovylina, M.; Garcia, M. d. M.; Konstantinovic, Z.; Varela, M.; Iglesias, O.; Labarta, A.; Batlle, X. Controlling exchange bias in Co-CoO x nanoparticles by oxygen content. *Nanotechnology* **2009,** *20* (17), 175702.

16. Ho, L. B.; Lan, T. N.; Hai, T. H. Monte Carlo simulations of core/shell nanoparticles containing interfacial defects: Role of disordered ferromagnetic spins. *Physica B: Condensed Matter 430* (0), 10.
17. Ong, Q. K.; Wei, A.; Lin, X.-M. Exchange bias in Fe/Fe_3O_4 core-shell magnetic nanoparticles mediated by frozen interfacial spins. *Physical Review B* **2009,** *80* (13), 134418.
18. Pichon, B. P.; Gerber, O.; Lefevre, C.; Florea, I.; Fleutot, S.; Baaziz, W.; Pauly, M.; Ohlmann, M.; Ulhaq, C.; Ersen, O.; Pierron-Bohnes, V.; Panissod, P.; Drillon, M.; Begin-Colin, S. Microstructural and Magnetic Investigations of Wüstite-Spinel Core-Shell Cubic-Shaped Nanoparticles. *Chem. Mater.* **2011,** *23*, 2886–2900.
19. Salazar-Alvarez, G.; Sort, J.; Surinach, S.; Baro, M. D.; Nogues, J. Synthesis and Size-Dependent Exchange Bias in Inverted Core-Shell MnO|Mn3O4 Nanoparticles. *Journal of the American Chemical Society* **2007,** *129* (29), 9102.
20. Simeonidis, K.; Martinez-Boubeta, C.; Iglesias, O.; Cabot, A.; Angelakeris, M.; Mourdikoudis, S.; Tsiaoussis, I.; Delimitis, A.; Dendrinou-Samara, C.; Kalogirou, O. Morphology influence on nanoscale magnetism of Co nanoparticles: Experimental and theoretical aspects of exchange bias. *Physical Review B* **2011,** *84* (14), 144430.
21. Vasilakaki, M.; Trohidou, K. N. Surface effects on the magnetic behaviour of nanoparticles with core/shell morphology. *Journal of Physics D: Applied Physics* **2008,** *41* (13), 134006.
22. Zheng, R. K.; Wen, G. H.; Fung, K. K.; Zhang, X. X. Training effect of exchange bias in g-Fe_2O_3 coated Fe nanoparticles. *Physical Review B* **2004,** *69* (21), 214431.
23. Mumtaz, A.; Maaz, K.; Janjua, B.; Hasanain, S. K.; Bertino, M. F. Exchange bias and vertical shift in CoFe2O4 nanoparticles. *Journal of Magnetism and Magnetic Materials* **2007,** *313* (2), 266.
24. Estradé, S.; Yedra, L.; Lopez-Ortega, A.; Estrader, M.; Salazar-Alvarez, G.; Baro, M. D.; Nogués, J.; Peiro, F. Distinguishing the core from the shell in MnOx/MnOy and FeOx/MnOx core/shell nanoparticles through quantitative electron energy loss spectroscopy (EELS) analysis. *Micron 43* (1), 30.
25. Krycka, K. L.; Borchers, J. A.; Salazar-Alvarez, G.; Lopez-Ortega, A.; Estrader, M.; Estradé, S.; Winkler, E.; Zysler, R. D.; Sort, J.; Peiro, F.; Baro, M. D.; Kao, C.-C.; Nogués, J. Resolving Material-Specific Structures within Fe_3O_4|g-Mn_2O_3 Core|Shell Nanoparticles Using Anomalous Small-Angle X-ray Scattering. *ACS Nano* **2013**, *7* (2), 921.
26. Skoropata, E.; Desautels, R. D.; Chi, C. C.; Ouyang, H.; Freeland, J. W.; van Lierop, J. Magnetism of iron oxide based core-shell nanoparticles from interface mixing with enhanced spin-orbit coupling. *Physical Review B* **2014,** *89* (2), 024410.
27. Thompson, P.; Cox, D. E.; Hastings, J. B. Rietveld refinement of Debye-Scherrer synchrotron X-ray data from Al2O3. *Journal of Applied Crystallography* **1987,** *20* (2), 79-83.
28. Rodriguez-Carvajal, J. Recent advances in magnetic structure determination by neutron powder diffraction. *Physica B: Condensed Matter* **1993,** *192*, 55-69.
29. Baaziz, W.; Pichon, B. P.; Lefevre, C.; Ulhaq-Bouillet, C.; Greneche, J.-M.; Toumi, M.; Mhiri, T.; Begin-Colin, S. High Exchange Bias in Fe_3O_4@CoO Core Shell Nanoparticles Synthesized by a One-Pot Seed-Mediated Growth Method. *The Journal of Physical Chemistry C* **2013,** *117* (21), 11436.

30. Baaziz, W.; Pichon, B. P.; Fleutot, S.; Liu, Y.; Lefevre, C.; Greneche, J.-M.; Toumi, M.; Mhiri, T.; Begin-Colin, S. Magnetic Iron Oxide Nanoparticles: Reproducible Tuning of the Size and Nanosized-Dependent Composition, Defects, and Spin Canting. *The Journal of Physical Chemistry C* **2014,** *118* (7), 3795.
31. Demortiere, A.; Panissod, P.; Pichon, B. P.; Pourroy, G.; Guillon, D.; Donnio, B.; Begin-Colin, S. Size-dependent properties of magnetic iron oxide nanocrystals. *Nanoscale* **2011,** *3* (1), 225.
32. Chih-Wei Tanga, Chen-BinWangb, Shu-Hua Chienc. Characterization of cobalt oxides studied by FT-IR, Raman, TPR and TG-MS. *Thermochimica Acta* **2008**, 473, 68-73.
33. Passamani, E. C.; Larica, C.; Marques, C.; Proveti, J. R.; Takeuchi, A. Y.; Sanchez, F. H. Exchange bias and anomalous vertical shift of the hysteresis loops in milled Fe/MnO2 material. *Journal of Magnetism and Magnetic Materials* **2006,** *299* (1), 11.
34. Marianna Vasilakaki and Kalliopi, N. T. Surface effects on the magnetic behaviour of nanoparticles with core/shell morphology. *Journal of Physics D: Applied Physics* **2008,** *41* (13), 134006.
35. Panagiotopoulos, I.; Basina, G.; Alexandrakis, V.; Devlin, E.; Hadjipanayis, G.; Colak, L.; Niarchos, D.; Tzitzios, V. Synthesis and Exchange Bias in Î¾Fe2O3/CoO and Reverse CoO/ Î¾Fe2O3 Binary Nanoparticles. *The Journal of Physical Chemistry C* **2009,** *113* (33), 14609.
36. Vazquez, M.; Luna, C.; Morales, M. P.; Sanz, R.; Serna, C. J.; Mijangos, C. Magnetic nanoparticles: synthesis, ordering and properties. *Physica B: Condensed Matter* **2004,** *354* (1-4), 71.
37. Walid Baaziz, Sylvie Begin-Colin, Benoit P. Pichon, et al. High-Density Monodispersed Cobalt Nanoparticles Filled into Multiwalled Carbon Nanotubes. *Chem. Mater.* **2012**, 24, 1549−1551.
38. Walid Baaziz, Benoit P. Pichon, Yu Liu, et al. Tuning of Synthesis Conditions by Thermal Decomposition toward Core−Shell $Co_xFe_{1-x}O$@$CoyFe_{3-y}O_4$ and $CoFe_2O_4$ Nanoparticles with Spherical and Cubic Shapes. Chem. Mater. **2014**, *26*, 5063−5073
39. McDaniel, H.; Shim, M. Size and Growth Rate Dependent Structural Diversification of Fe3O4/CdS Anisotropic Nanocrystal Heterostructures. *ACS Nano* **2009,** *3 (2)*, 434.
40. Seo, W. S.; Shim, J. H.; Oh, S. J.; Lee, E. K.; Hur, N. H.; Park, J. T. Phase- and Size-Controlled Synthesis of Hexagonal and Cubic CoO Nanocrystals. *Journal of the American Chemical Society* **2005,** *127* (17), 6188.
41. La Mer, V. K.; Dinegar, R. H. Theory, Production and Mechanism of Formation of Monodispersed Hydrosols. *Journal of the American Chemical Society* **1950,** *72* (11), 4847-4854.
42. Kwon, S. G.;Piao, Y.; Park, J.; Angappane, S.; Jo, Y.; Hwang, N.-M.; Park, J.-G.; Hyeon, T. Kinetics of Monodisperse Iron Oxide Nanocrystal Formation by "Heating-Up" Process. *J. Am. Chem. Soc.* **2007**, *129*, 12571-12584.
43. Salazar-Alvarez, G.; Sort, J.; Uheida, A.; Muhammed, M.; Surinach, S.; Baro, M. D.; Nogues, J. Reversible post-synthesis tuning of the superparamagnetic blocking temperature of [gamma]-Fe2O3 nanoparticles by adsorption and desorption of Co(ii) ions. *Journal of Materials Chemistry* **2007,** *17* (4), 322.

44. Tronc, E.; Jolivet, J.-P.; Lefebvre, J.; Massart, R. Ion adsorption and electron transfer in spinel-like iron oxide colloids. *Journal of the Chemical Society, Faraday Transactions 1: Physical Chemistry in Condensed Phases* **1984,** *80* (10), 2619.
45. Pellegrino, T.; Fiore, A.; Carlino, E.; Giannini, C.; Cozzoli, P. D.; Ciccarella, G.; Respaud, M.; Palmirotta, L.; Cingolani, R.; Manna, L. Heterodimers Based on CoPt3 Au Nanocrystals with Tunable Domain Size. *Journal of the American Chemical Society* **2006,** *128* (20), 6690.
46. Lee, K. S.; Anisur, R. M.; Kim, K. W.; Kim, W. S.; Park, T.-J.; Kang, E. J.; Lee, I. S. Seed Size-Dependent Formation of Fe3O4/MnO Hybrid Nanocrystals: Selective, Magnetically Recyclable Catalyst Systems. *Chemistry of Materials* **2012**, *24* (4), 682.
47. Lopez-Ortega, A.; Estrader, M.; Salazar-Alvarez, G.; Estrade, S.; Golosovsky, I. V.; Dumas, R. K.; Keavney, D. J.; Vasilakaki, M.; Trohidou, K. N.; Sort, J.; Peiro, F.; Surinach, S.; Baro, M. D.; Nogues, J. Strongly exchange coupled inverse ferrimagnetic soft/hard, MnxFe3-xO4/FexMn3-xO4, core/shell heterostructured nanoparticles. *Nanoscale* **2012,** *4* (16), 5138.
48. Masala, O.; Hoffman, D.; Sundaram, N.; Page, K.; Proffen, T.; Lawes, G.; Seshadri, R. Preparation of magnetic spinel ferrite core/shell nanoparticles: Soft ferrites on hard ferrites and vice versa. *Solid State Sciences* **2006,** *8* (9), 1015.
49. Song, Q.; Zhang, Z. J. Controlled Synthesis and Magnetic Properties of Bimagnetic Spinel Ferrite CoFe2O4 and MnFe2O4 Nanocrystals with Core-Shell Architecture. *Journal of the American Chemical Society* **2012,** *134* (24), 10182.
50. Lima, J. E.; Winkler, E. L.; Tobia, D.; Troiani, H. E.; Zysler, R. D.; Agostinelli, E.; Fiorani, D. Bimagnetic CoO core CoFe2O4 shell nanoparticles: Synthesis and magnetic properties. *Chemistry of Materials* **2012**. *24(3)*, 512-516.
51. Pauly, M.; Pichon, B. P.; Albouy, P.A.; Fleutot, S.; Leuvrey, C.; Trassin, M.; Gallani, J. L. Begin-Colin, S. *J. Mater. Chem.* **2011**, *21 (40)*, 16018-16027.
52. Pauly, M.; Pichon, B. P.; Fleutot, S.; Panissod, P.; Drillon M.; Begin-Colin, S. *J. Mater. Chem.* **2012**, *22 (13)*, 6343-6350.
53. Simeonidis, K.; Martinez-Boubeta, C.; Iglesias, Ã. s.; Cabot, A.; Angelakeris, M.; Mourdikoudis, S.; Tsiaoussis, I.; Delimitis, A.; Dendrinou-Samara, C.; Kalogirou, O. Conditions determining the morphology and nanoscale magnetism of Co nanoparticles: Experimental and numerical studies. *arXiv preprint arXiv:1109.2024* **2011**.
54. Gangopadhyay, S.; Hadjipanayis, G. C.; Sorensen, C. M.; Klabunde, K. J. Exchange anisotropy in oxide passivated Co fine particles. *Journal of Applied Physics* **1993,** *73* (10), 6964-6966.

Chapter IV. Nanoparticles encapsulated inside CNTs and biomedical applications

IV.1 Introduction

The design of metal oxide nanoparticles and their association with other nanomaterials to yield composites which combine properties of both entities is nowadays a subject in full development due to their wide range of potential applications (electronic and magnetic devices, data and energy storage, and theranostic vectors).[1-9]

Among such nanocomposites, there is currently intense interest in associating carbon nanotubes with metal oxide NPs in order to exploit the unique properties of each materials: electrical and thermal conductivities, architectural and mechanical properties of CNTs and magnetic properties and chemical stability of metal oxides NPs. In particular, superparamagnetic iron oxide nanoparticles (SPIONs) are widely developed in the biomedical field as MRI contrast agents and heat mediators for cancer hyperthermia, cell sorting, drug delivery, immunoassay and tissue repair.[10,11] Similarly CNTs are promising for biomedical applications as they are able to cross many biological and biophysical barriers with minimal cytotoxic effects.[12] Both single-walled (SWCNTs) and multi-walled CNTs (MWCNTs) have unique properties which make them suitable for applications in a variety of imaging modalities, such as near-infrared fluorescence, Raman spectroscopy, photoacoustic tomography and ultrasonography.[13-18] Furthermore CNTs possess a very broad absorbance spectrum, also covering the near infrared (NIR) optical transmission window where biological tissues are transparent.[19] Following exposure to NIR light, CNTs enter an excited state and release vibrational energy that is transformed into heat. In contrast to plasmonic nanoheaters such as gold nanorods or nanoshells, the energy transduction efficiency of CNTs is less dependent on particle characteristics and excitation wavelengths. Iron oxide nanoparticles and CNTs have also been recently reported as near-infrared photothermal agents for tumor ablation.[20,21] Therefore designing nanohybrids combining complementary functionalities of CNTs and nanomagnets should lead to promising nano-objects for theranostic applications. The real challenge is however to preserve the unique properties of each component once associated and to make the nanocomposites dispersible and compatible with biological media. Most recent attempts have led to the decoration of CNTs with magnetic nanoparticles on their outer layer. Although the nanohybrids could serve for MRI monitoring of CNTs,[22,23] the surface decoration changes the surface properties of nanotubes and do not lead to magnetically anisotropic structures. Another strategy is thus to fill the empty channel of CNTs with magnetic materials in order to obtain anisotropic nanomagnets embedded into the carbon template. It has been recently shown that according to the nature of the CNT surface, NPs could be incorporated preferentially outside or inside their channel.[24-27] In particular, it has been demonstrated that the encapsulation of NPs prevent them from oxidation and enhanced their chemical inertness. Indeed, cobalt-based NPs were encapsulated into CNTs and the chemical characterizations have shown a relatively high Co/O atomic ratio. This indicates that the surface oxidation remains relatively low in CNT embedded cobalt NPs in comparison to free NPs.[26] But the filling of CNTs with high efficiency, high density and high stability has not been achieved so far. Electrochemical methods,[28] direct incorporation of iron during the MWCNTs synthesis,[29-31] or magnetic capillary technique [32,33] or more frequently CNT filling with liquid salt by capillary effect have been investigated.[34] These approaches were generally followed by a suitable thermal treatment to obtain the desired NPs.[35,36] The incipient wetness impregnation is the most adapted method to control the filling yield.[37,38] We recently

proposed an alternative method to fill MWCNTs with iron oxide or cobalt-based NPs in a one-step under soft conditions: the synthesis of NPs by thermal decomposition of the metal precursor is induced inside CNTs which act as nanoreactors.[26,27] The size and the morphology of the NPs were very homogeneous and were found to depend on the nature of the metal precursor and on the MWCNT internal diameter. Cobalt stearate precursor led to large octahedral NPs which occupied the whole volume of CNTs and they were blocked inside the CNTs.[26] Despite their high filling density, iron oxide NPs inside CNTs displayed smaller diameters than the CNTs diameter (assimilated to peas in the peapods) and then they tend to slide outside CNTs when they are purified and further manipulated.[27] Thus, the filling density and the blocking of NPs inside CNTs has to be improved to envision multifunctional magnetic CNTs efficient for biomedical applications. Here a double filling process involving the thermal decomposition of either iron and/or cobalt stearate precursors inside CNTs has been developed in order to increase the filling rate and to block the NPs inside CNTs, Such process led to enhanced filling density and provided magnetic carbon CNTs manipulable by an external magnetic field (Schema 1). Then these magnetic CNTs have been functionalized to ensure their dispersibility in physiological media. For the first time, magnetic CNTs could be handled when interacting with cancer cells for controlling CNT orientation within the cell without toxicity. Such nanocomposites are suitable for combining MRI detection and photothermal ablation enhanced by applying an external magnetic field.

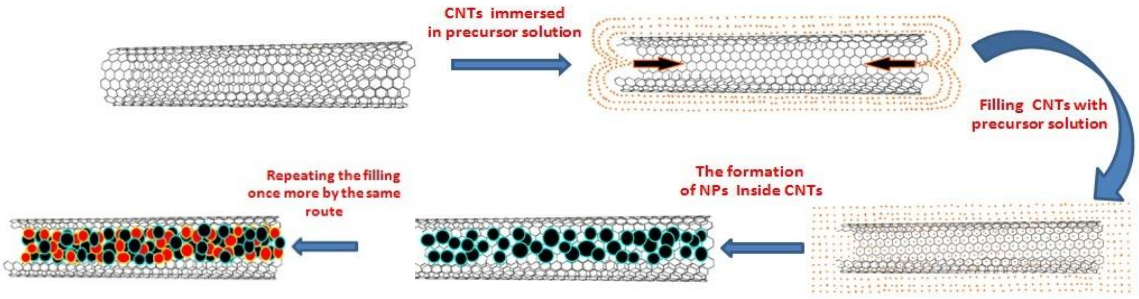

Schema 1. Schematic presentation of the two step filling process enhancing the filling of CNTs by metal oxide NPs.

In the first part of this chapter, iron oxide and cobalt oxide NPs were encapsulated inside carbon nanotubes by the typical solvothermal method already described. We will try to osberve the main differences between the NPs synthesized inside or outside of the CNTs and to appreciate the confinement effect inside the channel of the CNTs. Our aim is also to improve the filling rate of NPs inside CNTs and several synthesis conditions will be used like the modification of the NTCs surface, the nature of the solvent, the concentration of the salts…

In the second part of this chapter (paper accepted - under pressed - in ACS Nano and joined in its original version in the second part), carbon nanotubes (CNTs) were filled with ferrite nanoparticles (NPs) to develop the magnetic manipulation of the nanotubes and their theranostic applications. The challenges were both the filling of CNTs with a high amount of magnetic NPs and their functionalization to form biocompatible water suspensions.

IV.2 Synthesis and characterization of CNTs filled with $Fe_{3-x}O_4$ and CoO NPs

IV.2.1 Experimental details

IV.1.2.1 Preparation and characterization of pristine MWCNTs

Starting MWCNTs were provided by "Pyrograph Products" (City) and are produced by Chemical vapor deposition (CVD). Their inner diameters are typically comprised between 40 and 80 nm. Specific surface area of CNTs is close to 45 $m^2 \cdot g^{-1}$. In Figure IV.1, TEM images show that CNTs are rather straight and are characterized by open-ended channels (not always). They were washed with HNO_3 acid to remove the traces of the residual iron growth catalyst.

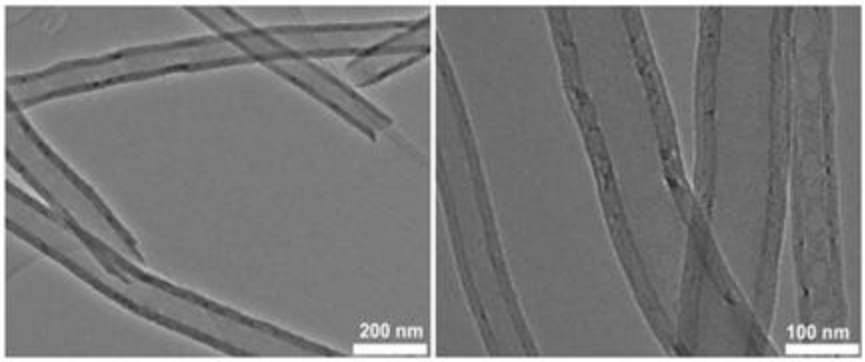

Figure IV.1. TEM images of pristine CNTs

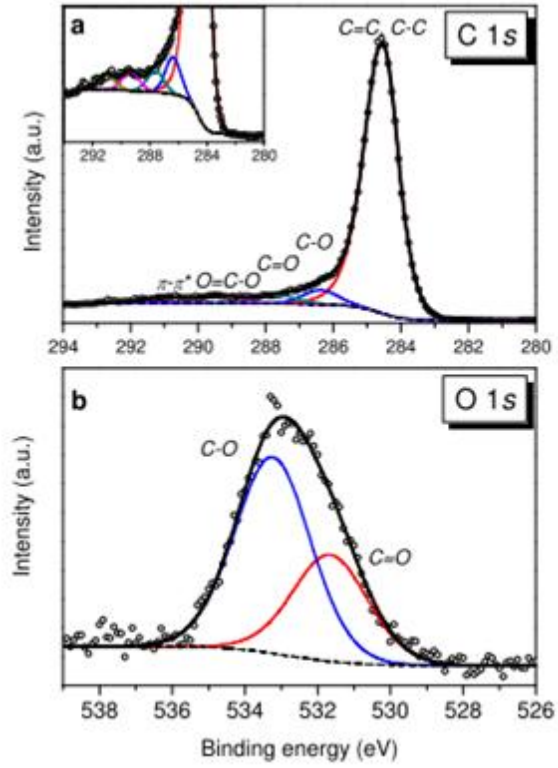

Figure IV.2. C1s (a) and O1s (b) core level XPS spectra of the pristine CNTs

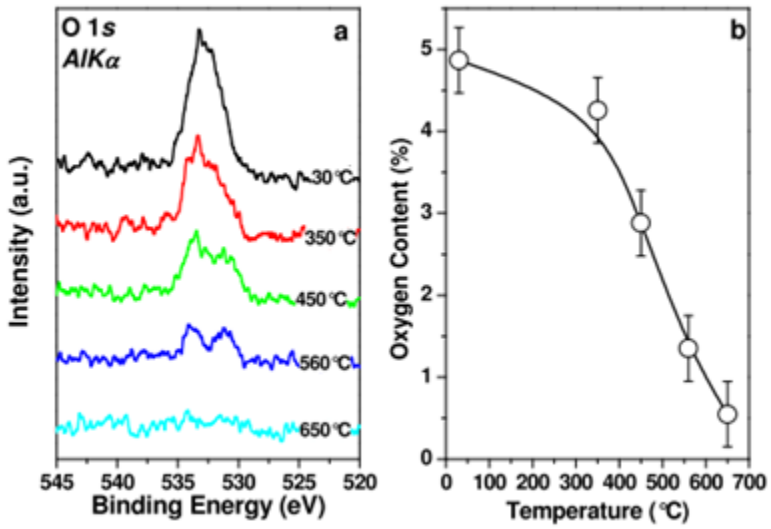

Figure IV.3. (a) O1s XPS spectra of CNTs annealed at different temperatures in UHV. (b) the oxygen atomic content calculated from the O1s to C1s peak area ratio assuming a homogeneous distribution of oxygen species in the analysis volume.

To remove the maximum of oxygenated species on their surface, CNTs were heated at 900 ℃ under an inert atmosphere (Ar) gas for 4 h. In Figure IV-2 is shown the C 1s spectrum of the pristine CNTs. The C 1s core level spectrum was deconvoluted to 5 components using standard procedure reported.[39] The C1s components are ascribed to single and double carbon-carbon bonds (C=C and C-C) at 284.5 eV. Meanwhile, at higher binding energies oxygen-containing moieties C-O (C-O-C, C-O-H), C=O and O-C=O (magnified in the inset of Figure IV-2a) are identified. The π-π* transition loss peak is also detected at ~291 eV. In Figure IV-2b, O 1s peak is observed. The deconvolution of O 1s shows broad peaks at 531.6 eV and 533.2 eV, which can confirm the existence of C=O and C-O respectively.

In Figure IV-3a, the evolution of the O1s peak with increasing temperature is shown. As the temperature increased, the O1s peak intensity decreased, indicating that all kinds of oxygen species diminished due to the heating treatment. In addition, the oxygen atomic content calculated from the O1s to C1s peak area ratio as function of temperature are shown in Figure IV-3b, which confirms the previous result: at 650 ℃, most of the oxygen is removed from the surface of the CNTs.

IV.1.2.2. Synthesis of Fe_3O_4 NPs inside CNTs

The typical procedure to fill the CNTs is the following: first of all, 1.38g $Fe(stearate)_2$, 1.24g oleic acid, 20 mL octadecene were mixed. After adding 50 mg of heat-treated CNTs, the solution was sonicated for 20 mins using a tip sonicator. Then the solution was kept at 100 ^oC for 1h to evaporate residual trace of water or ethanol. Subsequently, the temperature rose up to 288 ^oC (boiling point of octyl ether) with a 5^oC/min ramp and kept at this temperature for 2h under air. Finally, the products were washed four times with ethanol and chloroform followed each time by a centrifugation, and last put in suspension in a THF solution. Other

syntheses have been also performed using hexadecylamine, oleylamine and mixture of oleic acid and hexadecylamine (mass ratio of 1:1) to replace oleic acid and to study three influence of the ligand during the synthesis

IV.1.2.3. Synthesis of CoO NPs inside CNTs

In the cas of the cobalt, 1.38g $Co(stearate)_2$, 1.24g oleic acid, 20ml octadecene were mixed. After adding 50 mg of the heat- treated CNTs, the solution was sonicated for 20 mins using tip sonicator. Then, the solution kept at 100 ^oC for 1h to evaporate residual trace of water or ethanol. Subsequently, the temperature rose up to 318 ^oC (boiling point of octadecene) with a 5^oC/min ramp and kept at this temperature for 2h under Ar gas. Finally, the products were washed four times with ethanol and chloroform followed each time by a centrifugation, and last put in suspension in a THF solution. As in the case of the Fe_3O_4 NPs, Hexadecylamine, oleylamine and mixture of oleic acid and hexadecylamine (mass ratio of 1:1) were also used to replace the oleic acid.

IV.2.2 Characterization of CNTS filled with NPs

IV.2.2.1 $Fe_{3-x}O_4$ NPs inside CNTs

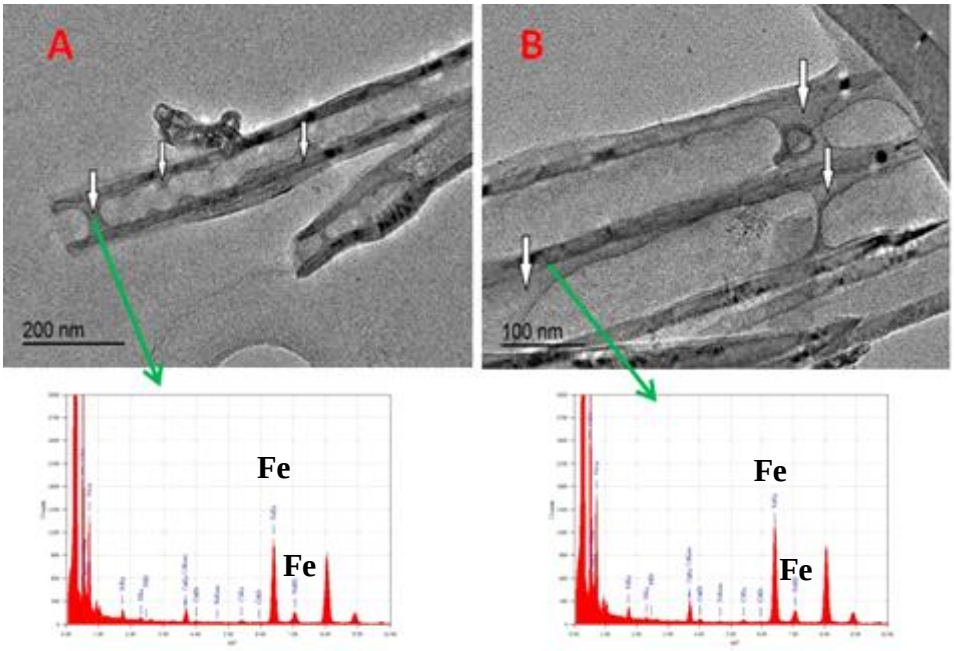

Figure IV.4. TEM images of CNTs obtained after 12 h suspension at 120 ^oC and before heating to boiling point of solvent. The white arrows indicate the liquid in CNTs. The below spectra correspond to the EDX of area indicated by green arrow.

As known, the driving force for solution entering the channel of CNTs is a capillarity effect, so that the wettability of the CNTs has a very high impact on the filling. In Figure IV.4 are represented the TEM images of CNTs obtained after 12 h suspension at 120 ^oC and before heating the mixture to the boiling point of the solvent. We can see that the inner walls of CNTs are wetted by $Fe(stearate)_2$ solution. The white arrows indicate the presence of precursor solution inside CNTs, according to the large contrast. The inner cavity is not totally filled by solution, which can be explained by a partial removal of the suspension because of

the applied vacuum during the TEM measurements. Furthermore, the corresponding electron diffraction spectra (EDS) confirms also that the Fe element is present in the zone where the white arrows are pointed to.

In Figure IV.5 are represented Fe_3O_4 nanoparticles synthesized inside CNTs using different ligands : oleic acid, Hexadecylamine and Oleylamine. In the presence of oleic acid, the CNTs were highly filled with Fe_3O_4 NPs (Figure IV-5A and B) : this part is well developped in the ACS Nano publication at the end of the chapter. As in the case of Fe_3O_4 NPs synthesized without CNTs, their shape is always spherical. The average size determined by statistical analyses of more than 300 NPs is 12.5±2.4 nm. Some NPs are also formed outside the CNTs and it is worthy of noting that their average size is 9.8±1.7 nm (as described in the 2nd chapter during the synthesis in the absence of CNTs) which attests of the specific conditions of temperature and pressure inside the CNTs channel (particularly the pressure) in agreement with a "confinment effect". X ray diffraction (XRD) pattern (Figure IV-6) displays the characteristic peaks of a spinel iron oxide phase and the peak at 44.8 ° is attributed to the CNTs (002 reflexion of the graphite) . The calculated lattice parameter of these NPs is a = 0.8394 nm, close to that of bulk magnetite (a = 0.8396nm, JCPDS file 19-0629). We may notice that NPs synthesized without CNTs have a lattice parameter of a= 0.8381 Å, value intermediate between those of magnetite and its oxidized form maghemite - Fe_2O_3 (a= 0.8346 nm, JCPDS file 39-1346) confirming that CNTs limit the oxidation of $Fe_{3-x}O_4$ NPs inside the channel.

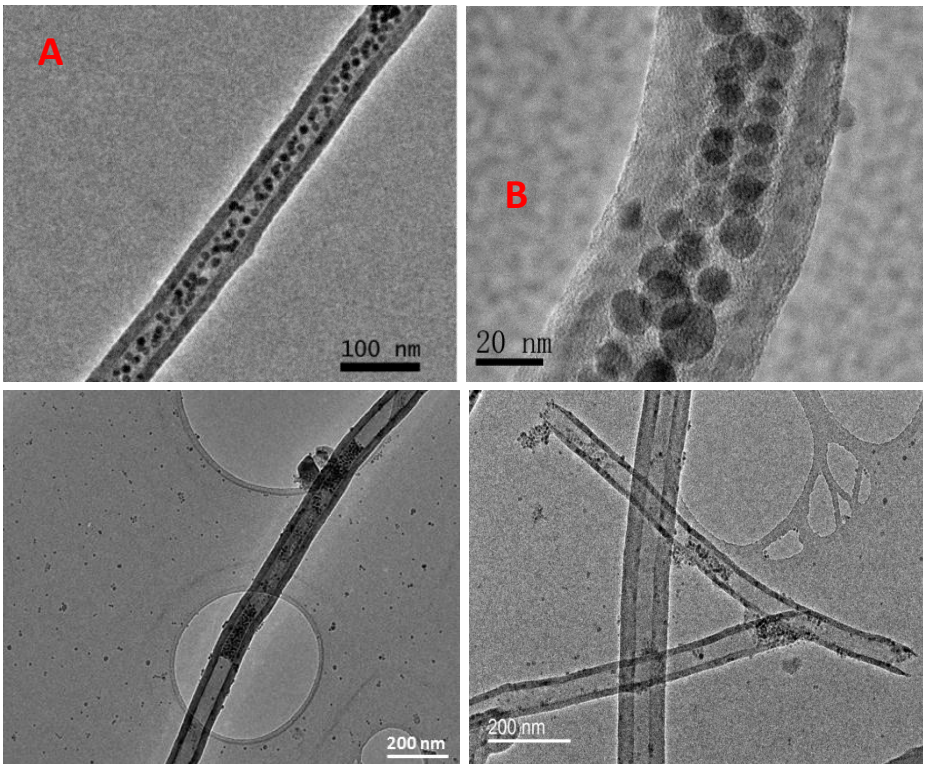

Figure IV.5. TEM images of $Fe_{3-x}O_4$ nanoparticles by using the ligand oleic acid (A-B), Hexadecylamine(C) and Oleylamine (D)**.**

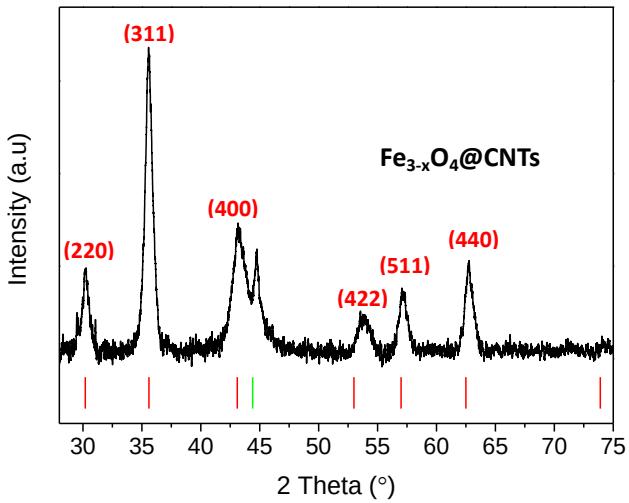

Figure IV.6. XRD pattern of $Fe_{3-x}O_4$@CNTs. Red line: Fe_3O_4 and green line: Graphite-2H as reference.

Hexadecylamine and oleylamine have also been used to replace oleic acid as ligand. In all the cases, the filling is very low as shown in Figure IV-5(C-D). The size of NPs is quite small, very close to that of NPs in the absence of CNTs: it is not so surprising; the confinement effect in this case does not take place. Hence, the results showed that oleic acid can be favorable for the NPs filling.

To appreciate the role of the heat -treatment of the CNTs on the filling level, NPs syntheses have been performed with CNTs just after their washing in the nitric acid media to remove the remaining catalyst. As can be seen in Figure IV.7A, most of the NPs remain on the outer walls of the CNTs, certainly due to strong interactions of the oxygenated groups with the iron stearate, decreasing their diffusion into the channel. Their shape is always spherical, and as expected, their size is close that of NPs synthesized in the absence of CNTs (close to 9 - 10 nm).

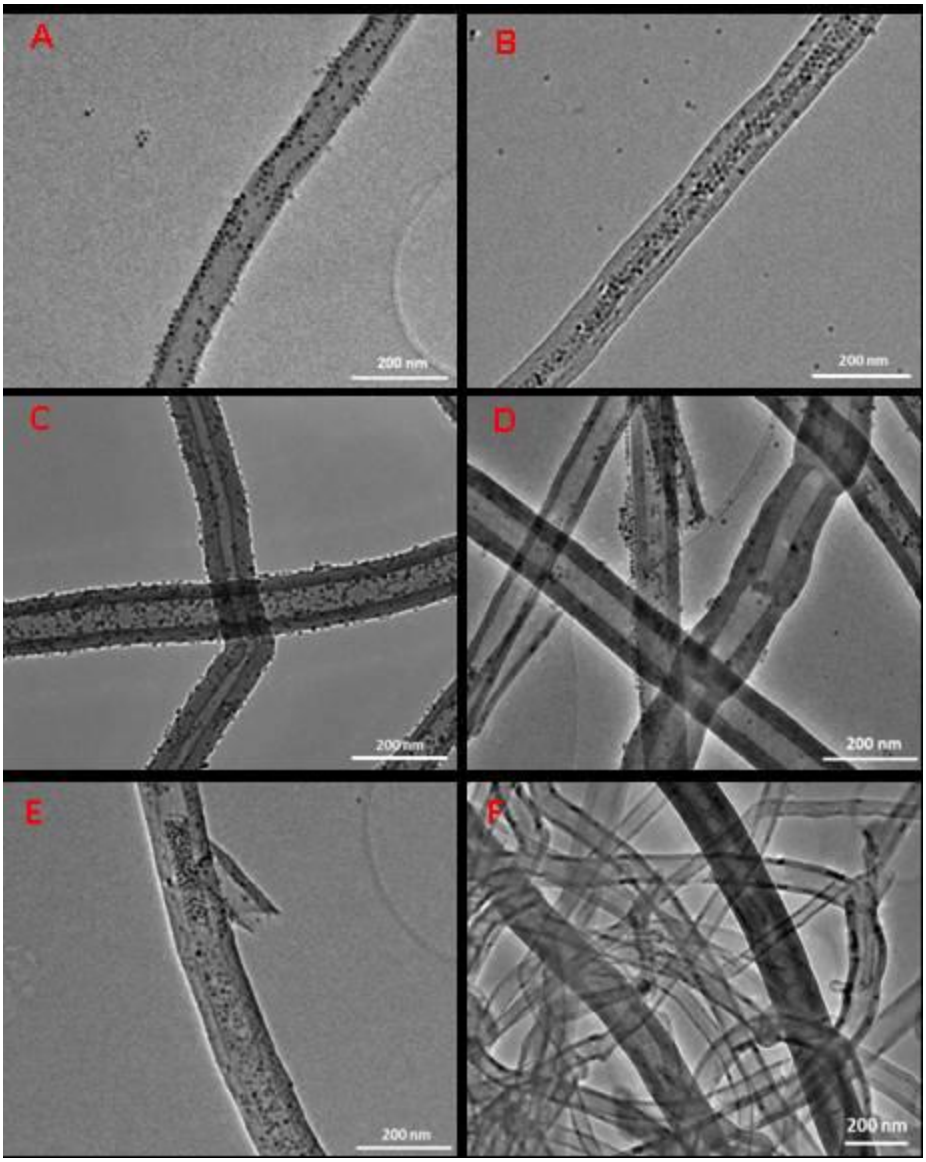

Figure IV.7. TEM images of $Fe_{3-x}O_4$ NPs synthesized in the presence of CNTs under different conditions A) CNTs treated by acid; B) amount of Fe complex increased by 1.5 times; C) under vacuum for 30 mins; D) dioctyl ether used as solvent; E) heating the suspension ay 160 ℃ during 12 h 00 before the thermal decomposition; F) increasing the amount of oleic acid by twice

To vary another parameter, we have increased the concentration of the iron stearate in the initial suspension by a factor 1.5 (CNTs were initially heat treated at 900 ℃ under Ar) : as can be seen in Figure IV 7B, NTCs are filled with a large amount of $Fe_{3-x}O_4$ NPs like un Figure IV-5. In order to facilitate and accelerate the filling of the CNTs during the impregnation process, the experiment has been performed under vacuum to remove the air out of the CNTs. After thermal decomposition, No significant increase has been observed attesting that the capillary force is the factor the most important in this case (Fig IV7 C) : in this case, we can even see many NPs on the surface of the CNTs. In the same approach, the suspension has been heated at 160 ℃ during 12h00 (instead of 100 ℃ during one hour) to decrease the viscosity of the solution: as can be seen in Figure IV-7E, CNTs are well filled, but no significant change has been observed.

We have also tried to increase the amount of oleic acid in the suspension by a factor 2 and three : surprisingly, as can be seen in Figure IV-7F, all the CNTs are empty and no NPs are visible on their outer walls : if the amount of ligands becomes too high the consequence is an increase of the energy barrier for the thermal decomposition of the stearates so that no NPs can be synthesized.

Last we have used another solvent to replace the octadecene by the dioctyl ether which has also a high boiling point and which has already been used for the NPs synthesis : as can be seen in Figure IV - 7D, most of the NTCs are empty, that can be attributed to a lower wettabilty of the CNTs in comparison with octadecene.

IV.2.2.2 CoO NPs inside CNTs

As in the case of $Fe_{3-x}O_4$, cobalt oxide nanoparticles were synthesized into the CNTs channels using three ligands: oleic acid, Hexadecylamine and Oleylamine. With the oleic acid (Figure IV.8A), we can observe that the channel of CNTs is filled with cubic shape of NPs forming like a chain along the CNTs. HRTEM (Figure IV.8B) shows a single nanoparticle which is composed of a number of irregular smaller NPs. The assembly structure of NPs inside CNTs is not even similar to triangular shape of NPs without CNTs in previous chapter. As a result, the confinement of CNTs might favor the self-assembly of NPs. Such aggregation is often mediated by ligands during solvothermal treatment and should be favored by the special pressure and temperature conditions inside CNTs. The XRD pattern (Figure IV.9) indicates the presence of two cobalt based phases: a Co metallic phase (hexagonal structure JCPDS file 89-4308) and a CoO phase (fcc structure JCPDS file 70-2856) confirming that CNTs limited the oxidation of cobalt (no metallic cobalt was obtained in the absence of CNTs. EELS-STEM analyses were also used to appreciate the elemental composition of NPs inside CNTs. In Figure IV.9 is displayed the relatively low oxygen content inside the particle in contrast with cobalt. (ratio C/O = 1/5).

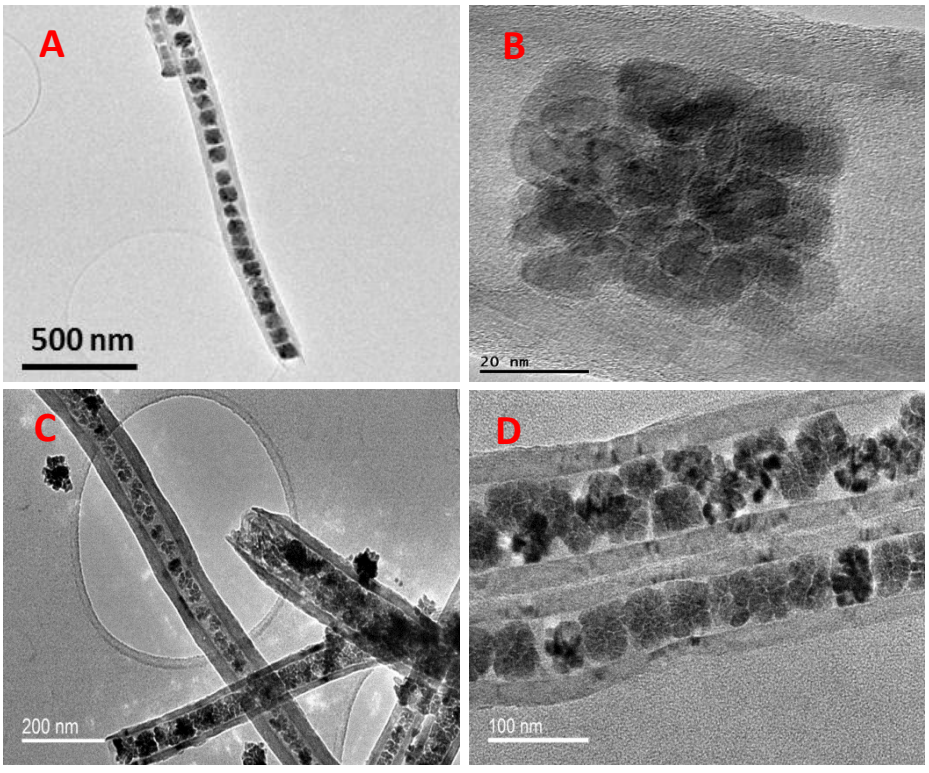

Figure IV.8. TEM images of CoO nanoparticles by using the ligand oleic acid (A-B), Hexadecylamine (C) and Oleylamine (D).

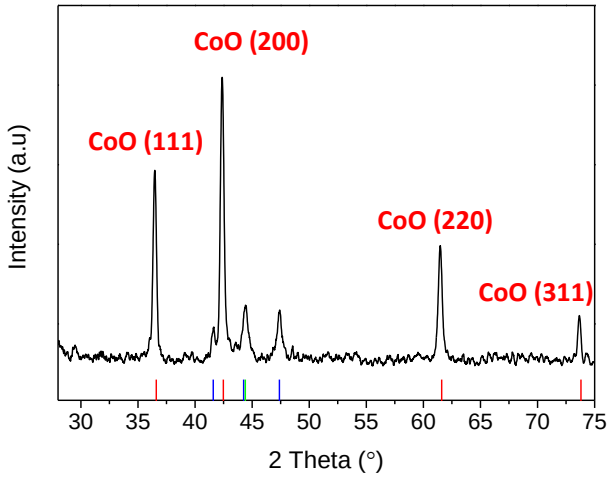

Figure IV.9. XRD pattern of CoO@CNTs with oleic acid. Red line: CoO, blue line:Co and green line: Graphite-2H as reference**.**

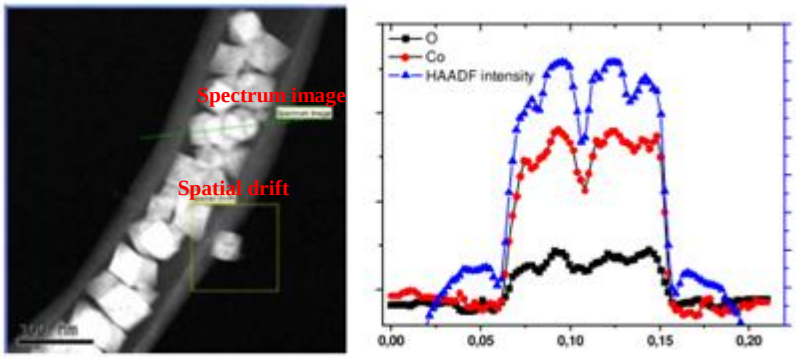

Figure IV.10. EELS-STEM analysis of the cobalt-based particle inside CNT. A: STEM image and green line indicating the scan line; B. EELS spectrum of Oxygen and Cobalt.

One may notice that in the previous chapter, the same synthesis without CNTs leaded to a highly impure product with CoO phase and an unknown phase, which is due to a low decomposition of the Co stearate (the product was too viscous to be suitably washed). The successful synthesis of cobalt-based NPs inside CNTs demonstrates that the formation of cobalt based NPs is favored inside the CNTs channel as already reported by Chen et al.[40] describing the CNTs as nano-reactors.

Hexadecylamine and oleylamine were also used to investigate the effect of ligands on the Cobalt oxide NPs in the presence of CNTs and the corresponding TEM images of both are shown in Figure IV-8C and 8D, respectively. For both amino ligands, the CNTs are highly filled with Co based NPs which have a similar assembled flower-like morphology. In the absence of CNTs (second chapter) Co based NPs synthesized in the same conditions was

under the form of bigger aggregates : in the presence of CNTs, the size of such aggregates is of course controlled by the inner diameter of the tubes.

As previously described in the previous paragraph, several parameters have been changed to optimize the NTCs filling : as in the case of Fe_3O_4, the vacuum or the increase of the temperature preceding the thermal decomposition has no real influence on the NPs formation. We have also replaced the octadecene with the squalane which present a very high boiling point (380 °C): CNTs in this case are also empty (problem of wettability?).

Last some preliminary tests have been performed (with iron and Cobalt stearate) to study the influence of the NTCs inner diameter (from few nm for single walled carbon nanotubes to 10 nm): at this time and in this size range, no composites with NPs inside the channel can have been synthesized.

IV.3 Design of functionalized magnetic carbon nanotubes for biomedical application

IV.3.1 Experimental details

IV.3.1.1 Nanohydrid Synthesis

For the first filling step, CNTs were first dispersed in octadecene under tip sonication. Iron stearate was then added and the solution was heated at 120 °C for 12 hours to dissolve the reactants, to eliminate the traces of water or impurities and to favor the diffusion of metal precursor inside CNTs. Then, the mixtures were heated at 318 °C (heating rate 5 °C/min) under air for 2 h. Finally, the products were washed four times with ethanol and chloroform, then centrifugated, followed by the conventional filtration method to remove NPs formed outside CNTs. After this first filling step, once the mixture was heated and cooled down to room temperature, the same synthesis was repeated again only with CNTs filled with iron oxide NPs without washing steps by adding either iron or cobalt stearate as a precursor. After this second step, the samples are denoted as $Fe_{3-x}O_4$/CoO@CNTs and $Fe_{3-x}O_4$/$Fe_{3-x}O_4$@CNTs, respectively.

IV.3.1.2 Functionalization of Filled CNTs

All reagents and solvents were purchased from different commercial suppliers and used as received.

a) Arylation of empty and filled MWCNTs

To a suspension of CNTs (15 mg) dispersed in *o*-dichlorobenzene (25 mL) using a water bath sonication for 1 min was added a solution of Pht-protected 4-aminomethyl-phenylamine derivative [41](55 mg) in acetonitrile (4 mL). The mixture was sonicated in a water bath for 1 min. Argon was bubbled in the suspension for 15 min. Isoamyl nitrite (100 µL) was added and the mixture was heated at 60 °C for 13 h. A solution of Pht-protected 4-aminomethyl-phenylamine derivative (55 mg) in acetonitrile (4 mL) and isoamyl nitrite (100 µL) were then added at 60 °C and the mixture was further heated at 60 °C for 4 h. After cooling to room temperature, the suspension was filtered over a PTFE membrane (0.1 µm, Omnipore™, Millipore). The solid recovered on the filter was dispersed in methanol (100 mL), sonicated for 1 min in a water bath, and filtered over a PTFE membrane (0.1 µm). This sequence was repeated with DMF, methanol, and dichloromethane. The resulting solid was dried under vacuum. The same procedure was repeated with the filled CNTs.

b) Pht deprotection of functionalized MWCNTs

To a suspension of functionalized CNTs (11 mg) in ethanol (11 mL) hydrazine hydrate (1.1 mL) was added. The dispersion was sonicated in a water bath for 1 min and stirred for 14 h. The suspension was filtered over a PTFE (0.1 µm) membrane. The solid recovered on the filter was dispersed in DMF (100 mL), sonicated for 1 min in a water bath, and filtered over a PTFE membrane (0.1 µm). This sequence was repeated with methanol and dichloromethane. The resulting solid was dried under vacuum. The same procedure was repeated with the filled CNTs. To assess the amount of amine functions on the CNTs, the Kaiser test was performed according to the procedure described before.[1]

IV.3.1.3 Cell Experiments

a) Cell Culture and Exposition to CNT-NPs.

SKOV3 human ovarian carcinoma cells were maintained as monolayer culture in McCoy 5A culture Medium supplemented with 10 % fetal bovine serum, 1% penicillin-streptomycin at 37 °C and 5% of CO_2. Cells were incubated with $Fe_{3-x}O_4$/CoO@CNTs and $Fe_{3-x}O_4$/$Fe_{3-x}O_4$@CNTs in complete McCoy culture medium at concentrations of 5, 10, 20 and 50 µg/mL in different conditions: for 1 or 24 hours without magnet or for 1 hour in the presence of a permanent magnet placed under the culture dish. After three rinsing steps with PBS, cells were observed by optical microscopy or prepared for further experiments.

b) Laser irradiation and thermographic measurements.

To quantify heat generation by $Fe_{3-x}O_4$/CoO@CNTs and $Fe_{3-x}O_4$/$Fe_{3-x}O_4$@CNTs, 50 µL of CNT suspension at concentrations of 200, 500 and 1000 µg/mL were irradiated in ependorf tubes using a 808 nm diode laser featuring a fiber delivery system (BWT) at a light fluence of 1, 2 or 4 W/cm². The temperature of the suspension was monitored using a FLIR SC7000 infrared camera. All the acquisitions were processed by Altair software (FLIR Systems, Inc.). Specific absorption rate (SAR) was deduced following the formula:

$$\mathrm{SAR} = \frac{C_{water} V_S}{m} \frac{dT}{dt}$$

where C_{water} is the volume specific heat capacity of the water (C_{water} = 4185 $J.L^{-1}.K^{-1}$), V_S is the volume of the suspension (V_S = 50 µL), m is the mass of CNTs and dT/dt is the initial temperature gradient.

For cell irradiation, cell monolayers seeded in 12-well plates were labelled with $Fe_{3-x}O_4$/CoO@CNTs at concentrations of 10, 20 and 50 µg/ml for 1hr in the presence of the magnet or for 24 h without magnet. After three washing step with PBS, cells were exposed to the 808 nm diode laser (4 W/cm^2) for 200 s or 500 s.

c) Cell Viability Test.

The cytotoxicity of CNTs labeling and of laser irradiation (IR) treatment was evaluated by AlamarBlue assay that assesses the metabolic activity of cells. After labeling with CNTs and IR treatment, the cells monolayers were cultured overnight in complete medium and then incubated with an AlamarBlue solution (10%, Invitrogen) in culture medium for 2 h,

following the protocol provided by manufacturer. The fluorescence in cell medium due to the reduction of resazurin (oxidized form) to resorufin by cell activity was analyzed with a microplate reader (BMG FluoStar Galaxy), with an excitation wavelength of 550 nm and by collecting the fluorescence at 590 nm. All the experimental points were performed in triplicate. Unlabeled SKOV3 cells were used as controls.

d) Electron Microscopy on Cells

For TEM localization of CNTs, SKOV3 cells were exposed to $Fe_{3-x}O_4$/CoO@CNTs (5 μg/mL) for 6 h at 37 ℃ with a magnetic field parallel or perpendicular to the cell layer. Following the incubation, cells were rinsed three times with PBS and fixed in presence of the magnetic field with 5 % glutaraldehyde in 0.1 mol/L sodium cacodylate buffer. Cell were post fixed with 1 % osmium tetroxide containing 1.5 % potassium cyanoferrate, gradually dehydrated in increasing concentrations of ethanol and embedded in Epon resin. Thin sections (70 nm) of cells parallel to the cell layer were examined with a Zeiss EM 902 transmission electron microscope at 80 kV (platform MIMA2, INRA, Jouy-en-Josas, France). For scanning electron microscopy (SEM), cells were exposed to $Fe_{3-x}O_4$/CoO@CNTs (5 μg/mL) for 1 h (without magnet or with the magnet under the flask (magnetic field perpendicular to the cell layer).

e) Quantification of Cell Mobility and CNT Uptake by Single-cell Magnetophoresis

To quantify the magnetophoretic mobility of labeled cells and the associated CNT load, cells were thoroughly washed after labeling and trypsinized to obtain a dilute suspension. The cell suspension was introduced in a quartz chamber and submitted to a magnet creating a magnetic field B of 150 mT and a uniform field gradient (grad B) of 17 T m^{-1}. The cell motion towards the magnet was recorded by videomicroscopy, as described previously.[42] Under the experimental conditions, the magnetic driving force acting on cells ($M \times$grad B, where M is the cell magnetic moment) is balanced by the viscous force ($3\pi\eta dv$, where d is the cell diameter, v is the cell velocity and η is the medium viscosity). The cell magnetization was thus deduced from the velocity and diameter of each cell. The magnetization and magnetic content of CNTs being calculated from elemental analysis and magnetic measurement, the amount of CNTs per cell could be deduced.

f) Magnetic Stirring Experiment

SKOV3 cells were labelled with $Fe_{3-x}O_4$/CoO@CNTs (5 μg/mL) for 1 h and washed three times with PBS. Immediately after labelling, the adherent cells were exposed to a rotating magnetic field (1 Hz) in the plane parallel to the cell layer and recorded by videomicroscopy. The experimental set up to generate the rotating field under microscope has been described previously. The miniaturized magnetic device consists of two pairs of coils magnetizing two pairs of soft iron assembled perpendicularly and separated by only 0.6 mm. The magnetic field created in the center can be tuned between 0 to 70 mT and rotated in the cell layer plane when the two pairs of coils are supplied with an alternating current 90 ° out of phase.

g) Protocol of the Kaiser Test

Three solutions were prepared separately:
- (I): 10 g of phenol dissolved in 20 mL of absolute ethanol.
- (II): 2 mL of 1 mM aqueous solution of potassium cyanide dissolved in 98 mL of pyridine.
- (IV): 1 g of ninhydrin dissolved in 20 mL of absolute ethanol.

A mass of approximately 200 µg of CNTs was weighted in a haemolysis test tube. 75 µL of solution (I) and 100 µL of solution (II) were successively added to the CNTs. The resulting dispersion was sonicated in a water bath for 5 minutes until disaggregation of the CNTs. Then, 75 µL of solution (IV) was added and the suspension was sonicated again in a water bath for 2 min. After heating at 110 °C for 5 min in a heating block (Bioblock Scientific), the suspension was immediately diluted with 4750 µL of 60% ethanol. After centrifugation at 15000 rpm, the supernatant was analyzed by UV-Vis spectroscopy. The absorbance at 570 nm was correlated to the amount of free amine functions on the nanotube surface (expressed in µmol/g) using the equation:

$$\frac{[\text{Abs } sample - \text{Abs } blank] \text{ x dilution (mL) x } 10^6}{\text{Extinction coefficent x sample weight (mg)}}$$

Dilution is 5 mL and extinction coefficient is 15000 M^{-1} cm^{-1}.
The blank was prepared exactly the same way but without CNTs.
The result is expressed as micromole of amino groups per gram of material.
The Kaiser test was repeated at least three times for each sample to ensure reproducibility.

IV.3.1.4 Characterization Techniques.

The concentrations of iron and cobalt metals in CNTs were determined by using a Spectro ARCOS ICP-AES. The samples were digested by boiling CNT suspensions in concentrated nitric acid (Sigma-Aldrich, trace metal basis grade) for 1 h and the solutions were diluted with filtered ultrapure water for analysis.

MRI Measurements: Magnetic resonance imaging was performed on a Bruker Bio-Spec 47/40 USR Scanner, a 40 cm bore actively shielded 4.7 T scanner equipped with a whole-volume radiofrequency (RF) coil in the Small Animal Imaging Platform Paris-Descartes PARCC-HEGP. The scanner was interfaced to ParaVision software for preclinical MRI research. Agarose gels (0.3%, 630 µL) containing CNTs at different concentrations up to 25 µg/mL were imaged using spin echo sequences with different echo time (T_E) and repetition time (T_R) in order to deduce the longitudinal and transverse relaxation time, T_1 and T_2, of proton magnetization.

IV.3.2 Structural and Magnetic Characterizations of NPs inside CNTs

IV.3.2.1 Filling and structural characterization of CNTs with Iron Oxide and/or Cobalt Based NPs through A Two-Step Process

As discussed in previous chapter, the CNTs were filled with Fe_3O_4 NPs by one-time filling. In order to increase the filling yield and to obtain easily manipulable magnetic CNTs, a second filling step was performed (Scheme IV-1) only with CNTs filled with iron oxide NPs

by inducing the thermal decomposition of either the cobalt or iron stearate precursor. The main objective of this process was to try to block NPs inside the channel of CNTs. It was not possible to increase the filling rate of CNTs with CoO/Co NPs because their large size with respect to the inner diameter of CNTs would not allow introducing additional precursor. Thus, $Fe_{3-x}O_4$@CNTs were dispersed again in the octadecene suspension in the presence of either iron stearate or cobalt stearate precursor and a second thermal decomposition step was performed.

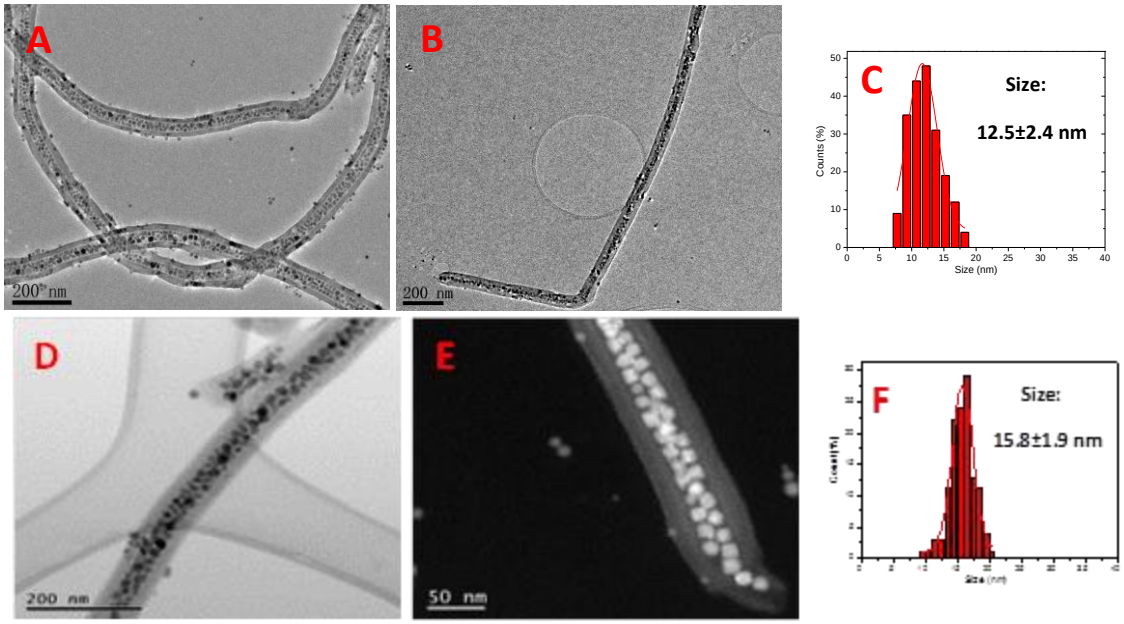

Figure IV.11. Representative TEM micrographs of $Fe_{3-x}O_4/Fe_{3-x}O_4$ NPs (A) and $Fe_{3-x}O_4$/CoO NPs inside CNTs (B). Size distribution of $Fe_{3-x}O_4/Fe_{3-x}O_4$ NPs inside the CNTs (C). Bright-field (D) and Dark-field (E) STEM images of $Fe_{3-x}O_4$/CoO inside CNTs. Size distribution of $Fe_{3-x}O_4$/CoO NPs inside CNTs (F).

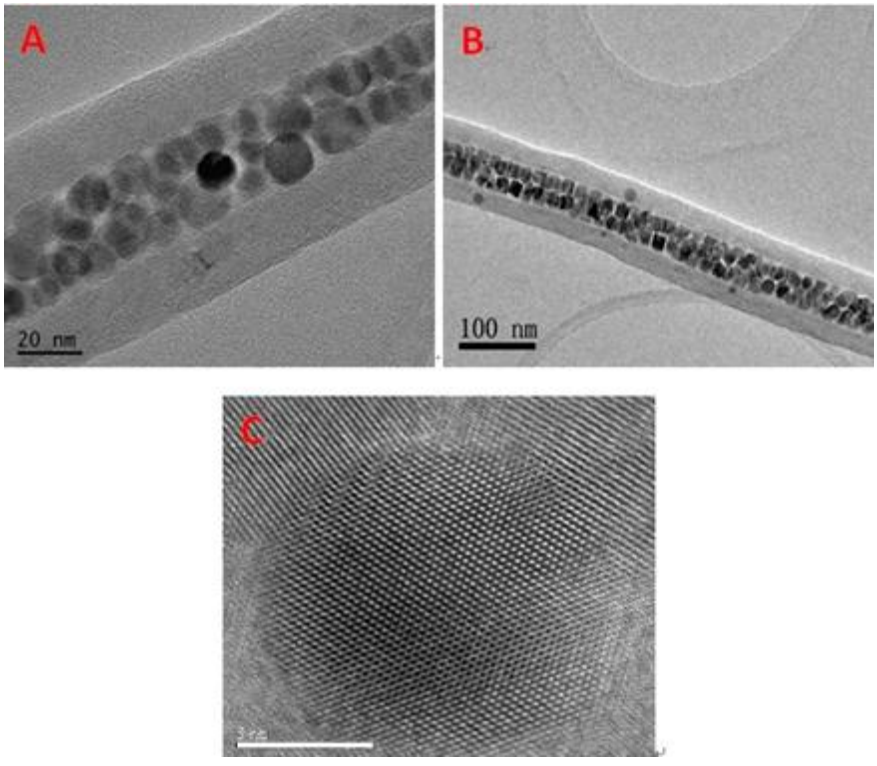

Figure IV.12. HRTEM micrographs of $Fe_{3-x}O_4$/$Fe_{3-x}O_4$@CNTs (A) and $Fe_{3-x}O_4$/CoO@CNTs (B-C).

When iron stearate was used, as can be seen in Figure IV.11A and Figure IV.12A, the filling rate with $Fe_{3-x}O_4$ NPs was increased and TGA experiments showed a weight gain in the range 15 to 20% (Figure IV.13). The iron oxide NPs density inside the channel was thus slightly higher and their size and shape did not change. An average diameter close to 12.5 nm is measured from TEM images (Figure IV. 12A). By contrast, when cobalt stearate was used, we obtained a larger weight gain (Figure IV.11B and Figure IV.12B), up to 50% from TGA (Figure IV.13) but one may take into account a contribution of the oxidation of cobalt based NPs in this weight gain. The chemical analysis showed an iron to cobalt weight ratio of 19:16 (Table IV-1) confirming the filling of $Fe_{3-x}O_4$@CNTs with cobalt. HRTEM image (Figure IV-12C) shows that NPs are well crystallized. Bright-field (Figure IV-11D) and dark-field (Figure IV-11E) STEM images confirmed that the density of NPs inside the channel was very high, and some cubic-shape particles were also observed. The average NPs size is close to 16 nm (Figure IV-11F) when the average iron oxide NPs size before this step was 12.5 nm. The fact that no characteristic cobalt based particles were visible (Figure IV-12C) and that only an increase of the iron oxide based NPs diameter was noticed, strongly suggests the deposition of $Co_{1-x}O$ onto iron oxide NPs.

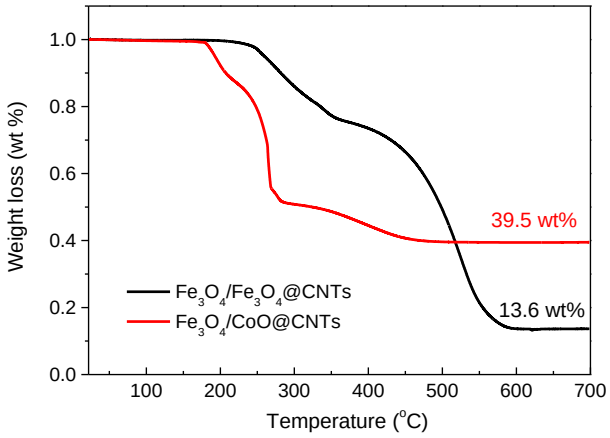

Figure IV.13. TGA of $Fe_{3-x}O_4$/ $Fe_{3-x}O_4$@CNTs and $Fe_{3-x}O_4$/ CoO@CNTs.

	Co wt%	Fe wt%
$Fe_{3-x}O_4$/$Fe_{3-x}O_4$@CNTs	< 0.03	10.4 ± 0.6
$Fe_{3-x}O_4$/CoO@CNTs	16.7 ± 0.6	19.2 ± 0.6

Table IV.1. Co and Fe mass of NPs@CNTs by double filling by IPC-AES.

In order to reveal the distribution of the new formed $Co_{1-x}O$ pahse with regard to the initial $Fe_{3-x}O_4$ NPs, energy-filtered TEM (EFTEM) analyses have been performed on the filled CNTs by the two step process. EFTEM is a powerful analytic technique which can elucidate if after the second filling with Co stearate, new Co based NPs are formed or the CoO phase is

deposited around the preexisted Fe_3O_4 NP by heterogeneous growth leading thus to "core-shell" structures. First, an EELS spectrum was acquired (Figure IV.14) displaying two peaks, which correspond to Fe and Co elements. Elemental maps acquired based on the EELS spectrum characteristics (see Figure IV.15) shows a homogeneous distribution of Fe and Co along all the CNTs. As can be observed in Figure IV.15B, Fe is distributed in well-defined areas proving the presence of $Fe_{3-x}O_4$ NPs synthesized during the first step. The Co map (Figure IV.15C) shows a relatively low signal which is due to the Co peak position in the EELS spectrum. However, it is clear that Co is homogenously distributed around the preexisted Fe_3O_4 NPs. This aspect is better highlight by the RGB composite of the Fe and Co maps presented in Figure IV-15D. As the low signal to noise ratio obtained for the Co elemental map does not allow us to precisely indicate the position of $Co_{1-x}O$ phase with respect to the $Fe_{3-x}O_4$ NPs, we have performed on the same system a STEM-EELS analysis. By scanning on single nanoparticle from one side to another and simultaneously extracting the EELS data the exact position of each element is extracted. The results shows that $Co_{1-x}O$ can either form a homogenous shell around the $Fe_{3-x}O_4$ NPs leading to a core-shell structure (Figure IV.16a) or can create patches, leading to an inhomogeneous coverage around the $Fe_{3-x}O_4$ NPs (Figure IV.16b).

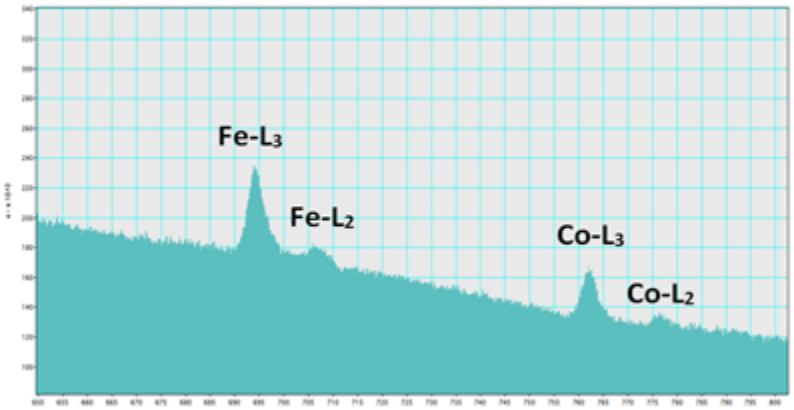

Figure IV.14. EELS spectrum of $Fe_{3-x}O_4$/CoO@CNTs**.**

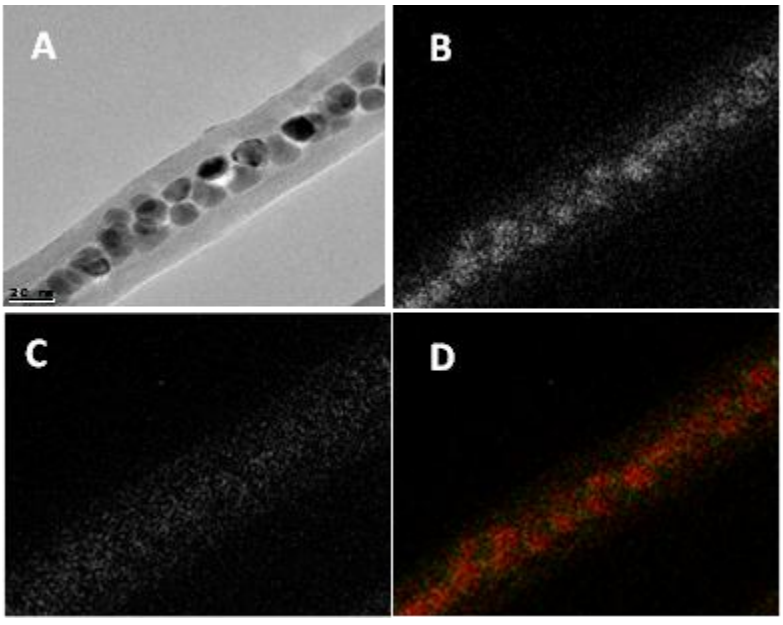

Figure IV.15. (A) TEM image of Fe_3O_4/CoO@CNTs. (B) Elemental map of Fe extracted from region presented in 15A. (C) Elemental map of Co extracted from region presented in 15A. (D) Color composite of the Fe (in red) and Co (in green) maps**.**

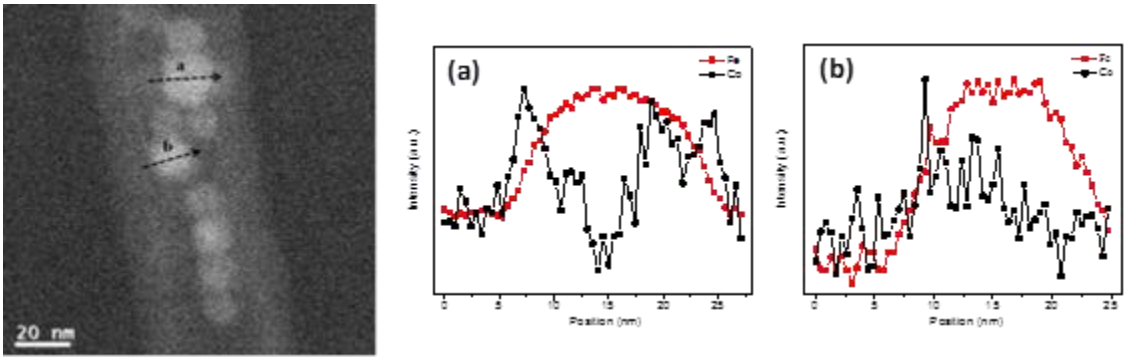

Figure IV.16. (Left) STEM dark-field image of $Fe_{3-x}O_4$/CoO@NPs inside CNTs showing the position of NPs [(a) and (b)] along line a and b: corresponding Fe and Co atoms amounts (%) as a function of the NP section.

XRD patterns displayed the characteristic XRD peaks of iron oxide and/or cobalt based phases (Figure IV-17). In the case of $Fe_{3-x}O_4$/$Fe_{3-x}O_4$@CNTs, all peaks match with a spinel iron oxide phase, while with $Fe_{3-x}O_4$/CoO@CNTs, the peak at 36.6 ° and the enlargement of the peaks at 42.5 ° may be attributed to the presence of CoO. Indeed, no Co metallic phase was identified in $Fe_{3-x}O_4$/CoO@CNTs, which can be because of low amount of metallic Co. The refinement was performed in these samples. For the $Fe_{3-x}O_4$/$Fe_{3-x}O_4$@CNTs, the calculated cell parameter is 8.393 Å, very close to that of the standard bulk magnetite 8.396 Å, confirmation the effective prevention from oxidation by CNTs. The calculated domain size of $Fe_{3-x}O_4$ is around 9 nm, which is slightly smaller than TEM results. For $Fe_{3-x}O_4$/CoO@CNTs, the calculated parameter cell is 8.389 Å. The domain size of $Fe_{3-x}O_4$ is 9 nm.

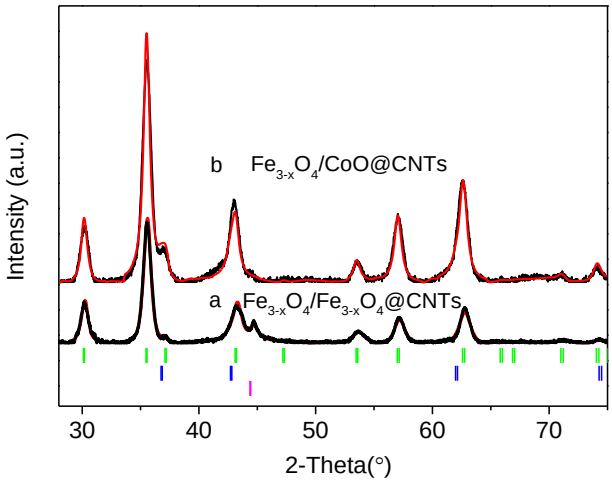

Figure IV.17. XRD recorded data (black) and refined data (red) of $Fe_{3-x}O_4$/$Fe_{3-x}O_4$@CNTs (a) and $Fe_{3-x}O_4$/CoO@CNTs (b). Green vertical bar: Fe_3O_4, blue vertical bar: CoO and pink vertical bar: Graphite-2H as reference.

IV.3.2.2 Magnetic Properties of NPs inside CNTs

Magnetic measurements were then performed to evaluate the composition of core-shell NPs. Indeed if they are constituted of iron oxide NPs coated with CoO ($Fe_{3-x}O_4$@CoO), exchange bias properties should be observed as $Fe_{3-x}O_4$ and CoO phases are ferrimagnetic and antiferromagnetic, respectively. Hysteresis loop measurements (Figure IV-18a) displayed at first their superparamagnetic behavior at 400 K. Exchange coupling at the FM/AFM interface of $Fe_{3-x}O_4$/CoO@CNTs was investigated by Field Cold (FC) measurements (magnetic measurements after cooling down magnetic CNTs under an applied magnetic field). In Figure IV-18b, only a slight horizontal shift of FC hysteresis loop can be observed, with respect to the ZFC hysteresis loop of $Fe_{3-x}O_4$/CoO@CNTs, indicating a weak exchange bias (H_E=355 Oe). Indeed, very large exchange fields (higher than 10000 Oe) are generally observed in $Fe_{3-x}O_4$@CoO core-shell NPs.[43] Hence, we can conclude that there is not a large population of uncompensated spins in a ferrimagnetic (FM)-$Fe_{3-x}O_4$/antiferromagnetic (AFM)-CoO interface. However, a large coercivity Hc (Hc=8250 Oe) of $Fe_{3-x}O_4$/CoO@CNTs was observed in comparison to the small value of H_E [44] and furthermore it was substantially larger than that of $Fe_{3-x}O_4$/$Fe_{3-x}O_4$@CNTs (Hc=330 Oe). Considering all these results and our recent results on the magnetic properties of core-shell $Fe_{3-x}O_4$@CoO NPs displaying different CoO shell thickness (to be published), this drastic enhancement of coercive field can only be explained by the formation of cobalt ferrite (that is known to display a large magnetocrystalline anisotropy) inside CNTs either as a fine layer at the surface of iron oxide NPs or as cobalt ferrite NPs. The NPs size increase and TEM analyses suggest the formation of a fine layer of cobalt ferrite at the iron oxide NP surface. This can be due either to the simultaneous decomposition of cobalt stearate and residual iron stearate (as the products are not purified before performing the second filling step) or to the Co diffusion into the first surface atomic layer of $Fe_{3-x}O_4$ NPs.[45,46] The identification of CoO by XRD suggests also that a fine layer of CoO is present and thus that some $Fe_{3-x}O_4$@Co_yFe_{2-y}O4@CoO core shell NPs were formed in the samples.

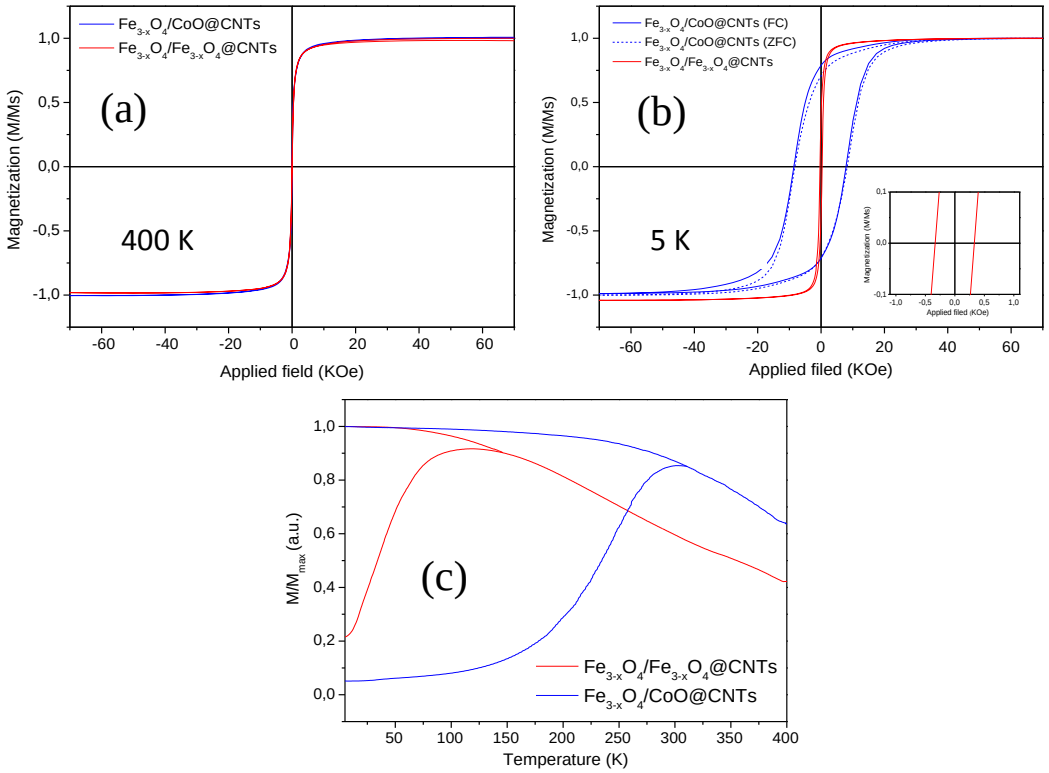

Figure IV.18. (a) Magnetization curves of $Fe_{3-x}O_4$/CoO@CNTs and $Fe_{3-x}O_4$/$Fe_{3-x}O_4$@CNTs at 400K and (b) before (ZFC) and after (FC) cooling from 400 K to 5 K under magnetic field and $Fe_{3-x}O_4$/$Fe_{3-x}O_4$@CNTs at 5K (Inset: enlargement of curve of $Fe_{3-x}O_4$/$Fe_{3-x}O_4$@CNTs). (c) Magnetization versus temperature (ZFC -blue - and FC - red - curves) of $Fe_{3-x}O_4$/CoO@CNTs and $Fe_{3-x}O_4$/ $Fe_{3-x}O_4$@CNTs.

The slightly smaller saturation magnetization at 5K of $Fe_{3-x}O_4$/CoO@CNTs (75 emu/g), in comparison with that of $Fe_{3-x}O_4$/$Fe_{3-x}O_4$@CNTs (81 emu/g) could be attributed to the non-magnetic contribution of the antiferromagnetic CoO phase. One may notice that the saturation magnetization value of $Fe_{3-x}O_4$/$Fe_{3-x}O_4$@CNTs is higher than that of NPs of similar sizes which were synthesized in the absence of CNTs (~ 60 emu/g).[47,48] Magnetization measurements as a function of temperature are also shown in Figure IV.18c. The ZFC maximum, often attributed to the blocking temperature T_B, is at 305K and 119K for $Fe_{3-x}O_4$/CoO@CNTs and $Fe_{3-x}O_4$/$Fe_{3-x}O_4$@CNTs respectively. The ZFC curve of $Fe_{3-x}O_4$/$Fe_{3-x}O_4$@CNTs is quite broad suggesting a distribution of blocking temperatures and/or of the distribution of strength of dipolar interactions as long as they induce a shift of the blocking temperature. The high ZFC maximum for $Fe_{3-x}O_4$/CoO@CNTs is in agreement with the presence of the anisotropic cobalt ferrite phase.[49] Thus, these filled CNTs display suitable magnetic properties to be manipulated by an external field. This was further confirmed by applying an external magnetic field on a suspension of magnetic CNTs (Figure IV.19). After 10 min, the sample was attracted towards the wall of the vial.

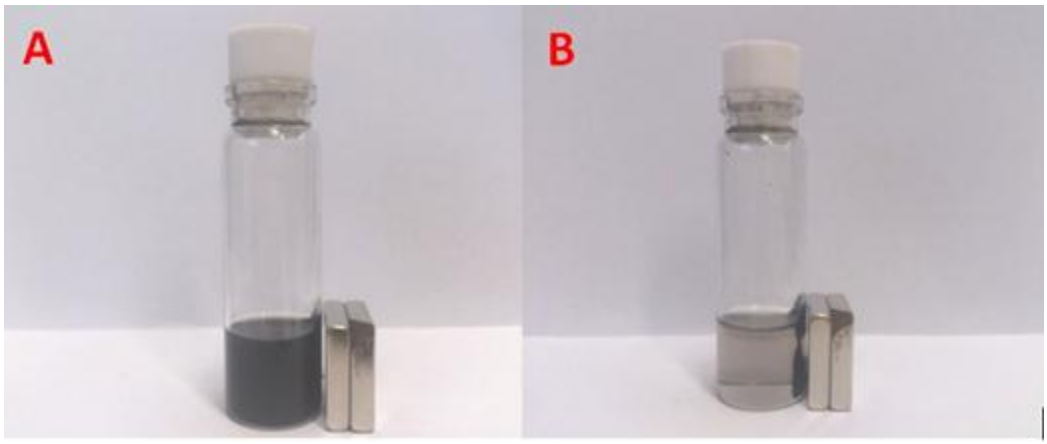

Figure IV.19. Optical photos after ultrasonication (A: 0 min) and after contacting with an external magnet for 10 mins (B) Sample: $Fe_{3-x}O_4$/CoO@CNTs.

IV.3.3 Functionalization of Magnetic CNTs

As the CNTs have been heat-treated to remove oxygenated groups prior to the formation of the NPs, they are not dispersible in water (Figure IV.20). Hence, we functionalized the filled CNTs by arylation to introduce amino groups on the nanotube sidewall. The reaction was first tested on the non-filled MWCNTs (Figure IV.21). For this purpose, the CNTs were reacted with diazonium salts generated in situ by reaction of a Pht-protected 4-aminomethyl-phenylamine derivative and isoamyl nitrite.[50,51] The Pht group was then removed in the presence of hydrazine. UV/Vis spectroscopy was used to assess the amount of amine functions by the Kaiser test.[52,53] The level of functionalization was 67 µmol NH_2 per gram of CNTs. As the diameter and the number of layers is high, the loading values are relatively low compared to the functionalization of thinner MWCNTs. However, the amount of amino groups was sufficient to impart water dispersibility. The functionalized CNTs were characterized by TGA under inert atmosphere (Figure IV-22). As expected, the pristine CNTs were stable up to high temperature and no significant weight loss was observed. In the case of Pht-functionalized CNTs, the weight loss observed corresponds to the amount of functional groups introduced on the nanotube surface that are thermally labile. The main weight loss takes place at 450 °C, while the Pht-protected 4-aminomethyl-phenylamine derivative is thermally degraded at a lower temperature (350 °C) (data not shown). These results confirm that covalent functionalization of the CNTs occurred. The so NH_2-functionalized CNTs were used as control for *in vitro* cell experiments (*vide infra*). The arylation reaction was then tested on the filled CNTs to increase their water dispersibility. The level of functionalization was 16 and 14 µmol NH_2 per gram of $Fe_{3-x}O_4$/CoO@CNTs and $Fe_{3-x}O_4$/$Fe_{3-x}O_4$@CNTs, respectively. The presence of amino groups allowed dispersing the filled CNTs in water (Figure IV.20). Compared to the functionalization of pristine CNTs, the loading values are inferior as the relative amount of amino groups per gram of CNT material is lower due to the presence of NPs inside the nanotubes. The water-dispersible filled CNTs were observed by TEM to check that the functionalization process did not induce any release of NPs. In addition, diameter and length of the tubes were not affected by the functionalization.

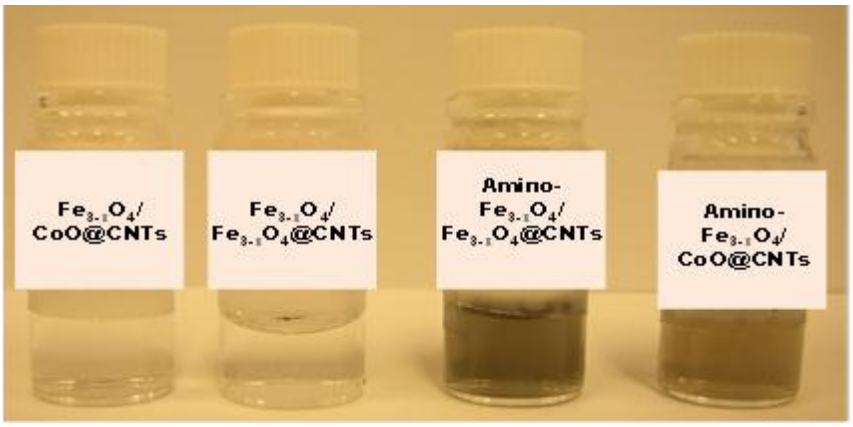

Figure IV.20. Images of dispersions of $Fe_{3-x}O_4$/CoO@CNTs and $Fe_{3-x}O_4$/$Fe_{3-x}O_4$@CNTs before and after functionalization with amino groups.

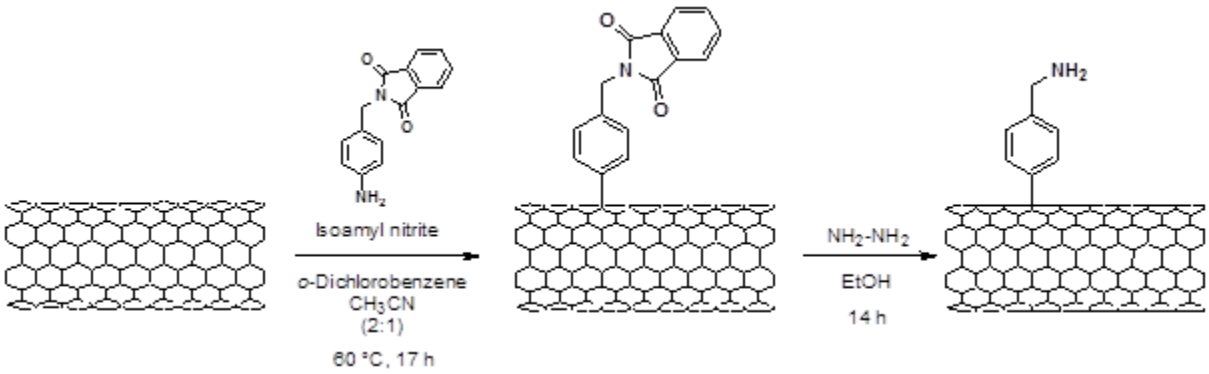

Figure IV.21. Functionalization of CNTs by arylation and subsequent Pht deprotection. For simplicity only one functional group per tube is shown.

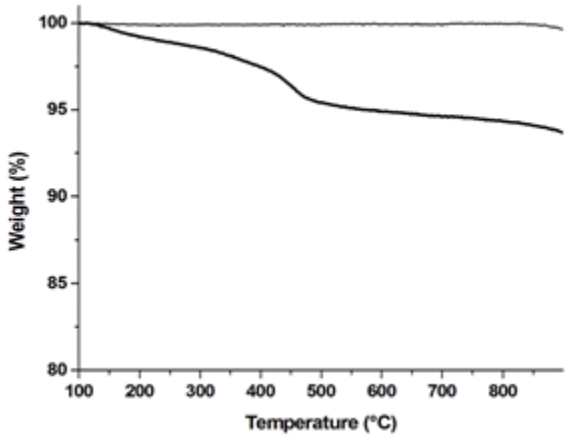

Figure IV.22. TGA of pristine MWCNTs and functionalized MWCNTs before Pht deprotection under N_2 atmosphere.

IV.4 Biomedical Potential of Functionalized Magnetic CNTs

IV.4.1 Photothermal Ablation and Contrast Agent for MRI

In order to demonstrate the biomedical potential of the water dispersible magnetic CNTs, we first evaluated their properties as heat mediator for photothermal ablation and as contrast agent for MRI, which are key features to combine monitoring and efficient treatment. We evaluated the heating efficiency of magnetically-loaded CNTs in comparison to the non-magnetic precursor CNTs. A 50 µL water suspension of CNTs (200 to 1000 µg/mL) was irradiated using a fiber optic laser device operating at the NIR wavelength of 808 nm. Soon after laser irradiation, the nanotube suspension started to heat and attained boiling temperature in less than one minute (Figure IV.23a) at a fluence of 4W/cm^2. In the same conditions of laser irradiation, CNTs-free water show a temperature increase of less than one degree. The nanotube heating capacity was evaluated at different CNT concentrations and radiant exposures (Figure IV.23b). When normalized to the laser fluence, the specific absorption rate (SAR) of CNTs, expressed in Watt per mass of materials, was maximum at 1W/cm^2 and CNTs concentration of 200 µg/mL (Table IV.2). Actually, with higher concentrations of CNTs, the light was strongly absorbed and did not penetrate the whole sample volume, therefore diminishing the overall relative heating efficiency. Comparatively, $Fe_{3-x}O_4$/$Fe_{3-x}O_4$@CNTs were more efficient heaters than $Fe_{3-x}O_4$/CoO@CNTs (Table IV.2). If we assume that the carbon backbone show better energy transduction in comparison to the magnetic particles, the lower magnetic content and higher carbon amount per gram of materials in $Fe_{3-x}O_4$/ $Fe_{3-x}O_4$@CNTs could explain their greater SAR. The later explanation is also in line with the slightly higher SAR of precursor nanotubes.

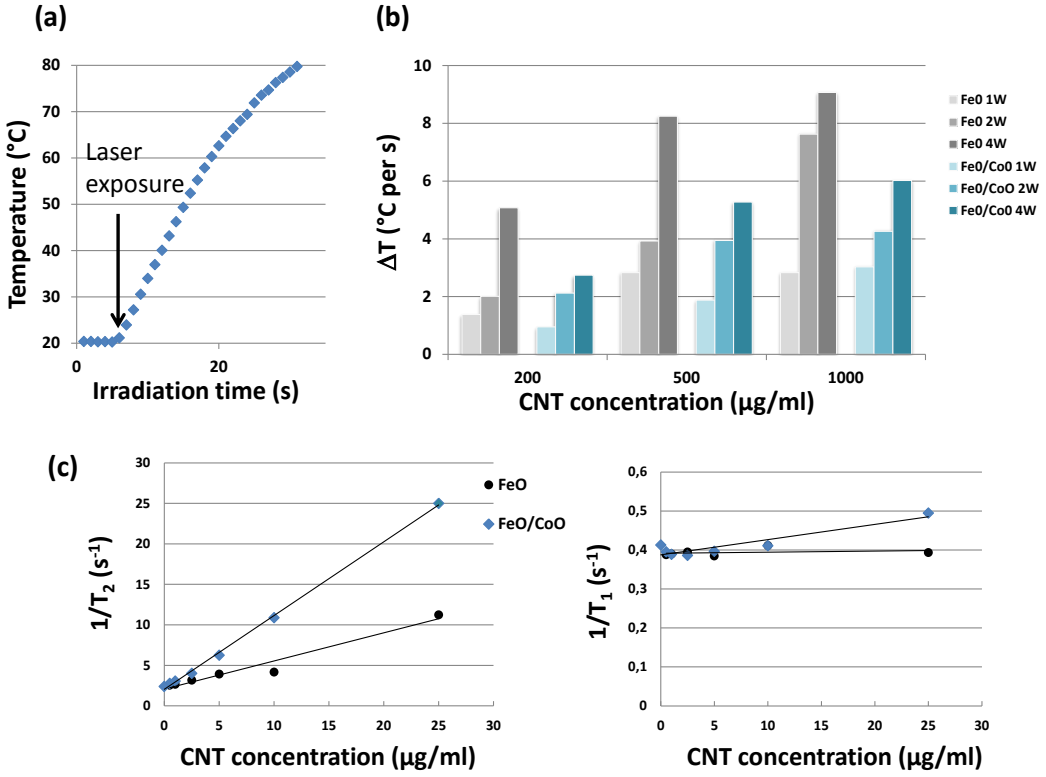

Figure IV.23. (a) Example of heating profile in a 50 µL water suspension of $Fe_{3-x}O_4$/CoO@CNTs (200 µg/mL) exposed to a 808 nm laser at a fluence of 4 W/cm^2. (b) Heating rate (in degree Celsius per second) of $Fe_{3-x}O_4$/CoO@CNTs and $Fe_{3-x}O_4$/ $Fe_{3-x}O_4$@CNTs (50 µL) as a function of CNT concentration and NIR fluence (1, 2 and 4 W/cm^2). (c) MRI

contrast properties of $Fe_{3-x}O_4$/CoO@CNTs and $Fe_{3-x}O_4$/$Fe_{3-x}O_4$@CNTs: the longitudinal and transverse relaxation rates of proton magnetization, $1/T_1$ and $1/T_2$, measured at 4.7 T (200 MHz) show a linear dependence with CNT concentration. The slope of the linear dependence represents the relaxivity r_1 and r_2.

While the encapsulated magnetic materials minimally affect the excellent photothermal properties of CNTs, it confers outstanding contrast properties for MRI detection. In order to determine their MRI relaxivities, CNTs were dispersed in agarose gels at seven different concentrations (from 0.2 µg/ml to 25 µg/ml) and imaged on the 4.7T MRI scanner. The spin-lattice (T1) relaxation time as well as the spin-spin (T2) transversal relaxation time were deduced from signal measurement at different repetition and echo times using spin echo sequences. The relaxation rates, 1/T1 and 1/T2 respectively, vary linearly with CNT concentrations (Figure IV.23c), allowing to define the concentration independent relaxivity r_1 and r_2 related to iron or to CNT concentrations (Table IV.2). It is worthy to note the very high values of the ratio r_2/r_1 which place both types of magnetic carbon nanotubes as excellent T2 contrast agent. The confinement of magnetic nanoparticles into the unidirectional hollow architecture of CNTs is favorable, on one part, to the reduction of longitudinal relaxivity due to diminished access of water proton to the magnetic centers, and, on the other part, to the enhancement of transverse relaxivity which arise from assembling nanoparticles in a small confined volume.[54,55,56] In addition, one dimentional cooperative assembly of iron oxide NPs was shown to enhance spin-spin relaxation of water molecules.[57] Here, the *in situ* growth of magnetic NPs, which mostly takes place into the cylindrical cavity of the tube, allows enhancing the magnetization and subsequently increasing the transverse relaxivity in comparison to previously reported CNTs decorated with magnetic particles on their outer layer.[58,59] Interestingly, related to CNT concentration, $Fe_{3-x}O_4$/CoO@CNTs are more efficient T_2 contrast agent than $Fe_{3-x}O_4$/$Fe_{3-x}O_4$@CNTs in line with their higher magnetic content (Table IV.2). Moreover, the greater confinement of nanoparticles into $Fe_{3-x}O_4$/CoO@CNTs results in lower r_1 and higher r_2 in comparison to $Fe_{3-x}O_4$/ $Fe_{3-x}O_4$@CNTs. On the basis of iron concentration, $Fe_{3-x}O_4$/ $Fe_{3-x}O_4$@CNTs show however much higher r_2 value than commercial iron oxide NPs and comparable value with polymer-embedded clusters of nanoparticles, 3D iron oxide cooperative nanoflowers or 1D iron oxide nanoworms.[60,61,62] Combined with the water dispersibility and the possibility to further functionalize the external layer of nanotubes, our system provide the first example of highly anisotropic magnetic structures with micrometric length and large aspect ratio (>20) that are evaluated for MRI.

Table IV.2: Iron and cobalt mass fraction, specific absorption rate under 808 nm NIR radiant exposure of 1 W/cm^2 and MRI relaxivities measured at 4.7 T.

	$Fe_{3-x}O_4$/CoO@CNTs	$Fe_{3-x}O_4$/ $Fe_{3-x}O_4$@CNTs	CNTs
Iron content (in mass)	39,70%	6,64%	0%
Cobalt content (in mass)	5,85%	0%	0%
SAR (W/g)			
CNT (200 µg/mL)	19855	28842	33649
CNT (500 µg/mL)	15717	23660	21067
CNT (1000 µg/mL)	12665	11830	14964
Relaxivity related to iron concentration (mM)			
r_1 ($s^{-1}mM^{-1}$)	0.55	2	
r_2 ($s^{-1}mM^{-1}$)	128	286	
Relaxivity related to the concentration of materials			
r_1 (s^{-1}(µg/ml)$^{-1}$)	0.004	0.024	
r_2 (s^{-1}(µg/ml)$^{-1}$)	0.9	0.34	
r_2/r_1	232	143	

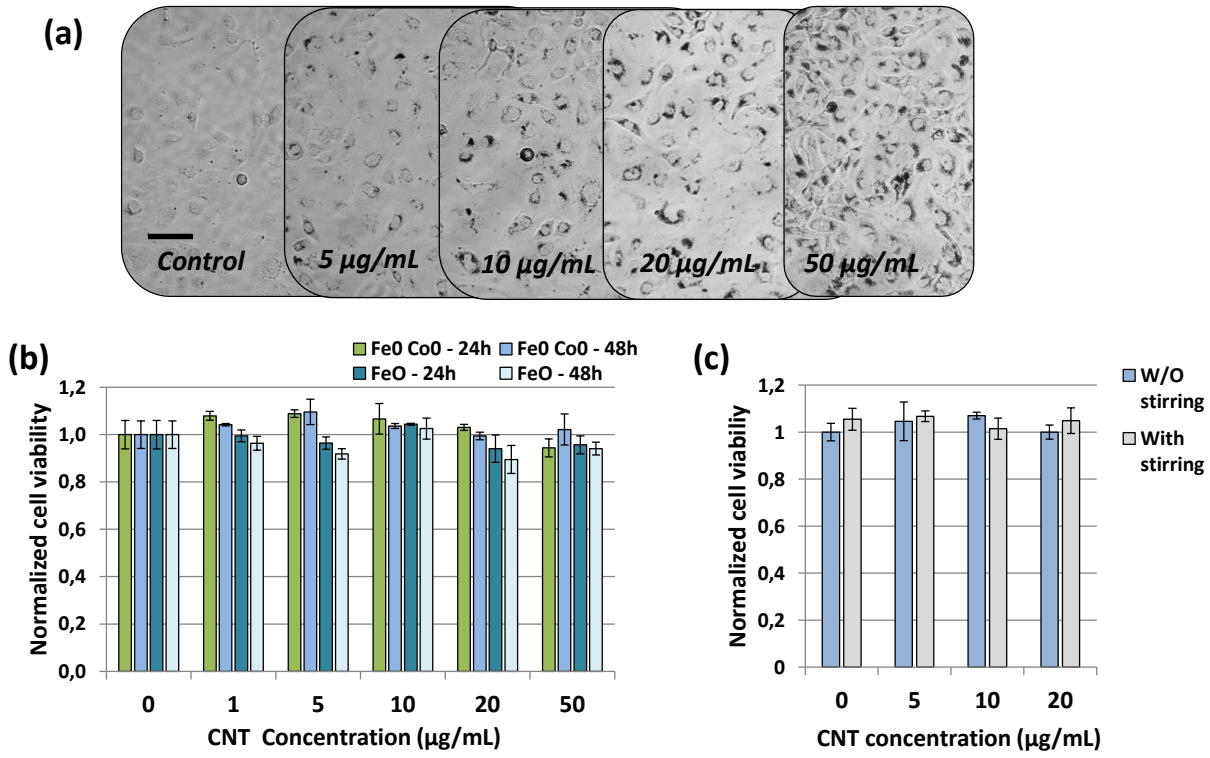

Figure IV.24. (a) Optical micrographs of SKOV3 cells after 24 h incubation with $Fe_{3-x}O_4$/CoO@CNTs at different concentrations. Scale bar = 50 µm. (b) Metabolic activity of SKOV3 ovarian carcinoma cells incubated for 24 h with $Fe_{3-x}O_4$/CoO@CNTs and $Fe_{3-x}O_4$/ $Fe_{3-x}O_4$@CNTs at concentrations of 0, 1, 5, 10, 20 and 50 µg/mL normalized to that of control non-exposed cells. Metabolic activity was measured at 24 h and 48 h after the start of incubation. (c) Metabolic activity of SKOV3 ovarian carcinoma cells incubated for 30 minutes with $Fe_{3-x}O_4$/CoO@CNTs and exposed (or non-exposed) to 30 min magnetic stirring at 1Hz. Metabolic activity was measured at 24h after treatment.

IV.4.2 CNTs in Contact with Cell

Encouraged by the high performance of CNTs for MRI and photothermal ablation, the next step was to assess their behavior on contact with cells. The magnetic CNTs were incubated with SKOV3 ovarian cancer cells. In order to assess the innocuousness of $Fe_{3-x}O_4$/CoO@CNTs and $Fe_{3-x}O_4$/ $Fe_{3-x}O_4$@CNTs, cells were incubated with those nanohybrids for 48 h up to concentration of 50 µg/mL. The cell aspect (Figure IV.24a) and metabolic activity measured by the Alamar Blue test at 24 h and 48 h after treatment (Figure IV.24b) were identical to the control non exposed cells regardless of the concentration of CNTs.

We then evaluated how magnetic fields can modulate the nanotube/cell interactions. As illustrated in Figure IV.25, the cellular uptake of CNTs consists in two phases: the early interaction with the plasma membrane which is clearly seen in SEM pictures of Figure IV.25a (30 min incubation) followed by internalization of CNTs from the plasma membrane into membrane-bound intracellular vesicles (90 min incubation, Figure IV.25b-c). Remarkably the application of a magnetic field parallel or perpendicular to the cell monolayer during the uptake process has the potential to direct nanotube orientation and further enhance cell internalization. As seen in Figure IV.25b, the vesicles containing CNTs attract each other and form bundles oriented along the field direction parallel to the cell layer. Conversely, when the magnetic field is applied perpendicularly to the cell layer, the CNTs stand perpendicularly as well and we observe transverse slices of the carbon backbone with membrane around and NPs inside (Figure IV.25c).

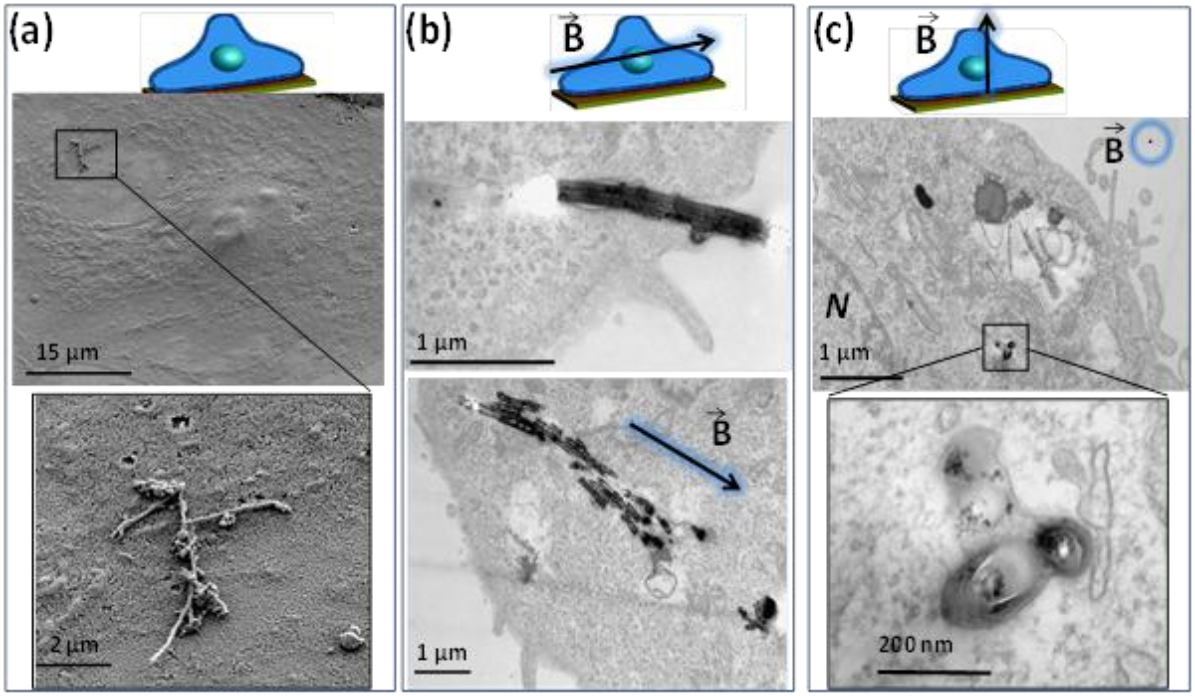

Figure IV.25. Magnetic control of CNT positioning to direct oriented cell uptake. (a) SKOV3 tumor cells were incubated with $Fe_{3-x}O_4$/CoO@CNTs (5 µg/ml) for 30 min without magnetic field. SEM observation reveals the early adsorption of CNTs on the plasma membrane. (b-c) Alternatively, the incubation with CNTs was carried out in presence of a magnetic field either parallel (b) or perpendicular (c) to the cell monolayer, for 90 min. Cells were fixed in

presence of the field and processed for TEM (TEM slice parallel to the cell layer). Electron micrographs show the CNTs within intracellular membrane compartments that are aligned in the direction of the applied field, either parallel (b) or perpendicular to the cell layer (c). CNTs penetrate the cell perpendicularly to the cell layer in presence of a perpendicular field. Note the presence of membranes all around internalized CNTs.

The magnetic responsivity of CNTs also allows their dynamical activation on the cell membrane. After short incubation with cells (30 min) the CNTs were shown to rotate on cell membrane when exposed to a rotating magnetic field in the plane of the monolayer. Indeed videomicroscopy of cells shows several black bundles rotating at the 1 Hz frequency of the applied field (Figure IV.26). Note that the phase lag of CNT orientation with respect to the applied field could vary depending on CNT anchorage on the cell membrane. Remarkably, no deleterious effect was observed on cells even after 30 min magneto-stirring: the cells kept their initial shape and aspect and were still able to divide following magnetic stimulation. Their metabolic activity assessed 24 h after magnetic stirring was identical for treated and non-treated cells regardless of CNT concentrations (Figure IV.24c). These observations contrast with previous experiments showing cell lysis induced by the rotation of large bundles of MWCNTs on the surface of cells.[63] In latter study, the magnetic response of nanotubes relied on the iron/nickel catalyst impurities that they contained and the rotating large aggregates of CNTs could impact the integrity of cell membrane. In our study, CNT functionalization, high water dispersibility, controlled magnetic content and magnetically-directed orientation allows a spatial and temporal control of their interaction with cells, without affecting cell viability.

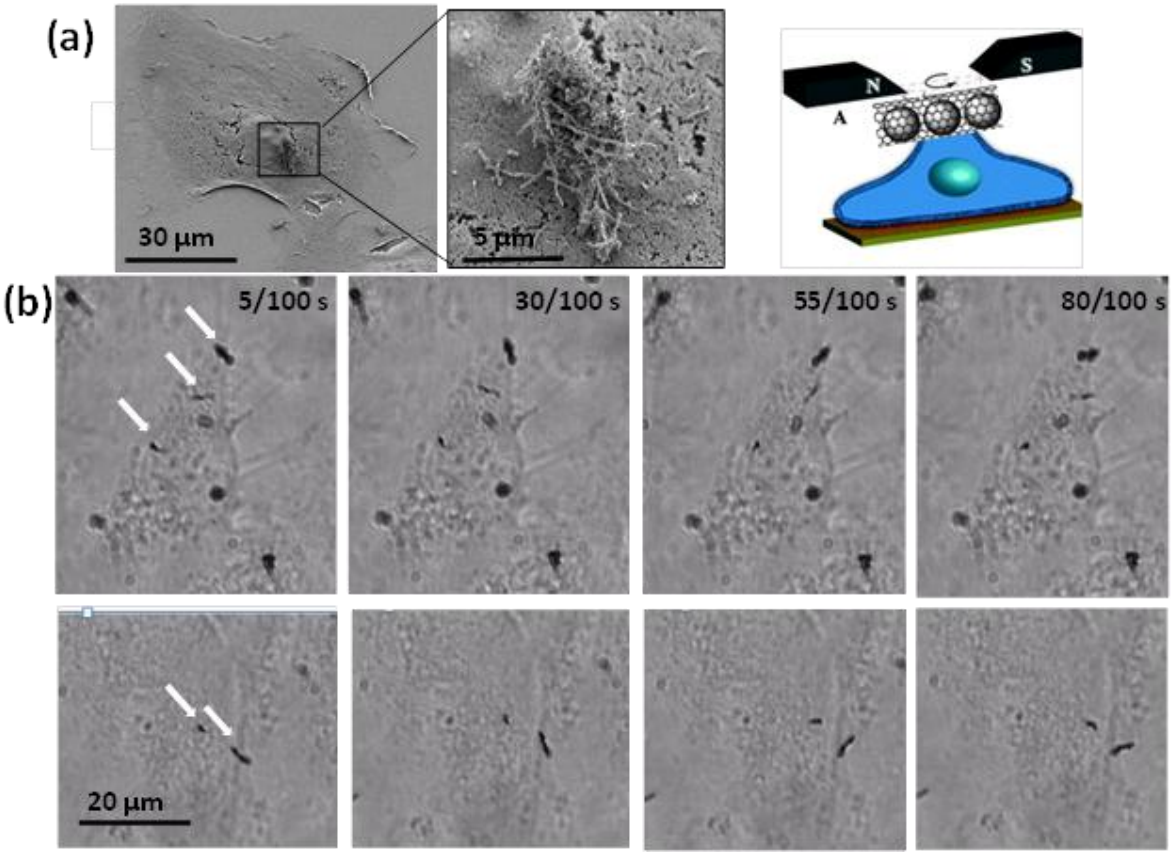

Figure IV.26. Magnetic stirring of CNTs on tumor cells. SKOV3 tumor cells were incubated with $Fe_{3-x}O_4$/CoO@CNTs (5 µg/ml) for 30 min. (a) SEM micrographs shows the nanotubes at the surface of the cells. (b) Cells were then submitted to a rotating magnetic field at a frequency of 1 Hz and videotaped. Pictures show the same cells at time intervals of 25/100 s. White arrows point out rotating CNTs on the cell surface.

IV.4.3 Metabolic Activity and Magnetophoretic Mobility Test

In addition, cellular uptake in single cells could be quantified thanks to the magnetic properties of the CNTs. As illustrated in Figure IV.27a, a labelled cell can be attracted by a magnet and its individual magnetophoretic mobility is proportional to the mass of CNT uptake. Indeed, using single cell magnetophoresis set up, the magnetic force on cells (proportional to the calibrated magnetic field gradient and to the magnetization of the cell) simply balance the viscous force (proportional to the cell diameter, cell velocity and to the viscosity of the carrier fluid), when the permanent regime is attained. Hence the cell-by-cell measurements of velocity and diameter provide the whole distribution of magnetic nanotube uptake, knowing the magnetization of nanotubes. In comparison to cells incubated with $Fe_{3-x}O_4$/ $Fe_{3-x}O_4$@CNTs, the cell labelled with $Fe_{3-x}O_4$/CoO@CNTs showed more than 3-fold higher magnetic mobility, which is consistent with the higher iron content and magnetization of those nanohybrid (Figure IV.27b). When expressed as mass of nanotube, however, cellular uptake was higher for $Fe_{3-x}O_4$/$Fe_{3-x}O_4$@CNTs (Figure IV.27d). For both nanohybrids, the cell load increased with increasing CNT concentrations during incubation. We also investigated the influence on cell uptake of 30 min magnetic stirring after 30 min incubation with $Fe_{3-x}O_4$/CoO@CNTs (Figure IV.27c). Interestingly, CNT uptake tends to be increased by magnetic stirring. To assess the effect of a perpendicular magnetic force on cell uptake (the so-called magnetofection effect), cells were also incubated for one hour, with or without magnet placed under the culture flask (Figure IV.27d). Interestingly, the presence of the magnet significantly increased cellular uptake, which can be explained by an enhanced accumulation of $Fe_{3-x}O_4$/CoO@CNTs on cell membrane due to the magnetic driving force and putatively to its normal orientation with respect to the cell basement. Further increase of incubation time up to 24 h (without the magnet) did not significantly increase CNT uptake in comparison to the 1 h magnet condition. Therefore, we can conclude that magnetically-assisted targeting of cancer cells by $Fe_{3-x}O_4$/CoO@CNTs allows fast and efficient uptake that could reach 64 pg CNTs/cell in one hour while preserving cell viability.

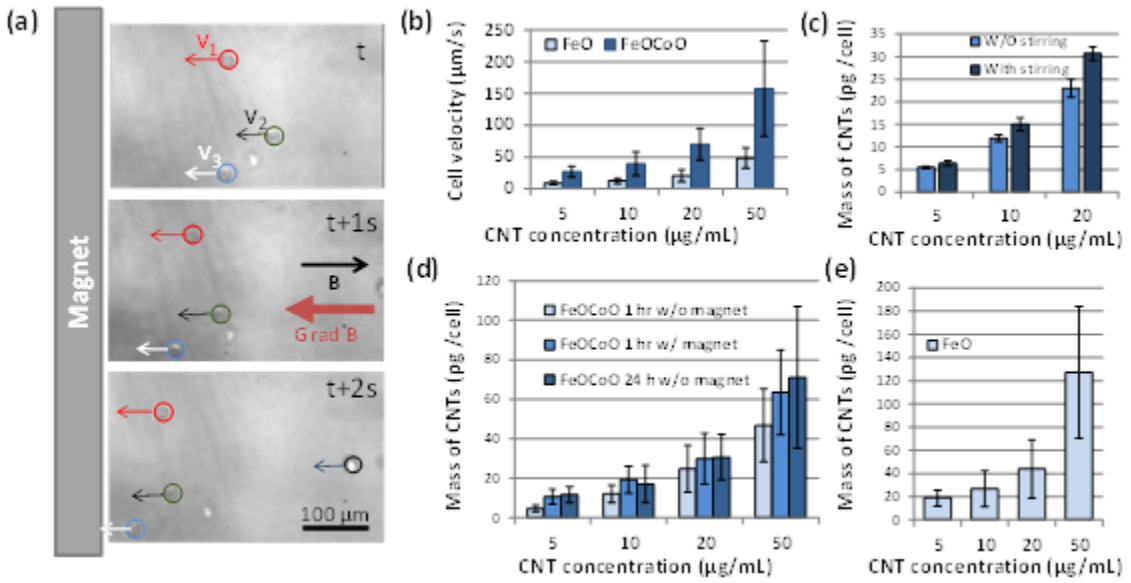

Figure IV.27. Magnetophoretic mobility of CNT labeled cells allows quantifying CNT uptake. SKOV3 cells were incubated with $Fe_{3-x}O_4$/CoO@CNTs (FeOCoO) or $Fe_{3-x}O_4$/ $Fe_{3-x}O_4$@CNTs (FeO) at concentrations of 5 to 50 µg/mL for 30 min to 24 h. The influence of a magnet which both orients and attracts CNTs perpendicularly to the cell layer was tested for the 1 h condition. The influence of magnetic stirring on cell uptake was also tested. The labelled cells were then trypsinized and put in suspension in presence of a calibrated magnetic field gradient that makes cells moving to the magnet. In permanent regime (constant cell velocity) (see v_1, v_2, v_3 as examples of cell velocity in (a)), the viscous force experienced by the moving cells directly balance the magnetic force. Thus the measurement of cell velocity (b) allows quantifying magnetic force on each cell and corresponding CNT uptake (c-e). Here the cell velocity (b) and the mass of CNTs per cell (c-e) were averaged over 40 individual cells. Bars represent standard deviation of the distribution of velocity or CNT mass over the cell population. (b) Magnetophoretic velocity of cells incubated for 24 h with FeOCoO or FeO. (c) Mass of CNTs in cells (pg per cell) incubated with FeOCoO for 30 min and submitted or not to 30 min magnetic stirring. Magnetic stirring tends to increase cellular uptake. (d) Mass of CNTs in cells (pg per cell) incubated with FeOCoO for 1 h with or without magnet or for 24 h without magnet. (e) Mass of CNTs in cells incubated with FeO for 24 h without magnet.

IV.4.4 Photothermal Cytolysis Evaluation

Finally, the efficacy of $Fe_{3-x}O_4$/CoO@CNTs for photothermal cytolysis was evaluated. Adherent cells were treated for 200 s or 500 s with NIR irradiation (4 W/cm^2) soon after incubation with CNTs and rinsing (1 h with magnet or 24 h without magnet). Cell viability was quantified 24 hrs after NIR treatment which is a sufficient delay to observe apoptosis or necrosis (Figure IV.28). The laser had no deleterious effect on control non-labeled cells. In contrast, we observed a dose dependent NIR light-induced toxicity on labeled cells, which increased with increasing cellular load of CNTs and with the time of laser exposure. Remarkably, 80% cell death was attained with the 1 h magnet condition (50 µg/ml, 64 pg CNTs/cell). It is worthy to note that despite the comparable amount of CNTs in cells after 24

h incubation, NIR toxicity was significantly higher after 1 h incubation with the magnet, regardless of the irradiation time. One hypothesis is that the localization of CNTs near the plasma membrane at short times amplified cell damage due to local heating in comparison with CNTs having intracellular localization at 24 h. Further studies are underway in order to unravel this interesting localization effect. Overall our data indicate excellent potential of $Fe_{3-x}O_4$/CoO@CNTs for photothermal ablation. The comparison with other nanotubes is not straightforward since the quantity of CNTs per cell is rarely measured.[22] Here the magnetic properties of nanotubes uniquely allow for accurate quantification of CNTs uptake by single cells. In addition, we have shown very efficient uptake by tumor cells, which could be enhanced by magnetic targeting and magnetic stirring. Finally, for similar amount of CNTs per cell, the localization of nanotubes appears to play a role on the NIR-induced damage on cells.

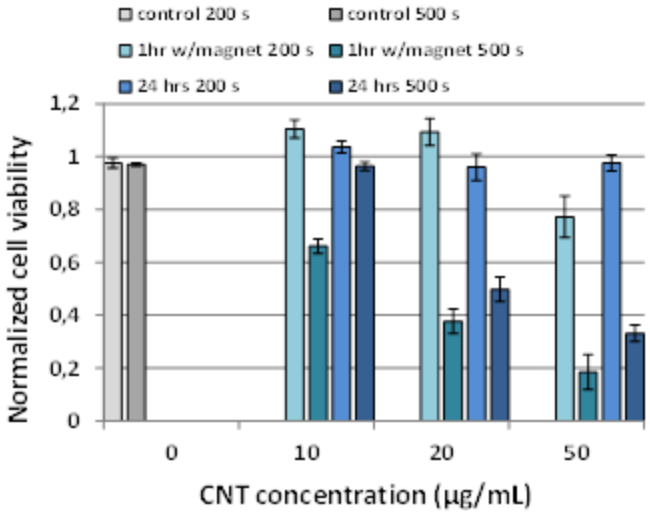

Figure IV.28. Viability of SKOV3 cells exposed to 808 nm NIR laser at a fluence of 4 W/cm^2 for 200 s or 500 s laser for different labeling condition with $Fe_{3-x}O_4$/CoO@CNTs in comparison to irradiated non-labelled control cells. The metabolic activity of cells was normalized.

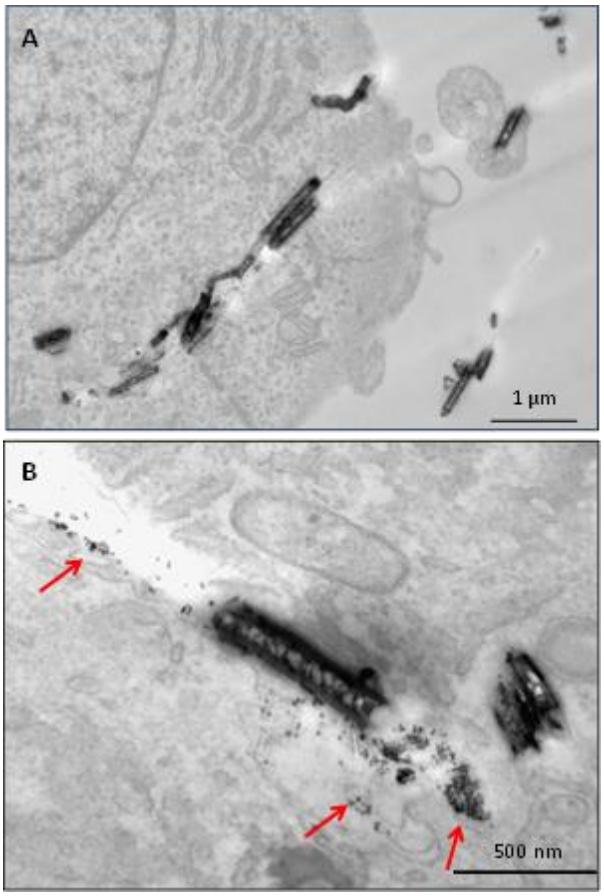

Figure IV.29. Electron micrographs show the NPs are entrapped into the CNTs once internalized by cells (A). Occasionally, one observes the intracellular release of NPs from CNTs within lysosomal compartments (B).

Although the magnetic CNTs were not injected *in vivo* in this study, their high heating efficiency and high dispersibility make them suitable for intratumoral injection and precise photothermal ablation of tumors using NIR radiation that can penetrate the tissue more than one cm. In addition to the photothermal response of NP-loaded CNTs, we also tested the magnetically-induced heating when submitted to an alternative magnetic field of 700 kHz and 24 kA/m. However at CNT concentrations used for photothermal ablation (<1000 µg/mL), we did not observe any significant heating under magnetic field. This is consistent with typical magnetic SAR of the order of 10 to 1000 W/g of magnetic NPs to be compared with the huge SAR of CNTs under laser exposure (>10000 W/g). Thus NP-loaded CNTs are much more efficient photothermal agents than magnetothermal agents, but their magnetic properties are uniquely exploited both for MRI monitoring and magnetic manipulation. Another concern for *in vivo* applications is the biodegradability of CNTs. The filling of CNTs with nanoparticles provides a unique label to investigate the structural integrity of the carbon backbone during cell processing. A comprehensive study to investigate the long term behavior of NPs-loaded nanotubes is underway. We confirm here that there is no release of NPs in water, neither in cell culture incubation medium since no isolated NPs could be seen in different cell compartments. After 6 hours of incubation with tumor cells, we mainly observe NPs entrapped into the internalized nanotubes. However, in one cell we could observe the release

of NPs from the nanotubes (Figure IV-29) suggesting that degradation process can rapidly occur taking place first at the nanotube extremities.

IV.5 CONCLUSION

Carbon nanotubes filled with magnetic NPs have been successfully obtained with a high filling rate (up to 50 wt%) by an original double filling process. Despite the removal of oxidizing groups at the surface of CNTs to trigger the synthesis of NPs inside CNTs, we succeed in functionalizing them by amino groups to ensure for a good dispersibility in aqueous medium.

The properties of the filled magnetic CNTs as heat mediator for photothermal ablation and as contrast agent for MRI were then evaluated and promising results were obtained. They are capable of absorbing and efficiently converting NIR light into heat to generate thermoablative temperatures and cell lysis. They have potential for use as agents for T_2 MR contrast imaging and MR image-guided photothermal therapy. Last but not least they can be magnetically manipulated in order to accumulate in a target site, to control their orientation and cell uptake, to drive cell motion and to trigger remote stirring in the biological environment.

References:

1. Laurent, S.; Forge, D.; Port, M.; Roch, A.; Robic, C.; Vander, E. L.; Muller, N. R. Magnetic Iron Oxide Nanoparticles: Synthesis, Stabilization, Vectorization, Physicochemical Characterizations, and Biological Applications. *Chem. Rev.* **2008**, *108*, 2064-2110.
2. Molenbroek, A. M.; Helveg, S.; Topsøe, H.; Clausen, S.B. Nano-Particles in Heterogeneous Catalysis. *Top Catal.* **2009**, *52*, 1303-1311.
3. Yin, Y.; Talapinb, D.V. The Chemistry of Functional Nanomaterials. *Chem. Soc. Rev.* 2013,*42*, 2484-2487.
4. Sun, S.; Zheng, H. Size-Controlled Synthesis of Magnetite Nanoparticles. *J. Am. Chem. Soc*. **2002**,*124*, 8204-8205.
5. Pichon, B. P.; Barbillon, G.; Marie, P.; Pauly, M.; Begin, C. S. Iron Oxide Magnetic Nanoparticles Used as Probing Agents to Study the Nanostructure of Mixed Self-Assembled Monolayers. *Nanoscale* **2011**, *3*, 4696-4705.
6. Papaefthimiou, V.; Florea, I.; Baaziz, W.; Janowska, I.; Doh, W. H.; Begin, D.; Blume, R.; Knop-Gericke, A.; Ersen, O.; Pham-Huu, C.; et al. Effect of the Specific Surface Sites on the Reducibility of α-Fe_2O_3/Graphene Composites by Hydrogen. *J. Phys. Chem. C* **2013**, *117*, 20313-20319.
7. Qu, Q.; Yang, S.; Feng, X. 2D Sandwich-like Sheets of Iron Oxide Grown on Graphene as High Energy Anode Material for Supercapacitors. *Adv. Mater.* **2011**, *23*, 5574-5580.
8. Baaziz, W.; Phuoc, L. T.; Duong, C. V.; Melinte, G.; Janowska, I.; Ersen, O.; Zafeiratos, S.; Begin, D.; Begin, S. C.; Pham, C. H. Few Layer Graphene Decorated with Homogeneous Magnetic Fe_3O_4 Nanoparticles with Tunable Covering Densities. *J. Mater. Chem. A* **2014**, *2*, 2690-2700.

9. Kim, I.T.; Magasinski, A.; Jacob, K.; Yushin, G.; Tannenbaum, R. Synthesis and Electrochemical Performance of Reduced Graphene Oxide/Maghemite Composite Anode for Lithium Ion Batteries *Carbon* **2013**, *52*, 56-64.
10. Pankhurst, Q. A.; Connolly, J.; Jones, S. K.; Dobson, J. Applications of Magnetic Nanoparticles in Biomedicine. *J. Phys. Appl. Phys.* **2003**, *36*, R167-R181.
11. Reddy, L.H., Arias, J.L.; Nicolas, J.; Couvreur, P. Magnetic Nanoparticles: Design and Characterization, Toxicity and Biocompatibility, Pharmaceutical and Biomedical Applications. *Chem. Rev.* **2012**, *112*, 5818-5878.
12. Kostarelos, K.; Bianco, A.; Prato, M. Promises, Facts and Challenges for Carbon Nanotubes in Imaging and Therapeutics. *Nat. Nanotechnol.* **2009**,*4*, 627-633.
13. Hong, H.; Gao, T.; Cai, W. Molecular Imaging with Single-walled Carbon Nanotubes. *Nano Today* **2009**, *4*, 252-261.
14. Kim, J.W.; Galanzha, E.I.; Shashkov, E.V.; Moon, H.M.; Zharov, V.P. Golden Carbon Nanotubes as Multimodal Photoacoustic and Photothermal High-Contrast Molecular Agents. *Nat. Nanotechnol.* **2009**, *4*, 688-694.
15. Welsher, K.; Liu, Z.; Sherlock, S.P.; Robinson, J.T.; Chen, Z.; Daranciang D.; Dai H. A Route to Brightly Fluorescent Carbon Nanotubes for Near-infrared Imaging in Mice. *Nat. Nanotechnol.***2009**, *4*, 773-780.
16. Lamanna, G.; Garofalo, A.; Popa, G.; Wilhelm, C.; Begin, S. C.; Flesch, D. F.; Bianco, A.; Gazeau, F.; Moyon, M. C. Endowing Carbon Nanotubes with Superparamagnetic Properties: Applications for Cell Labeling, MRI Cell Tracking and Magnetic Manipulations. *Nanoscale* **2013**, *5*, 4412-4421.
17. Delogu, L. G.; Vidili, G.; Venturelli, E.; Ménard-Moyon, C.; Zoroddu, M. A.; Pilo, G.; Nicolussi, P.; Ligios, C.; Bedognetti, D.; Sgarrella, F.; et al. Functionalized Multiwalled Carbon Nanotubes as Ultrasound Contrast Agents. *PNAS* **2012**, *109*, 16612-16617.
18. Wang C.; Ma X.; Ye S.; Cheng L.; Yang K.; Guo L.; Li C.; Li Y.; Liu Z. Protamine Functionalized Single-Walled Carbon Nanotubes for Stem Cell Labeling and *in Vivo* Raman/Magnetic Resonance/Photoacoustic Triple-Modal Imaging. *Adv. Funct. Mater.* **2012**, *22*, 2363-2375.
19. Singh, R.; Torti, S. V. Carbon Nanotubes in Hyperthermia Therapy. *Adv. Drug Deliv. Rev.* **2013**, *65*, 2045-2060.
20. Shen, S; Kong, F.; Guo, X.; Wu, L.; Shen, H.; Xie, M.; Wang, X.; Jin, Y.; Ge, Y. CMCTS Stabilized Fe_3O_4 Particles with Extremely Low Toxicity as Highly Efficient Near-infrared Photothermal Agents for *in Vivo* Tumor Ablation. *Nanoscale* **2013**, *5*, 8056-8066.
21. Liu X.; Tao H.; Yang K.; Zhang S.; Lee S. T.; Liu Z. Optimization of Surface Chemistry on Single-Walled Carbon Nanotubes for *in Vivo* Photothermal Ablation of Tumors. *Biomaterials* **2011**, *32*, 144-151.
22. Wu, H.; Liu, G.; Zhuang, Y.; Wu, D.; Zhang, H.; Yang, H.; Hu, H.; Yang, S. The Behavior after Intravenous Injection in Mice of Multiwalled Carbon Nanotube / Fe_3O_4 Hybrid MRI Contrast Agents. *Biomaterials* **2011**, *32*, 4867-4876.
23. Wang, J.T.W.; Cabana, L.; Bourgognon, M.; Kafa, H.; Protti, A.; Venner, K.; Shah, A.M.; Sosabowski, J.K.; Mather, S.J.; Roig, A.; et al. Magnetically Decorated Multiwalled Carbon Nanotudes as Direct MRI and SPECT Contrast Agent. *Adv.Funct.Mater*. **2014**, *24*, 1880-1894.
24. Tessonnier, J. P.; Rosenthal, D.; Girgsdies, F.; Amadou, J.; Bégin, D.; Pham-Huu, C.; Su, S. D.; Schlögl, R. Influence of the Graphitisation of Hollow Carbon Nanofibers on Their

Functionalisation and Subsequent Filling with Metal Nanoparticles. *Chem. Comm*. **2009**, *46*, 7158-7160.
25. Castillejos, E.; Debouttiere, P. J.; Roiban, L.; Solhy, A.; Martinez, V.; Kihn, Y.; Ersen, O.; Philippot, K.; Chaudret, B.; Serp, P. An Efficient Strategy to Drive Nanoparticles into Carbon Nanotubes and the Remarkable Effect of Confinement on Their Catalytic Performance. *Angew. Chem. Int. Ed.***2009**, *48*, 2529-2533.
26. Baaziz, W.; Begin, S.; Pichon, B.P.; Florea, I.; Ersen, O.; Zafeiratos, S.; Barbosa, R.; Begin, D.; Pham-Huu, C. High-Density Monodispersed Cobalt Nanoparticles Filled into Multiwalled Carbon Nanotubes. *Chem. Mater*.**2012**, *24*, 1549-1551.
27. Baaziz, W.; Liu, X.; Florea, I.; Begin S.; Pichon, B. P.; Ulhaq, C.; Ersen, O.; Soria, S. M.; Zafeiratos, S.; Janowska, I.; et al. Carbon Nanotube Channels Selectively Filled with Monodispersed $Fe_{3-x}O_4$ Nanoparticles. *J. Mater. Chem. A* **2013**, *1*, 13853-13861.
28. Bao, J.; Tie, C.; Xu, Z.; Suo, Z.; Zhou, Q.; Hong, J. A Facile Method for Creating an Array of Metal‐Filled Carbon Nanotubes. *Adv. Mater.* **2002**,*14*, 1483-1486.
29. Hampel, S.; Leonhardt, A.; Selbmann D.; Biedermann, K.; Elefant, D.; Müller, Ch.; Gemming, T.; Büchner, B. Growth and Characterization of Filled Carbon Nanotubes with Ferromagnetic Properties. *Carbon* **2006**, *44*, 2316-2322.
30. Leonhardt, A.; Haampel, S.; Müller, C.; Mönch, I.; Koseva, R.; Ritschel, M.; Elefant, D.; Biedermann, K.; Büchner, B. Synthesis, Properties, and Applications of Ferromagnetic-Filled Carbon Nanotubes. *Chem. Vap. Deposition* **2006**, *12*, 380-387.
31. Gui, X.; Wei, J.; Wang K.;Wang, W.; Lv, R.; Chang, J.; Kang, F.; Gu, J.; Wu, D. Improved Filling Rate and Enhanced Magnetic Properties of Fe-filled Carbon Nanotubes by Annealing and Magnetic Separation. *Mat. Res. Bull.* **2008**, *43*, 3441-3446.
32. Korneva, G.; Ye, H.; Gogotsi, Y.; Halverrson, D.; Friedman, G.; Bradley, J. C.; Kornev, K. Carbon Nanotubes Loaded with Magnetic Particles. *Nano lett*. **2005**, *5*, 879-884.
33. Kopyl, S.; Bystrov, V.; Bdikin, I.; Maiorov, M.; Sousa, A.C.M. Filling Carbon Nanotubes with Magnetic Particles. *J. Mat. Chem. C* **2013**,*1*, 2860-2866.
34. Ersen, O.; Bégin, S.; Houllé, M.; Amadou, J.; Janowska, I.; Grenèche, J.M.; Crucifix, C.; Pham-Huu, C. Microstructural Investigation of $CoFe_2O_4$ Nanowires Inside Carbon Nanotubes by Electron Tomography. *Nano let.* **2008**, *8*, 1033-1040.
35. Belesi, M.; Philippe, T.; Rousochatzakis, I.; Wu, H.C.; Berger, H.; Granville, S.; Shvets, I.V.; Ansermet, J.-Ph. Magnetic Properties of the Magnetoelectric Compound Cu_2OSeO_3: Magnetization and 77Se NMR Study. *Journal of Physics: Conference Series* **2011**, *303*, art. no. 012069.
36. Yu, W. J.; Hou, P. X.; Li, F.; Liu, C. Improved Electrochemical Performance of Fe_2O_3 Nanoparticles Confined in Carbon Nanotubes. *J. Mat. Chem.* **2012**, *22*, 13756-13763.
37. Tessonnier, J. P.; Ersen, O.; Weinberg, G.; Pham, H. C.; Su, D. S.; Schlögl, R. Selective Deposition of Metal Nanoparticles Inside or Outside Multiwalled Carbon Nanotubes. *ACS Nano* **2009**, *64*, 2081-2089.
38. Costa, P.M.F.J.; Sloan, J.; Rutherford, T.; Green, M.L.H. Encapsulation of Re_xO_y Clusters within Single-Walled Carbon Nanotubes and Their in Tubulo Reduction and Sintering to Re Metal. *Chem. Mater.* **2005**, *17*, 6579-6582.
39. W. Xia,Y. Wang,R. Bergsträßer,S. Kundu, M. Muhler. Surface Characterization of Oxygen-Functionalized Multi-Walled Carbon Nanotubes by High-Resolution X-ray

Photoelectron Spectroscopy and Temperature-Programmed Desorption. Appl. Surf. Sci. 2007, **254**, 247-250.
40. Chen, S., Wu, G., Sha, M., & Huang, S. Transition of Ionic Liquid [bmim][PF_6] from Liquid to High-Melting-Point Crystal When Confined in Multiwalled Carbon Nanotubes, J. Am. Chem. Soc. 2007, 129, 2416–2417.
41. Ménard, M. C.; Fabbro, C.; Prato, M.; Bianco, A. One-Pot Triple Functionalization of Carbon Nanotubes. *Chem. Eur. J.* **2011**, *17*, 3222-3227.
42. Wilhelm, C.; Gazeau, F.; Bacri, J.C. Magnetophoresis and Ferromagnetic Resonance of Magnetically Labeled Cells. *Eur. Biophys. J.* **2002**, *31*, 118-125.
43. Baaziz, W.; Pichon, B. P.; Lefevre, C.; Bouillet, U. C.; Greneche, J.M.; Toumi, M.; Mhiri, T.; Bégin, C.S. High Exchange Bias in $Fe_{3-\delta}O_4$@CoO Core Shell Nanoparticles Synthesized by a One-Pot Seed-Mediated Growth Method. *J. Phys. Chem. C* **2013**, *117*, 11436-11443.
44. Leighton C.; Nogues J.; Jonsson-Akerman B. J.; Schuller I.K. Coercivity Enhancement in Exchange Biased Systems Driven by Interfacial Magnetic Frustration. *Phys. Rev. Lett.* **2000**, *84*, 3466-3469.
45. Cheon J.; Park J.I.; Choi J.S.; Jun Y.W.; Kim S.; Kim M. G.; Kim Y.M.; Kim Y.J. Magnetic Superlattices and Their Nanoscale Phase Transition Effects. *PNAS* **2006**, *103*, 3023-3027.
46. Song Q.; Zhang Z. J. Controlled Synthesis and Magnetic Properties of Bimagnetic Spinel Ferrite $CoFe_2O_4$ and $MnFe_2O_4$ Nanocrystals with Core−Shell Architecture. *J. Am. Chem. Soc*.**2012**, *134*, 10182-10190.
47. Demortière, A.; Panissod, P.; Pichon, B.; Pourroy, G.; Guillon, D.; Donnio, B.; Bégin, C. S. Size-Dependent Properties of Magnetic Iron Oxide Nanocrystals. *Nanoscale* **2011**, *3*, 225-232.
48. Baaziz, W.; Pichon, B.; Fleutot, S.; Liu, Y.; Lefevre, C.; Greneche, J. M.; Toumi, M.; Mhiri, T.; Begin, C. S. Magnetic Iron Oxide Nanoparticles: Reproducible Tuning of the Size and Nanosized-Dependent Composition, Defects, and Spin Canting. *J. Phys. Chem. C* **2014**, *118*, 3795-3810.
49. Pallai, V.; Shah, D. O. Synthesis of High-Coercivity Cobalt Ferrite Particles Using Water-in-oil Water Microemulsions. *J. Magn. Magn. Mater.* **1996**, *163*, 243-258.
50. Bahr, J. L.; Tour, J. M. Highly Functionalized Carbon Nanotubes Using *in Situ* Generated Diazonium Compounds. *Chem. Mater.* **2001**, *13*, 3823-3824.
51. Ménard, M. C.; Fabbro, C.; Prato, M.; Bianco, A. One-Pot Triple Functionalization of Carbon Nanotubes. *Chem. Eur. J.* **2011**, *17*, 3222-3227.
52. Kaiser, E.; Colescott, R. L.; Bossinger, C. D.; Cook, P. I. Color Test for Detection of Free Terminal Amino Groups in the Solid-Phase Synthesis of Peptides. *Anal. Biochem.* **1970**, *34*, 595-598.
53. Samorì, C.; Sainz, R.; Ménard, M. C.; Toma, F. M.; Venturelli, E.; Singh, P.; Ballestri, M.; Prato, M.; Bianco, A. Potentiometric Titration as a Straightforward Method to Assess the Number of Functional Groups on Shortened Carbon Nanotubes. *Carbon* **2010**, *48*, 2447-2454.
54. Gillis, P.; Moiny, F.; Brooks, R. A. On T2-shortening by Strongly Magnetized Spheres: A Partial Refocusing Model. *Magn. Reson. Med.* **2002**, *47*, 257-263.

55. Perez, J. M.; Josephson, L.; O'Loughlin, T.; Hogemann, D.; Weissleder, R. Magnetic Relaxation Switches Capable of Sensing Molecular Interactions. *Nat. Biotechnol*.**2002**, *20*, 816-820.
56. Vuong, Q. L.; Berret, J. F.; Fresnais, J.; Gossuin, Y.; Sandre, O. A Universal Scaling Law to Predict the Efficiency of Magnetic Nanoparticles as MRI T2-Contrast Agents. *Adv. Healthcare Mater*.**2012**, *1*,502-512.
57. Park, J.H.; von Maltzahn, G.; Zhang, L.; Schwartz, M.P.; Ruoslahti, E.; Bhatia, S.N.; Sailor, M.J. Magnetic Iron Oxide Nanoworms for Tumor Targeting and Imaging. *Adv Mater*.**2008**, *20*, 1630-1635.
58. Yin, M.; Wang, M.; Miao, F.; Ji, Y.; Tian, Z.; Shen, H.; Jia, N. Water-Dispersible Multiwalled Carbon Nanotube/Iron Oxide Hybrids as Contrast Agents for Cellular Magnetic Resonance Imaging. *Carbon* **2012**, *50*, 2162-2170.
59. Liu, Y.; Hughes, T.C.; Muir, B.W.; Waddington, L.J.; Gengenbach, T.R.; Easton, C.D.; Hinton, T.M.; Moffat, B.A.; Hao, X.; Qiu, J. Water-Dispersible Magnetic Carbon Nanotubes as T2-Weighted MRI Contrast Agents. *Biomaterials* **2014**, *35*, 378-386.
60. Paquet, C.; de Haan, H. W.; Leek, D. M.; Lin, H.Y.; Xiang, B.;Tian, G.; Kell, A.; Simard, B. Clusters of Superparamagnetic Iron Oxide Nanoparticles Encapsulated in a Hydrogel: A Particle Architecture Generating a Synergistic Enhancement of the T2 Relaxation. *ACS Nano* **2011**, *5*, 3104-3112.
61. Park, J.H.; von Maltzahn, G.; Zhang, L.; Schwartz, M. P.; Ruoslahti, E.; Bhatia, N. S.; Sailor, J. M. Magnetic Iron Oxide Nanoworms for Tumor Targeting and Imaging. *Adv. Mater*. **2008**, *20*, 1630-1635.
62. Lartigue, L.; Hugounenq, P.; Alloyeau, D.; Clarke, S.P.; Lévy, M.; Bacri, J.C.; Bazzi, R.; Brougham, D.F.; Wilhelm, C.; Gazeau, F. Cooperative Organization in Iron Oxide Multi-Core Nanoparticles Potentiates Their Efficiency as Heating Mediators and MRI Contrast Agents. *ACS Nano.* **2012**, *6*, 10935-10949.
63. Liu, D.; Wang, L.; Wang, Z.; Cuschieri, A. Magnetoporation and Magnetolysis of Cancer Cells *via* Carbon Nanotubes Induced by Rotating Magnetic Fields. *Nano Lett*.**2012**,*12*, 5117-5121.

Chapter V : Synthesis of Nb_2O_5 and their carbon based composites: use as anode in Li-ion battery

V.1 Introduction

Actually, lithium ion batteries (LIBSs) are knowing a huge increase of interests in all the world research community because such power sources are more and more needed for portable electronic applications but also in the transport area (Chinese government has an objective of 5 millions of electrical (or hybrid) vehicles for the 2020 horizon). Up to now, if we only consider the anode, the most used material is graphite or specific carbon materials because of its voltage cyclic stability and charge/ discharge capacity[1,2,3,4]. However, the highest amount of Li stored in graphite corresponds to the typical stage 1 (LiC_6) so that the maximal theoretical capacity is limited to a value of 372 $mAh.g^{-1}$. More recently different kinds of transition metal oxides have replaced graphite because of their potential capacity which can be increased closed to 3 times [5,6,7,8,9] and even reach a value of 4200 $mAh.g^{-1}$ in the case of silicon[10]. Moreover, such metal oxides present a low cost and can be easily synthesized but we have to consider a drastic volume variation when the amount of lithium in the metal oxides nanoparticles increase which can results to their destruction. Due to their low electrical conductivity, they must be associated with a conducting support. Tarascon et al proposed for instance an original and simple method to associate Fe_3O_4 nanoparticules with a copper foil by electrodeposition [6], but most of the supports are generally graphite-based materials and particularly carbon shells, carbon nanotubes and more recently graphene like materials[11,12,13].

Fe_3O_4 nanostructures associated with acetylene black have shown interesting performances as electrode material[14,15] and more recently Chen et al claimed capacities as high as 1039 mAh/g obtained from a composite Fe_3O_4/reduced graphene[16]. To obtained anode with high capacities, the total amount of metallic oxide in the anode must be as high as possible, but it is necessary to take into account a minimal quantity of carbonaceous material to ensure the conductivity of the electrode. So, graphenes or graphene like material are good candidates in this kind of anode because of their good electrical conductivity and their very thin thickness allowing good coatings of metal oxides all along their surface. Recently, the team of Sylvie Bégin at the IPCMS developed a one–pot synthesis in a polyol solvent where the Fe_3O_4 raspberry nanostructures grew directly on the graphene sheets which assure the excellent interface between the iron oxide nanostructures and the graphene and give a high conductivity of the hybrid material with a massic ratio Fe_3O_4/graphene equal to 10.

In this work we propose to study another promising metal oxide supported on carbonaceous materials, Nb_2O_5. Two supports have been selected, the CNTs and graphene-like materials synthesized at the ICPEES and niobium oxides were directly grown on these nanocarbons by two methods : the solvothermal method as described in the previous chapters and the hydrothermal method recently developed at the IPCMS for the synthesis of Fe_3O_4 raspberry nanostructures.

V.2 Experimental session

V.2.1 Solvothermal synthesis

We adopted a method described by Jana et al.[17] to produce nanoplatelets of Nb_2O_5 (with minor modifications) close to that described in the second chapter to synthesize CoO or Fe_3O_4. The used precursor is an $Nb(oleate)_5$, which was synthesized from Niobium pentachloride ($NbCl_5$). The detailed procedure is as follows: 2.92 g (2.5 mmol) of $NbCl_5$ (>99.9%, Sigma Aldrich) was dissolved in a mixture of 50 mL of ethanol and 34 mL of distilled water. 16.5g of sodium oleate (>99.9% TCI) was dissolved in 90 mL hexane. Then, the mixture of both solutions was refluxed at 80 ^oC for 6h. After completion of the reaction, the Nb oleate complex was washed several times with 30ml water in a separating funnel to remove the salts. Subsequently, the addition of $MgSO_4$ was conducted to remove water. Finally, the hexane was evaporated by rotary evaporator. An orange waxy product was obtained.

The synthetic protocol for the preparation of niobium oxide nanoparticles was based on the decomposition of niobium oleate complex. Seed mediated growth was performed to produce niobium oxide. Firstly, 0.849 g of Nb oleate and 0.715 g of oleic acid were dissolved in 11.2 mL of squalane (99%, Sigma Aldrich). First, the temperature was kept at 120 ^oC for 1h to remove the residual water. Then, the flask was heated up to the 380 ^oC with a ramp of 4 ^oC/min and kept at that temperature for 30 mins. Then, 4.5 mL of squalane solution containing 0.34 g of Nb oleate was injected to the reaction mixture and kept for an additional time of 30 min, and then cooled to the room temperature. At the end, the resulting product was washed and centrifugated 3 times in Chloroform. The obtained sample is denoted as Nb_2O_5-1. To synthesize NPs/Carbon nanocomposites, few layered graphene or CNTs were previously added into the Nb oleate solution before heating. The subsequent procedure is the same. The as-prepared carbon based composites are named in the following as Nb_2O_5-1-Graphenes and Nb_2O_5-1-CNTs.

V.2.2 Autoclave synthesis

The procedure is as follows: Firstly, 0.54 g of $NbCl_5$, 0.24g of succinic acid (99.5%, Sigma Aldrich) as reductant and 3.6 g of urea (99.3%, Alfa Aesar) as source of OH^- were dissolved in 60 mL of ethylene glycol (99%, Alfa Aesar) as solvent. After stirring for 20 minutes and sonication for 30 minutes, the solution was transferred in a 120 ml autoclave. Then, the autoclave was heated up to 220 ^oC with a heating rate of 2 ^oC/min and kept at this temperature for 24h. After cooling down to room temperature, the products are washed and centrifugated several times in water to remove the salts. Finally, the resultant white product was dried in an oven at 50 ^oC. In the following, this sample is denoted as Nb_2O_5-2. To synthesize NPs/Carbon nanocomposites, few layered graphene or CNTs was previously added

into the Nb oleate solution. The as-prepared carbon based composites was named in the following Nb_2O_5-2-Graphenes and Nb_2O_5-2-CNTs, respectively.

V.2.3 Few layer graphene (FLG) synthesis

FLG was synthesized at the ICPEES by mechanical ablation of graphitic materials (pencil lead) assisted by ultrasonication and followed by acid/base purification processes to remove the binders.[18] The developed synthesis method is attractive due to its simplicity, the absence of toxic solvents or high temperature process and the direct formation of reduced graphene (FLG), i.e. without large amounts of oxygenated groups. Indeed, a weak sonication step introduces a relatively low amount of defects onto the graphene sheets compared to other methods where a large amount of oxygenated functional groups are present, requiring a subsequent defunctionalisation step which could severely modify the final properties of the material.

V.2.4 Surface area measurement

The specific surface areas of as-prepared samples were measured by Brunauer–Emmett–Teller (BET) method, which was carried out in a micromeritics sorptometer (Tristar) by using N_2 as adsorbent at liquid N_2 temperature with a p/p_0 ratio comprised between 0.05 and 0.99. Before measurement, the samples were outgassed at 200 ℃ under vacuum for 8 h to desorb moisture and adsorbed species on its surface.

V.2.5 Electrochemical measurements

Coin-type cells were assembled in an argon-filled glove box (moisture level < 1 ppm) using the niobium oxide as the positive electrode and the Li metal as the negative electrode. Both positive and negative electrodes were electronically separated by a Whatman GF/D borosilicate glass-fibre sheet saturated with 1M $LiPF_6$ electrolyte solution (in EC:DMC/1:1 in volume ratio). The schematic illustration of battery test is shown in schema Ⅵ-1. When Nb_2O_5 active materials NPs was not associated with CNTs or graphene (FLG), 20 % of carbon black (Timcal Super C65) was added to ensure a sufficient

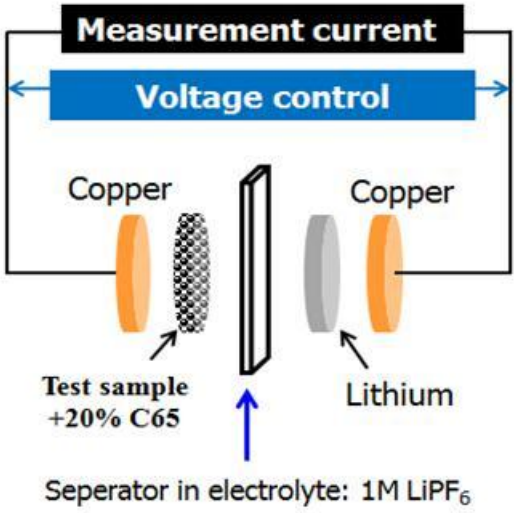

Schema V-1. The representation of Battery lithium test set-up.

electrical contact. The mixture was packed into the microcavity and subsequently immersed in the electrolyte. A 1 cm^2 platinum foil (Alfa Aesar) was used as the counter electrode and a lithium foil as the reference. The slurry was drop-cast onto 12-mm-diameter copper-disc current collectors and dried at 80 ^oC for 12 h. The electrode loading was between 1 and 1.5 mg/cm^2 with a thickness of 40 ± 5 µm. All measurements were carried out in argon-filled glove boxes between 0.01 and 3V (versus Li/Li+) using a Bio-Logic VMP3 potentiostat.

V.3 Nb_2O_5 and their carbon based composites synthesized by solvothermal approach

V.3.1 Characterization of Nb-Oleate

For the solvothermal synthesis, the Niobium oleate was used as the precursor by anions exchange from chloride to oleate. As shown in Figure V-1 on the TGA curve, after anion exchange, Nb oleate is decomposed in a broader temperature range than $NbCl_5$. Besides, the decomposition temperature is shifted to higher value. According to IR spectrum of Figure V-2, the absorption at 2923 cm^{-1} and 2842 cm^{-1} can be the asymmetric C-H stretching and symmetric C-H stretching of oleic acid, respectively. The two strong peaks at 1551 and 1400 cm^{-1} can be assigned to C=O bond of oleic acid. Last, the peak corresponding to the metal-oleate is typically present at 718 cm^{-1}, and is very different to that correponding to the Nb - Cl bonds (peak very broad). These observations can confirm the successful synthesis of Nb-oleate.

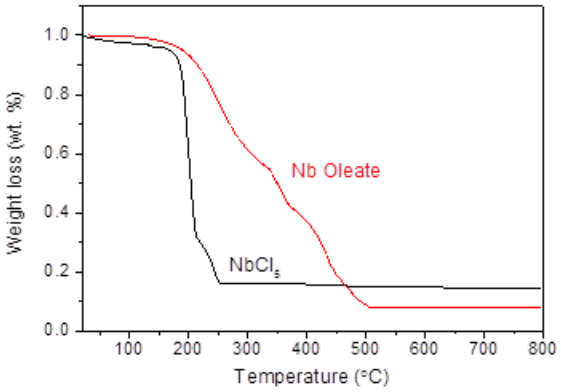

Figure V-1. TGA of $NbCl_5$ and obtained Nb Oleate.

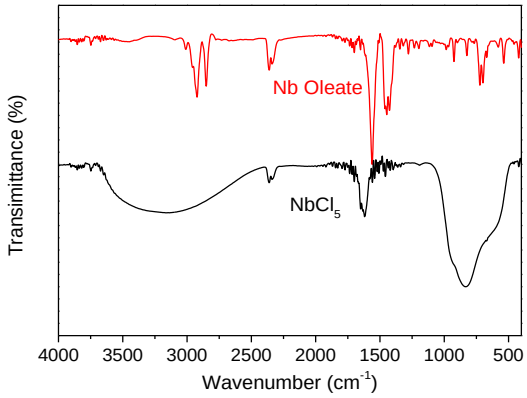

Figure V-2. IR spectra of $NbCl_5$ and obtained Nb Oleate.

V.3.2 TGA and electronic microscopic characterizations of the carbon based composites

After the reaction, Nb_2O_5 NPs are generally fully coated by the oleic acid, which leads to a homogenous size and a good dispersibility of the NPs. However, in the case of their use in lithium battery for instance, the ligands must be removed to insure a better conductivity of the composite. A typical calcination has been performed at some temperatures taking into account the TGA curves (in the presence of air) of the NPs in the presence or not of the carbon nanostructures (Figure V3). The first weight loss corresponds to the removal of the ligand and the second to the carbon burning. So, to avoid this last reaction (carbon combustion), calcinations were performed at some temperatures comprised between 400 and 450 ℃. We can see from this curve that CNTs burn at a temperature much lower in comparison with that of graphene (500 - 550 ℃ against 700 ℃) attesting the difference of their graphitization degree.

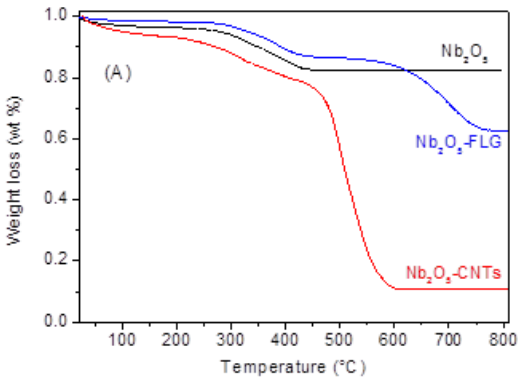

Figure V-3. TGA of Nb_2O_5 and Nb_2O_5 associated with carbon materials prepared by solvothermal method.

Figure V-4 shows TEM pictures of the Nb_2O_5 NPs synthesized by solvothermal method before and after calcination which have a platelet-like form and very well crystallized (Figure V-4B). After calcination in air, the shape and size nearly remained the same: the conformation of NPs was slightly deformed and more aggregates were found out, (beginning of sintering).

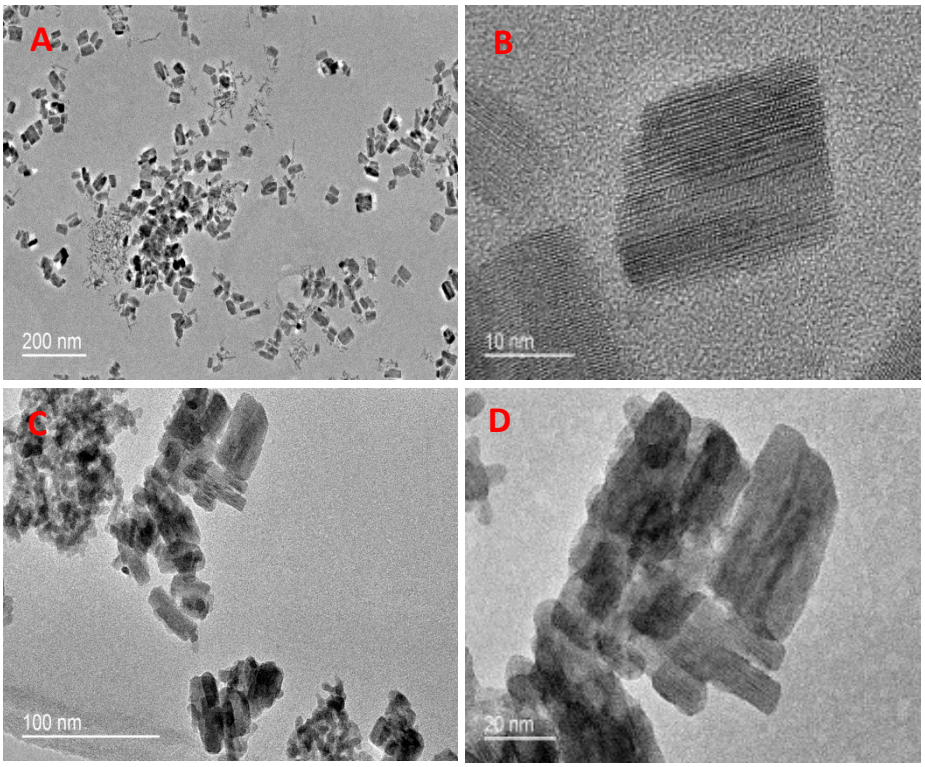

Figure V-4. TEM of Nb_2O_5 before (A and B) and after (C and D) calcination

In Figure V-5 and V-6 are represented respectively the nanocomposites Nb_2O_5 /graphenes and Nb_2O_5/CNTs before and after calcination. In all the cases, we can see that the level of coating is very high, for graphene, or for CNTs. As expected, Nb_2O_5 NPs have a platelet like

shape (size typically comprised between 10 and 20 nm) and after calcination, we can observe a beginning of aggregation, but no sintering. In the case of CNTs, we can observe that all the NPs are outside of the channel: this phenomenon can have two origins which must be more studied: the Nb_2O_5 NPs can have a too big size (they are synthesized before to be mixed with the CNTs) or the wettability of the squalane with CNTs is not favorable...

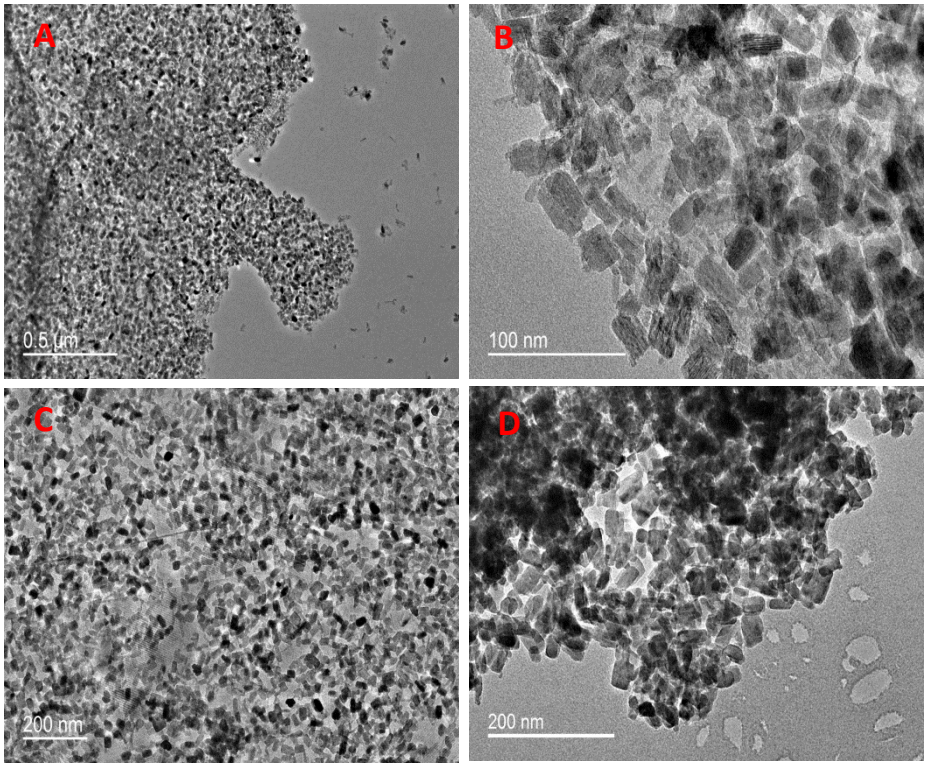

Figure V-5. TEM of Nb_2O_5 coating on graphenes before (A and B) and after (C and D) calcination

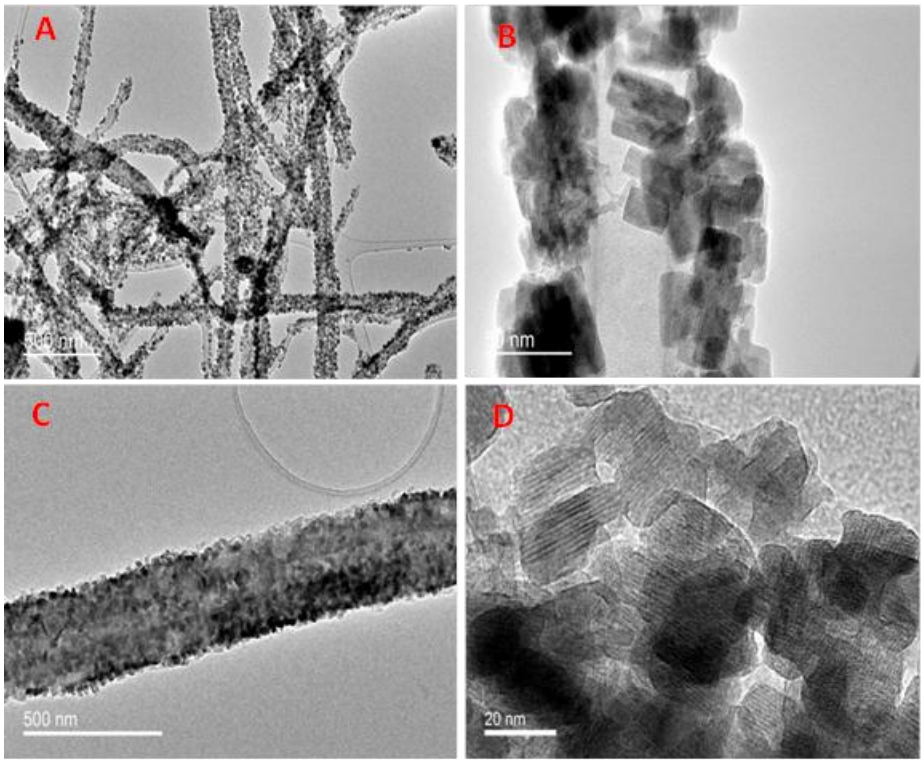

Figure V-6. TEM of Nb_2O_5 coating on CNTs before (A and B) and after (C and D) annealing.

V.3.3 XRD analysis

XRD measurements have been performed before annealing and are represented in the Figure V-7. As described in the literature [17], Nb_2O_5 NPs have a tetragonal structure. all the patterns match well with the Nb_2O_5 with tetragonal structure (JCPDS-72-1484). In the case of Nb_2O_5/CNTs and Nb_2O_5/FLG, the intense peak at 26.4° is indexed to the graphitic reflection of carbon (JCPDS-26-1077). In addition, due to the presence of the nano-carbon material with a rather high degree of crystallinity (mainly in the case of the graphene) , the peaks ascribed to Nb_2O_5 were relatively decreased.

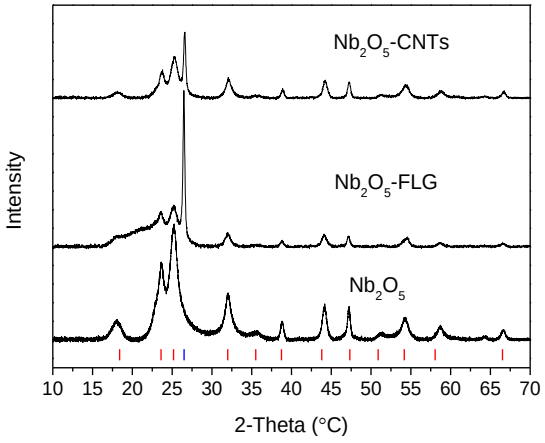

Figure V-7. XRD of Nb_2O_5 and Nb_2O_5 associated with carbon materials prepared by solvothermal method. Red bars: reflection attributed toNb_2O_5 (tetragonal structure) and blue bar to Graphitic carbon.

V.3.4 BET analysis

The surface area of Nb_2O_5 NPs and carbon based composites are collected in Table V-1. The specific surface areas of carbon based composites are of course higher than that of NPs alone which is due to the higher surface area of carbonaceous materials

Table V-1. Surface area, of Nb_2O_5-1 and corresponding carbon based composites by solvothermal method.

	Nb_2O_5-1	Nb_2O_5-FLG-1	Nb_2O_5-CNTs-1
Surface area (m^2/g)	40.1	75.2	72.3

V.4 Nb_2O_5 and their carbon based composites synthesized by hydrothermal approach

TGA curves of Nb_2O_5 and their carbon based composites in the presence of air are presented in Figure V-9: after a weight loss corresponding to water, organic compounds are removed near 350 ℃ and as in the case of carbon based composites synthesized by the solvothermal method, CNTs and graphene burn close to 500 ℃ and 650 ℃, respectively. So to remove the organic compounds without burning the carbon of the composites and to crystallize the Nb_2O_5 particles, a calcination temperature of 450 ℃ has been applied to all the samples during one hour. Finally, we can see in the presence of CNTs or graphenes that the deposited amount of Nb_2O_5 NPs is still close of 55 - 65%.

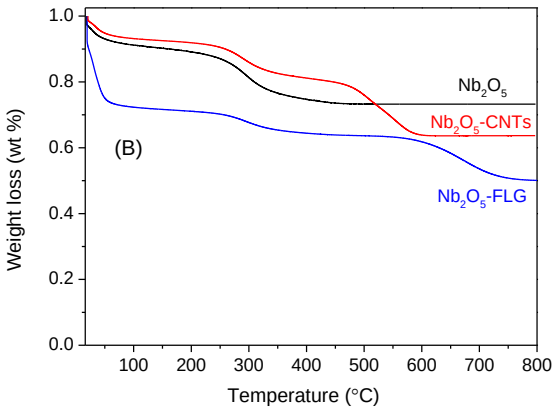

Figure V-8. TGA of Nb_2O_5 and Nb_2O_5 associated with carbon materials prepared by

hydrothermal method.

V.4.1 Microscopic characterization

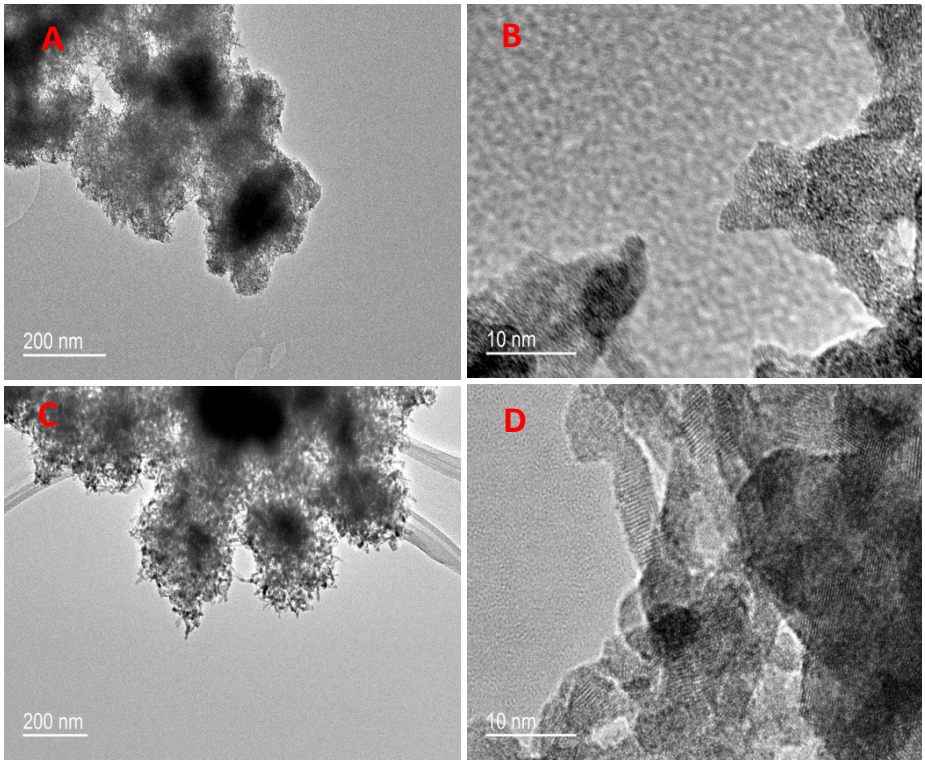

Figure V-9. TEM images of Nb_2O_5 before (A and B) and after (C and D) calcination.

Figure V-**9**A shows that niobium oxide has a porous like structure and that small Needle-like NPs are highly aggregated. In HRTEM, before calcination, Nb_2O_5 NPs are amorphous (Figure V9B) and after calcination, (Figure V9D), we can see the presence of well crystallized Nb_2O_5 NPs justifying such a heat treatment.

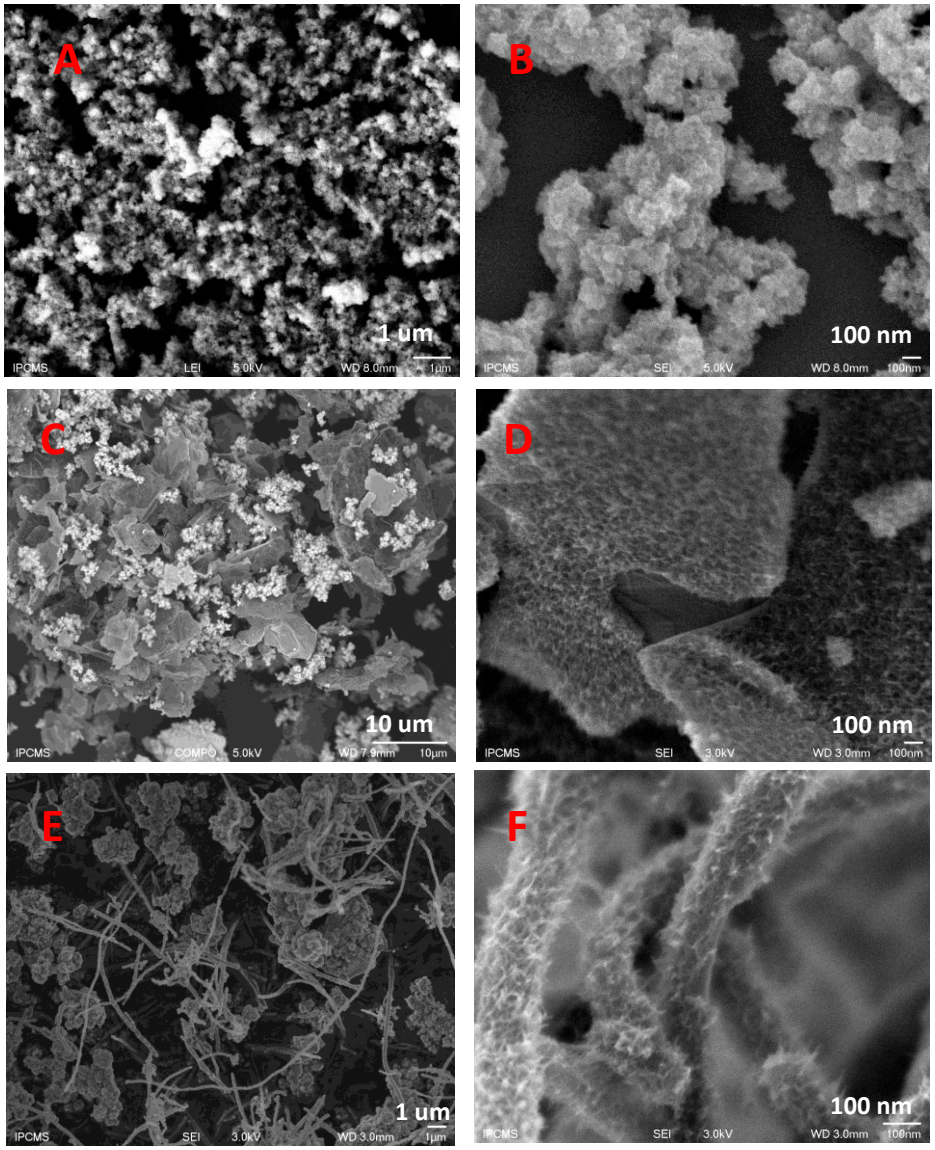

Figure V-10. SEM of Nb_2O_5 (A-B), Nb_2O_5-graphene (C-D) and Nb_2O_5-CNTs (E-F) after calcination.

SEM images of Nb_2O_5 NPs after calcination are shown in Figure -10A-B and show the presence of large aggregates. When NPs are incorporated with graphene, needle-like structures are observed on the surface of graphene. The density of needles is very high, (up to 55 wt% of uploading as seen by ATG measurments). In the case of CNTs (Figure-V10E and F), we can see that the CNTs are also covered by a great amount of needle like Nb_2O_5 NPs (Weight uptake close to 65%).

Figure V-11 represents HRTEM pictures of the composite Nb_2O_5 NPs/graphene before and after calcination. Before calcination, the structure of NPs seems amorphous, in agreement with the TEM results of single niobium oxide without graphene (Figure V-9). After calcination, some aggregates appear on the surface of the graphene (sintering beginning) but most of the surface is well coated. In Figure V-12, we can see a lot of nanorods of Nb_2O_5 NPs everywhere on the surface on the CNTs, and at high magnification (Figure V-12D) we can

appreciate their size: few nm in diameter and 20 to 30 nm in length). However, such a nano-rod like structure does not allow to the Nb_2O_5 NPs penetrating inside the channels of the CNTs.

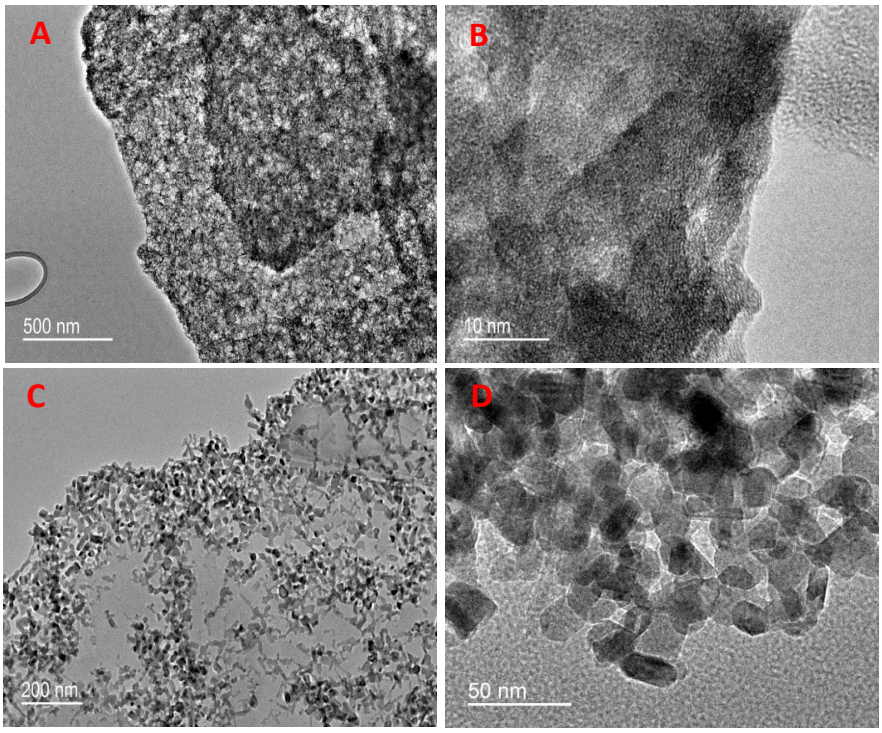

Figure V-11. TEM of Nb_2O_5 coating on Graphene before (A and B) and after(C and D) annealing

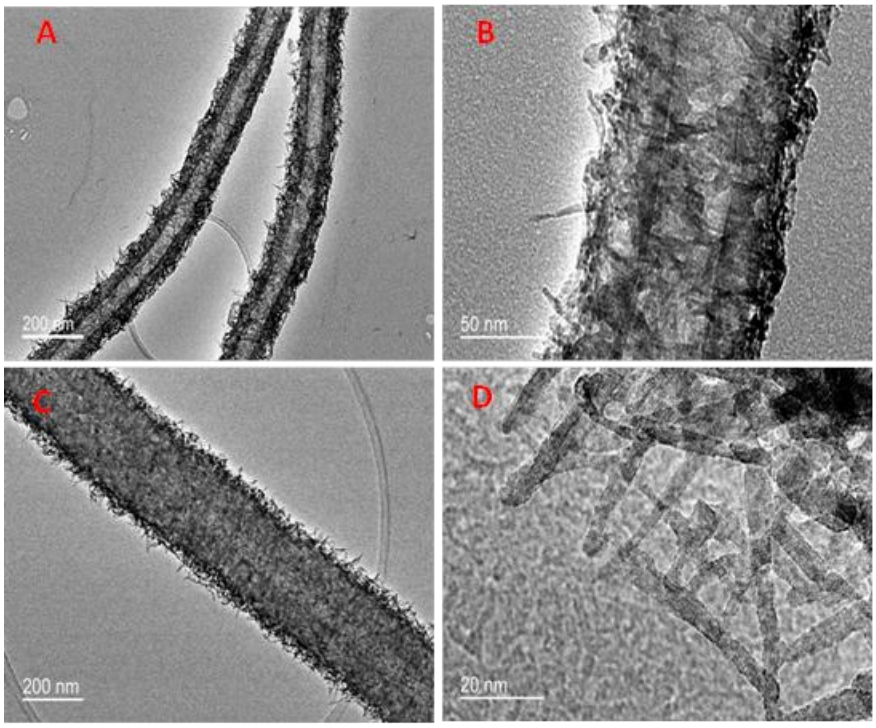

Figure V-12. TEM of Nb_2O_5 coating on CNTs before (A and B) and after(C and D) annealing

V.4.2 XRD analysis

Diffractogramms of the Nb_2O_5 and their carbon based composites synthesized by hydrothermal approach are represented in Figure V-13. Before calcination, a rather broad peak appears at 22.5 ° and others in between 25 and 30 ° attesting that most of the oxide is amorphous. After calcination, new peaks appear and are stronger and sharper, which displays that the NPs are well crystallized, in agreement with an orthorhombic structure (JCPDS-30-0873). In the case of Nb_2O_5@FLG, the extra peak at 26.4^o corresponds to the graphitic carbon (JCPDS-26-1077). Peaks obtained in the case of Nb_2O_5/CNTs are not so well defined but correspond to the same orthorhombic structure : longer analyses time would be needed to increase their resolution.

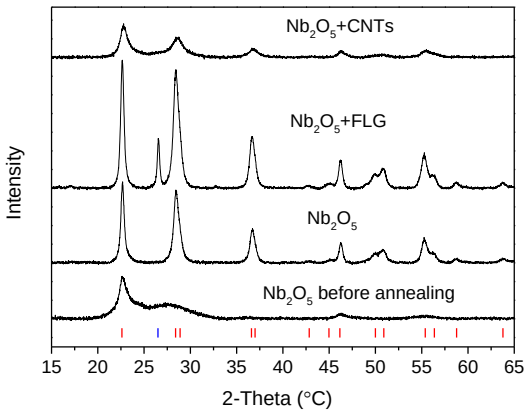

Figure V-13. XRD of Nb_2O_5 (before and after annealing) and Nb_2O_5 associated with carbon materials after annealing. Red bars: Nb_2O_5 with orthorhombic structure and blue bar: Graphite as reference.

V.4.3 BET analysis

In Table V-2, the surface areas of the Nb_2O_5-2 and of the carbon based composites are presented. Those of carbon based composites are higher in comparison with the case of Nb_2O_5-1, and more particularly in the case of CNTs that must be attributed to the small size of the nanorods of N_2O_5.

Table V-2. Surface area of Nb_2O_5 and corresponding carbon based composites by hydrothermal method.

	Hydrothermal method		
	Nb_2O_5-2	Nb_2O_5-FLG-2	Nb_2O_5-CNTs-2
Surface area (m^2/g)	55.1	69.8	108.7

V.5 Electrochemical test

As already specified, these results are very recent and have been performed few weeks ago in Toulouse (CIRIMAT, in collaboration with Patrice Simon and Barbara Daffos). As they are rather interesting, we have just reported the most significant results without getting in details from an electrochemical point of view.

V.5.1 Nb_2O_5 and corresponding carbon based composites by solvothermal method

Like a lot of metal oxides, it has been reported that Nb_2O_5 can be a promising candidate as anode material for lithium-ion battery because of its property to be able to store a lot of lithium ions.[19,20,21] However, at this day, only the 'classical orthorhombic' phase was used and to our knowledge, it is the first time that the tetragonal phase is used as anode. In Figure V-14, discharge-charge cycles were carried out in a voltage window of 0.01-3.0 V (vs. Li/Li^+) at a current rate of C/5 (5 hours for a total charge discharge cycle) up to 10 cycles at room temperature (RT) for Nb_2O_5-1, Nb_2O_5-FLG-1 and Nb_2O_5-CNTs-1. We have reported in the first figure the charge/discharge cycles (first columns on the left), then the value of the capacity as a function of the number of cycles, and in the last column the typical voltamogamms. As often observed in the case of metal oxides, the first discharge of the three samples is rather typical : the voltage rapidly drops to approximately 1.6 V, then, decreases more or less rapidly before being stopped at 0,1 V : the high capacity observed during the first cycle indicates a very large amount of lithium stored during the first discharge. But during the second cycle, we can observe a drastic decrease of this capacity: in fact during the first cycle, a lot of lithium is used to form the Solid Electrolyte Interface (SEI), lithium which is blocked and will be not restituted during the following cycles. After three or four cycles, the capacity remains quite stable, so that the lithium storage performance becomes rather stable. From a quantitative point of view, we can see higher values obtained when Nb_2O_5 NPs are directly synthesized in the presence of CNTs or graphene. The highest capacity obtained with Nb_2O_5 NPs in the presence of C65 is close to 220 mAh/g then stabilize at 60 mAh/g. In the presence of CNTs or graphene, the first value is rather high (close to 500 mAh/g) and stabilize at 150 mAh/g in the case of graphene and 180 mAh/g with CNTs. This large difference cannot be attributed to the presence of CNTs or graphene for which the capacitance represents only a few dozens of mAh/g. In fact we assume that Nb_2O_5 NPs are well dispersed and crystallized on the carbonaceous materials favoring a good contact between the two entities that not necessarily the case in the case of the Nb_2O_5 NPs/C65 mixture.

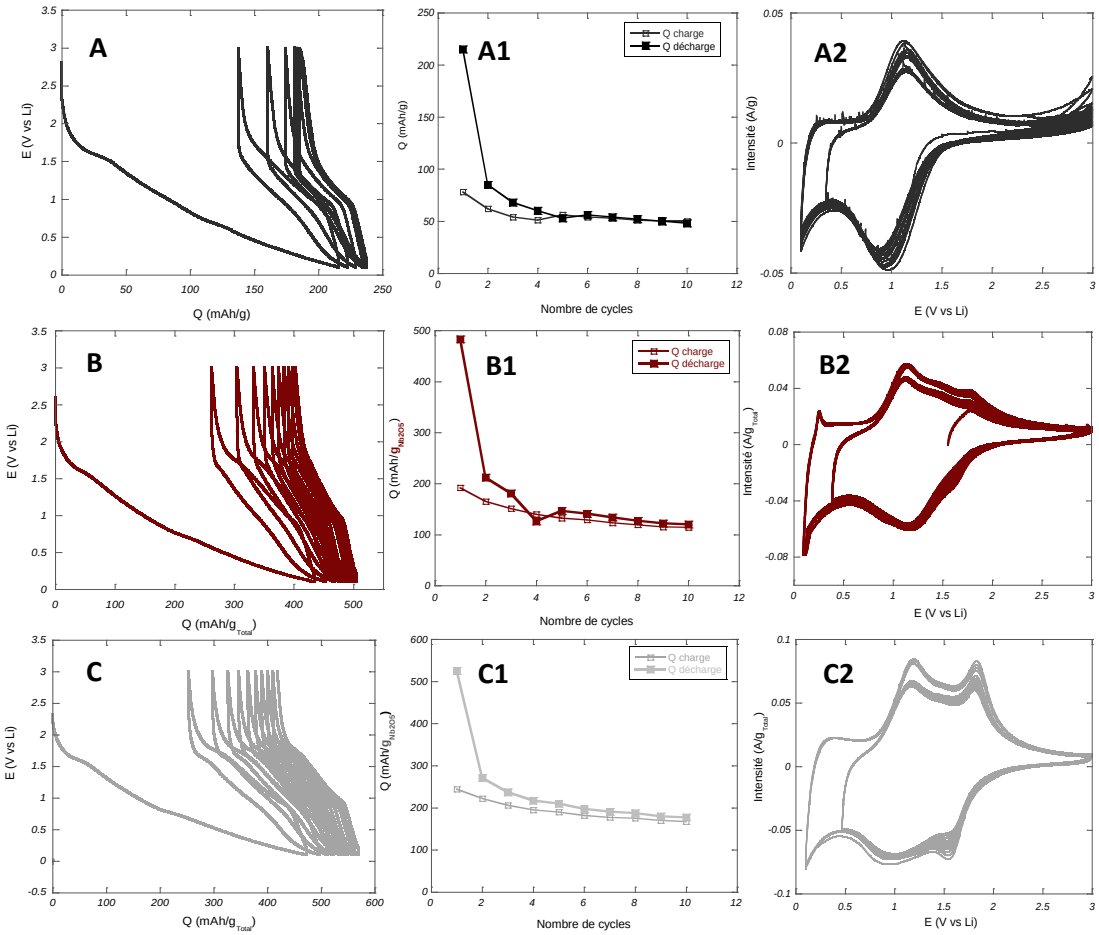

Figure V-14. Charge-discharge curves of Nb_2O_5-1(A), Nb_2O_5-FLG-1(B) and Nb_2O_5-CNTs-1(C) synthesized by solvothermal method in the voltage range 0.01–3.0 V (vs. Li) at a rate C/5. Capacity versus cycle number plot of Nb_2O_5-1(A1), Nb_2O_5-FLG-1(B1) and Nb_2O_5-CNTs-1(C1). Cyclic voltammograms of Nb_2O_5-1(A2), Nb_2O_5-FLG-1(B2) and Nb_2O_5-CNTs-1(C2) in the voltage range 0.01–3.0 V at a scan rate 0.2mv/s

Voltammograms were recorded at room temperature (RT) in the 0.01-3.0 V range at scan rate of 0.2 mV/s. Electrochemical Li^+ intercalation and de-intercalation process which takes place at Nb_2O_5 electrodes can be expressed as the following: $Nb_2O_5+xLi^++xe^- \leftrightarrows LixNb_2O_5$, where the maximum capacity x=2. [19,20] In the case of Nb_2O_5-1, one broad cathodic peak appears at 0.85V, which corresponds to the insertion of Li^+, leading to the reduction of Nb^{5+} ions to Nb^{4+}. The anodic peak, corresponding to the desertion of Li^+ and oxidation of Nb^{4+} into Nb^{5+}, was identified at 1.15 V. We can also notice that a slightly positive shift of cathodic peak occurs at higher voltage after the 1st cycle, which is caused by a polarisation effect of the electrode in the first cycle.[22] In the case of Nb_2O_5-FLG-1 and Nb_2O_5-CNTs-1, two anodic peaks were observed, at 1.15V and 1.8V, respectively. The extra peak at 1.8V cannot be ascribed to the graphene or CNTs and has never been observed: it could be attributed to two oxidation degrees of the niobium (from Nb^{3+} to $Nb^{5+)}$ but it would involve the presence of

four electrons. We can also consider the presence of two kinds of sites needing different energy for the lithium diffusion. At this time, we cannot conclude and no reference in the literature can be found relating the tetragonal form of Nb_2O_5 so that additional works have to be performed.

To valid such results, additional works have been performed to study the response of the electrode as a function of the speed of the charge/discharge cycles. The results are presented in Figure V-15. in the case of Nb_2O_5-FLG-1 and Nb_2O_5-CNTs-1. With increasing current rate from lower values (C/40 – 40 hours) to higher values (8C – 7min and 30 sec), : we can see that the curves show a good linearity up to 4C attesting a good response of the system. From 8C, the speed becomes too high and Li ions cannot move so fast.

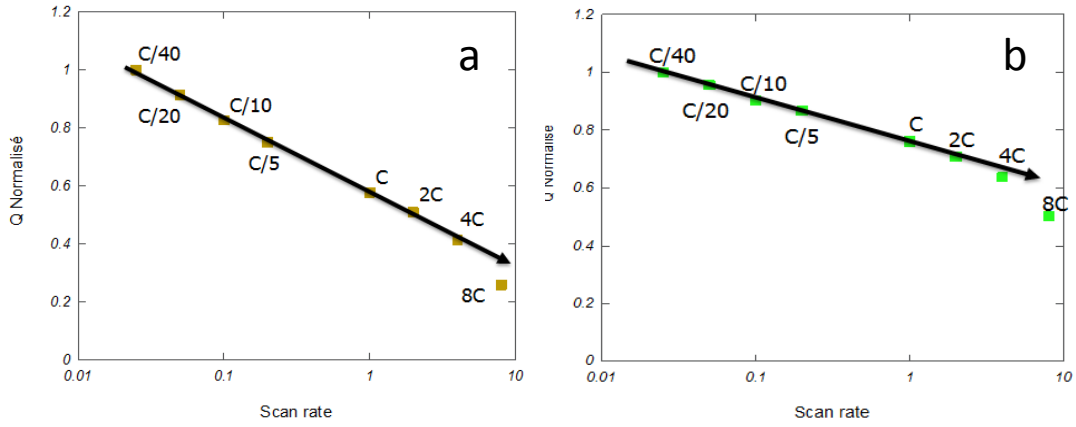

Figure V-15. Normalized Rate capability of Nb_2O_5-FLG-1 (a) and Nb_2O_5-CNTs-1 (b)

V.5.2 Nb_2O_5 and Corresponding Carbon Based Composites synthesized by Hydrothermal Method

Discharge-charge cycles for Nb_2O_5-2, Nb_2O_5-FLG-2 and Nb_2O_5-CNTs-2 synthesized by hydrothermal route are presented in Figure V-16. In the same measurement conditions that for samples obtained by solvothermal route. As observed in Figure V-16, regarding the first discharge of each sample, the voltage steeply drops to approximately 1.9 V. It then gradually decreases before to reach a very small plateau at roughly 0.9 V, which is generally attributed to the formation of SEI layers on the surface of anode [6] (in the subsequent cycles, this plateau disappears). As previously described, a great capacity decrease occurs as soon as the second cycle and

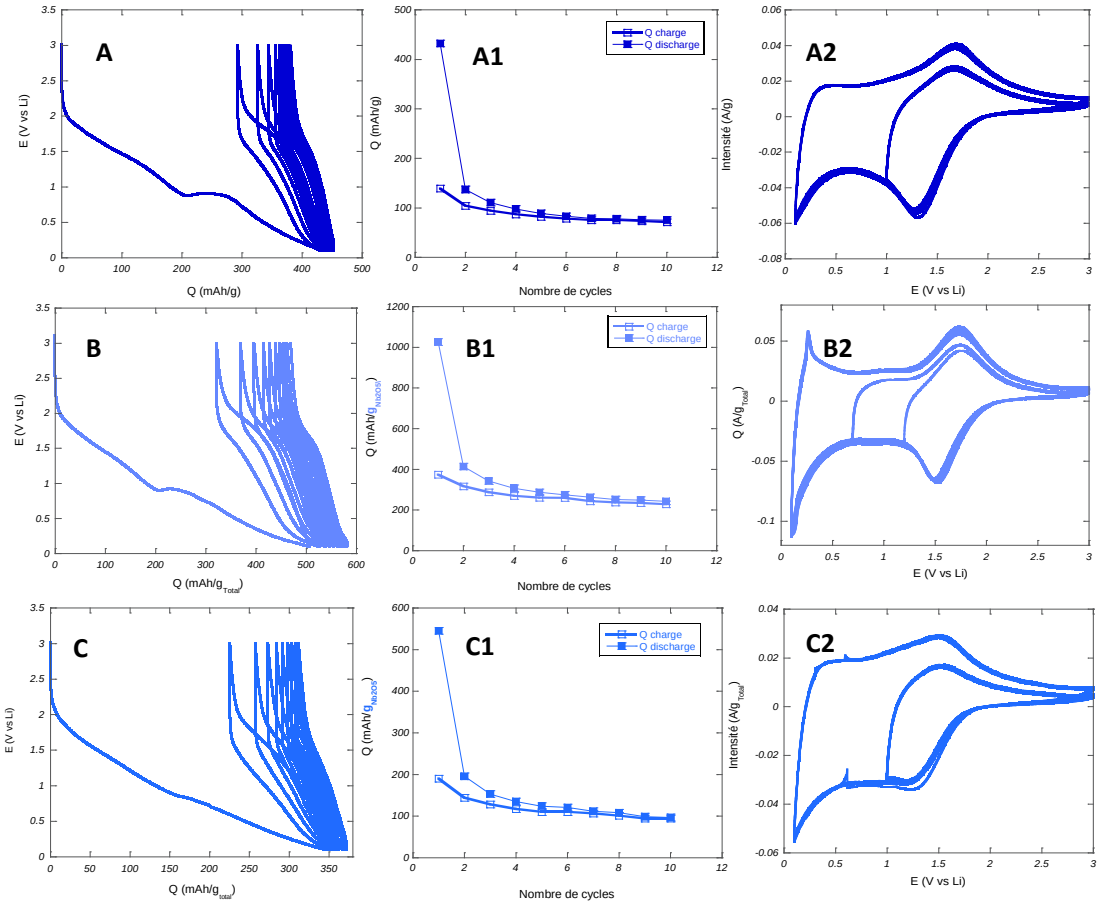

Figure V-16. Charge-discharge curves of Nb_2O_5-2(A), Nb_2O_5-FLG-2 (B) and Nb_2O_5-CNTs-2(C) by hydrothermal method in the voltage range 0.01–3.0 V (vs. Li) at a rate C/5. Capacity versus cycle number plot of Nb_2O_5-2(A1), Nb_2O_5-FLG-2(B1) and Nb_2O_5-CNTs-2(C1). Cyclic voltammograms of Nb_2O_5-2(A2), Nb_2O_5-FLG-2(B2) and Nb_2O_5-CNTs-2(C2) in the voltage range 0.01–3.0 V at a scan rate 0.2mv/s.

then stabilizes. If we compare with the tetragonal Nb_2O_5 phase, the initial capacity is twice higher (430 mAh/g) at this time, we are yet able to explain such a difference between these two behaviors certainly in relation with the number of sites accessible to the Li ion. In the case of Nb_2O_5 NPs associated with nanocarbon structures, a same behavior is observed and we can observe a very high initial capacity in the case of the Nb_2O_5-FLG (close to 1000 mAh/g). The capacity then stabilize to reach a value close to 260 mAh/g in the case of the graphene compsites. If we take into account the voltammograms, in the case of Nb_2O_5-2, one broad cathodic peak appears at 1.68V, which corresponds to the insertion of Li^+, accompanied by the reduction of Nb^{5+} ions into Nb^{4+}. The oxidation peak, corresponding to the desertion of Li^+ and oxidation of Nb^{4+} ions into Nb^{5+}, was identified at 1.38 V. In the presence of CNTs and graphene, no additional peaks are this time observed, that is a more typical behavior.

To study the power of such battery system, many experiments have been performed at different sweep speeds as in the case of the Nb_2O_5 tetragonal phase. Once again, the response

of the system is quite stable from C/40 up to 4C and the normalized rate capability as a function of the scan rate id linear. When the rate is increased to 8C, the capability deviates from the linear trend, lithium ions being unable to move so far.

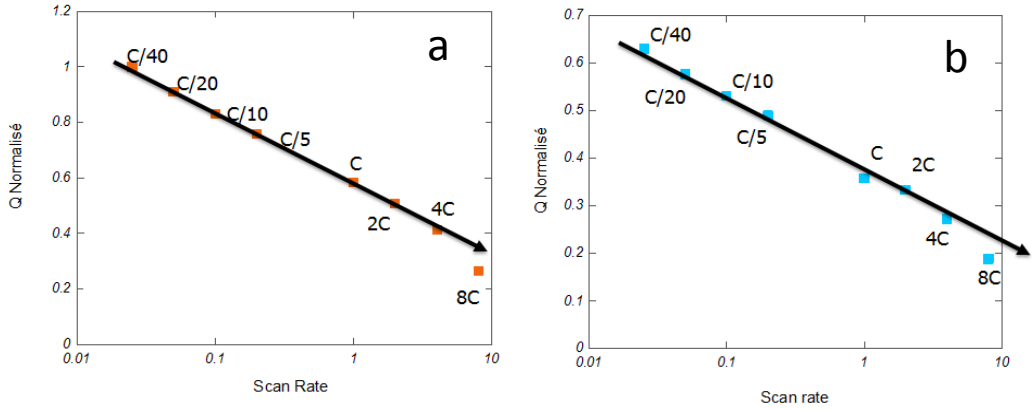

Figure V-17. Normalized rate capability of Nb_2O_5-FLG-2 (a) and Nb_2O_5-CNTs-2 (b)

V.6 Conclusions

In this chapter, we reported preliminary results concerning two different routes to synthesize two different types of Nb_2O_5: the solvothermal way giving rise to Nb_2O_5 NPs with tetragonal structure and the hydrothermal way giving Nb_2O_5 NPs with an orthorhombic structure. Such syntheses have been performed in the presence or not of CNTs or graphene and we have seen that in the two cases a high coating of the carbonaceous material is obtained. XRD, TEM and SEM analyses have shown that a calcination to a temperature close to 400 ℃ was necessary to obtain well crystallized NPs which are platelet like in the case of the tetragonal structure and under the form of nanorod in their orthorhombic phase.

Such composites have been then studied in Lithium-ion battery as anode, works which are very recent and have not yet been in-depth studied. As in the case of most of metal oxides used in such conditions, a great irreversibility is observed after the first charge/discharge due to the Solid Electrolyte interphase (SEI) formation and capacity stabilities after five cycles: the best result is obtained in the case of the composite Nb_2O_5 (orthorhombic)-graphene (260 mAh/g). Power test have been performed with success (linearity of the curve representing the capability as a function of the scan rate of the potential) but more experiments have to be performed, mainly to see if the system is stable after several hundred of cycles.

References

1. Tarascon, J. M. & Armand, M. Issues and challenges facing rechargeable lithium batteries. *Nature* **414,** 359–67 (2001).

2. Yazami, R. & Universitaire, D. A reversible graphite-lithium electrochemical generators. **9,** 365–371 (1983).

3. Flandrois, S. & Simon, B. Carbon materials for lithium-ion rechargeable batteries. *Carbon N. Y.* **37,** 165–180 (1999).

4. Endo, M., Kim, C., Nishimura, K., Fujino, T. & Miyashita, K. Recent development of carbon materials for Li ion batteries. *Carbon N. Y.* **38,** 183–197 (2000).

5. Poizot, P., Laruelle, S., Grugeon, S., Dupont, L. & Tarascon, J. M. Nano-sized transition-metal oxides as negative-electrode materials for lithium-ion batteries. *Nature* **407,** 496–9 (2000).

6. Taberna, P. L., Mitra, S., Poizot, P., Simon, P. & Tarascon, J.-M. High rate capabilities Fe3O4-based Cu nano-architectured electrodes for lithium-ion battery applications. *Nat. Mater.* **5,** 567–73 (2006).

7. Chen, J., Xu, L., Li, W. & Gou, X. ?-Fe2O3 Nanotubes in Gas Sensor and Lithium-Ion Battery Applications. *Adv. Mater.* **17,** 582–586 (2005).

8. Cabana, J., Monconduit, L., Larcher, D. & Palac ń, M. R. Beyond intercalation-based Li-ion batteries: the state of the art and challenges of electrode materials reacting through conversion reactions. *Adv. Mater.* **22,** E170–92 (2010).

9. Wang, H., Cui, L., Yang, Y. & Casalongue, H. S. Mn 3 O 4 - Graphene Hybrid as a High-Capacity Anode Material for Lithium Ion. 13978–13980 (2010).

10. Chan, C. K. *et al.* High-performance lithium battery anodes using silicon nanowires. *Nat. Nanotechnol.* **3,** 31–35 (2008).

11. Yang, S., Feng, X., Ivanovici, S. & M ü llen, K. Fabrication of graphene-encapsulated oxide nanoparticles: towards high-performance anode materials for lithium storage. *Angew. Chem. Int. Ed. Engl.* **49,** 8408–8411 (2010).

12. Shi, W., Rui, X., Zhu, J. & Yan, Q. Design of Nanostructured Hybrid Materials Based on Carbon and Metal Oxides for Li Ion Batteries. *J. Phys. Chem. C* **116,** 26685–26693 (2012).

13. Du, M., Xu, C., Sun, J. & Gao, L. Synthesis of α-Fe2O3 nanoparticles from Fe(OH)3 sol and their composite with reduced graphene oxide for lithium ion batteries. *J. Mater. Chem. A* **1,** 7154 (2013).

14. Xu, J. & Zhu, Y. Monodisperse Fe 3 O 4 and γ - Fe 2 O 3 Magnetic Mesoporous Microspheres as Anode Materials for Lithium-Ion Batteries. 2–7 (2012).

15. Xiong, Q. Q. *et al.* Synthesis of Hierarchical Hollow-Structured Single-Crystalline Magnetite (Fe 3 O 4) Microspheres: The Highly Powerful Storage versus Lithium as an Anode for Lithium Ion Batteries. **c,** (2012).

16. Chen, Y., Song, B., Tang, X., Lu, L. & Xue, J. One-step synthesis of hollow porous Fe3O4 beads–reduced graphene oxide composites with superior battery performance. *J. Mater. Chem.* **22,** 17656 (2012).

17. Jana, S. & Rioux, R. M. Seeded growth induced amorphous to crystalline transformation of niobium oxide nanostructures. *Nanoscale* **4,** 1782–1788 (2012).

18. Janowska, I. *et al.* Mechanical thinning to make few-layer graphene from pencil lead. *Carbon N. Y.* **50,** 3106–3110 (2012).

19. Augustyn, V. *et al.* High-rate electrochemical energy storage through Li+ intercalation pseudocapacitance. *Nat. Mater.* **12,** 518–522 (2013).

20. Li, G., Wang, X. & Ma, X. Nb2O5-carbon core-shell nanocomposite as anode material for lithium ion battery. *J. Energy Chem.* **22,** 357–362 (2013).

21. Sasidharan, M., Gunawardhana, N., Yoshio, M. & Nakashima, K. Nb2O5 hollow nanospheres as anode material for enhanced performance in lithium ion batteries. *Mater. Res. Bull.* **47,** 2161–2164 (2012).

22. Rahman, M. M. *et al.* A vein-like nanoporous network of Nb2O5 with a higher lithium intercalation discharge cut-off voltage. *J. Mater. Chem. A* **1,** 11019 (2013).

Conclusions and Perspectives

The objective of this work was to synthesize magnetic nanoparticles and carbon based nanohybrid materials for biomedical and energy applications In a first part,we studied the influence of the nature of ligands on the composition and shape of CoO and Fe_3O_4 nanoparticles (NPs) synthesized by thermal decomposition of a metal (iron and cobalt) stearate in the presence of a ligand as surfactant in a high boiling solvent. The morphologies of both iron oxide and cobalt oxide NPs are completely different depending of the nature of ligands (amine based or carboxylate based ligands: oleic acid, oleylamine, hexadecylamine). For iron oxide, whatever the nature of ligands, the shape is spherical and the size is decreased in the presence of amine ligands. Concerning cobalt oxide, depending on the nature of ligands, the shape may be either spherical or under the form of stars or spherical clusters made of small nanocrystals. The thermal decomposition of cobalt stearate occurs at a temperature much higher than that of the iron stearate and such a behavior has been partially studied by in situ X-ray photoelectron spectroscopy. Modeling works have shown that the process of the degradation of these stearates was completely different.

In a second part, we have allied iron oxide which is ferrimagnetic and cobalt oxide which is antiferromagnetic, resulting to the formation of core shell nanoparticles (Fe_3O_4@CoO core-shell NPs) giving rise to an exchange bias phenomenon. Core-shell Fe_3O_4@CoO has been synthesized by tuning the thickness of the cobalt shell at the surface of iron oxide NPs and were obtained via a seed-mediated growth method. The CoO coating evolves from a homogeneous to a heterogeneous growth on the surface of iron oxide NPs when the amount of Co precursor increases. The evolution of the magnetic properties as a function of the shell thickness have been explained by the formation of an interfacial phase displaying a high anisototropy and exchange bias properties. The highest coupling exchange account was obtained for the Fe_3O_4@CoO core-shell NPs obtained from a precursor ratio Co/Fe, which displays the highest interface and thickness of AFM (antiferromagnetic) shell. In contrast, the formation of a discontinuous and polycrystalline AFM shell results in a strong decrease of the exchange field despite the average shell thickness increases. Last, the core-shell NPs have been assembled in films by the Langmuir-Blodgett techniques. The quality of the films was related to the quality of NPs: NPs with a homogeneous size assembled in monolayer films when NPs with a heterogeneous shape formed multilayer films. Magnetic measurements performed on films have shown that the dipolar interactions resulting from the assembling in films induce a decrease of the exchange bias properties of NPs.

The following chapter has been devoted to the nanoparticle encapsulation inside CNTs and such nanohybrid materials have been used in a specific biomedical application. This works which have been published in ACS Nano are the result of a strong collaboration between four laboratories: ICPEES, IPCMS (synthesis and

characterization) and IBMC (functionalization) in Strasbourg and LMSC (biomedical) in Paris Diderot. In a first part, we have optimized the conditions of CNTs filling by metal oxide NPs to form NPs@CNTs. We have shown in a first step that all the oxygenated functions on the surface of the NTCs must be removed by an appropriate heat treatment (900 ℃ under inert atmosphere) to favor the diffusion of the salt in the NTCs cavity. The synthesis conditions are the same than those described in the 2th chapter, the CNTs being added in the precursor solution. We have shown that the NTCs play the role of nano-reactors: indeed they prevent oxidation and allow synthesizing metal oxide NPs not obtained without their presence. In the case of iron oxide, we obtained spherical NPs but with higher size and a lower oxidation level. In the case of cobalt, we obtained cubic clusters for which the size was tuned by the inner diameter of the NTCs; furthermore as only CoO was obtained without CNTs, in their presence metallic cobalt has been identified.

Then, Carbon nanotubes filled with magnetic NPs have been successfully obtained with a high filling rate (up to 50 wt%) by an original double filling process. Despite the removal of oxidizing groups at the surface of CNTs to trigger the synthesis of NPs inside CNTs, we succeed in functionalizing them by amino groups to ensure a good dispersibility in aqueous medium. The properties of the filled magnetic CNTs as heat mediator for photo-thermal ablation and as contrast agent for MRI were then evaluated and promising results were obtained. They are capable of absorbing and efficiently converting NIR light into heat to generate thermoablative temperatures and cell lysis. They have potential for use as agents for T_2 MR contrast imaging and MR image-guided photo-thermal therapy. Last but not least they can be magnetically manipulated in order to accumulate in a target site, to control their orientation and cell uptake, to drive cell motion and to trigger remote stirring in the biological environment.

In the last chapter, we have synthesized Nb_2O_5 NPs and their carbon based composites (with graphene-like materials and CNTs) and tested their potential as anode in Li-ion battery, works which have been performed in collaboration with the CIRIMAT in Toulouse. Two different routes have been used to synthesize two different types of Nb_2O_5: the solvothermal way giving rise to Nb_2O_5 NPs with tetragonal structure and the hydrothermal way giving Nb_2O_5 NPs with an orthorhombic structure. Such syntheses have been performed in the presence or not of CNTs or graphene and we have seen that in both cases a high coating level of the carbonaceous material is obtained. XRD, TEM and SEM analyses have shown that a calcination to a temperature close to 400 ℃ was necessary to obtain well crystallized NPs which are platelet like in the case of the tetragonal structure and under the form of nanorod in their orthorhombic phase.

Such composites have been then studied in Lithium-ion battery as anode, works

which are very recent and have not yet been in-depth studied. As in the case of most of metal oxides used in such conditions, a great irreversibility is observed after the first charge/discharge due to the Solid Electrolyte Interphase (SEI) formation and capacity stabilize after five cycles: the best result is obtained in the case of the composite Nb_2O_5 (orthorhombic)-graphene (260 mAh/g). Power tests have been performed with success (linearity of the curve representing the capability as a function of the scan rate of the potential) but more experiments have to be performed, mainly to see if the system is stable after several hundred of cycles.

Perspectives

For the synthesis of nanoparticles, a lot of parameters, such as ligands and temperature, influence the shape and the size of NPs, which further determinate their intrinsic properties. So, in order to obtain the desirable properties, the "design" of NPs become a key issue. However, the mechanism of formation of the NPs synthesized in this study is not yet well understood and must be in-depth studied. Furthermore, functionalization of NPs can be also a promising route to modify their properties instead of varying their shape and size. For instance, exchange bias coupling is introduced by coating antiferromagnetic CoO on ferrimagnetic Fe_3O_4, but we can imagine a multi-shell synthesis that can have significant impact on the feature of such materials and their "multi-functionality".

Concerning the magnetic NPs encapsulated inside CNTs, promising results were obtained : They are capable of absorbing and efficiently converting NIR light into heat to generate thermoablative temperatures and cell lysis. They have potential for use as agents for T_2 MR contrast imaging and MR image-guided photothermal therapy and a study on the in vivo therapeutic potential of these hybrids and on the evaluation of their pharmacokinetic profile are actually in progress.

Last, promising results have been obtained with carbon-based Nb_2O_5 materials for lithium battery : they are preliminary results which must be more in-depth studied and in a short future, we have to study their behavior during many charge/discharge cycles. With NTCs, we have seen that the niobium oxide is deposited on their outer surface : one of the challenge would be to synthesize them inside the channel that could decrease the swelling during the insertion/de-insertion cycles.

Acknowledgements

My Ph.D study was carried out in Institut de chimie et procédés pour l'énergie, l'environnement et la Santé (ICPEES) and Institut de Physique et Chimie des Matériaux de Strasbourg (IPCMS), where I have learnt a lot about how to be a good scientist from my supervisors and colleagues and spent wonderful three years with them in my life. So, in my thesis, i would like to dedicate my gratitude to the people who help me in the Ph.D study and influence me in my scientific career.

Foremost, I would like to express my sincere gratitude to my supervisors Dr. Dominique Bégin and Prof. Sylvie Bégin-Colin for their patience, enthusiasm, immense knowledge and consistent support of my Ph.D study. Their guidance helped me in all the time of research and writing of this thesis. More importantly, under their responsible supervision, my level of expertise and research skills has been expanded greatly.

I would also like to give my special thanks to Dr. Cuong Pham-Huu for his excellent ideas and discussion on the nanoparticles encapsulated carbon nanotube and Dr. Benoît Pichon for his broad knowledge and significant guidance on the synthesis of magnetic core-shell nanoparticles. Besides, my grateful thanks are also extended to Dr. Alberto Bianco (IBMC Strasbourg), Dr. Florence Gazeau (MSC-Paris Diderot) and Prof. Patrice Simon (CIRIMAT Toulouse), who performed our materials for biological and lithium battery application, as well as Dr. Carlo Massobrio and Dr. Mauro Boero (IPCMS) for the simulation.

I would like to thank members of defense jury Katerina Soulantika (LPCNO Toulouse), Alain Celzard (ENSTIB-Epinal), Corinne Petit (ICPEES Strasbourg) and Olivier Sandre SANDRE (LPMC Bordeaux) for their carefully reviewing and constructive coments on my thesis.

Thanks to the assitance of my colleagues in these two institutes, the results can be presented systematically and thoroughly in my thesis. So, I would like to give my appreciation to them: Corinne Ulhaq, Ovidiu Ersen, Dris Ihiawakrim and Damien Mertz for transmission electron microscopy measurment and analysis; Thierry Dintzer for X-ray diffraction and particularlly Christophe Lefevre for the XRD data refinement; Alain Derory for magnetic measurement; Cedric Leuvrey for scanning electron microscopy; Didier Burger and Secou Sall for the thermogravimetric analysis; Spiros Zafeiratos for X-ray photoelectron spectroscopy analysis; Sergey Pronkin for the electrochemcial measurements; Yu liu for nanoparticle film fabrication and atomic force microscopy; Céline Kieffer for infrared spectroscopy and management of

chemicals. My appreciation also equally goes to the all the researchers and direction in these two group, in particular Pierre Rabu (leader of DCMI), Izabela Janowska, Sylvie Mainge (secretary of DCMI), Véronique Verkruysse (Secretary of ICPEES) for their kindness.

I would also like to give my deep thanks to the Ph.D students and postdoctoral fellows in my group for their helpful and energetic discussion, Georgian Melinte, Walid Baaziz, Delphine Toulemon, Aurelie Walter, Geoffrey Cotin, Mathias Dolci, Olivier Gerber, Mathilde Menard, Solenne Fleutot, Cristina Blanco-Andujar, YueFeng Liu, Fabric Vigneron, Cuong Duong Viet, Benoit de Tymowski, Housseinou Ba, Jean-Mario Nhut, Elodie Pardieu, Azhar Pirzado, Lai Truong-Phuoc. In addition, grateful thanks are given to chinese friends and nice people from different countries i meet in Strasbourg for the wonderful time with them.

Last but not the least, I would like to thank my family for their unconditional support and encourage.

Thank you very much.

Xiao Jiu LIU

Synthesis of Magnetic Nanoparticles and Carbon Based Nanohybrid Materials for Biomedical and Energy Application

Résumé

Les travaux de cette thèse ont été consacrés à la synthèse de nanoparticules magnétiques d'oxyde de fer et d'oxyde de cobalt et de nanoparticules cœur-coquille constituées d'un cœur d'oxyde de fer recouvert d'oxyde de cobalt et à l'élaboration de nanomatériaux - composites nanostructures carbonées/nanoparticules d'oxyde métallique - pour des applications dans le domaine biomédical et celui de l'énergie. Pour la synthèse des NPs, la forme et la taille des NPs sont fortement dépendantes des conditions de réaction (nature des ligands, des solvants, température de réaction...) , ce qui affecte leurs propriétés magnétiques. De plus, des simulations ont montré que les chaînes de stéarate peuvent désorber plus facilement les atomes de fer que les atomes de cobalt et se libérer pour former des germes, ce qui pourrait expliquer le comportement distinctif entre les deux complexes. Ces nanoparticules magnétiques ont été synthétisées à l'intérieur de nanotubes de carbone en deux étapes aboutissant à des taux de remplissage très importants. Après fonctionnalisation, ces nanocomposites ont été introduits dans de cellules tumorales et ont été magnétiquement manipulées. Ils se sont révélés être très efficaces en tant qu'agents de contraste en IRM mais également dans le daomaine de l'hyperthermie (activation sous éclairage dans le domaine de l'Infrarouge proche). Enfin, de nouveaux composites à partir de nanoparticules de Nb_2O_5 et de graphène (ou NTCs) ont été synthétisés et des résultats prometteurs ont été obtenus dans des tests de batterie lithium-ion : leur utilisation en tant qu'anode a permis d'obtenir des capacités réversibles de 260 mAh/g.

Résumé en anglais

This thesis was focused on the synthesis of magnetic nanoparticles of iron oxide and cobalt oxide and core-shell nanoparticles, consisting of a cobalt oxide coated iron oxide and on the development of composite nanomaterials - nanostructures carbon /metal oxide nanoparticles - for applications in the biomedical field and the energy. For the synthesis of NPs, the shape and size of NPs are dependent of the reaction conditions, which further affect their magnetic properties. Meanwhile, simulation showed that stearate chains can desorb more easily from iron atoms and release to form seeds than from cobalt atoms, which might explain distinctive behavior between the both complexes. Regarding nanostructures carbon/metal oxide nanoparticles hybrid materials, the properties of the filled magnetic CNTs as heat mediator for photothermal ablation and as contrast agent for MRI were then evaluated and promising results have been obtained. Last, new composite materials (Nb_2O_5 nanoparticles/graphene or NTCs) were synthesized and promising results were obtaines in lithium battery tests : their use as anode allowed obtaining reversible capacities of 260 mAh/g.